

# UC Santa Cruz

## UC Santa Cruz Electronic Theses and Dissertations

### Title

Chemically Modified Metal Oxide Nanostructure for Photoelectrochemical Water Splitting

### Permalink

<https://escholarship.org/uc/item/4117n460>

### Author

Wang, Gongming

### Publication Date

2013

Peer reviewed|Thesis/dissertation

UNIVERSITY OF CALIFORNIA  
SANTA CRUZ

**Chemically Modified Metal Oxide Nanostructure for Photoelectrochemical  
Water Splitting**

Dissertation submitted in partial satisfaction  
of the requirements for the degree of

DOCTOR OF PHILOSOPHY

in

CHEMISTRY

by

**Gongming Wang**

June 2013

The Dissertation of Gongming Wang is  
approved:

---

Professor Yat Li, chair

---

Professor Scott R. J. Oliver

---

Professor Jin Z. Zhang

---

Tyrus Miller  
Vice Provost and Dean of Graduate Studies

Copyright © by  
Gongming Wang  
2013

## Table of Contents

List of Figures .....	vi
Abstract .....	xiv
Dedication .....	xvi
Acknowledgements .....	xvii
Chapter 1 .....	1
Introduction of Chemically Modified Nanostructures for Photoelectrochemical Water Splitting.....	1
Abstract .....	1
Introduction.....	2
1.1 The Principle of Photoelectrochemical Water Splitting.....	3
1.2 Common Materials for PEC Water Splitting and Their Limitations .....	5
1.3 Nanostructure and Chemical Modification .....	9
Reference .....	12
Chapter 2 .....	22
Nitrogen-doped ZnO Nanowire Arrays for Photo-electrochemical Water Splitting .....	22
Abstract .....	22
Introduction.....	23
Experimental Section .....	25
Results and Discussions .....	27
Conclusion .....	39
References:.....	40
Chapter 3 .....	45
Double-sided CdS and CdSe Quantum Dot Co-sensitized ZnO Nanowire Arrays for Photoelectrochemical Hydrogen Generation .....	45
Abstract .....	45



Introduction.....	46
Experimental Section .....	48
Results and Discussion .....	51
Conclusion .....	65
References.....	66
Chapter 4.....	69
Facile Synthesis of Highly Photoactive $\alpha$ -Fe <sub>2</sub> O <sub>3</sub> -based Films for Water Oxidation.....	69
Abstract .....	69
Introduction.....	70
Experimental Section .....	73
Results and Discussion .....	77
Conclusion .....	107
Reference .....	107
Chapter 5.....	117
Hydrogen Treated TiO <sub>2</sub> Nanostructures for PEC Water Splitting .....	117
Abstract .....	117
Introduction.....	118
Experimental section:.....	120
Results and Discussion .....	124
Conclusion .....	149
References.....	150
Chapter 6.....	154
Hydrogen Treated WO <sub>3</sub> Nanoflakes for Enhanced Photoactivity and Photostability for PEC Water Splitting.....	154
Abstract .....	154
Introduction.....	154
Experimental Section .....	157
Results and Discussion .....	161
Conclusion .....	176

Reference .....	177
Chapter 7 .....	182
Hydrogen Treated BiVO <sub>4</sub> for Enhanced Photoactivity for PEC Water Splitting .....	182
Abstract .....	182
Introduction.....	183
Experimental Section .....	185
Results and Discussion .....	188
Conclusion .....	208
Reference .....	209
Chapter 8 .....	215
A Mechanistic Study into the Catalytic Effect of Ni(OH) <sub>2</sub> on Hematite for Photoelectrochemical Water Oxidation .....	215
Abstract .....	215
Introduction.....	216
Experimental Section .....	217
Conclusion .....	235
Reference .....	236
Chapter 9 .....	240
Solar Driven Hydrogen gas releasing from Urea and Human Urine .....	240
Abstract .....	240
Introduction.....	241
Experimental Section .....	244
Results and Discussion .....	247
Conclusion .....	258
Reference .....	259

## **List of Figures**

### **Chapter 1**

**Figure 1.1** Schematic of photoelectrochemical cell.

**Figure 1.2** solar spectrum

**Figure 1.3** semiconductor bandgap and band structure

### **Chapter 2**

**Figure 2.1** SEM and TEM image of ZnO nanowires

**Figure 2.2** UV-vis spectra of ZnO and N-ZnO nanowires

**Figure 2.3** XPS and XRD of ZnO and N-ZnO nanowires

**Figure 2.4** Mott-schottky plots of N-ZnO nanowires

**Figure 2.5** IPCE spectra of ZnO and N-ZnO

**Figure 2.6** PEC performances of ZnO and N-ZnO

**Figure 2.7** photostability of N-ZnO for PEC water splitting

### **Chapter 3**

**Figure 3.1** Schematic and band structure of CdS and CdSe quantum dot co-sensitized ZnO nanowires.

**Figure 3.2** Schematic shows the synthesis and device fabrication

**Figure 3.3** SEM and TEM images of ZnO nanowire arrays

**Figure 3.4** TEM image of CdS and CdSe sensitized ZnO nanowires

**Figure 3.5** XRD patterns of ITO, ZnO, CdS-ZnO and CdSe-ZnO.

**Figure 3.6** Linear sweeps of double sided ZnO, only CdSe, only CdSe and co-sensitized ZnO nanowire arrays.

**Figure 3.7** Digital image and UV-vis spectra of ZnO and CdS and CdSe sensitized ZnO samples

**Figure 3.8** IPCE spectra of double sided ZnO, only CdSe, only CdSe and co-sensitized ZnO samples

**Figure 3.9** IPCE and band structure of single sided ZnO sensitized with only CdS, only CdSe and cosensitization.

**Figure 3.10** Linear sweep of single sided ZnO sensitized with only CdS, only CdSe and cosensitization.

**Figure 3.11** comparison of PEC performance of single sided electrode and double sided electrode

## **Chapter 4**

**Figure 4.1** XRD of prepared  $\text{Fe}_2\text{O}_3$

**Figure 4.2** schematic of the synthesis and digital image of prepared  $\text{Fe}_2\text{O}_3$

**Figure 4.3** SEM image of  $\text{Fe}_2\text{O}_3$  with different precursor concentrations

**Figure 4.4** Raman spectra of  $\text{Fe}_2\text{O}_3$  with different precursor concentrations

**Figure 4.5** photocurrent versus deposition cycles

**Figure 4.6** Cross sectional SEM image of  $\text{Fe}_2\text{O}_3$  on FTO glass

**Figure 4.7** Optimized photocurrent densities with different precursor concentration

**Figure 4.8** Schematic showing the particle size dependent depletion and diffusion thickness

**Figure 4.9** linear sweep of  $\text{Fe}_2\text{O}_3$  with different annealing temperature

**Figure 4.10** temperature dependent photocurrent density

**Figure 4.11** temperature dependent raman spectra

**Figure 4.12** SEM image of Ti doped  $\text{Fe}_2\text{O}_3$

**Figure 4.13** XPS spectra of  $\text{Fe}_2\text{O}_3$  and Ti doped  $\text{Fe}_2\text{O}_3$

**Figure 4.14** XPS valence band and Fe 2p spectra

**Figure 4.15** PEC performance of  $\text{Fe}_2\text{O}_3$  with Ti dopant concentration and deposition cycles

**Figure 4.16** PEC performance comparison of  $\text{Fe}_2\text{O}_3$  and Ti doped  $\text{Fe}_2\text{O}_3$

**Figure 4.17** Mott-schottky plots of  $\text{Fe}_2\text{O}_3$  and Ti doped  $\text{Fe}_2\text{O}_3$

**Figure 4.18** Nyquist plots of  $\text{Fe}_2\text{O}_3$  and Ti doped  $\text{Fe}_2\text{O}_3$

**Figure 4.19** Transition absorption spectra of  $\text{Fe}_2\text{O}_3$  and Ti- $\text{Fe}_2\text{O}_3$

## **Chapter 5**

**Figure 5.1** SEM images of  $\text{TiO}_2$  nanowire arrays

**Figure 5.2** TEM images of  $\text{TiO}_2$  nanowire

**Figure 5.3** digital image of  $\text{TiO}_2$  and hydrogen treated  $\text{TiO}_2$

**Figure 5.4** XRD of  $\text{TiO}_2$  and hydrogen treated  $\text{TiO}_2$

**Figure 5.5** photocurrents versus hydrogen treatment temperature

**Figure 5.6** I-V curves of  $\text{TiO}_2$  and hydrogen treated  $\text{TiO}_2$  at different temperatures

**Figure 5.7** Solar to hydrogen conversion efficiency curve of  $\text{TiO}_2$  and hydrogen treated  $\text{TiO}_2$  samples

**Figure 5.8** The schematic of home built gas collection

**Figure 5.9** Gas production profile of hydrogen treated  $\text{TiO}_2$

**Figure 5.10** I-V curves of hydrogen treated  $\text{TiO}_2$  under front and back side light illumination

**Figure 5.11** IPCE and integrated solar to hydrogen conversion efficiency of  $\text{TiO}_2$  and hydrogen treated  $\text{TiO}_2$  samples.

**Figure 5.12** XPS survey of  $\text{TiO}_2$  and hydrogen treated  $\text{TiO}_2$

**Figure 5.13** XPS Ti 2p and O1s

**Figure 5.14** XPS valence band spectra

**Figure 5.15** band structure of hydrogen treated  $\text{TiO}_2$

**Figure 5.16** Mott-schottky curves of  $\text{TiO}_2$  and hydrogen treated  $\text{TiO}_2$

**Figure 5.17** SEM and XRD of  $\text{TiO}_2$  nanotube arrays

**Figure 5.18** PEC performance of  $\text{TiO}_2$  and hydrogen treated  $\text{TiO}_2$  nanotube arrays

## Chapter 6

**Figure 6.1** SEM and TEM images of  $\text{WO}_3$  nanoflakes

**Figure 6.2** UV-vis spectra of  $\text{WO}_3$  and hydrogen treated  $\text{WO}_3$

**Figure 6.3** XRD and Raman spectra of  $\text{WO}_3$  and H- $\text{WO}_3$

**Figure 6.4** I-V curves, temperature dependent photocurrent and photocurrent retention.

**Figure 6.5** Photostability of  $\text{WO}_3$  and hydrogen treated  $\text{WO}_3$

**Figure 6.6** IPCE spectra of  $\text{WO}_3$  and hydrogen treated  $\text{WO}_3$

**Figure 6.7** XPS W 4f spectra

**Figure 6.8** XPS O1s spectra

**Figure 6.9** The study of photostability of hydrogen treated  $\text{WO}_3$  and electrochemical reduced  $\text{WO}_3$

**Figure 6.10** XPS valence band spectra of  $\text{WO}_3$  and hydrogen treated  $\text{WO}_3$

**Figure 6.11** Mott-schottky plots of  $\text{WO}_3$  and hydrogen treated  $\text{WO}_3$

## Chapter 7

**Figure 7.1** Simulated supercells of  $\text{BiVO}_4$  and hydrogen treated  $\text{BiVO}_4$

**Figure 7.2** Range of possible stoichiometric regimes for the atomic chemical potential of Bi, V and O to sustain stable growth of  $\text{BiVO}_4$

**Figure 7.3** Plots of formation energies of defects in  $\text{BiVO}_4$  versus the

electrochemical chemical potentials for four kinds of conditions.

**Figure 7.4** Cross sectional SEM image of BiVO<sub>4</sub>/FTO glass.

**Figure 7.5** UV-vis spectra of BiVO<sub>4</sub> and H-BiVO<sub>4</sub>

**Figure 7.6** XRD and Raman spectra of BiVO<sub>4</sub> and H-BiVO<sub>4</sub>

**Figure 7.7** XPS survey and O1s of BiVO<sub>4</sub> and H-BiVO<sub>4</sub>

**Figure 7.8** XPS spectra of V 2p and Bi 4f.

**Figure 7.9** Mott-schottky and Nyquist plots of BiVO<sub>4</sub> and H-BiVO<sub>4</sub>

**Figure 7.10** I-V curves and IPCE spectra of BiVO<sub>4</sub> and H-BiVO<sub>4</sub>

**Figure 7.11** Photostability of H-BiVO<sub>4</sub> for long time testing

## Chapter 8

**Figure 8.1** SEM and XRD of Fe<sub>2</sub>O<sub>3</sub> nanowire arrays

**Figure 8.2** SEM and EDS of Ni catalyst modified Fe<sub>2</sub>O<sub>3</sub> nanowires.

**Figure 8.3** I-V curves of Fe<sub>2</sub>O<sub>3</sub> and Ni-Fe<sub>2</sub>O<sub>3</sub>

**Figure 8.4** I-t curves and photocurrent retention of Fe<sub>2</sub>O<sub>3</sub> and Ni-Fe<sub>2</sub>O<sub>3</sub>

**Figure 8.5** Proposed mechanism for Ni-Fe<sub>2</sub>O<sub>3</sub> during water oxidation

**Figure 8.6** Scan rate dependent photocurrents of Ni-Fe<sub>2</sub>O<sub>3</sub> and Fe<sub>2</sub>O<sub>3</sub>

**Figure 8.7** XPS Ni 2p spectra of Ni-Fe<sub>2</sub>O<sub>3</sub> before and after light illumination

**Figure 8.8** The proposal mechanism using glucose to regenerate Ni<sup>2+</sup>, and I-V curves of Ni-Fe<sub>2</sub>O<sub>3</sub> with/without glucose

**Figure 8.9** I-t curves and photocurrent retention curve of Ni-Fe<sub>2</sub>O<sub>3</sub> with/without



glucose

**Figure 8.10** XPS Ni2p of Ni-Fe<sub>2</sub>O<sub>3</sub> before and after light illumination with glucose

**Figure 8.11** SEM image and EDX of Ni-Fe<sub>2</sub>O<sub>3</sub> with small loading amount of Ni catalyst

**Figure 8.12** I-V curves and photocurrent retention of Ni-Fe<sub>2</sub>O<sub>3</sub> with small loading amount of Ni catalyst

## Chapter 9

**Figure 9.1** Schematic diagram of Ni modified semiconductor for urea splitting

**Figure 9.2** SEM and XRD of TiO<sub>2</sub> nanowire arrays

**Figure 9.3** Cyclic voltammograms of TiO<sub>2</sub>, Ni-TiO<sub>2</sub> with/without urea

**Figure 9.4** I-V curves of TiO<sub>2</sub> and Ni-TiO<sub>2</sub>, and I-t curves at zero bias of Ni-TiO<sub>2</sub>

**Figure 9.5** I-t curves of Ni-TiO<sub>2</sub> in urea solution and GC analysis indicating the hydrogen gas production

**Figure 9.6** Cyclic voltammograms of Ni-TiO<sub>2</sub> in human solution

**Figure 9.7** I-V curves of Ni-TiO<sub>2</sub> in urea and human solution, and I-t curve of Ni-TiO<sub>2</sub> in human urine solution

**Figure 9.8** I-t curves of Ni-TiO<sub>2</sub> at zero bias in human urine solution

**Figure 9.9** SEM and XRD of Fe<sub>2</sub>O<sub>3</sub> on FTO glass

**Figure 9.10** Cyclic voltammograms of  $\text{Fe}_2\text{O}_3$  and  $\text{Ni-Fe}_2\text{O}_3$  with/without urea

**Figure 9.11** I-V curves of  $\text{Fe}_2\text{O}_3$  and  $\text{Ni-Fe}_2\text{O}_3$  in urea solution and the comparison I-V curves of  $\text{Ni-Fe}_2\text{O}_3$  in urea and human urine solution.

## **Abstract**

### **Chemically Modified Metal Oxide Nanostructures for Photoelectrochemical Hydrogen Generation**

By

Gongming Wang

Hydrogen gas is chemical fuel with high energy density, and represents a clean, renewable and carbon-free burning fuel, which has the potential to solve the more and more urgent energy crisis in today's society. Inspired by natural photosynthesis, artificial photosynthesis to generate hydrogen energy has attracted a lot of attentions in the field of chemistry, physics and material. Photoelectrochemical water splitting based on semiconductors represents a green and low cost method to generate hydrogen fuel. However, the current overall efficiency of solar to hydrogen is quite low, due to some intrinsic limitations such as bandgap, diffusion distance, carrier lifetime and photostability of semiconductors. Although nanostructured semiconductors can improve their photoelectrochemical water splitting performance to some extent, by increasing electrolyte accessible area and shortening minority carrier diffusion distance, nanostructure engineering cannot change their intrinsic electronic properties. Recent development in chemically modified

nanostructures such as surface catalyst decoration, element doping, plasmonic modification and interfacial hetero-junction design have led to significant advancement in the photoelectrochemical water splitting, by improving surface reaction kinetics and charge separation, transportation and collection efficiency.

In this thesis, I will give a detailed discussion on the chemically modified metal oxide nanostructures for photoelectrochemical hydrogen generation, with a focus on the element doping, hydrogen treatment and catalyst modification. I have demonstrated nitrogen doping on ZnO and Ti doping on hematite can improve their photoelectrochemical performance. In addition, we found hydrogen treatment is a general and effective method to improve the photocatalytic performance, by increasing their carrier densities. Hydrogen treatment has been demonstrated on  $\text{TiO}_2$ ,  $\text{WO}_3$  and  $\text{BiVO}_4$ . In the end, we also used electrochemical catalyst to modify these metal oxide photoelectrode for waste water treatment and chemical fuel generation.

## **Dedication**

**DEDICATED  
TO  
MY PAPERENTS**

## **Acknowledgements**

First of all, I want to express my thanks to my advisor, Prof. Yat Li, because I cannot come to UC Santa Cruz for my PhD studies without your offer. More importantly, I have learnt a lot of things from you, especially research skills and logics. You always asked me what are the key points and what is the novelty of your work. At the beginning, it is really hard for me to answer these questions. However, it is indeed a good training for me to be a good researcher. Now, I am always thinking these questions when I start a new project. I also need to thank Prof. Li's wife, Fang Qian, for her nice help and discussion in my research. I feel I am so lucky to join your group and this is a wonderful experience for me.

Secondly, I would like to thank my oral and thesis committee, Prof. Jin Z. Zhang, Prof. Scott R. J. Oliver and Prof. Claire Gu. You always hold a high standard for each student and try your best to make the start of their career a success. Especially, I want to thank Prof. Jin Z. Zhang. We have joint group meeting together and you provided a lot of nice suggestions for my research work.

Thirdly, I need thank my labmates, Yichuan Ling, Hanyu Wang, Xihong Lu, Feng Luan, Ying-Chih Pu, Yi Yang, and TianYu Liu for their helps in my research projects. Especially, I need thank Yichuan Ling and Xihong Lu for the material characterization during past two years. In addition, I also want to

express my thanks to my friends in Shaowei's lab, including Xiongwu Kang, Yang Song, Ke Liu, Peiguang Hu, Limei Chen. Xiongwu Kang treated me like a brother and helped me a lot not only in research but also in life when I came to UC Santa Cruz. Although he has left for postdoc studies, I still hope we can work together in future.

Finally, I really need thank my family. Without their support, I can not come to UC Santa Cruz and finish my PhD studies. I know my parents always hold a great hope for me and I want them to be proud of me, which is also why I was being working hard during the last five years. I also want to express my thanks to my wife, Ping Wei. Without your understanding and support, I cannot be here. I cherish everything you have done for me in my heart, and I love you.

---

The text of this dissertation includes reprints of the following previously published or subsequently published materials.

1. "Chemically modified Nanostructures for Photoelectrochemical Water Splitting" **G. Wang**, Y. Ling, X. Lu, and Y. Li, *J. Photochem. Photobiol. C: Reviews*, **2013**, (invited review).
2. "Nitrogen-doped ZnO nanowire arrays for photoelectrochemical water splitting" X. Yang, A. Wolcott, **G. Wang**, A. Sobo, R.C. Fitzmorris, F. Qian,

- J. Z. Zhang and Y. Li, *Nano Lett.* **2009**, 9, 2331-2336. (co-first author)
3. “Double-sided CdS and CdSe quantum dot co-sensitized ZnO nanowire arrays for photoelectrochemical hydrogen generation” **G. Wang**, X. Yang, F. Qian, J. Z. Zhang and Y. Li, *Nano Lett.* **2010**, 10, 1088-1092.
  4. “Facile synthesis of highly photoactive  $\alpha$ -Fe<sub>2</sub>O<sub>3</sub> based films for water oxidation” **G. Wang**, Y. Ling, D. A. Wheeler, K. George, K. Horsley, C. Heske, J. Z. Zhang and Y. Li, *Nano Lett.* **2011**, 11, 3503-3509.
  5. “Hydrogen-treated TiO<sub>2</sub> nanowire arrays for photoelectrochemical water splitting” **G. Wang**, H. Wang, Y. Ling, Y. Tang, X. Yang, R. C. Fitzmorris, C. Wang, J. Z. Zhang and Y. Li, *Nano Lett.* **2011**, 3026-3033.
  6. “Hydrogen-treated WO<sub>3</sub> nanoflakes show enhanced photostability” **G. Wang**, Y. Ling, H. Wang, X. Yang, C. Wang, J. Z. Zhang, and Y. Li, *Energy Environ. Sci.* **2012**, 5, 6180-6187.
  7. “Computational and photoelectrochemical study of hydrogenated bismuth vanadate” **G. Wang**, Y. Ling, X. Lu, F. Qian, Y. Tong, J. Z. Zhang, V. Lordi, C. R. Leao and Y. Li, *J. Phys. Chem. C* **2013**, accepted.
  8. “A mechanistic study into the catalytic effect of Ni(OH)<sub>2</sub> on hematite for photoelectrochemical water oxidation” **G. Wang**, Y. Ling, X. Lu, T. Zhai, F. Qian, Y. Tong and Y. Li, *Nanoscale*, **2013**, 5, 4129-4133.
  9. “Solar driven hydrogen releasing from urea and human urine” **G. Wang**, Y. Ling, X. Lu, H. Wang, F. Qian, Y. Tong, and Y. Li, *Energy Environ. Sci.*



**2012**, 5, 8215-8219.

## **Chapter 1**

### **Introduction of Chemically Modified Nanostructures for**

#### **Photoelectrochemical Water Splitting**

##### **Abstract**

Hydrogen energy with high energy density represents a clean, renewable and carbon-free burning fuel, which has the potential to solve the more and more urgent energy crisis in today's society. Inspired by natural photosynthesis, artificial photosynthesis to generate hydrogen energy has attracted a lot of attentions in the field of chemistry, physics and material. Photoelectrochemical water splitting based on semiconductors represents a green and low cost method to generate hydrogen fuel. However, the current overall efficiency of solar to hydrogen is quite low, due to some intrinsic limitations such as bandgap, diffusion distance, carrier lifetime and photostability of semiconductors. Although nanostructured semiconductors can improve their photoelectrochemical water splitting performance to some extent, by increasing electrolyte accessible area and shortening minority carrier diffusion distance, nanostructure engineering cannot change their intrinsic electronic properties. Recent development in chemically modified nanostructures such as surface

catalyst decoration, element doping, plasmonic modification and interfacial hetero-junction design have led to significant advancement in the photoelectrochemical water splitting, by improving surface reaction kinetics and charge separation, transportation and collection efficiency. In the part, we will give an overview of the basic mechanism of photoelectrochemical water splitting, the semiconductor material selection criteria, with an emphasis of the recent advancement of chemically modified nanostructure for photoelectrochemical water splitting. Finally, we will briefly discuss the current challenges and future opportunities in the area of photoelectrochemical water splitting.

## **Introduction**

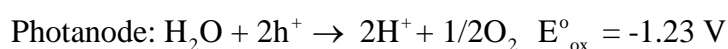
With the ever-growing of global population and the standard of living, the steadily increased energy demanding and the faced energy crisis is becoming one of the most urgent issues in today's society. The renewable solar energy is believed a potential solution to solve the faced energy crisis. A lot of efforts have been devoted into the studies of solar energy, especially solar cells, and significant advancements have been achieved in the past years. However, before large scale deployment of solar energy system, the intermittent solar irradiation raises new problems. In order to obtain continuous and stable power supply during day and night, it requires efficient and cost effective energy storage

devices to store the excess energy for later utilization. One of the most attractive means proposed is to store solar energy into the chemical bonding of fuels, such as carbohydrates and hydrogen. Inspired by the natural photosynthesis in plants which fix solar energy into carbohydrates, researchers tried to mimic this process using man-made materials and artificial solar hydrogen generation from water splitting has been proposed. Hydrogen is clean and carbon-free, especially with high energy density of  $\sim 140$  MJ/Kg and natural abundant water source on earth, which could be beneficial to address the issue of energy storage and energy crisis.

### **1.1 The Principle of Photoelectrochemical Water Splitting**

Water cannot be directly decomposed by light, because it is transparent to visible light, but only with the irradiation wavelength shorter than 190nm (deep ultraviolet light).<sup>1</sup> For electrochemical water electrolysis, a potential of at least 1.23 V is necessary to drive water splitting. This driving voltage is equivalent to the energy irradiance with a wavelength of  $\sim 1000$  nm. If light can be effectively used in the electrochemical system, it should be possible that water splitting can be achieved under visible light. The first artificial photosynthesis of  $H_2$  by water splitting was demonstrated by Honda and Fujishima in 1972, using semiconductor  $TiO_2$  in a photoelectrochemical (PEC) cell.<sup>2</sup> The schematic diagram of PEC water splitting cell is shown in figure 1.1. The PEC water

splitting cells typically is composed of a photoanode of n type TiO<sub>2</sub> semiconductor and a Pt counter electrode. When the semiconductor is contacted with the electrolyte; the charge transfer at the interface between semiconductor and electrolyte, results in charging of the surface layer of the semiconductor. The charge transfer from the *n* type semiconductor to the electrolyte leads to the formation of a surface charge and results in upwards band bending. The potential barrier at the upward band bending is known as *Helmholtz barrier*, which depends on the nature of the aqueous electrolyte and the properties of the semiconductors.<sup>3</sup> The potential barrier at the interface could drive electron-hole separation and facilitate charger's transportation at the band bending layers. When TiO<sub>2</sub> photoelectrode is exposed under light illumination, the UV light will be absorbed by TiO<sub>2</sub> and generate electron-hole pairs in TiO<sub>2</sub>. The photoexcited electrons transfer to Pt counter electrode and reduce water to generate H<sub>2</sub>, while holes diffuse to the surface of TiO<sub>2</sub> and oxidize water to form O<sub>2</sub>.<sup>3-6</sup> The reaction equations on each electrode are shown in the following:



According to the Nernst equation, it requires at least 1.23V to drive water electrolysis. To compensate the required electrochemical energy, the semiconductor electrode must absorb radiant light with photon energies larger than 1.23 eV to drive solar water splitting. However, for sustainable water

splitting without external bias, the bandgap larger than 1.23 eV is necessary but not enough. In many cases, external bias is needed to drive the water splitting reaction, even if the bandgap of the photoelectrodes such as  $\text{WO}_3$  and  $\text{Fe}_2\text{O}_3$  is much larger than 1.23 eV. To a large extent, the external bias is related to the electronic band structure of the photoelectrodes.

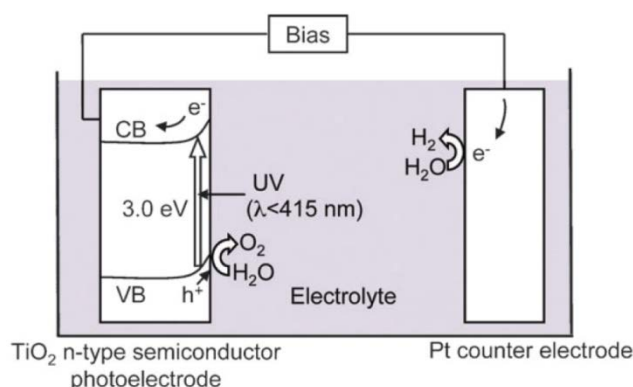


**Figure 1.1** Photoelectrochemical water splitting cell based on n type semiconductor  $\text{TiO}_2$  photoelectrode. <sup>7</sup>

## 1.2 Common Materials for PEC Water Splitting and Their Limitations

In order to achieve efficient solar water splitting, there are some basic requirements for the semiconductors. In an ideal perspective, the conduction band and valence band of semiconductors should straddle the electrochemical potentials of  $E^\circ(\text{H}^+/\text{H}_2)$  and  $E^\circ(\text{O}_2/\text{H}_2\text{O})$ . <sup>6, 8</sup>In such ways, the photo-excited electrons and holes can have enough electrochemical potential to drive water splitting without external bias. Besides, the semiconductors should also own efficient solar light absorption properties and excellent chemical stability during

water splitting. The solar light absorption is related to the semiconductor band gap and the solar to hydrogen conversion efficiency. Figure 1.2 shows the solar energy spectrum in terms of number of photons and radiation energy. As we can see, the photon numbers and energy portion for UV region is very small in the whole solar spectrum.<sup>3, 9, 10</sup> Theoretically, the lowest bandgap for PEC water splitting is 1.23 eV. However, in practice, the used photon energy is relatively larger than the theoretical limits of 1.23 eV and actual energy conversion efficiency is much smaller than the expectation, due to the energy loss during PEC water splitting. The energy loss can be attributed to the electron-hole recombination, polarization within PEC and the potential loss due to the resistance of electrode and contact.<sup>3</sup> The estimated energy loss is around 0.8 eV; therefore, the practical limitation of photons used for PEC water splitting is ~2.0 eV. This is also why researchers try to develop materials to utilize visible light for PEC water splitting.

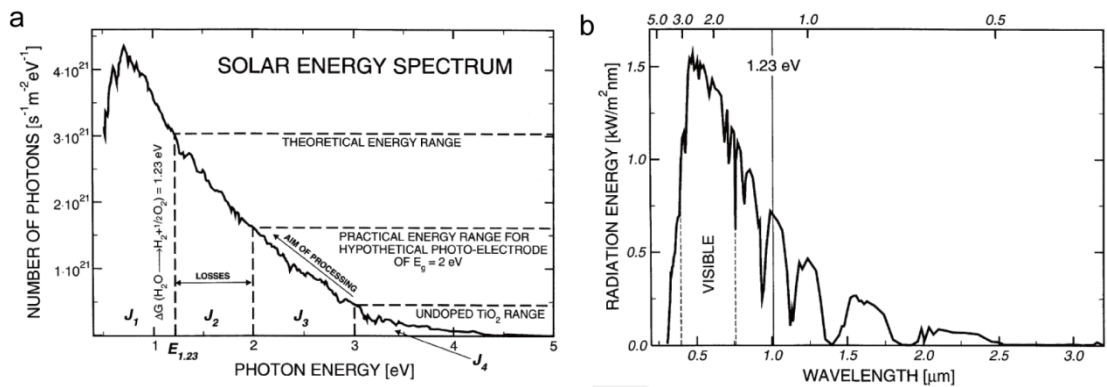


**Figure 1.2** (a) Number of photons in solar spectrum, versus photon energy. (b)

The radiation energy in solar spectrum as a function of wavelength.<sup>3, 9, 10</sup>

Inspired by the first demonstration of PEC water splitting on TiO<sub>2</sub>, a lot of efforts have been devoted to develop TiO<sub>2</sub> and other semiconductor materials for PEC water splitting. Up to now, the most common used materials for PEC water splitting in literature are metal oxides such as TiO<sub>2</sub>,<sup>11-23</sup> ZnO,<sup>24-31</sup> Fe<sub>2</sub>O<sub>3</sub>, BiVO<sub>4</sub><sup>32-46</sup>, WO<sub>3</sub><sup>47-54</sup>, metal nitrides and phosphides such as Ta<sub>3</sub>N<sub>5</sub><sup>55-58</sup> and GaP<sup>59, 60</sup>, metal oxynitrides such as TaON<sup>61-64</sup> and silicon such as *n* type and *p* type silicon. Based on the reaction on the semiconductor surface, these material photoelectrodes can be divided into photoanodes and photocathodes. PEC water splitting typically undergoes three steps: light harvesting process; charge separation and transportation process; and catalytic reaction process.<sup>65</sup> Importantly, these processes are close related the properties of materials, such as band structure, bandgap and electronic conductivity.

Figure 1.3 shows the band structure potential of typical semiconductors versus vacuum potential and normal hydrogen electrode potential and their corresponded bandgaps.<sup>66</sup> For metal oxides, only large bandgap metal oxides such as TiO<sub>2</sub>, SrTiO<sub>3</sub> and ZnO can cover the water reduction and water oxidation potentials.<sup>5</sup> However, the large bandgap limits their light absorption and photoelectrochemical water splitting. For those metal oxides with small bandgap such as Fe<sub>2</sub>O<sub>3</sub> and WO<sub>3</sub>, their conduction band potentials are not



negative enough and external bias is needed to drive water splitting. Besides, the conductivity of  $\text{Fe}_2\text{O}_3$  is bad and its carrier diffusion distance is very short, which usually results in significant recombination during PEC water splitting.<sup>5</sup>

In the perspective of band structure, those metal sulfides such as CdS and CdSe can satisfy this requirement; but the stability is a big issue, because it can be easily oxidized to metal oxides and loses the benefits of band structure.<sup>16, 26, 67, 68</sup>

For metal nitrides or metal oxynitrides, the nitride materials also suffer photocorrosion and gradually lose their photoactivity, although nitrogen incorporation can modify electronic property and band structure of materials.<sup>58</sup>

Silicon with a very small bandgap of 1.1 eV, can absorb a large portion of solar spectrum, although the valence band of silicon is not positive enough to oxidize water and external bias is needed.<sup>4</sup> The external bias can be compensated by forming hybrid devices such as dye sensitized solar cell-PEC hybrid devices.<sup>4,</sup>

<sup>69-72</sup> However, the issues for silicon are also the photo-stability, due to the surface oxidation and large surface overpotentials.<sup>73</sup> Nanostructure and chemical modification such as element doping, surface heterojunction design and surface catalyst modification could potentially address light absorption, electronic property, band structures and chemical stability of semiconductors.

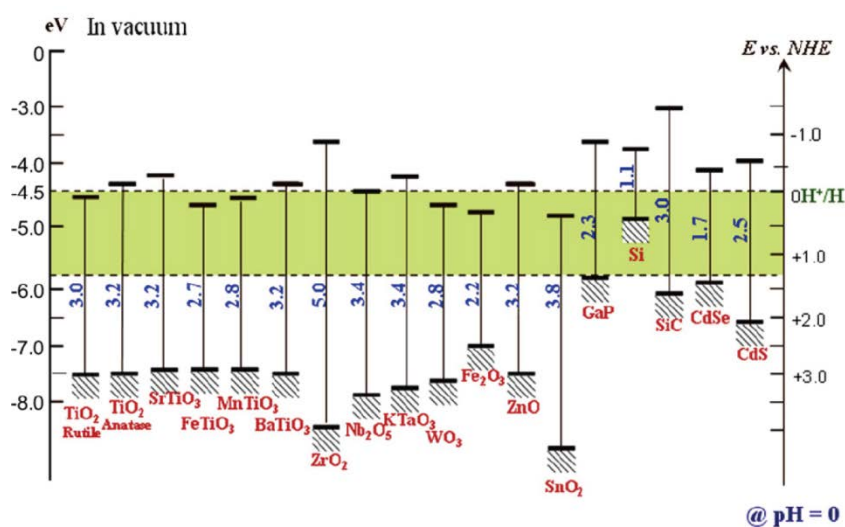


**Figure 1.3** The bandgap and band structure potentials of typical semiconductors; the potentials are versus normal hydrogen electrode (NHE) at pH=0 and vacuum potential.<sup>66</sup>

### 1.3 Nanostructure and Chemical Modification

Nanostructure and chemical modification could provide new opportunities to address the current challenges in the PEC water splitting, such as photostability, electronic conductivity, light absorption efficiency and band structures. Nanostructure could provide large interfacial area with electrolyte and short minority carrier diffusion distance, which can increase the charge separation and collection efficiency at the interface and thus decrease electron-hole recombination.<sup>6, 74, 75</sup> Nanostructure also increase light absorption efficiency, via increasing light scattering in the nanostructured matrix. Besides, quantum confinement could further modify the band structure of semiconductors; for

instance, the tunable conduction band potential of CdSe and CdSe has been demonstrated via the control of the quantum dot sizes.<sup>76</sup> Besides nanostructure engineering, chemical modification is another important approach to improve PEC performance of semiconductors. Up to now, chemical modification including element doping, surface electrochemical catalyst modification such as oxygen evolution catalyst and hydrogen evolution catalyst, surface plasmonic effect modification, and heterojunction design, has been extensively used to increase the PEC water splitting performance.

Element doping has been demonstrated effective in the modification of electronic and optical properties of semiconductors.<sup>77-80</sup> For instance, nitrogen doped TiO<sub>2</sub> has shown visible light absorption and visible light photoactivity, by introduction of nitrogen dopant energy states into TiO<sub>2</sub> band structure.<sup>19, 20, 77</sup> Pristine hematite Fe<sub>2</sub>O<sub>3</sub> has a notorious conductivity and PEC performance;<sup>74, 81, 82</sup> Silicon, titanium and tin doped hematite exhibits substantially increased conductivity and PEC performance.<sup>81, 83-87</sup> In addition, self-doping of oxygen vacancies has been demonstrated a general method to increase the conductivity and PEC performance of metal oxides semiconductors.<sup>5, 15, 17, 47</sup>

Surface modification is another important strategy to stabilize and increase PEC performance of photoelectrodes. For example, metal oxide coating such as TiO<sub>2</sub> and Fe<sub>2</sub>O<sub>3</sub> on silicon has shown stabilized photoactivity of silicon,

suggesting metal oxide coating could prevent silicon surface oxidation.<sup>73</sup> Some semiconductors have large surface reaction over-potentials, which increase the energy loss of photo-excited carriers and result in a needed large external bias. Electrochemical catalysts have been used to reduce the overpotential for water oxidation or reduction. Oxygen evolution catalysts (OER) such as Co-Pi, CoO<sub>x</sub> and RuO<sub>x</sub> modified *n* type photoanodes and hydrogen evolution catalyst (HER) such as Ni, Pt and MoS<sub>2</sub> modified *p* type photocathode, have been extensively studies for PEC water splitting, recently.<sup>40, 88-92</sup> For example, Gamelin et al. reported that Co-Pi modification shows a substantial photocurrent onset shift of hematite (Fe<sub>2</sub>O<sub>3</sub>) for photoelectrochemical water oxidation, indicating the surface oxygen evolution catalyst modification is effective to improve PEC performance.<sup>38, 93</sup> Besides suppression of the overpotentials of chemical reactions, oxygen evolution catalyst modification also exhibits its advantage in the prevent self-oxidation/reduction of photoelectrode and stabilization of photoelectrochemical performance. For example, the photocatalytic instability is an issue for Ta<sub>3</sub>N<sub>5</sub> due to self-oxidation during water oxidation, although it owns suitable bandgap and band edge positions. Co-Pi OER catalyst shows the capability in stabilizing PEC performance of Ta<sub>3</sub>N<sub>5</sub>, compared to bared Ta<sub>3</sub>N<sub>5</sub> photoanode.<sup>58</sup> Plasmonic metal nanoparticles such as Au and Ag nanoparticles have been used to increase visible light absorption of large bandgap semiconductors such as ZnO and TiO<sub>2</sub>, via Plasmon induced visible light

absorption.<sup>94-97</sup> Heterojunction (type II junction) formed by surface coating of another semiconductor can facilitate charge separation at interface and increase PEC performance. For example, WO<sub>3</sub>/BiVO<sub>4</sub> heterojunction photoelectrode shows enhanced photoelectrochemical performance, compared to the photoactivity of both WO<sub>3</sub> and BiVO<sub>4</sub>.<sup>36, 98, 99</sup>

Combining the both benefits of nanostructure and chemical modification, chemically modified nanostructure recently has attracted a lot of attentions in the area of photoelectrochemical water splitting. Substantial efforts have been devoted to improve PEC performance of nanostructured semiconductors via chemical modifications. Recent development in chemical modification such as surface catalyst decoration, element doping, plasmonic modification and interfacial hetero-junction design have led to significant advancement in the photoelectrochemical water splitting of nanostructure. In this review, we will focus on these chemical modification methods and their application in PEC water splitting. Finally, we give an overview of the current challenges and future opportunities in the area of photoelectrochemical water splitting

## Reference

1. Coehn, A., Photochemical Equilibria. IV. Detonating Gas and Water Vapor. *Berichte der Deutschen Chemischen Gesellschaft* **1910**, 43, 880.
2. Fujishima, A.; Honda, K., *Nature* **1972**, 238, 37.

3. Bak, T.; Nowotny, J.; Rekas, M.; Sorrell, C. C., *Int. J. Hydrogen Energy* **2002**, 27, 991-1022.
4. Walter, M. G.; Warren, E. L.; McKone, J. R.; Boettcher, S. W.; Mi, Q. X.; Santori, E. A.; Lewis, N. S., *Chem. Rev.* **2010**, 110, 6446-6473.
5. Wang, G. M.; Ling, Y. C.; Li, Y., *Nanoscale* **2012**, 4, 6682-6691.
6. Li, Y.; Zhang, J. Z., *Laser Photon. Rev.* **2010**, 4, 517-528.
7. Kudo, A.; Miseki, Y., *Chem. Soc. Rev.* **2009**, 38, 1,253-278.
8. Abe, R., *J. Photochem. Photobiology C-Photochemistry Reviews* **2010**, 11, 179-209.
9. Tools, O.-I. B. o. P., *Oriel-Instruments. Book of Photon Tools* **1999**, 1-3.
10. Wenham, S. R.; Green, M. A.; Watt, M. E., *Applied Photovoltaics, Centre for Photovoltaic Devices and Systems, Sydney.* **1994**, 239-246.
11. Park, J. H.; Kim, S.; Bard, A. J., *Nano Lett.* **2006**, 6, 24-28.
12. Lu, N.; Quan, X.; Li, J. Y.; Chen, S.; Yu, H. T.; Chen, G. H., *J. Phys. Chem. C* **2007**, 111, 11836-11842.
13. Rockafellow, E. M.; Stewart, L. K.; Jenks, W. S., *Applied Catalysis B-Environmental* **2009**, 91, 554-562.
14. Park, Y.; Kim, W.; Park, H.; Tachikawa, T.; Majima, T.; Choi, W., *Appl. Catalysis B-Environ.* **2009**, 91, 355-361.
15. Wang, G. M.; Wang, H. Y.; Ling, Y. C.; Tang, Y. C.; Yang, X. Y.; Fitzmorris, R. C.; Wang, C. C.; Zhang, J. Z.; Li, Y., *Nano Lett.* **2011**, 11, 3026-3033.

16. Hensel, J.; Wang, G. M.; Li, Y.; Zhang, J. Z., *Nano Lett.* **2010**, 10, 478-483.
17. Wang, H. Y.; Wang, G. M.; Ling, Y. C.; Lepert, M.; Wang, C. C.; Zhang, J. Z.; Li, Y., *Nanoscale* **2012**, 4, 1463-1466.
18. Wang, G. M.; Ling, Y. C.; Lu, X. H.; Wang, H. Y.; Qian, F.; Tong, Y. X.; Li, Y., *Energy Environ. Sci.* **2012**, 5, 8215-8219.
19. Hoang, S.; Guo, S. W.; Hahn, N. T.; Bard, A. J.; Mullins, C. B., *Nano Lett.* **2012**, 12, 26-32.
20. Hoang, S.; Berglund, S. P.; Hahn, N. T.; Bard, A. J.; Mullins, C. B., *J. Am. Chem. Soc.* **2012**, 134, 3659-3662.
21. Hwang, Y. J.; Hahn, C.; Liu, B.; Yang, P. D., *Acs Nano* **2012**, 6, 5060-5069.
22. Xu, M.; Da, P. M.; Wu, H. Y.; Zhao, D. Y.; Zheng, G. F., *Nano Lett.* **2012**, 12, 1503-1508.
23. Hwang, Y. J.; Boukai, A.; Yang, P. D., *Nano Lett.* **2009**, 9, 410-415.
24. Cooper, J. K.; Ling, Y. C.; Longo, C.; Li, Y.; Zhang, J. Z., *J. Phys. Chem. C* **2012**, 116, 17360-17368.
25. Yang, X. Y.; Wolcott, A.; Wang, G. M.; Sobo, A.; Fitzmorris, R. C.; Qian, F.; Zhang, J. Z.; Li, Y., *Nano Lett.* **2009**, 9, 2331-2336.
26. Wang, G. M.; Yang, X. Y.; Qian, F.; Zhang, J. Z.; Li, Y., *Nano Lett.* **2010**, 10, 1088-1092.
27. Qiu, Y. C.; Yan, K. Y.; Deng, H.; Yang, S. H., *Nano Lett.* **2012**, 12, 407-413.
28. Shi, J.; Starr, M. B.; Xiang, H.; Hara, Y.; Anderson, M. A.; Seo, J. H.; Ma, Z.

- Q.; Wang, X. D., *Nano Lett.* **2011**, 11, 5587-5593.
29. Xie, S. L.; Lu, X. H.; Zhai, T.; Li, W.; Yu, M. H.; Liang, C. L.; Tong, Y. X., *J. Mater. Chem.* **2012**, 22, 14272-14275.
30. Li, H. X.; Cheng, C. W.; Li, X. L.; Liu, J. P.; Guan, C.; Tay, Y. Y.; Fan, H. J., *J. Phys. Chem. C* **2012**, 116, 3802-3807.
31. Lin, Y. G.; Hsu, Y. K.; Chen, Y. C.; Chen, L. C.; Chen, S. Y.; Chen, K. H., *Nanoscale* **2012**, 4, 6515-6519.
32. Sayama, K.; Nomura, A.; Arai, T.; Sugita, T.; Abe, R.; Yanagida, M.; Oi, T.; Iwasaki, Y.; Abe, Y.; Sugihara, H., *J. Phys. Chem. B* **2006**, 110, 11352-11360.
33. Ng, Y. H.; Iwase, A.; Kudo, A.; Amal, R., *J. Phys. Chem. Lett.* **2010**, 1, 2607-2612.
34. Long, M. C.; Cai, W. M.; Kisch, H., *J. Phys. Chem. C* **2008**, 112, 548-554.
35. Chatchai, P.; Murakami, Y.; Kishioka, S. Y.; Nosaka, A. Y.; Nosaka, Y., *Electrochimica Acta* **2009**, 54, (3), 1147-1152.
36. Su, J. Z.; Guo, L. J.; Bao, N. Z.; Grimes, C. A., *Nano Lett.* **2011**, 11, 1928-1933.
37. Iwase, A.; Kudo, A., *J. Mater. Chem.* **2010**, 20, 7536-7542.
38. Zhong, D. K.; Choi, S.; Gamelin, D. R., *J. Am. Chem. Soc.* **2011**, 133, 18370-18377.
39. Su, J. Z.; Guo, L. J.; Yoriya, S.; Grimes, C. A., *Cryst. Growth Design* **2010**, 10, 856-861.



40. Pilli, S. K.; Furtak, T. E.; Brown, L. D.; Deutsch, T. G.; Turner, J. A.; Herring, A. M., *Energy Environ. Sci.* **2011**, 4, 5028-5034.
41. Berglund, S. P.; Flaherty, D. W.; Hahn, N. T.; Bard, A. J.; Mullins, C. B., *J. Phys. Chem. C* **2011**, 115, 3794-3802.
42. Ye, H.; Lee, J.; Jang, J. S.; Bard, A. J., *J. Phys. Chem. C* **2010**, 114, 13322-13328.
43. Liang, Y. Q.; Tsubota, T.; Mooij, L. P. A.; van de Krol, R., *J. Phys. Chem. C* **2011**, 115, 17594-17598.
44. Luo, W. J.; Yang, Z. S.; Li, Z. S.; Zhang, J. Y.; Liu, J. G.; Zhao, Z. Y.; Wang, Z. Q.; Yan, S. C.; Yu, T.; Zou, Z. G., *Energy Environ. Sci.* **2011**, 4, 4046-4051.
45. Abdi, F. F.; van de Krol, R., *J. Phys. Chem. C* **2012**, 116, 9398-9404.
46. Berglund, S. P.; Rettie, A. J. E.; Hoang, S.; Mullins, C. B., *Phys. Chem. Chem. Phys.* **2012**, 14, 7065-7075.
47. Wang, G. M.; Ling, Y. C.; Wang, H. Y.; Yang, X. Y.; Wang, C. C.; Zhang, J. Z.; Li, Y., *Energy Environ. Sci.* **2012**, 5, 6180-6187.
48. Zhang, X. H.; Lu, X. H.; Shen, Y. Q.; Han, J. B.; Yuan, L. Y.; Gong, L.; Xu, Z.; Bai, X. D.; Wei, M.; Tong, Y. X.; Gao, Y. H.; Chen, J.; Zhou, J.; Wang, Z. L., *Chem. Commun.* **2011**, 47, 5804-5806.
49. Liu, X.; Wang, F. Y.; Wang, Q., *Phys. Chem. Chem. Phys.* **2012**, 14, 7894-7911.
50. Qin, D. D.; Tao, C. L.; Friesen, S. A.; Wang, T. H.; Varghese, O. K.;

- Bao, N. Z.; Yang, Z. Y.; Mallouk, T. E.; Grimes, C. A., *Chem. Commun.* **2012**, 48, 5, 729-731.
51. Esposito, D. V.; Forest, R. V.; Chang, Y. C.; Gaillard, N.; McCandless, B. E.; Hou, S. Y.; Lee, K. H.; Birkmire, R. W.; Chen, J. G. G., *Energ Environ.Sci.* **2012**, 5, 9091-9099.
52. Cristino, V.; Caramori, S.; Argazzi, R.; Meda, L.; Marra, G. L.; Bignozzi, C. A., *Langmuir* **2011**, 27, 7276-7284.
53. Hill, J. C.; Choi, K. S., *J. Phys. Chem. C* **2012**, 116, 7612-7620.
54. Kronawitter, C. X.; Vayssieres, L.; Shen, S. H.; Guo, L. J.; Wheeler, D. A.; Zhang, J. Z.; Antoun, B. R.; Mao, S. S., *Energy Environ. Sci.* **2011**, 4, 3889-3899.
55. Feng, X. J.; LaTempa, T. J.; Basham, J. I.; Mor, G. K.; Varghese, O. K.; Grimes, C. A., *Nano Lett.* **2010**, 10, 948-952.
56. Cong, Y. Q.; Park, H. S.; Wang, S. J.; Dang, H. X.; Fan, F. R. F.; Mullins, C. B.; Bard, A. J., *J. Phys. Chem. C* **2012**, 116, 14541-14550.
57. Yang, Y.; Ling, Y. C.; Wang, G. M.; Lu, X. H.; Tong, Y. X.; Li, Y., *Nanoscale* **2013**, 5, 1820-1824.
58. Li, Y. B.; Takata, T.; Cha, D.; Takanabe, K.; Minegishi, T.; Kubota, J.; Domen, K., *Adv. Mater.* **2013**, 25, 125-131.
59. Sun, J. W.; Liu, C.; Yang, P. D., *J. Am. Chem. Soc.* **2011**, 133, 19306-19309.
60. Liu, C.; Sun, J. W.; Tang, J. Y.; Yang, P. D., *Nano Lett.* **2012**, 12, 5407-5411.

61. Maeda, K.; Higashi, M.; Siritanaratkul, B.; Abe, R.; Domen, K., *J. Am. Chem. Soc.* **2011**, 133, 12334-12337.
62. Banerjee, S.; Mohapatra, S. K.; Misra, M., *Chem. Commun.* **2009**, 7137-7139.
63. Higashi, M.; Domen, K.; Abe, R., *J. Am. Chem. Soc.* **2012**, 134, 6968-6971.
64. Higashi, M.; Domen, K.; Abe, R., *Energy Environ. Sci.* **2011**, 4, 4138-4147.
65. Tachibana, Y.; Vayssieres, L.; Durrant, J. R., *Nature Photon.* **2012**, 6, 511-518.
66. Jing, D. W.; Guo, L. J.; Zhao, L. A.; Zhang, X. M.; Liu, H. A.; Li, M. T.; Shen, S. H.; Liu, G. J.; Hu, X. W.; Zhang, X. H.; Zhang, K.; Ma, L. J.; Guo, P. H., *Int. J. Hydrogen Energy* **2010**, 35, 7087-7097.
67. Liu, L. P.; Wang, G. M.; Li, Y.; Li, Y. D.; Zhang, J. Z., *Nano Res.* **2011**, 4, 249-258.
68. Larsen, G. K.; Fitzmorris, B. C.; Longo, C.; Zhang, J. Z.; Zhao, Y. P., *J. Mater. Chem.* **2012**, 22, 14205-14218.
69. Shin, K.; Yoo, J. B.; Park, J. H., *J. Power Sources* **2013**, 225, 263-268.
70. Swierk, J. R.; Mallouk, T. E., *Chem. Soc. Rev.* **2013**, 42, 2357-2387.
71. Khaselev, O.; Turner, J. A., *Science* **1998**, 280, 425-427.
72. Brillet, J.; Yum, J. H.; Cornuz, M.; Hisatomi, T.; Solaraska, R.; Augustynski, J.; Graetzel, M.; Sivula, K., *Nature Photon.* **2012**, 6, 823-827.
73. Chen, Y. W.; Prange, J. D.; Duhnen, S.; Park, Y.; Gunji, M.; Chidsey, C. E.

- D.; McIntyre, P. C., *Nature Mater.* **2011**, 10, 539-544.
74. Wheeler, D. A.; Wang, G. M.; Ling, Y. C.; Li, Y.; Zhang, J. Z., *Energy Environ. Sci.* **2012**, 5, 6682-6702.
75. Zhang, J. Z., *Mrs Bulletin* **2011**, 36, 48-55.
76. Liu, L. P.; Peng, Q.; Li, Y. D., *Inorganic Chem.* **2008**, 47, 5022-5028.
77. Irie, H.; Watanabe, Y.; Hashimoto, K., *J. Phys. Chem. B* **2003**, 107, (23), 5483-5486.
78. Khan, S. U. M.; Al-Shahry, M.; Ingler, W. B., *Science* **2002**, 297, 2243-2245.
79. Chen, X. B.; Liu, L.; Yu, P. Y.; Mao, S. S., *Science* **2011**, 331, 746-750.
80. Serpone, N., *J. Phys. Chem. B* **2006**, 110, 24287-24293.
81. Ling, Y. C.; Wang, G. M.; Wheeler, D. A.; Zhang, J. Z.; Li, Y., *Nano Lett.* **2011**, 11, 2119-2125.
82. Ling, Y. C.; Wang, G. M.; Reddy, J.; Wang, C. C.; Zhang, J. Z.; Li, Y., *Angew. Chem. Int. Ed.* **2012**, 51, 4074-4079.
83. Kay, A.; Cesar, I.; Gratzel, M., *J. Am. Chem. Soc.* **2006**, 128, 15714-15721.
84. Wang, G. M.; Ling, Y. C.; Wheeler, D. A.; George, K. E. N.; Horsley, K.; Heske, C.; Zhang, J. Z.; Li, Y., *Nano Lett.* **2011**, 11, 3503-3509.
85. Chemelewski, W. D.; Hahn, N. T.; Mullins, C. B., *J. Phys. Chem. C* **2012**, 116, 5256-5262.
86. Cesar, I.; Kay, A.; Martinez, J. A. G.; Gratzel, M., *J. Am. Chem. Soc.* **2006**,

128, 4582-4583.

87. Cesar, I.; Sivula, K.; Kay, A.; Zboril, R.; Graetzel, M., *J. Phys. Chem. C* **2009**, 113, 772-782.

88. Wang, G. M.; Ling, Y. C.; Lu, X. H.; Zhai, T.; Qian, F.; Tong, Y. X.; Li, Y., *Nanoscale* **2013**, DOI: 10.1039/C3NR00569K.

89. Hou, Y. D.; Abrams, B. L.; Vesborg, P. C. K.; Bjorketun, M. E.; Herbst, K.; Bech, L.; Setti, A. M.; Damsgaard, C. D.; Pedersen, T.; Hansen, O.; Rossmeisl, J.; Dahl, S.; Norskov, J. K.; Chorkendorff, I., *Nature Mater.* **2011**, 10, 434-438.

90. Wang, X.; Peng, K. Q.; Pan, X. J.; Chen, X.; Yang, Y.; Li, L.; Meng, X. M.; Zhang, W. J.; Lee, S. T., *Angew. Chem. Int. Ed.* **2011**, 50, 9861-9865.

91. Barroso, M.; Mesa, C. A.; Pendlebury, S. R.; Cowan, A. J.; Hisatomi, T.; Sivula, K.; Gratzel, M.; Klug, D. R.; Durrant, J. R., *PNAS* **2012**, 109, 15640-15645.

92. Badia-Bou, L.; Mas-Marza, E.; Rodenas, P.; Barea, E. M.; Fabregat-Santiago, F.; Gimenez, S.; Peris, E.; Bisquert, J., *J. Phys. Chem. C* **2013**, 117, 3826-3833.

93. Zhong, D. K.; Sun, J. W.; Inumaru, H.; Gamelin, D. R., *J. Am. Chem. Soc.* **2009**, 131, 6086-6088.

94. Chen, H. M.; Chen, C. K.; Chen, C. J.; Cheng, L. C.; Wu, P. C.; Cheng, B. H.; Ho, Y. Z.; Tseng, M. L.; Hsu, Y. Y.; Chan, T. S.; Lee, J. F.; Liu, R. S.; Tsai, D. P., *Acs Nano* **2012**, 6, 7362-7372.

95. Liu, J.; Chen, F. Y., *Int. J. Electrochem. Sci.* **2012**, 7, 9560-9572.
96. Shi, X.; Ueno, K.; Takabayashi, N.; Misawa, H., *J. Phys. Chem. C* **2013**, 117, 2494-2499.
97. Zhang, Z. H.; Zhang, L. B.; Hedhili, M. N.; Zhang, H. N.; Wang, P., *Nano Lett.* **2013**, 13, 14-20.
98. Hong, S. J.; Lee, S.; Jang, J. S.; Lee, J. S. *Energy Environ. Sci.* **2011**, 4, 1781-1787.
99. Saito, R.; Miseki, Y.; Sayama, K., *Chem. Commun.* **2012**, 48, 3833-3835.

## Chapter 2

### Nitrogen-doped ZnO Nanowire Arrays for Photo-electrochemical Water

#### Splitting

##### Abstract

We report the rational synthesis of nitrogen-doped zinc oxide (N:ZnO) nanowire arrays, and their implementation as photoanodes in photoelectrochemical (PEC) cells for water splitting. Dense and vertically aligned ZnO nanowires were first prepared from a hydrothermal method, and then annealed in ammonia to incorporate N as dopant. X-ray photoelectron spectroscopy (XPS) studies reveal N incorporates substitutionally at O site in ZnO nanowires. Nanowires with N concentration (atomic ratio of Zn to N) up to ~ 4 % can be prepared depending on the annealing time. Incident-photon-to-current-efficiency (IPCE) measurements carried out on PEC cell with N:ZnO nanowire arrays as photoanodes demonstrate a significant increase of photoresponse in the visible region compared to undoped ZnO nanowires. Mott-Schottky measurements on a representative 3.7 at% N:ZnO sample give a flat-band potential of -0.97 V, a carrier density of  $1.65 \times 10^{19} \text{ cm}^{-3}$ , and a space-charge layer of 6.3 nm. Upon illumination at a power density of  $100 \text{ mW/cm}^2$  (AM 1.5), water splitting is observed in both ZnO and 3.7 at% N:ZnO nanowires. In comparison to ZnO

nanowires, N:ZnO nanowires show an order of magnitude increase in photocurrent density, with photo-to-hydrogen efficiency of 0.15 % at an applied potential of +0.5 V (versus Ag/AgCl). These results suggest that aligned 1D metal oxide nanostructures with controlled doping are promising for PEC water splitting applications.

## **Introduction**

Hydrogen is an energy carrier, which combines oxygen in a fuel cell to produce electricity and water without producing pollutants, represents an environmentally benign fuel of the future.<sup>1-3</sup> However, most of the hydrogen generated currently comes from steam reforming of natural gas, and the process produces carbon dioxide as an undesired byproduct.<sup>4</sup> Central to the success of hydrogen technology is the efficient generation of hydrogen from a renewable energy source.<sup>5, 6</sup> A promising approach for hydrogen generation is light-driven splitting of water into hydrogen and oxygen,  $\text{H}_2\text{O} + \text{light} \rightarrow \text{H}_2 + \frac{1}{2}\text{O}_2$ , using PEC cells.<sup>7-11</sup>

To serve as high performance photoanodes of PEC cells, semiconductors need to satisfy several criteria such as appropriate band-gap and flat band potential, low electrical resistance and good corrosion resistance in aqueous solution.<sup>7</sup> To date, metal oxides have been recognized as most promising



photoanode materials due to their excellent corrosion resistance in aqueous solution.<sup>10</sup> Moreover, it has been recently reported that nanostructured metal oxides<sup>12-14</sup> such as nanocrystals<sup>15</sup>, nanosheets<sup>16</sup>, nanotubes<sup>17</sup> and nanorods<sup>18</sup> offer advantages over their bulk counterparts for photoelectrodes due to their large surface area, short diffusion length and low reflectivity. Despite this progress, the enhancement of photo-to-hydrogen efficiency remains challenge as a result of limited light absorption efficiency in the visible region of interest due to the large band-gap of metal oxides.

To overcome this issue, we have explored the potential use of doped metal oxide nanowires for PEC water splitting. This work has been motivated by studies of n-type N-doped ZnO film that have been shown a significant reduction of band-gap.<sup>19, 20</sup> ZnO is a direct band-gap semiconductor with similar band-gap and band edge positions as TiO<sub>2</sub>. Furthermore, ZnO ( $\sim 100 \text{ cm}^2/\text{Vs}$ )<sup>21</sup> has even a higher electron mobility than TiO<sub>2</sub> ( $\sim 1\text{-}10 \text{ cm}^2/\text{Vs}$ )<sup>22</sup>, which could improve the electron transfer efficiency. Despite ZnO nanowires have been studying for many years,<sup>23, 24</sup> there is a no report of doped ZnO nanowires for PEC water splitting yet. Here we report the rational synthesis of N:ZnO nanowire arrays showing significant photoresponse in the visible region of the electromagnetic spectrum, and the implementation of these nanowires as photoanodes of PEC cells. To our best knowledge, this is the first demonstration

of PEC water splitting based on aligned 1D metal oxide nanowire arrays doped with N.

## **Experimental Section**

**Synthesis:** ZnO nanowire arrays were grown on ITO glass using a simple two step synthesis. In the first step, ZnO nanocrystal film were deposited on the conducting side of ITO glass by thermal decomposition of zinc acetate ethanol solution at 350 °C for 30 min. In the second step, hydrothermal ZnO growth was carried out by suspending the ITO glass in a beaker filled with an aqueous solution of 0.025 M zinc nitrate and 0.025 M hexamethylenetetramine at 90 °C for 4 hours. Then, the ITO glass was taken out from the solution, rinsed with deionized water, and dried.

**Device Fabrication and Measurement:** Nanowires were fashioned into photoanodes by the placement of a copper wire onto a bare portion of the ITO substrate and secured with high-purity silver conducting paint. Cells were then sealed on all edges with epoxy resin except for a working electrode surface area of 0.25–0.50 cm<sup>2</sup>. Electrolyte solutions of 0.5 M NaClO<sub>4</sub> were prepared and then buffered to pH of 7.0 with phosphate buffer solution. Prior to PEC experiments, all solutions were deaerated with nitrogen, and during experimentation a constant positive pressure of nitrogen also flowed through a three-neck vessel at all times. An Ag/AgCl reference electrode (+0.198 V versus

NHE) was employed along with a coiled Pt wire counter electrode during all runs. All PEC and impedance measurements were carried out on a Solartron 1280B and was coupled to an infrared water-filled filter (Oriel #6127), and then aligned into a monochromator (Oriel Cornerstone 130 1/8m). A 1000W Xe lamp was utilized as a white-light source and irradiance were measured with power meter.

**Material Characterization:** XPS data were collected in a Kratos Axis Ultra XPS system operated under charge compensation and with monochromated Al as X-ray source. Peak positions were calibrated by setting the true position of the C1s line to 285.0 eV. The survey scan and high-resolution scan were collected using pass energy of 80 and 40 eV, respectively. Peak fitting is performed by assuming the observed peak as a convolution of a Gaussian and Lorentzian function. We restricted the FWHM of the deconvoluted peak to a maximum 1.9 eV, and then vary the peak shape to match the experimental data. SEM images were collected in a Hitachi 2700 SEM. NWs were dispersed in ethanol solution and then transferred onto Cu/lacey-carbon TEM grids. TEM images were collected in a FEI monochromated F20 UT Technai TEM/STEM operated with a 200 kV electron beam. The NW films on ITO substrate were characterized by PXRD with a Rigaku Americas Miniflex Plus powder diffractometer. Diffraction patterns were recorded from 20 to 80° 2 $\theta$  with a step

size of  $0.04^\circ$  at  $1^\circ/\text{min}$ .

## Results and Discussions

The synthesis of N:ZnO nanowire arrays involves two steps. First, we grow ZnO nanowires on a ZnO nanoparticle seeded indium-tin oxide (ITO) substrate using hydrothermal method reported elsewhere.<sup>25</sup> Scanning electron microscopy (SEM) image (Figure 2.1a) of as prepared ZnO nanowires shows that nanowires are dense ( $\sim 3 \times 10^9$  wires/cm<sup>2</sup>) and vertically well aligned on the substrate. Homogeneous growth of these nanowire arrays can be obtained over a large area ( $2\text{ cm} \times 2.5\text{ cm}$ ), as shown in the optical image of nanowires on substrate (Figure 2.1b). Transmission electron microscopy (TEM) image (Figure 2.1c) of ZnO nanowires reveal that they are uniform in diameter (80-130 nm) with typical nanowire lengths, which depend on the growth time, of 1-2  $\mu\text{m}$ . High-resolution TEM analysis (Figure 2.1d) further showed that ZnO nanowires are single-crystal structures. Electron diffraction data recorded along the [2-1-10] zone axis (inset, Figure 2.1d) can be indexed to the ZnO wurtzite structure and enable assignment of the nanowire growth direction to be  $\langle 0002 \rangle$ . Second, ZnO nanowires were annealed in ammonia at  $530^\circ\text{C}$  for N incorporation and then in nitrogen for 30 minutes. The annealing was performed in a two-zone tube furnace (with zone I at upstream and zone II at downstream). The substrate was placed in zone I of  $530^\circ\text{C}$  and the temperature of zone II was set to be  $900^\circ\text{C}$

for pre-activation of ammonia.

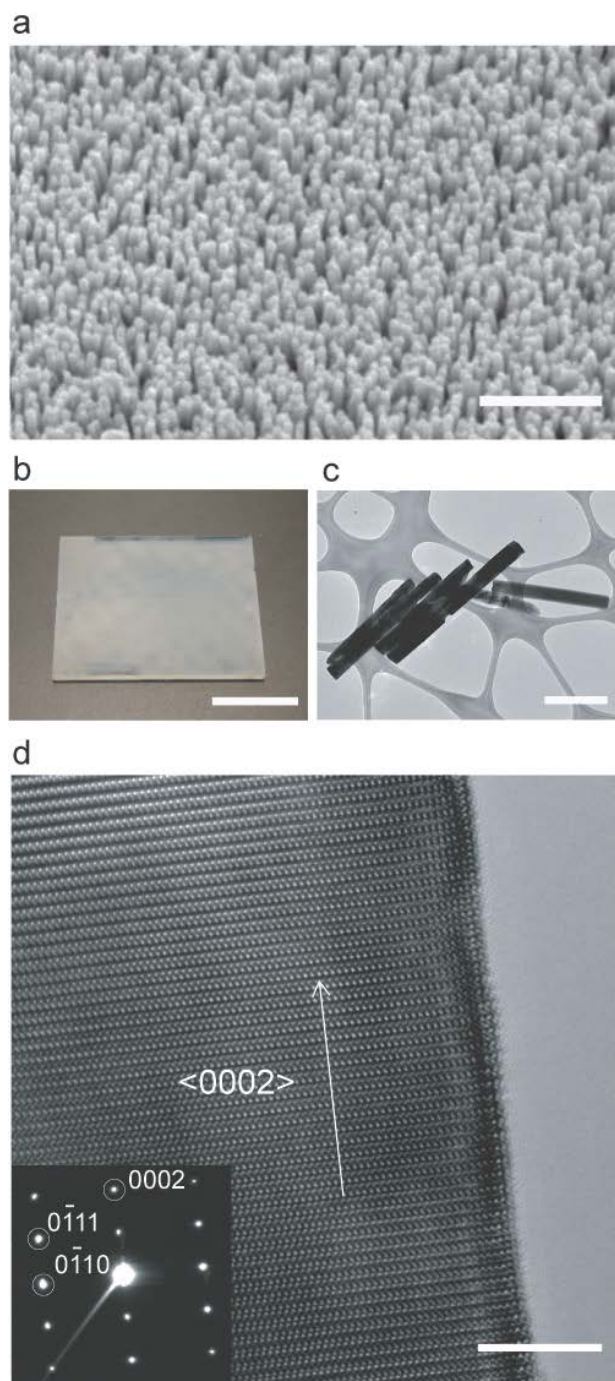


**Figure 2.1.** (a) SEM image of ZnO nanowire arrays on ITO substrate. Scale bar is 2  $\mu\text{m}$ . (b) Optical micrograph of ITO substrate after ZnO nanowire growth. Scale bar is 1 cm. (c) Bright-field TEM image of ZnO nanowires. Scale bar is 500 nm. (d) High-resolution TEM image of single crystalline ZnO nanowire

taken along the [2-1-10] zone axis. The white arrow highlights the <0002> growth direction for the nanowire. Scale bar is 5 nm. Inset: corresponding electron diffraction pattern indexed for the [2-1-10] zone axis.

After the annealing process, we observed the color of as grown ZnO nanowires changed from white to yellowish grey. UV-vis absorption spectra collected from these nanowires indicate a red shift of absorption peak, from ZnO band edge absorption of 376 nm (3.3 eV)<sup>26</sup> to visible region (Figure 2.2). These results suggest the band-gap of ZnO is narrowed due to possible incorporation of N.

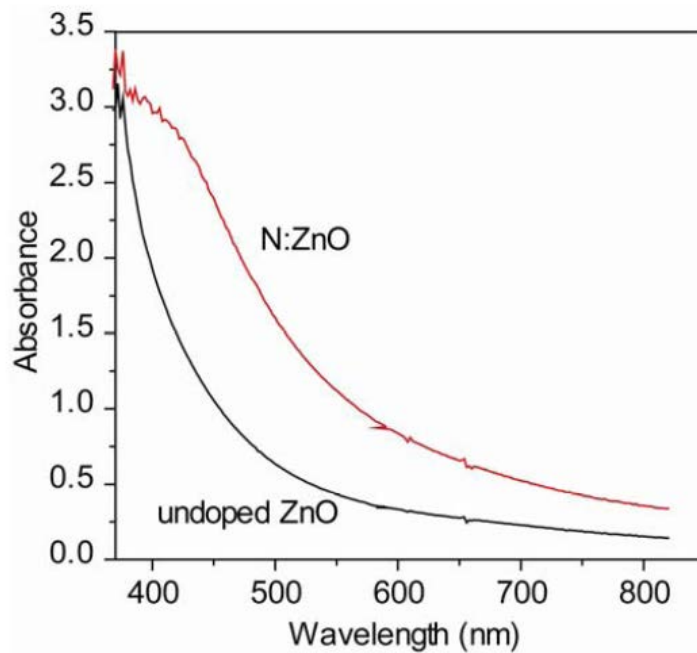


**Figure 2.2.** UV-vis spectra of undoped ZnO and ZnO:N nanowires showing a red shift of absorption wavelength to the visible region of interest in ZnO:N sample.

To enable control the N concentration of N:ZnO nanowires, it is necessary to understand how N incorporation interplays with annealing

conditions. We performed systematic XPS surveys<sup>27</sup> to quantitatively determine the N concentration of N:ZnO nanowires. In this presentation, the N concentration refers to the atomic ratio of Zn to N in nanowires, since it is not viable to obtain accurate oxygen concentration of ZnO nanowires on ITO substrate. Figure 2.3a shows the N concentration of N:ZnO nanowires versus the time of ammonia annealing. N concentration increases with the increase of annealing time and then reaches a plateau of ~ 4 at.%. To this point, efforts to further increase N concentration by increasing the annealing time have met little success. Electron microscopy studies showed that a prolonged ammonia annealing process (e.g. > 1 hours) will etch the nanowires, probably due to the presence of atomic hydrogen originating from ammonia decomposition.<sup>28</sup> A more detail study on optimizing the nitrogen concentration is currently in progress.

It is well known that the N can be incorporated into ZnO lattice in at least two chemical states, either a N<sub>2</sub><sup>-</sup> molecule (O<sub>N2</sub>) or a N atom (ON) occupying an O site, depending on the synthetic methods.<sup>29</sup> The chemical environments of these two types of N dopant are different and we performed high-resolution XPS studies to identify the chemical states on N dopant in N:ZnO nanowires. The core level spectrum of the N 1s region shows an asymmetric broad peak centered at 398.5 eV with full-width-half-maximum

(FWHM) of  $\sim 4$  eV (Figure 2.3b), which suggests more than one chemical states of N are present. By fitting the experimental line profile<sup>27</sup>, two deconvoluted peaks centered respectively at 399.6 eV and 398.3 eV were identified. First, this data suggests the chemical state of  $\text{O}_{\text{N}_2}$  does not exist in these ZnO nanowires because no peak was observed in the reported binding energy of  $\text{O}_{\text{N}_2}$  of 404 eV.<sup>19, 30</sup> Second, the peak of 399.6 eV is a typical N 1s binding energy of amines<sup>31</sup>. Given that the ammonia was used as N precursor, it is reasonable to expect the presence of N-H compounds on nanowire surface due to the incomplete decomposition of ammonia. Last, the peak of 398.3 eV, is a intermediate between the typical binding energy found for zinc nitride ( $\sim 396$ - $397$  eV)<sup>32</sup> and NO type species (above 400 eV), can be attributed to the N1s of oxynitride (O-Zn-N).<sup>30, 33</sup> This data indicates the N dopant incorporates substitutionally at O site in ZnO nanowire, and ammonia as N precursor favors the formation of ON. Powder X-ray diffraction patterns of undoped ZnO and a 3.7 at.% N:ZnO nanowire are presented in Figure 2.3c. The results reveal that both ZnO nanowires are in wurtzite structure and there is no significant shift in the lattice constants and phase change due to N doping.<sup>26</sup>



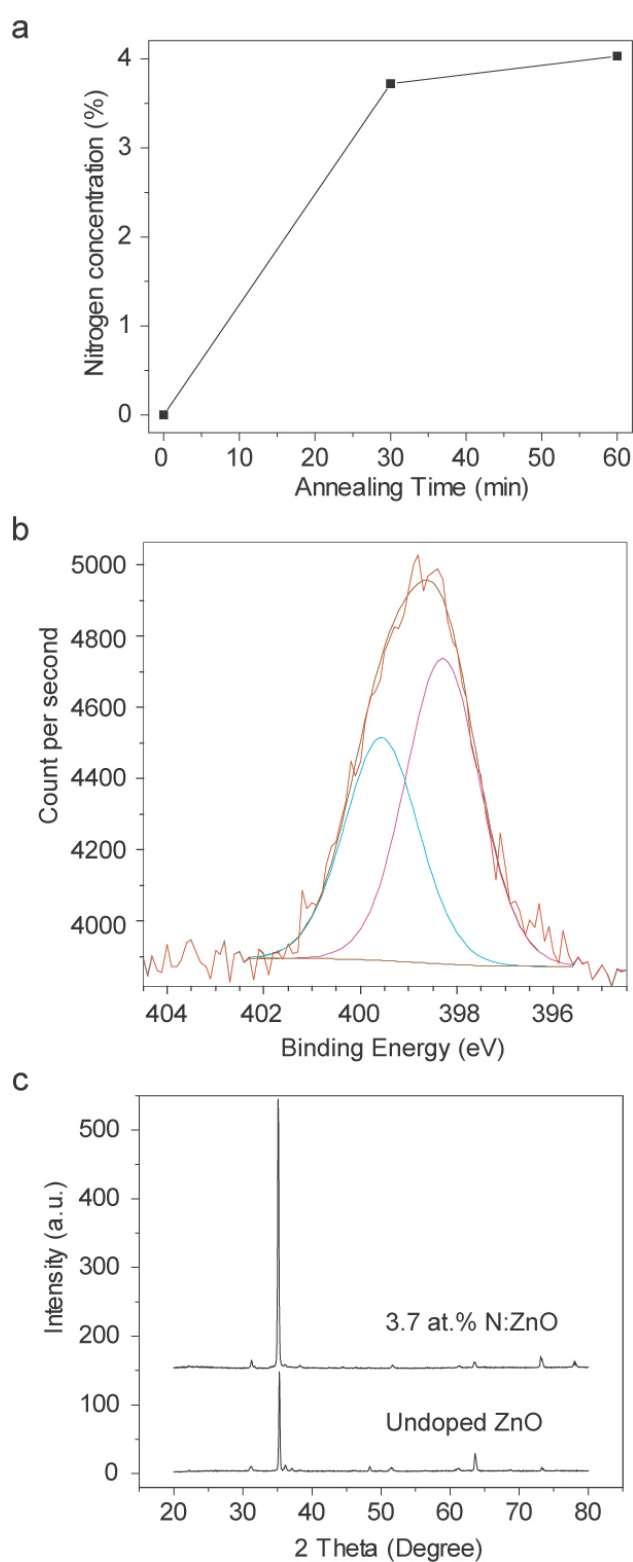


**Figure 2.3.** (a) The plot of N concentration (at.%) of ZnO nanowires versus time of ammonia annealing. (b) High-resolution XPS spectrum of N 1s peak of N:ZnO nanowires on ITO substrate. The red curve is the experimental result.

The brown curve is the summation of the synthetic peaks 399.6 eV (blue curve) and 398.3 eV (purple curve). (c) Powder X-ray diffraction patterns of undoped and N-doped ZnO nanowires.

The chemical state of the N dopant affects the electronic properties of ZnO nanowires.<sup>29</sup> In order to understand the intrinsic electronic properties of ZnO nanowires in electrolyte solution, we performed electrochemical impedance measurements<sup>34</sup> in the dark to determine the capacitance of nanowires. Nanowire dopant density and flatband potential at nanowire/electrolyte interface can be quantified by the Mott–Schottky equation<sup>35</sup>  $1/C^2 = (2/e_0\epsilon\epsilon_0N_d)[(V - V_{FB}) - kT/e_0]$ , wherein  $e_0$  is the electron charge,  $\epsilon$  the dielectric constant of ZnO,  $\epsilon_0$  the permittivity of vacuum,  $N_d$  the dopant density,  $V$  the electrode applied potential,  $V_{FB}$  the flatband potential, and  $kT/e_0$  is a temperature-dependent correction term. The Mott-Schottky plot collected from a 3.7 at.% N:ZnO nanowires is presented in Figure 2.4. In contrast to planar samples, they exhibit a non-linear behavior due to the cylindrical geometry of nanowires.<sup>36</sup>  $V_{FB}$  of nanowires was determined from the extrapolation of X intercepts in Mott–Schottky plots ( $1/C^2$  versus  $V$ ) at varies frequencies, which was found to be -0.97 V (versus SHE). The  $V_{FB}$  required for a water splitting reaction to proceed should be more cathodic than the reduction potential of hydrogen ( $E_h$ ), which varies as a function of pH value and can be quantified by the equation  $E_h = 0 - 0.059(\text{pH})$ . In our case, the electrochemical impedance measurements were conducted at pH = 7, the observed  $V_{FB}$  of N:ZnO nanowire is more cathodic

than the calculated minimum of  $V_{FB}$  of -0.42 V, as expected. In addition, the slopes determined from the analysis of Mott-Schottky plot were used to estimate the carrier density using the equation,  $N_d = -(2/e_0\epsilon\epsilon_0)[d(1/C^2)/dV]^{1/2}$ . The negative slope indicates N:ZnO nanowires are n-type material with electron conduction. With an  $\epsilon$  value of 10 for ZnO,<sup>36</sup> the electron density of N:ZnO nanowires was then calculated to be  $1.7 \times 10^{19} \text{ cm}^{-3}$ . The carrier density is comparable to the value of  $6.2 \times 10^{19} \text{ cm}^{-3}$  has been reported in ZnO nanowires grown by electrodeposition method.<sup>36</sup>

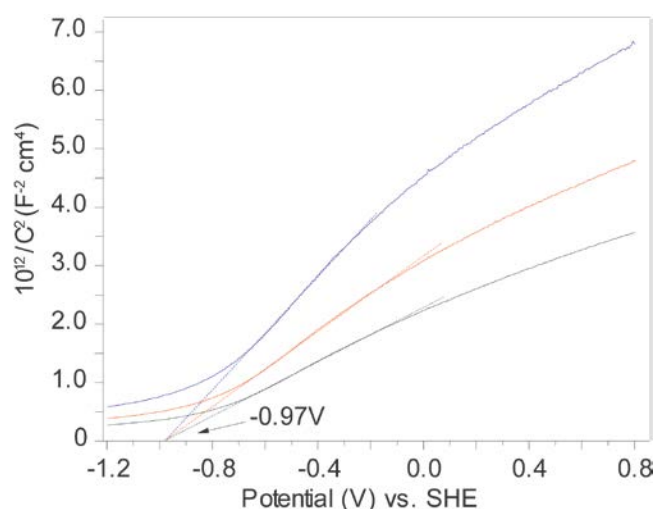


**Figure 2.4.** Mott-Schottky plots of a 3.7 at.% N:ZnO nanowire in the dark at frequencies of 5000 (black line), 7000 (red line) and 10000 Hz (blue line) and an AC current of 7 mV with a three-electrode system. The potential was measured against a Ag/AgCl reference and converted to SHE potentials by using  $E(\text{Ag/AgCl}) = E(\text{SHE}) + 0.197 \text{ V}$ . Dash lines represent the extrapolated lines from the linear portion of the Mott-Schottky plots.

Our goal is to address the limited absorption and conversion efficiency of ZnO nanowires as photoanodes by reducing the band-gap of ZnO through

controlled N doping. So it is important to understand how the N dopant affects the absorption efficiency of ZnO nanowires. UV-vis spectroscopy studies, however, cannot provide a quantitative result on absorption properties of nanowires due to the strong scattering effect of nanowires on substrate. Therefore, we performed incident-photon-to-current-conversion efficiency (IPCE) measurements to study the photoactive wavelength regime for undoped and N-doped ZnO nanowires (Figure 2.5). IPCE can be expressed as:  $IPCE = (1240 \times I) / (\lambda \times J_{light})$ ,<sup>37</sup> where  $I$  is the photocurrent density,  $\lambda$  is the incident wavelength and  $J_{light}$  is the measured irradiance. Undoped ZnO nanowires showed a minimal photoresponse below the band-gap energy (~3.3 eV, 376 nm)<sup>26</sup>. In contrast, IPCE data collected from the N:ZnO nanowires showed a significant red shift towards lower energy compare to the undoped nanowires. At below band-gap illumination, for example, the IPCE of ZnO and N:ZnO nanowires at the incident wavelength of 400 nm are 3.3 % and 14.6 %, respectively. This data is a direct evidence of N dopant narrows the band-gap of ZnO and improves the light collection and conversion efficiency in visible region of interest.

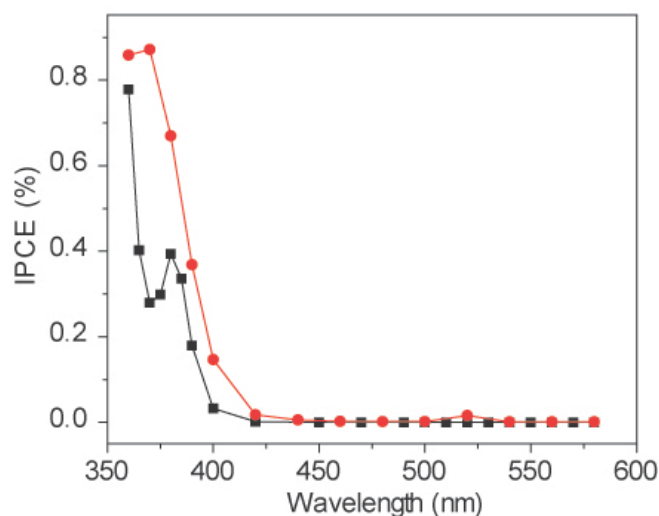


**Figure 2.5.** Measured IPCE spectra of undoped ZnO nanowires (square) and 3.7 at% N:ZnO nanowires (circle) in the region of 360 nm to 580 nm at a potential of +0.8 V and +0.5 V, respectively.

Systematic electrochemical measurements<sup>34</sup> were carried out to evaluate the PEC properties of photoanodes fabricated from ZnO and N:ZnO nanowires. Figure 2.6a shows a set of linear sweep voltammograms recorded on these nanowires in the dark and at illumination of 100 mW/cm<sup>2</sup> (AM 1.5). Dark scan linear sweep from -0.5 V to +1.3 V showed a small current in the range of 10<sup>-7</sup> A/cm<sup>2</sup>. Upon illumination, undoped ZnO nanowires showed a pronounced photocurrent starting at ~ -0.4 V and continues to increase to 17  $\mu$ A/cm<sup>2</sup> at +1.0 V. In comparison to undoped nanowires, N:ZnO nanowires showed a significant enhancement in photoresponse with a photocurrent density of 400  $\mu$ A/cm<sup>2</sup> at +1.0 V. Significantly, there is no saturation of photocurrent has been observed in all studied nanowires at more positive potential, which indicates a good charge separation occurs in nanowires upon illumination and the depletion layer is not

fully optimized yet. The width of the space-charge layer ( $W$ ) at the semiconductor/solution interface can be derived from the Mott–Schottky plot relationship and be expressed as  $W = [2\epsilon\epsilon_0(V-V_{FB}) / e_0N_d]^{1/2}$ .<sup>38</sup> At a potential of +1.0 V,  $W$  has been calculated to be 6.2 nm, which is much smaller than the radius of ZnO nanowires.

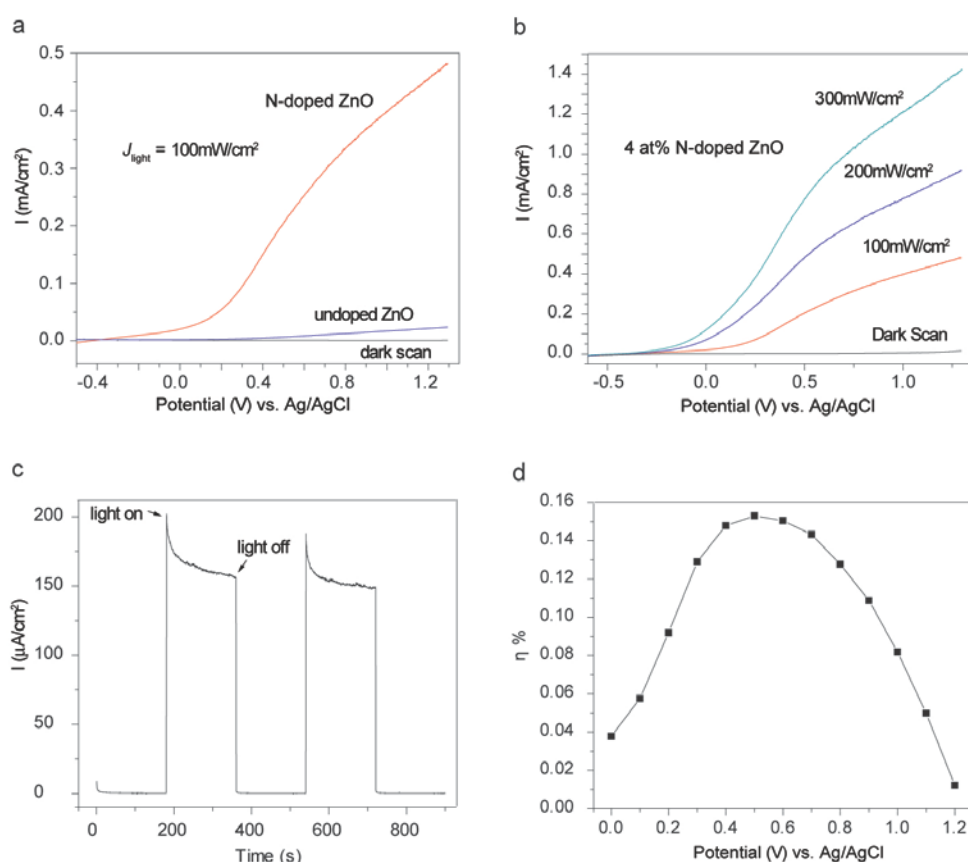


**Figure 2.6.** (a) Linear sweep voltammograms, collected at a scan rate of 10 mV/s at applied potentials from -0.5 V to +1.3 V, from undoped ZnO nanowires in the dark (black line), undoped ZnO nanowires (blue line) and 3.7 at.% N:ZnO nanowires (red line) at 100 mW/cm<sup>2</sup>. (b) Linear sweep voltammograms of the N:ZnO nanowires in the dark (black line), at 100 mW/cm<sup>2</sup> (red line), 200 mW/cm<sup>2</sup> (blue line) and 300 mW/cm<sup>2</sup> (green line). (c) Amperometric  $I$ - $t$  curves of the N:ZnO nanowires at an applied voltage of +0.5 V at 100 mW/cm<sup>2</sup> with 180 s light on/off cycles. (d) Photoconversion efficiency of the PEC cell with N:ZnO nanowire electrode as a function of applied potential.

Power-dependence linear sweep voltammograms (Figure 2.6b) collected from the N:ZnO nanowire photoanode showed the photocurrent density increases almost proportionally with the increase of the incident white light power and the photocurrent is not saturated even at  $300 \text{ mW/cm}^2$ . This is of practical importance for the development of solar concentrated PEC cells. In addition, we performed amperometric I-t studies to examine the photoresponse of nanowires over time. I-t curves collected from the N:ZnO sample with light on/off cycles at  $100, 200$  and  $300 \text{ mW/cm}^2$  at  $+0.5 \text{ V}$  are presented in Figure 2.6c. The data shows a very low dark current of  $< 10^{-7} \text{ A/cm}^2$ . Upon illumination, we observed a spike in photoresponse at all power densities due to the transient effect in power excitation, and then the photocurrent quickly decrease to a steady state. We only observed a small decay of photocurrent density after addition runs ( $\sim 10 \mu\text{A}$  in  $5000\text{s}$ ), which indicates N:ZnO nanowires as photoanodes are stable in the photo-oxidation process. (Figure 2.7) We carried out systematic amperometric I-t studies on N:ZnO nanowire as a function of applied overpotential at  $100 \text{ mW/cm}^2$ . The efficiency of photon-to-hydrogen ( $\eta$ ) generation was used the question,  $\eta = I (1.23\text{-V}) / J_{\text{light}}$ .<sup>39</sup> The plot of efficiency versus applied potential (Figure 2.6d) showed the maximum value of efficiency is  $0.11\%$ , which is obtained at an applied potential of  $+0.5 \text{ V}$ . To determine the intrinsic  $\eta$  of ZnO nanowires, the optical losses due to measurement set up ( $\sim 25 \%$ ) should be corrected. The effective photonconversion efficiency of a  $3.7 \text{ at.}\%$  N:ZnO

nanowires is then calculated to be 0.15%, which is higher than the recent reported values for undoped TiO<sub>2</sub> nanorods<sup>18</sup> and N:ZnO film<sup>19</sup> as photoanodes. Significantly, N:ZnO nanowires showed a 15 times enhancement in efficiency compare to undoped ZnO nanowires with typical photonconversion efficiencies of ~0.01 %. Given that the overlap between the absorption spectrum of the 3.7 at.% N:ZnO nanowires and the solar spectrum (~ 5%) is still limited, these PEC results are very encouraging.

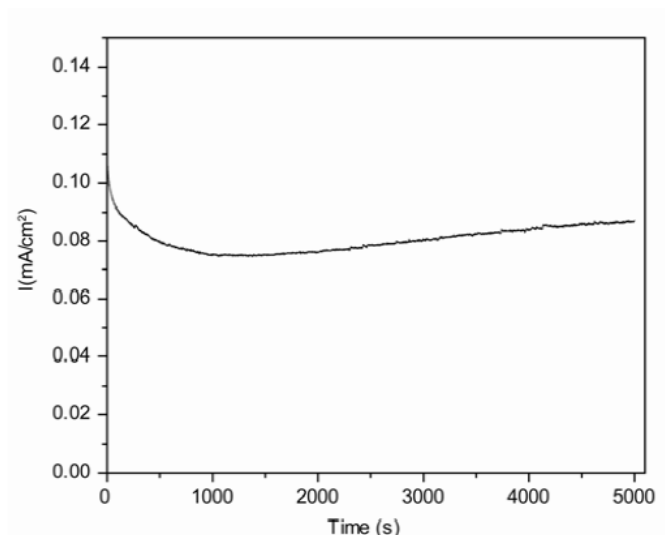


**Figure 2.7.** Amperometric I-t curvs of the ZnO:N nanowires collected at applied potential of 0.5V vs. Ag/AgCl for 5000 s.

## Conclusion

In summary, we have synthesized N:ZnO nanowire arrays with well controlled of N dopant. IPCE studies of N:ZnO nanowires show a significant enhancement in conversion efficiency in the visible region. In comparison to undoped ZnO nanowires, 3.7 at.% N:ZnO nanowires demonstrate a order of magnitude



increase in photoresponse with a overall efficiency of 0.15 %. The overall efficiency is still somewhat low since the system has not been optimized. However, the advantage afforded by N-doping is clearly demonstrated in terms of enhancing visible absorption and photocurrent conversion. Further improvement of conversion efficiency of these nanowires might be achieved by optimizing the N concentration to further increase the light absorption efficiency, reducing the wire diameter to increase active surface area and optimize the width of depletion layer, and minimizing the resistance between nanowires and ITO substrate. These N:ZnO nanowire arrays offer substantial promise as reliable photoanodes of PEC cells for water splitting.

## **References:**

1. Balat, M. *Int. J. Hydrogen Energy* **2008**, 33, 4013-4029.
2. Grimes, C. A.; Varghese, O. K.; Ranjan, S., *Light, Water, Hydrogen: The Solar Generation of Hydrogen by Water Photoelectrolysis*. Springer Science+Business Media, LLC: New York, 2008.
3. Ogden, J. M. *Annu. Rev. Energy. Environ.* **1999**, 24, 227-229.
4. Hartstein, A., Hydrogen Production from Natural Gas. In *Hydrogen Coordination Meeting*, 2003.
5. Dresselhaus, M. S.; Crabtree, G. W.; Buchanan, M. V., Basic Research Needs for the Hydrogen Economy. In Office of Basic Energy Sciences, D. O. E.,

Washington, DC, Ed. 2003.

6. Crabtree, G. W.; Dresselhaus, M. S. *MRS Bulletin* **2008**, 33, 421-428.
7. Bak, T.; Nowotny, J.; Rekas, M.; Sorrell, C. C. *Int. J. Hydrogen Energy* **2002**, 27, 991-1022.
8. Bard, A. J.; Fox, M. A. *Acc. Chem. Res.* **1995**, 28, 141-145.
9. Honda, K.; Fujishima, A. *Nature* **1972**, 238, 37-39.
10. Khan, S. U. M.; Al-Shahry, M.; B., I. J. W. *Science* **2002**, 297, 2243-2245.
11. Lewis, N. S. *Nature* **2001**, 414, 589.
12. Burube, V.; Dresselhaus, M. S., Nano-structured materials to address challenges of the hydrogen initiative. In *MRS Symposium Proceeding*, 2008; Vol. 1041, pp R02-01.
13. Kudo, A.; Miseki, Y. *Chem. Soc. Rev.* **2009**, 38, (1), 253-278.
14. Mao, S. S.; Chen, X. *Int. J. Energy Res.* **2007**, 31, 619-636.
15. Bak, T.; Nowotny, J.; Rekas, M.; Sorrell, C. C. *Int. J. Hydrogen Energy* **2002**, 27, 19-26.
16. Compton, O. C.; Mullet, C. H.; Chiang, S.; Osterloh, F. J. *Phys. Chem. C* **2008**, 112, (15), 6202-6208.
17. Chen, S.; Paulose, M.; Ruan, C.; Mor, G. K.; Varghese, O. K.; Kouzoudis, D.; Grimes, C. A. *J. Photochem. Photobio. A: Chem.* **2006**, 177, 177-184.
18. Wolcott, A.; Smith, W. A.; Kuykendall, T. R.; Zhao, Y. P.; Zhang, J. Z. *Small* **2008**, 5, (1), 104-111.

19. Ahn, K. S.; Yan, Y.; Lee, S. H.; Deutsch, T.; Turner, J.; Tracy, C. E.; Perkins, C. L.; Al-Jassim, M. M. *J. Electrochem. Soc.* **2007**, 154, (9), B956-B959.
20. Yan, Y.; Ahn, K. S.; Shet, S.; Deutsch, T.; Huda, M.; Wei, S. H.; Turner, J.; Al-Jassim, M. M. *Solar Hydrogen and Nanotechnology II Proceeding of SPIE* **2007**, 6650, 66500H.
21. Kaidashev, E. M.; Lorenz, M.; von Wenckstern, H.; Rahm, A.; Semmelhack, H. C.; Han, K. H.; Benndorf, G.; Bundesmann, C.; Hochmuth, H.; Grundmann, M. *Appl. Phys. Lett.* **2003**, 82, 3901-3903.
22. Hendry, E.; Koeberg, M.; O'Regan, B.; Bonn, M. *Nano. Lett.* **2006**, 6, 755-759.
23. Heo, Y. W.; Norton, D. P.; Tien, L. C.; Kwon, Y.; Kang, B. S.; Ren, F.; Pearton, S. J.; LaRoche, J. R. *Mater. Sci. Eng. R* **2004**, 47, 1-47.
24. Wang, Z. L. *J. Nanoscience & Nanotechnology* **2008**, 8, (1), 27-55.
25. Greene, L.; Law, M.; Goldberger, J.; Kim, F.; Johnson, J. C.; Zhang, Y. F.; Saykally, R. J.; Yang, P. D. *Angew. Chem. Int. Ed.* **2003**, 42, 3031-3034.
26. Ozgur, U.; Alivov, Y. I.; Liu, C.; Teke, A.; Reshchikov, M. A.; Dogan, S.; Avrutin, V.; Cho, S. J.; Morkoc, H. *J. Appl. Phys.* **2005**, 98, 041301.
27. XPS data were collected in a Kratos Axis Ultra XPS system operated under charge compensation and with monochromated Al as X-ray source. Peak positions were calibrated by setting the true position of the C1s line to 285.0 eV. The survey scan and high-resolution scan were collected using

pass energy of 80 and 40 eV, respectively. Peak fitting is performed by assuming the observed peak as a convolution of a Gaussian and Lorentzian function. We restricted the FWHM of the deconvoluted peak to a maximum 1.9 eV, and then vary the peak shape to match the experimental data.

28. Bruno, G.; Giangregorio, M. M.; Malandrino, G.; Capezzuto, P.; Fragala, I. L.; Losurdo, M. *Adv. Mater.* **2009**, 21, 1-7.
29. Yan, Y.; Zhang, S. B.; Pantelides, S. T. *Phys. Rev. Lett.* **2001**, 86, (25), 5723-5726.
30. Perkins, C. L.; Lee, S. H.; Li, X.; Asher, S. E.; Coutts, T. J. *J. Appl. Phys.* **2005**, 97, 034907.
31. Musat, V.; Rego, A. M.; Monteiro, R.; Fortunato, E. *Thin Solid Films* **2008**, 516, 1512-1515.
32. Toyoura, K.; Tsujimura, H.; Goto, T.; Hachiya, K.; Hagiwara, R.; Ito, Y. *Thin Solid Films* **2005**, 492, 88-92.
33. Bian, J. M.; Li, X. M.; Gao, X. D.; Yu, W. D.; Chen, L. D. *Appl. Phys. Lett.* **2004**, 84, (4), 541-543.
34. Nanowires were fashioned into photoanodes by the placement of a copper wire onto a bare portion of the ITO substrate and secured with high-purity silver conducting paint. Cells were then sealed on all edges with epoxy resin except for a working electrode surface area of 0.25–

0.50 cm<sup>2</sup>. Electrolyte solutions of 0.5 M NaClO<sub>4</sub> were prepared and then buffered to pH of 7.0 with phosphate buffer solution. Prior to PEC experiments, all solutions were deaerated with nitrogen, and during experimentation a constant positive pressure of nitrogen also flowed through a three-neck vessel at all times. An Ag/AgCl reference electrode (+0.198 V versus NHE) was employed along with a coiled Pt wire counter electrode during all runs. All PEC and impedance measurements were carried out on a Solartron 1280B and was coupled to an infrared water-filled filter (Oriel #6127), and then aligned into a monochromator (Oriel Cornerstone 130 1/8m). A 1000W Xe lamp was utilized as a white-light source and irradiance were measured with power meter.

35. Cardon, F.; Gomes, W. P. *J. Phys. D: Appl. Phys.* **1978**, 11, (4), L63-L67.
36. Mora-Sero, I.; Fabregat-Santiago, F.; Denier, B.; Bisquert, J.; Tena-Zaera, R.; Elias, J.; Levy-Clement, C. *Appl. Phys. Lett.* **2006**, 89, 203117.
37. Murphy, A. B.; Barnes, P. R. F.; Randeniya, L. K.; Plumb, I. C.; Grey, I. E.; Horne, M. D.; Glasscock, J. A. *Int. J. Hydrogen Energy* **2006**, 31, 1999-2017.
38. Schottky, W. Z. *Phys.* **1942**, 118, 539.
39. Parkinson, B. *Acc. Chem. Res.* **1984**, 17, 431-437.

## Chapter 3

### Double-sided CdS and CdSe Quantum Dot Co-sensitized ZnO Nanowire

#### Arrays for Photoelectrochemical Hydrogen Generation

##### Abstract

We report the design and characterization of a novel double-sided CdS and CdSe quantum dot co-sensitized ZnO nanowire arrayed photoanode for photoelectrochemical (PEC) hydrogen generation. The double-sided design represents a simple analog of tandem cell structure, in which the dense ZnO nanowire arrays were grown on an indium-tin oxide substrate followed by respective sensitization of CdS and CdSe quantum dots on each side. As-fabricated photoanode exhibited strong absorption in nearly the entire visible spectrum up to 650 nm, with a high incident-photon-to-current-conversion efficiency (IPCE) of ~45 % at 0V vs. Ag/AgCl. Based on a single white light illumination of 100 mW/cm<sup>2</sup>, the photoanode yielded a significant photocurrent density of ~12 mA/cm<sup>2</sup> at 0.4 V vs. Ag/AgCl. The photocurrent and IPCE were enhanced compared to single quantum dot sensitized structures as a result of the band alignment of CdS and CdSe in electrolyte. Moreover, in comparison to single-sided co-sensitized layered structures, this double-sided architecture that enables direct interaction between quantum dot and nanowire showed improved

charge collection efficiency. Our result represents the first double-sided nanowire photoanode that integrates uniquely two semiconductor quantum dots of distinct bandgaps for PEC hydrogen generation, and can be possibly applied to other applications such as nanostructured tandem photovoltaic cells.

## **Introduction**

Metal oxide nanowire (NW) arrays with large surface area and short diffusion length for minority carriers represent a new class of photoelectrode materials that hold great promise for photoelectrochemical (PEC) hydrogen generation applications.<sup>1-3</sup> However, both bulk and nanostructured wide bandgap metal oxide photoelectrodes, such as ZnO and TiO<sub>2</sub>, face the major limitation of poor visible light absorption. Considerable efforts have been made to improve their visible light absorption, including elemental doping,<sup>4,5</sup> dye or quantum dot (QD) sensitization,<sup>6-11</sup> and constructing hybrid structures,<sup>12-14</sup> yet the complete absorption of solar light have not been realized. Photovoltaic (PV) studies have demonstrated that tandem structure made of a combination of semiconductors with optimal bandgap energies can maximize the absorption of solar light.<sup>15, 16</sup> However, rational synthesis of the multi-junction nanostructures for photovoltaic or PEC devices has been technically challenging.

Double-sided structure serves as an analog of tandem cell, offering new opportunities for design and fabrication of PV and PEC devices. Several

double-sided PV or PEC structures based on metal oxide nanotube<sup>17, 18</sup> and nanowire<sup>19</sup> arrays have recently been reported. For example, Grimes reported the self-biased heterojunction PEC diodes with *n*-type TiO<sub>2</sub> on the front and *p*-type Cu-Ti-O nanotubes on the back side of a substrate.<sup>17</sup> Although this work combined a photoanode and a photocathode on the same substrate, the device was not targeted at increasing visible light absorption. In addition, Wang developed a double-sided nanowire structured hybrid cell for concurrently scavenging solar and mechanical energies,<sup>19</sup> and Misra demonstrated the double-sided illuminated TiO<sub>2</sub> nanotubes for hydrogen generation.<sup>18</sup> Yet these devices required the two sides operated separately and therefore two energy sources. Here we report a novel double-sided CdS and CdSe QD co-sensitized ZnO NW arrayed photoanode (denoted as CdS-ZnO-ZnO-CdSe) that exhibits strong absorption in the wavelength region up to 650 nm and can be operated using a single white light source (Figure 3.1). This unique structure integrates the motif of QD sensitization and tandem cell to provide a simple approach to enhance simultaneously the visible light absorption and carrier collection of nanostructured metal oxide photoelectrodes. In comparison to double-sided single-sensitized structures and single-sided co-sensitized structures, the double-sided co-sensitized sample showed substantially enhanced photocurrent density and IPCE due to the improved carrier transfer and collection efficiency.



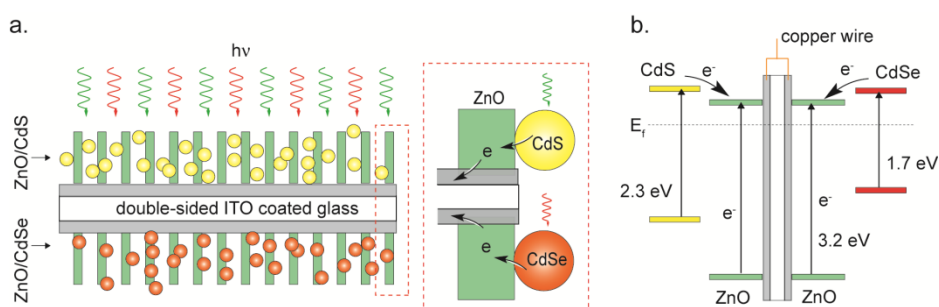


**Figure 3.1.** Schematic diagrams illustrating (a) the architecture and (b) the corresponding energy diagram of double-sided CdS-ZnO-ZnO-CdSe NW arrayed photoanode. Dashed square highlight the CdS-ZnO and CdSe-ZnO interfaces.

## Experimental Section

**Synthesis of ZnO NW arrays:** we grew ZnO nanowires on a ZnO nanoparticle seeded ITO substrate using hydrothermal method.

*ZnO seed coating* -- both sides of ITO glass were deposited with zinc acetate ethanol solution, then rinsed by ethanol solution and blew dry. This coating step was repeated five times. Then, the sample was annealed at 350 °C for 30 min. The zinc acetate deposition and annealing processes were carried out twice to ensure a uniform coating of ZnO nanocrystal seeds on ITO glass.

*Hydrothermal synthesis* -- ITO glass coated with ZnO seeds was vertically put into a rubber holder. The substrate with holder was placed into a Telfon-lined stainless steel autoclave, filled with 20 ml 0.05 M zinc nitrate and 0.05 M hexamethylenetetramine aqueous solution. The sealed autoclave was heated in an electric oven at 90 °C for 6 hours. ITO glass coated with uniform white film

on both sides was rinsed with deionized water and air dried.

**CdS and CdSe QD sensitization:** ZnO NW arrays were sensitized with CdS and CdSe QDs sequentially, using chemical bath deposition (CBD).{Lokhande, 2005 #20; Spoerke, 2009 #21} For double-sided samples, we first sensitized ZnO NW arrays with CdS QD on one side of the substrate, while the other side was protected by a parafilm foil and all edges were sealed with adhesive tape. Then the other side of the substrate was sensitized with CdSe QDs using the same approach. For single-sided co-sensitized samples, we sensitized ZnO NW sequentially with CdS and CdSe QDs.

CdS QDs were deposited on ZnO NWs with a modified CBD method. As prepared double-sided ZnO NW array with one side protected was incubated in an aqueous solution of 10 mM  $\text{Cd}(\text{NO}_3)_2$  and 10 mM thioacetamide at 40 °C for 10 min. White ZnO NW film became yellow. The substrate was washed with deionized water and air dried.

CdSe QDs were deposited on ZnO NWs using a reported CBD method. Cadmium nitrate ( $\text{Cd}(\text{NO}_3)_2$ ) was used as Cd source and sodium selenosulphate ( $\text{Na}_2\text{SeSO}_3$ ) as Se source. The  $\text{Na}_2\text{SeSO}_3$  aqueous solution was prepared by refluxing Se powder in an aqueous  $\text{Na}_2\text{SO}_3$  solution at 80 °C overnight. Freshly prepared 0.1 M  $\text{Na}_2\text{SeSO}_3$  (8 ml) was mixed with the same volume 0.02 M  $\text{Cd}(\text{NO}_3)_2$  and 0.5 M sodium citrate in a 20 ml glass vial. CdS QD sensitized

ZnO NW sample with CdS side protected was placed into the vial, and heated in water bath at 60 °C for 15 min. The process above was termed as a CBD cycle. We carried out two CBD cycles, the color of ZnO NW arrays were changed from white to deep red.

**Electron microscopy:** SEM images were collected in a Hitachi 2700 SEM. NWs were dispersed in ethanol solution and then transferred onto Cu/lacey-carbon TEM grids. TEM images were collected in a FEI monochromated F20 UT Technai TEM/STEM operated with an 200 kV electron beam.

**Powder X-ray diffraction:** The NW films on ITO substrate were characterized by PXRD with a Rigaku Americas Miniflex Plus powder diffractometer. Diffraction patterns were recorded from 20 to 80° 2 $\theta$  with a step size of 0.04° at 1°/min.

**UV-vis spectroscopy:** The UV-vis absorption spectra of NW films were taken on a Hewlett-Packard 8452A diode array spectrophotometer at room temperature.

**Fabrication and PEC measurement of NW photoanodes:** NW arrays were fashioned into photoanodes by securing a copper wire onto a bare portion of ITO substrate with silver conducting paint. Both sides of the substrate were connected to the same copper wire by soldering. The substrate was then sealed

on all edges with epoxy resin except for a working area of  $0.18\text{ cm}^2$  on both sides. All PEC measurements were carried out in a three-electrode electrochemical cell in a stirred solution bubbled with nitrogen, with a coiled Pt wire as a counter electrode and an Ag/AgCl electrode as a reference. The electrolyte was a mixture of 0.25 M  $\text{Na}_2\text{S}$  and 0.35 M  $\text{Na}_2\text{SO}_3$  aqueous solution with a pH of  $\sim 9.5$ , which were used as sacrificial reagents to maintain the stability of CdS and CdSe. I-V measurements were made on a Solartron 1280B potentiostat coupled to an infrared water-filter (Oriel no. 6127) using a 1000 W Xenon Arc Lamp as the white light source. The light power of  $100\text{ mW/cm}^2$  was measured with a power meter (Molelectron, PM5100). IPCE characteristics were measured with a monochromator (Oriel Cornerstone 130 1/8m).

## Results and Discussion

ZnO NW arrays were first synthesized to cover the entire surface of both sides of a double-sided indium-tin-oxide (ITO) glass substrate using hydrothermal method.<sup>20</sup> The double-sided ZnO NWs were then sequentially sensitized with CdS and CdSe QDs by chemical bath deposition.<sup>21, 22</sup> The detailed synthetic strategy is illustrated in Figure 3.2. At equilibrium, the Fermi levels of the three semiconductors will be aligned with electrolyte solution as shown in the simplified energy diagram (Figure 3.1b). Importantly, the conduction band edges (CBEs) of CdS and CdSe are higher than that of ZnO,

allowing efficient transfer of photoexcited electrons from CdS and CdSe QDs to ZnO NWs. While the electrons are transported to cathode for hydrogen generation in a PEC device, the holes will be consumed for an oxidation reaction at the anode/electrolyte interface.

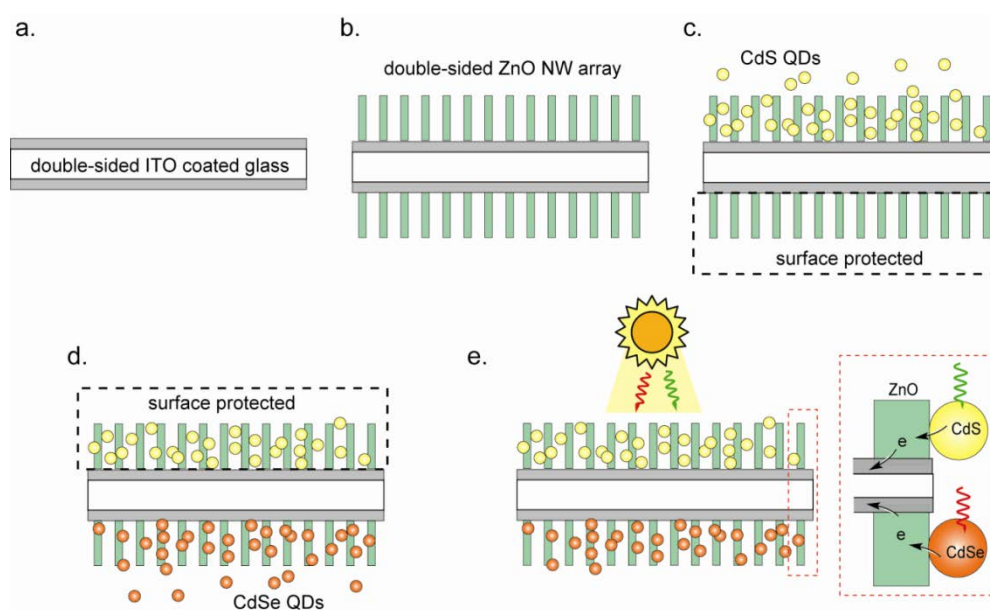
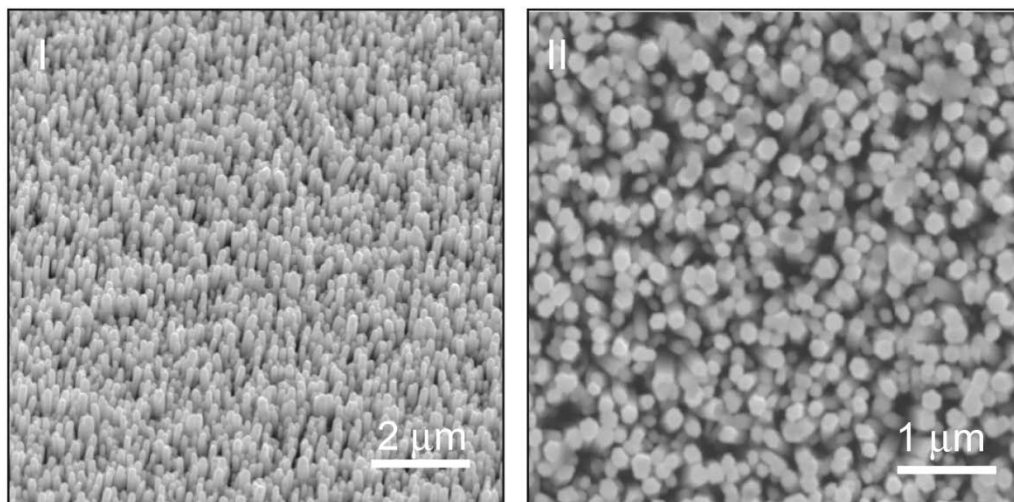


**Figure 3.2** The schematic shows the fabrication of double sided CdS and CdSe quantum dots sensitized ZnO nanowire arrays.

To investigate the structural properties of these QD-coupled nanowires, we carried out electron microscopy and powder X-ray diffraction (PXRD) studies. Scanning electron microscopy (SEM) images revealed the growth of dense and vertically aligned ZnO NWs on both sides of the ITO substrate, with typical wire diameter of ~100-150 nm and wire length of ~ 2  $\mu\text{m}$ . High-resolution transmission electron microscopy (TEM) image showed that ZnO nanowires were single crystal wurtzite structures with growth direction of  $\langle 0001 \rangle$  (Figure

3.3).

a.



b.

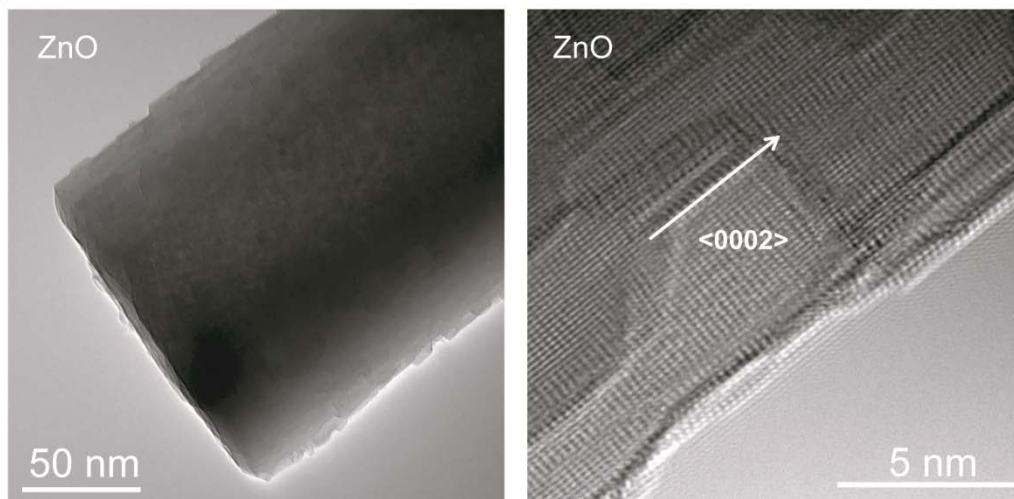


**Figure 3.3** (a-b) SEM images of ZnO nanowires on ITO glass. (c-d) low resolution and high resolution TEM images of ZnO nanowire.

After QD sensitization, TEM images verified that individual ZnO NWs were covered with nanoparticle aggregates with diameters about 10 – 30 nm (Figure 3.4). Each aggregate consisted of a number of QDs with average diameter of 3 – 10 nm and the measured lattice spacings was consistent with the  $d$ -spacings of

CdS or CdSe. Importantly, the QD/NW and QD/QD interfaces were clean without noticeable contamination from organic solvent residues, which could reduce the interfacial carrier loss.

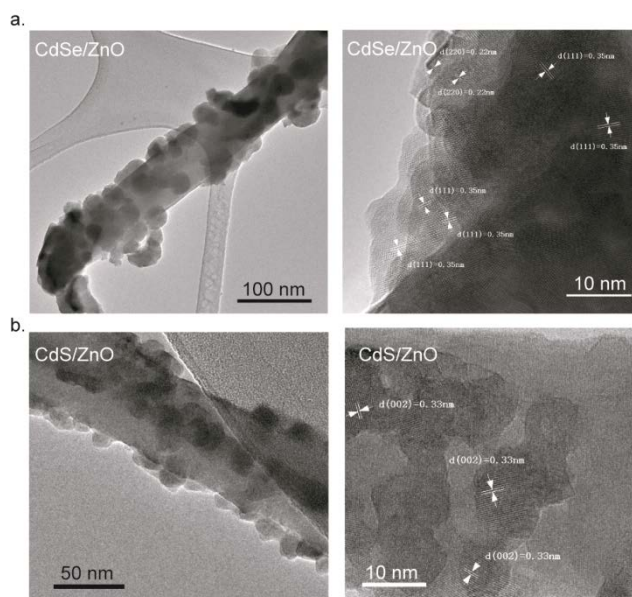


**Figure 3.4** TEM images of CdS and CdSe sensitized ZnO nanowire.

Powder X-ray diffraction (PXRD) studies further confirmed that the nanoparticle aggregates were CdS and CdSe based on their characteristic diffraction peaks (Figure 3.5).<sup>23</sup> These peaks were identified and can be indexed to CdSe cubic and CdS hexagonal structure respectively. In addition, no observable change in the ZnO crystal phase was observed after QD sensitization.

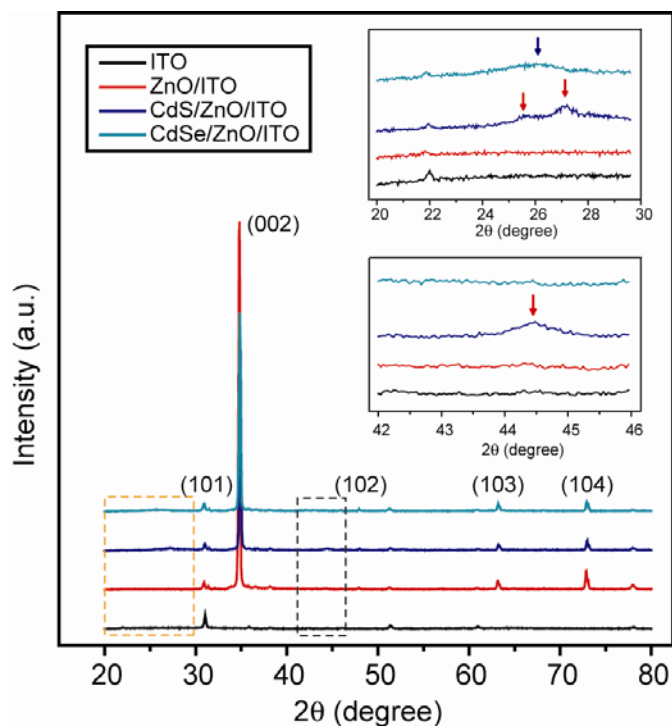


**Figure 3.5** XRD patterns of ITO glass, ZnO, CdS/ZnO, CdSe/ZnO. The insets are the magnified XRD pattern highlighted by the dashed boxes.

PEC measurements were performed to study the photoelectrochemical properties of the photoanodes fabricated from double-sided, CdS and CdSe co-sensitized ZnO NW arrays. All PEC measurements were carried out in a three-electrode electrochemical cell in a stirred solution bubbled with nitrogen, with a coiled Pt wire as a counter electrode and an Ag/AgCl electrode as a reference. A mixture of 0.25 M Na<sub>2</sub>S and 0.35 M Na<sub>2</sub>SO<sub>3</sub> aqueous solution was used as electrolyte and sacrificial reagent to maintain the stability of CdS and CdSe. The electrolyte had a pH of ~9.5 and the solution potential was about -0.56 V. I-V measurements were made on a Solartron 1280B potentiostat coupled to an infrared water-filter (Oriel no. 6127) using a 1000 W Xenon Arc



Lamp as the white light source. The CdS QD sensitized ZnO NWs were faced towards the incident light in all PEC measurements. In order to allow light penetrates through the first layer, we intentionally reduced the loading of CdS QDs. The CdSe QD was in maximum loading for complete light absorption. For comparison, double-sided ZnO NWs (denoted as ZnO-ZnO), CdS QD sensitized ZnO NWs (denoted as CdS-ZnO-ZnO-CdS) and CdSe QD sensitized ZnO NWs (denoted as CdSe-ZnO-ZnO-CdSe) were prepared in similar growth and sensitization conditions, and used as control samples for measurements. Figure 3.6 shows a set of linear sweep voltammograms recorded from these NW photoanodes in dark and at illumination of  $100 \text{ mW/cm}^2$  (AM 1.5). All samples showed small dark current density, in the order of  $10^{-1}$  to  $10^{-3} \text{ mA/cm}^2$  from -0.7 V to 0.4 V vs. Ag/AgCl. Only the dark scans of ZnO-ZnO and CdS-ZnO-ZnO-CdSe samples are plotted in Figure 3.6 for clarity. While all NW photoanode showed pronounced photoresponse under light illumination, QD sensitized NW samples exhibited substantially enhanced photocurrent compared to pristine ZnO NWs. This can be attributed to the improved visible light absorption by the QDs, as shown in UV-vis absorption studies (Figure 3.7). The results confirmed efficient interfacial charge transfer between CdS, CdSe QDs and ZnO NW. Significantly, the co-sensitized CdS-ZnO-ZnO-CdSe NW showed a maximum photocurrent density of  $\sim 12 \text{ mA/cm}^2$  at 0.4 V, which is about two times larger than that of single sensitized samples (CdS-ZnO-ZnO-CdS and

CdSe-ZnO-ZnO-CdSe). The data indicate that the incident light transmitted through the CdS-ZnO layer to the CdSe-ZnO layer at the back of the substrate and the light was absorbed by both layers. More importantly, there was a synergistic effect in the co-sensitized sample that led to the photocurrent enhancement.

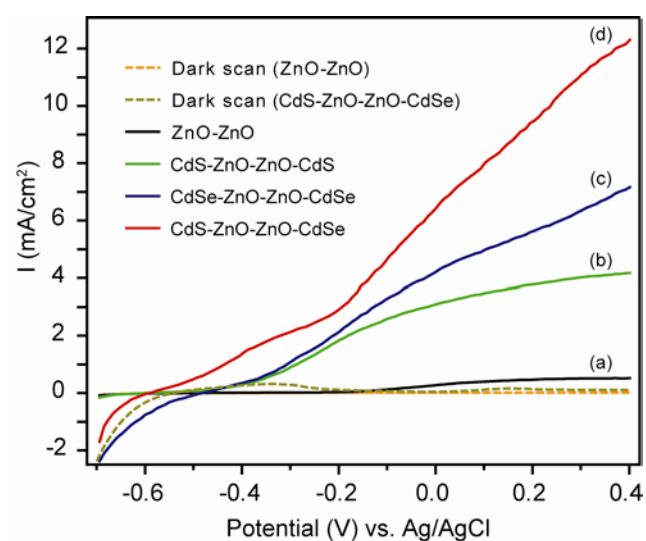


**Figure 3.6** PEC performances of double sided ZnO nanowire arrays, CdS sensitized ZnO nanowires, CdSe sensitized ZnO and CdS and CdSe co-sensitized ZnO nanowire arrays.

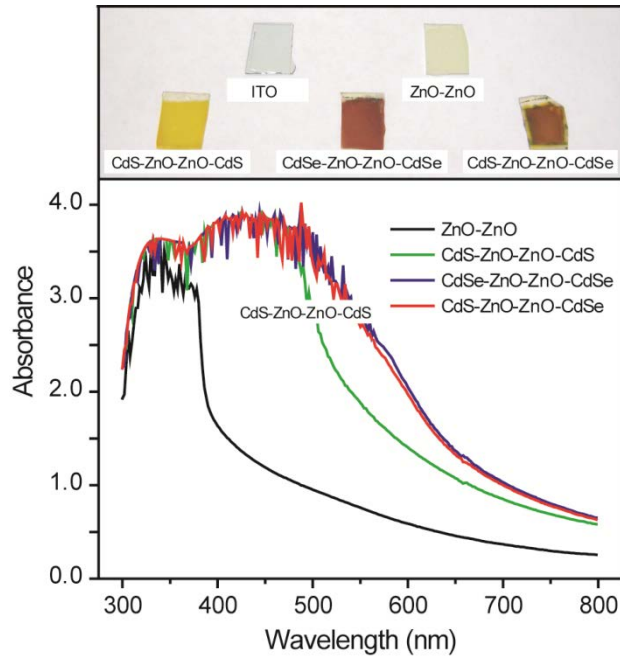


**Figure 3.7** Digital images of ITO glass, ZnO nanowire arrays, CdS sensitized ZnO, CdSe sensitized ZnO and CdS and CdSe cosensitized ZnO, and their corresponding UV-vis spectra.

To quantitatively address the photoactivity of QD sensitized NW photoanodes, we performed incident-photon-to-current-conversion efficiency (IPCE) measurements to study their photoresponse as a function of incident light wavelength (Figure 3.8). IPCE is expressed as:  $IPCE = (1240 \times I) / (\lambda \times J_{light})$ , where  $I$  is the photocurrent density,  $\lambda$  is the incident light wavelength and  $J_{light}$  is the incident light power density. In comparison to pristine ZnO NWs, sensitized ZnO NWs showed substantially enhanced IPCE in both the visible and UV regions due primarily to increased light absorption by the QDs. Lower IPCE are registered in UV region than visible region could be attributed to two possible reasons, 1) saturation of absorption due to the large absorption cross section for

most materials in the UV region than in the visible, which leads to apparently lower effective IPCE; and 2) insufficient UV penetration as UV light is more strongly scattered and absorbed than visible light, and a substantial absorption of UV light by ITO substrate. The CdS-ZnO-ZnO-CdS sample had a pronounced IPCE of ~35 - 45% at the wavelength up to 500 nm and then the IPCE dropped to a minimal level at wavelength below the CdS bandgap energy of ~550 nm (bandgap of bulk CdS: 2.3 eV). On the other hand, the CdS-ZnO-ZnO-CdSe sample showed photoactivity at a broader range of wavelength from 400 nm to 650 nm due to the smaller bandgap of CdSe (bandgap of bulk CdSe: 1.7 eV), with a lower IPCE value of ~25%. At the same incident wavelength (400 – 500 nm), the higher IPCE revealed that the CdS-ZnO composite was more efficient than CdSe-ZnO in separating and/or collecting photoexcited electrons, which is in agreement with the larger potential difference between the CBEs of CdS and ZnO. The photoactivity related to the QD excitonic absorption was not obvious due to the relatively broad size distribution of CdS and CdSe QDs. It is worth noting that the co-sensitized CdS-ZnO-ZnO-CdSe NW photoanode showed a nearly constant IPCE of ~45 % in the whole visible region from 400 nm to 650 nm, clearly demonstrating the advantage of this tandem structure. The high photoactivity at the incident wavelength from 400 nm to 500 nm is expected as both CdS and CdSe layers have substantial absorption in this region. More importantly, the IPCE of CdS-ZnO-ZnO-CdSe photoanode is about two times

higher than that of CdSe-ZnO-ZnO-CdSe at the incident wavelength of 550 nm - 650 nm, where the CdS layer in the co-sensitized sample has minimal light absorption. We attributed the enhanced IPCE to the Fermi level alignment between CdS and CdSe. It has been reported that the CBE of CdSe is elevated when its Fermi level is aligned with CdS in a CdSe/CdS/TiO<sub>2</sub> film.<sup>8, 24</sup> Similarly, we believe that the potential difference between the CBE of CdSe and ZnO in the co-sensitized sample was increased as the Fermi levels of CdS and CdSe were aligned in the electrolyte solution. The increased potential difference would facilitate the electron separation and transfer from CdSe QD to ZnO NW in the co-sensitized sample, and thereby improves the IPCE. Overall, the IPCE CdS-ZnO-ZnO-CdSe was enhanced by a factor of two compared to CdSe-ZnO-ZnO-CdSe, which is consistent with the observed enhancement of photocurrent density (Figure 3.6).

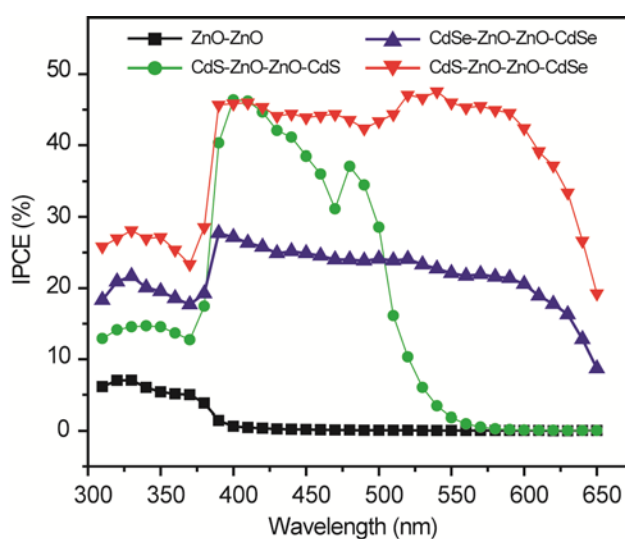


**Figure 3.8** Measured IPCE spectra of double-sided NW samples collected at the incident wavelength range from 310 nm to 650 nm at a potential of 0 V vs.

Ag/AgCl.

To understand the potential advantages of double-sided tandem structure over single-sided structure for solar hydrogen generation, we also carried out PEC studies on single-sided QD sensitized and co-sensitized ZnO nanowire samples for comparison. Two sensitized samples (denoted as CdS-ZnO and CdSe-ZnO) and two co-sensitized ZnO NW samples (denoted as CdSe-CdS-ZnO and CdS-CdSe-ZnO) were prepared for PEC measurements. Single-sided NW samples were illuminated from the backside of the substrate in all PEC measurements. The IPCE spectra of these single-sided NW samples are depicted in Figure 3.9a. We observed several important features. First, CdS-CdSe-ZnO and CdS-ZnO had similar IPCE characteristics, indicating the intermediate CdSe layer in CdS-CdSe-ZnO sample had little or no contribution to the photocurrent. This can be understood by the band alignment between CdS and CdSe, where the photoexcited holes in CdSe cannot be transferred to electrolyte due to the large potential difference between the valence band edges of CdSe and CdS (Figure 3.9b). Second, CdSe-ZnO showed higher photocurrent density than CdS-ZnO and CdS-CdSe-ZnO samples as a result of strong visible light absorption (figure 3.10). CdSe-ZnO exhibited almost constant IPCE of 25 % in the wavelength range from 400 nm to 650 nm, suggesting efficient electron transfer from CdSe QD to ZnO NW (Figure 3.9a). In addition, the IPCE was almost the same as double-sided CdSe-ZnO-ZnO-CdSe sample, indicating the

maximum loading of CdSe QD. Finally, CdSe-CdS-ZnO sample presented the most pronounced photocurrent among all single-sided samples. As shown in Figure 3.9b, the band alignment allows transportation of both electrons and holes in this composite structure. The enhanced IPCE observed in CdSe-CdS-ZnO sample compared to CdSe-ZnO can be attributed to the elevation of CBE of CdSe via band alignment between CdS and CdSe, and the incorporation of CdS middle layer that leads to the enhancement in light absorption below the wavelength of 550 nm.

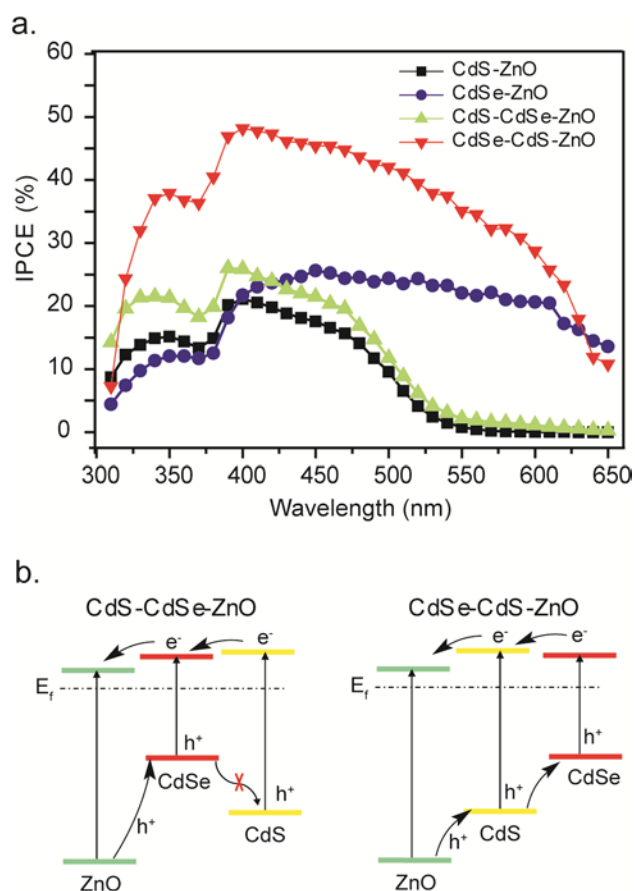


**Figure 3.9** (a) Measured IPCE spectra of single-sided NW samples in the wavelength region of 310 nm to 650 nm at a potential of 0 V vs. Ag/AgCl; (b)

Energy band diagram of CdS-CdSe-ZnO and CdSe-CdS-ZnO NW photoanodes.

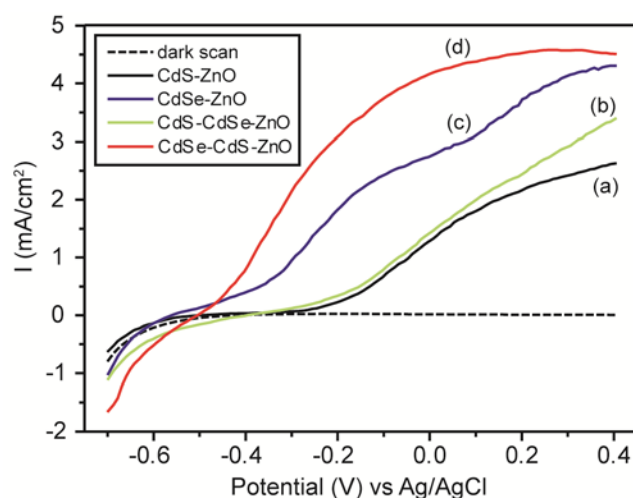


**Figure 3.10.** Linear sweep voltammograms, collected at a scan rate of 10 mV/s at applied potentials from -0.7 V to +0.4 V, from photoanodes fabricated from (a) CdS-ZnO; (b) CdS-CdSe-ZnO; (c) CdSe-ZnO; and (d) CdSe-CdS-ZnO nanowire samples at incident light of 100 mW/cm<sup>2</sup>. Dashed line is the linear sweep voltammogram of CdS-ZnO in the dark.

The comparison of PEC performance between CdS-CdSe-ZnO and CdS-ZnO-ZnO-CdSe NW samples clearly reveal the advantages of a double-sided photoanode structure. As shown in Figure 3.11a, they had similar current-voltage profile at a bias below -0.1 V. While the photocurrent of CdS-CdSe-ZnO saturated quickly with a maximum current density of ~6 mA/cm<sup>2</sup>, there was no current saturation for the double-sided CdS-ZnO-ZnO-CdSe sample at large bias. The data suggests that electron transfer in the CdSe-CdS-ZnO is less efficient compared to CdS-ZnO-ZnO-CdSe. As the Fermi levels of CdS, CdSe and ZnO are aligned, the CBEs of CdS and CdSe are similar that allows electrons to delocalize



between the conduction bands (Figure 3.10b).<sup>25-27</sup> Although the electrons created in CdSe can be transferred to ZnO through the CdS layer, the presence of this intermediate layer would increase the chance of electron-hole recombination and limit electron collection efficiency and thereby the maximum photocurrent. The limited electron transfer efficiency from CdSe QD to ZnO NW was also reflected in the IPCE data. The IPCE of CdSe-CdS-ZnO sample at the wavelength above 500 nm was smaller compared to CdS-ZnO-ZnO-CdSe sample (Figure 3.11b), indicative of relatively low collection efficiency of electrons created in CdSe. Importantly, the double-sided co-sensitized sample, with CdS and CdSe QDs directly contact with ZnO NWs that facilitates the electron transfer from QD to NW, addressed this limitation.

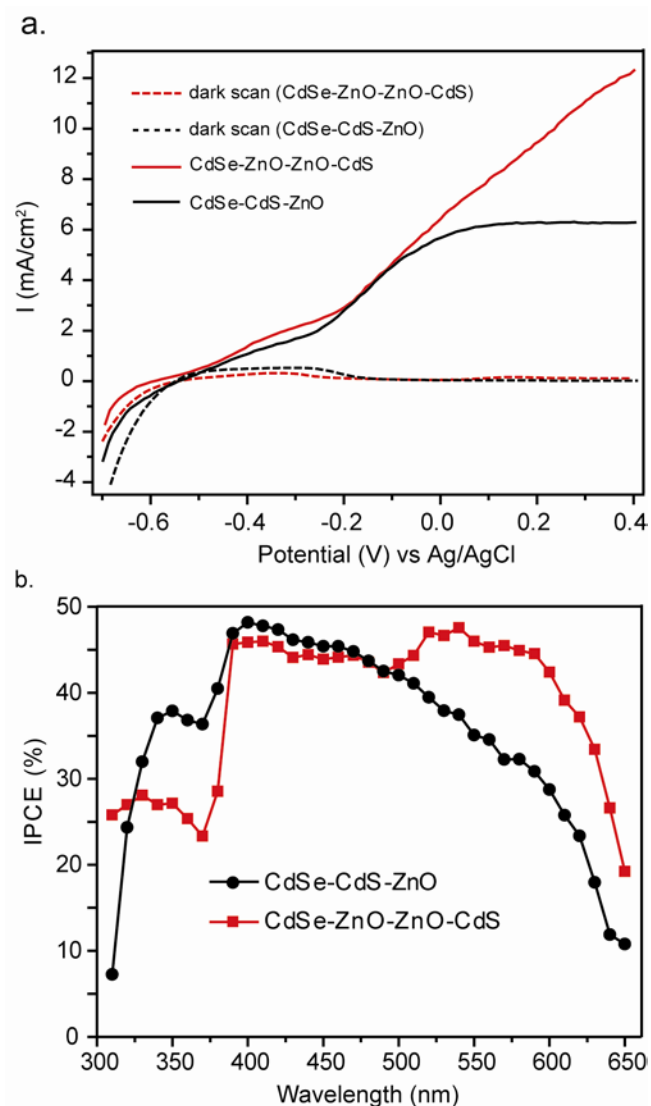


**Figure 3.11.** Comparison of PEC performance of double-sided CdS-ZnO-ZnO-CdS NWs and single-sided CdSe-CdS-ZnO NWs. (a) Linear sweep voltammograms, collected at a scan rate of 10 mV/s at applied potentials from -0.7 V to +0.4 V vs. Ag/AgCl at 100 mW/cm<sup>2</sup>; red and black dashed line are the dark scan of CdS-ZnO-ZnO-CdSe and CdSe-CdS-ZnO sample respectively; and (b) Measured IPCE spectra at the incident wavelength from 310 nm to 650 nm at a potential of 0 V vs. Ag/AgCl.

## Conclusion

In summary, we have successfully developed a double-sided CdS and

CdSe QD co-sensitized ZnO NW arrayed photoanode for PEC hydrogen generation. This unique photoanode exhibits strong light absorption in almost the entire visible region using a single light source. The band alignment between CdS and CdSe in electrolyte improves the electron transfer from CdSe QD to ZnO NW and thereby the IPCE. In comparison to single-sided co-sensitized NWs, the double-sided sample showed substantially improved charge collection efficiency. This work has demonstrated the potential advantages of double-sided NW photoanode for hydrogen generation and possibly other applications such as PV cells and provided important insights into the design and fabrication of composite nanostructures.

## References

1. Grimes, C. A.; Varghese, O. K.; Ranjan, S., *Light, Water, Hydrogen: The Solar Generation of Hydrogen by Water Photoelectrolysis*. Springer Science+Business Media, LLC: New York, 2008.
2. Li, Y.; Zhang, J. Z. *Laser & Photonics Reviews* **2009**.
3. van de Krol, R.; Liang, Y. Q.; Schoonman, J. *J. Mater. Chem.* **2008**, 18, (20), 2311-2320.
4. Yang, X.; Wolcott, A.; Wang, G.; Sobo, A.; Fitzmorris, R. C.; Qian, F.; Zhang, J. Z.; Li, Y. *Nano Lett.* **2009**, 9, (6), 2331-2336.
5. Park, J. H.; Kim, S.; Bard, A. J. *Nano Lett.* **2006**, 6, (1), 24-28.

6. Blackburn, J. L.; Selmarten, D. C.; Nozik, A. J. *J. Phys. Chem. B* **2003**, 107, 14154-14157.
7. Kong, F. T.; Dai, S. Y.; Wang, K. J. *Advances in OptoElectronics* **2007**, 2007, 75384.
8. Lee, Y. L.; Chi, C. F.; Liao, S. Y. *Chem. Mater.* **2009**, asap.
9. Sun, W. T.; Yu, Y.; Pan, H. Y.; Gao, X. F.; Chen, Q.; Peng, L. M. *J. Amer. Chem. Soc.* **2008**, 130, (4), 1124-1125.
10. Tak, Y.; Hong, S. J.; Lee, J. S.; Yong, K. *Cryst. Growth Des.* **2009**, 9, (6), 2627-2632.
11. Gratzel, M. *Chem. Lett.* **2005**, 34, 8-13.
12. Wang, H.; Deutsch, T.; Turner, J. A. *J. Electrochem. Soc.* **2008**, 155, (5), F91-F96.
13. Khaselev, O.; Turner, J. A. *Science* **1998**, 280, 425-427.
14. Hwang, Y. J.; Boukai, A.; Yang, P. D. *Nano Lett.* **2009**, 9, (1), 410-415.
15. Kongkanand, A.; Tvrđy, K.; Takechi, K.; Kuno, M.; Kamat, P. V. *J. Amer. Chem. Soc.* **2008**, 130, 4007-4015.
16. Goetzberger, A.; Hebling, C.; Schock, H. W. *Mater. Sci. Eng., R* **2003**, 40, 1-46.
17. Mor, G. K.; Varghese, O. K.; Wilke, R. H. T.; Sharma, S.; Shankar, K.; Latempa, T. J.; Choi, K. S.; Grimes, C. A. *Nano Lett.* **2008**, 8, 1906-1911.

18. Mohapatra, S. K.; Mahajan, V. K.; Misra, M. *Nanotechnology* **2007**, 18, 445705.
19. Xu, C.; Wang, X. D.; Wang, Z. L. *J. Amer. Chem. Soc.* **2009**, 131, (16), 5866-5872.
20. Greene, L.; Law, M.; Goldberger, J.; Kim, F.; Johnson, J. C.; Zhang, Y. F.; Saykally, R. J.; Yang, P. D. *Angew. Chem. Int. Ed.* **2003**, 42, 3031-3034.
21. Lokhande, C. D.; Lee, E. H.; Jung, K.; Joo, O. *Mater. Chem. Phys.* **2005**, 91, 200-204.
22. Spoerke, E. D.; Lloyd, M. T.; Lee, Y. J.; Lambert, T. N.; McKenzie, B. B.; Jiang, Y. B.; Olson, D. C.; Sounart, T. L.; Hsu, J. W. P.; Voigt, J. A. *J. Phys. Chem. C* **2009**, 113, (37), 16329-16336.
23. Liu, L. P.; Peng, Q.; Li, Y. D. *Inorg. Chem.* **2008**, 47, 3182-3187.
24. Lee, Y.; Lo, Y. *Adv. Funct. Mater.* **2009**, 19, 604-609.
25. Mahler, B.; Spinicelli, P.; Buil, S.; Quelin, X.; Hermier, J.; Dubertret, B. *Nature Mater.* **2008**, 7, 659.
26. Oron, D.; Kazes, M.; Banin, U. *Phys. Rev. B* **2007**, 75, 035330.
27. Saba, M.; Minniberger, S.; Quochi, F.; Roither, J.; Marceddu, M.; Gocalinska, A.; Kovalenko, M. V.; Talapin, D. V.; Heiss, W.; Mura, A.; Bongiovanni, G. *Adv. Mater.* **2009**, 21, 1-5.

## Chapter 4

### Facile Synthesis of Highly Photoactive $\alpha$ -Fe<sub>2</sub>O<sub>3</sub>-based Films for Water

#### Oxidation

##### Abstract

This work reports the synthesis and characterization of  $\alpha$ -Fe<sub>2</sub>O<sub>3</sub> films as well as their implementation as photoanodes for photoelectrochemical water splitting. High-quality, transparent  $\alpha$ -Fe<sub>2</sub>O<sub>3</sub> films were prepared on a fluorine-doped tin oxide substrate by a facile deposition-annealing process using non-toxic iron(III) chloride as the Fe precursor, followed by annealing at 550 °C in air. In addition, Ti-doped  $\alpha$ -Fe<sub>2</sub>O<sub>3</sub> films were prepared by the same method, adding titanium butoxide as the Ti precursor. X-ray photoelectron spectroscopy confirms the incorporation of Ti atoms in an oxidized chemical environment. Impedance measurements show that the Ti-dopant serves as an electron donor and causes an increase of two orders of magnitude in the charge carrier density of the  $\alpha$ -Fe<sub>2</sub>O<sub>3</sub> film. The photoelectrochemical performance of undoped and Ti-doped  $\alpha$ -Fe<sub>2</sub>O<sub>3</sub> films was characterized and optimized through controlled variation of the Fe and Ti precursor concentration, annealing conditions, and the number of

deposition-annealing cycles. Undoped and Ti-doped  $\alpha$ -Fe<sub>2</sub>O<sub>3</sub> films yield high photocurrent densities of 0.91 and 2.80 mA/cm<sup>2</sup> at 1.23 V *vs.* RHE, respectively. The photocurrent density of the Ti-doped  $\alpha$ -Fe<sub>2</sub>O<sub>3</sub> film is comparable to the benchmark value previously reported for Si-doped  $\alpha$ -Fe<sub>2</sub>O<sub>3</sub> under the same bias. Compared to the undoped sample, the photocurrent onset potential of Ti-doped  $\alpha$ -Fe<sub>2</sub>O<sub>3</sub> is shifted about 0.1–0.2 V to lower potential, thus improving the photocurrent and incident-photon-to-current-conversion-efficiency (IPCE) at lower bias voltage. Significantly, the optimized Ti-doped  $\alpha$ -Fe<sub>2</sub>O<sub>3</sub> film achieved a photocurrent density of 1.64 mA/cm<sup>2</sup> at 1.0 V *vs.* RHE, which is the highest value obtained for  $\alpha$ -Fe<sub>2</sub>O<sub>3</sub> at this bias. The enhanced photocurrent is attributed to the improved donor density and electrical conductivity, as a result of Ti-doping. Ultrafast laser spectroscopy studies have been used to probe the fundamental charge carrier dynamics and reveal that, compared to the undoped sample, the excited charge carriers in the Ti-doped  $\alpha$ -Fe<sub>2</sub>O<sub>3</sub> film decay slightly slower on the timescale beyond a few picoseconds, suggesting a reduced electron-hole recombination on that time scale.

## **Introduction**

Since the direct photoelectrolysis of water into oxygen and hydrogen was reported by Honda and Fujishima in 1972,<sup>1</sup> a number of metal oxide semiconductors such as TiO<sub>2</sub>, ZnO, WO<sub>3</sub>, and  $\alpha$ -Fe<sub>2</sub>O<sub>3</sub> have been investigated

for photoelectrochemical (PEC) water splitting. Significant progress has been achieved in enhancing the efficiency of hydrogen generation.<sup>2-19</sup> Among these metal oxide semiconductors,  $\alpha$ -Fe<sub>2</sub>O<sub>3</sub> (hematite) has received much attention due to its favorable optical bandgap ( $\sim 2.2$  eV),<sup>20</sup> excellent chemical stability, natural abundance, and low cost. It has been theoretically predicted that a semiconductor with this bandgap can achieve a solar-to-hydrogen efficiency of 16.8 %.<sup>21</sup> However, the reported solar-to-hydrogen efficiencies of  $\alpha$ -Fe<sub>2</sub>O<sub>3</sub> are notoriously lower than the predicted value, mainly due to its very short lifetime of photogenerated charge carriers ( $< 10$  ps)<sup>22, 23</sup> and short hole diffusion length ( $\sim 2-4$  nm)<sup>24-26</sup>. The majority of photoexcited electrons in  $\alpha$ -Fe<sub>2</sub>O<sub>3</sub> is typically lost via different recombination processes within the first few picoseconds, and only holes created close enough to the semiconductor/electrolyte interface can be used for water oxidation. In this regard, very thin  $\alpha$ -Fe<sub>2</sub>O<sub>3</sub> films should be used for facilitating transport/collection of electrons and holes. However,  $\alpha$ -Fe<sub>2</sub>O<sub>3</sub> is an indirect bandgap semiconductor, and thus it requires a relatively thick layer of active material for the complete absorption of solar light. Besides, the band positions of  $\alpha$ -Fe<sub>2</sub>O<sub>3</sub> do not necessarily straddle the H<sub>2</sub> and O<sub>2</sub> evolution potentials. Therefore, a relatively large external bias (0.8-1.0 V) is typically required for water splitting using  $\alpha$ -Fe<sub>2</sub>O<sub>3</sub> materials as photoanodes.<sup>3, 27,</sup>

28

To address these limitations, a number of unique element-doped,



nanostructured  $\alpha\text{-Fe}_2\text{O}_3$  materials have been designed and fabricated. First, both nonmetal<sup>2, 3, 29-38</sup> and metal elements<sup>28, 39-52</sup> have been extensively investigated as dopants for  $\alpha\text{-Fe}_2\text{O}_3$  materials. These dopants have been shown to play important roles in improving the optical absorption coefficient, the donor density, electrical conductivity, and the flat band potential of  $\alpha\text{-Fe}_2\text{O}_3$ . For example, Ti-doping was reported to increase the conductivity of  $\alpha\text{-Fe}_2\text{O}_3$  by several orders of magnitude.<sup>53</sup> Second, nanostructured materials with very large interfacial area between electrolyte and semiconductor would facilitate the charge collection by reducing the diffusion length for photoexcited holes. Nanostructured  $\alpha\text{-Fe}_2\text{O}_3$  materials have thus been synthesized by numerous approaches, including hydrothermal methods,<sup>19, 54-56</sup> spray pyrolysis,<sup>10, 20, 39-41, 45, 48-50, 57, 58</sup> DC magnetron sputtering,<sup>43</sup> electrochemical deposition,<sup>42, 59-61</sup> atmospheric pressure chemical vapor deposition (APCVD),<sup>2, 3, 16, 32, 34, 36</sup> colloidal solution assembly,<sup>28, 35</sup> sol-gel,<sup>62</sup> anodization,<sup>5, 63-65</sup> flame oxidation of iron foils,<sup>30, 66</sup> and atomic layer deposition (ALD)<sup>8</sup>. Among these methods, the nanostructured  $\alpha\text{-Fe}_2\text{O}_3$  films prepared by spray pyrolysis, APCVD, and ALD have shown excellent PEC performance. However, these techniques require special instruments such as atomizers<sup>20, 67, 68</sup> or chemical vapor deposition and ALD<sup>8</sup> systems that use toxic and flammable metal-organics as precursors<sup>2, 3, 32, 34, 36</sup>.

It is highly desirable to develop a facile, safe, and cost-effective method to

fabricate high-quality, element-doped nanostructured  $\alpha$ -Fe<sub>2</sub>O<sub>3</sub> films with good PEC performance at low external bias. In this work, we report a simple deposition-annealing (DA) method for the fabrication of transparent, mesoporous  $\alpha$ -Fe<sub>2</sub>O<sub>3</sub> films on a conducting glass substrate, using non-toxic iron(III) chloride (FeCl<sub>3</sub>) as the Fe precursor. This is also a versatile method that allows dopants such as Ti to be easily incorporated into  $\alpha$ -Fe<sub>2</sub>O<sub>3</sub> structures. The size of  $\alpha$ -Fe<sub>2</sub>O<sub>3</sub> nanoparticles, film thickness, as well as the doping level can be tailored by tuning the growth conditions. In comparison to the spray pyrolysis and APCVD methods, this growth approach avoids the use of specialized equipment and the very toxic and highly flammable iron pentacarbonyl (Fe(CO)<sub>5</sub>) as the Fe precursor.<sup>2, 3, 32, 34, 36</sup> Significantly, the undoped and Ti-doped  $\alpha$ -Fe<sub>2</sub>O<sub>3</sub> films prepared by this method show excellent PEC performance. In particular, the photocurrent onset potential of Ti-doped  $\alpha$ -Fe<sub>2</sub>O<sub>3</sub> is shifted about 0.1–0.2 V to lower potential and achieves the best photocurrent density of 1.64 mA/cm<sup>2</sup> at relatively low bias, 1.0 V *vs.* RHE. To shed light on the origins of the improvement induced by Ti-doping,  $\alpha$ -Fe<sub>2</sub>O<sub>3</sub> films were investigated by X-ray photoelectron spectroscopy, electrochemical measurements, and ultrafast laser spectroscopy.

## Experimental Section

**Preparation of  $\alpha$ -Fe<sub>2</sub>O<sub>3</sub> Nanoparticle Films:** A series of ethanol solutions with

various  $\text{FeCl}_3$  concentrations, ranging from 5 to 80 mM, were prepared by dissolving  $\text{FeCl}_3 \cdot 6\text{H}_2\text{O}$  (99 %, Fisher Scientific) in ethanol. Fluorine-doped tin oxide (FTO) coated glass substrates (TEC 15, Hartford Glass Co.) were pre-cleaned with acetone, followed by ethanol and water. The ethanol-based  $\text{FeCl}_3$  solution was drop-deposited onto the FTO-coated glass and blow-dried with compressed air after 30 seconds. The dried FTO-coated glass was subsequently heated on a hotplate in air at 350 °C for 5 min. This deposition-annealing procedure is denoted as one “DA cycle”. The film thickness was controlled by the number of DA cycles as well as the  $\text{FeCl}_3$  precursor concentration. The as-prepared films were then further annealed in air at 550 °C for 4 hours. Ti-doped  $\alpha\text{-Fe}_2\text{O}_3$  films were prepared under similar conditions as for undoped  $\alpha\text{-Fe}_2\text{O}_3$ , adding titanium butoxide (99 % Aldrich) as the Ti precursor. Titanium butoxide and 70  $\mu\text{L}$  concentrated HCl (37.2 wt %, Aldrich) were added into 20 ml of 10 mM  $\text{FeCl}_3$  solution, and Ti-doped  $\alpha\text{-Fe}_2\text{O}_3$  samples with nominal Ti:Fe atomic ratios of 1, 5, 10, 15, and 20 % were prepared by varying the amount of titanium butoxide. We note that the Ti concentration levels are higher than those generally referred to as “doping” in semiconductor physics. Nevertheless, to be consistent with the common usage of the term “doping” in the PEC community, we will continue to refer to these samples as “Ti-doped”.

**Structural Characterization:** Scanning electron microscopy images were

collected with a field-emission SEM (Hitachi S-4800 II). Raman spectra were collected with a Nicolet Almega XR Dispersive Raman Spectrometer (laser wavelength 780 nm).

**X-ray Photoelectron Spectroscopy (XPS):** Survey and detail XPS spectra were collected using non-monochromatized Mg  $K_{\alpha}$  excitation and a SPECS PHOIBOS 150 MCD electron analyzer in a modified Vacuum Generators ESCALab MkII at a pressure of  $3 \times 10^{-10}$  mbar. To minimize surface contamination during sample handling, the samples were sealed in a dry nitrogen environment immediately after the 4 hour air-annealing step, shipped from Santa Cruz to Las Vegas, and introduced into ultra-high vacuum without further air exposure.

**Ultrafast Studies of Photoexcited Electron Dynamics:** The ultrafast Quantronix-designed femtosecond laser system consists of an Er-doped fiber oscillator, a regenerative/multi-pass amplifier, and a diode-pumped, Q-switched, second harmonic Nd:YLF pump laser (527 nm, 10 W capacity). Before injection into the amplifier, chirped pulse amplification was performed to temporally stretch, amplify, and recompress the initial short pulse, resulting in a pulse near its original duration, yet with a vastly higher energy. After amplification, the as-generated fundamental (795 nm) was beam-split to generate both a white light continuum (WLC) probe pulse as well as feed a tunable optical parametric amplifier (OPA) that consists of two delay stages: a signal pre-amplification

stage and a power amplification stage. The output of the OPA was passed through wavelength separators in order to achieve a tunable pump wavelength. The system operates at 750 Hz repetition rate. The final output consisted of ~130 fs pulses, with a power output of ~100 nJ/pulse at the sample, centered at 440 nm excitation wavelength, and was attenuated with neutral density filters. The pump beam was overlapped spatially and temporally with the WLC probe beam at the sample. The time delay between the pump and probe beam was controlled by a translation stage with 1  $\mu\text{m}$  resolution. Each sample was tested for six cycles to achieve an average response with reduced noise.

**PEC Measurements:**  $\alpha\text{-Fe}_2\text{O}_3$  films were fashioned into photoanodes by soldering a copper wire onto a bare portion of the FTO substrate. The photoanodes were sealed on the edges with epoxy resin, except for a well-defined working electrode surface area in the range of 0.15–0.25  $\text{cm}^2$ . An aqueous solution of 1.0 M NaOH with a pH of 13.6, deaerated with nitrogen flow, was used as an electrolyte. Linear sweeps were measured in a three-electrode electrochemical cell with a Ag/AgCl reference electrode and a Pt foil counter electrode, using an electrochemical station (CHI 660D). Sunlight was simulated with a 150W xenon lamp (Newport 6255) with an AM 1.5 global filter (Newport 81094). IPCE spectra were measured by a Solartron 1280B electrochemical station with a solar simulator (Newport 69920 1000W xenon lamp), coupled to an infrared water filter (Oriel No. 6127) and an aligned

monochromator (Oriel Cornerstone 130 1/8m). Electrochemical impedance spectroscopy (EIS) measurements were performed in a three-electrode configuration using the CHI 660D electrochemical station. A sinusoidal voltage perturbation with 5 mV amplitude and frequencies ranging from 100,000 to 1 Hz was superimposed on a bias of 1.0 V vs. RHE in the dark and under illumination (AM 1.5G; 100 mW/cm<sup>2</sup>). Mott-Schottky plots were generated using the obtained electrochemical impedance in the dark to derive capacitance at each potential with 10 kHz frequency.

## Results and Discussion

□  $\alpha$ -Fe<sub>2</sub>O<sub>3</sub> films were prepared on FTO-coated glass substrates by a facile DA method. Upon heating at 350 °C in air, the color of the FeCl<sub>3</sub>-covered FTO substrate turned pale yellow, which is believed to be due to the conversion of FeCl<sub>3</sub> into a thin  $\beta$ -FeOOH film. This film was subsequently converted into a red film by further sintering at 550 °C for 4 hours. X-ray diffraction (XRD) data collected from the yellow and red films were indexed to the characteristic peaks of  $\beta$ -FeOOH (JCPDS 34-1266) and  $\alpha$ -Fe<sub>2</sub>O<sub>3</sub> (JCPDS 33-0664), respectively (Figure 4.1). These data confirm the successful fabrication of the  $\alpha$ -Fe<sub>2</sub>O<sub>3</sub> phase and indicate that the  $\beta$ -FeOOH phase was the process intermediate.

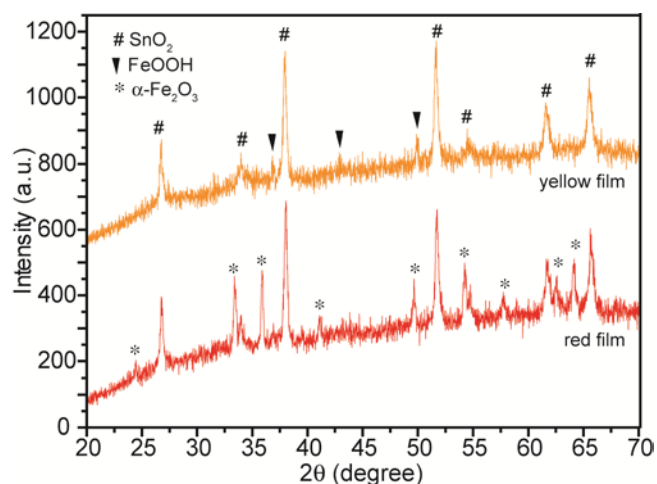


**Figure 4.1** XRD spectra of the as prepared  $\beta$ -FeOOH (yellow) film and the  $\alpha$ -Fe<sub>2</sub>O<sub>3</sub> (red) film with 80 mM FeCl<sub>3</sub> as precursor sintered at 550 °C.

Figure 4.2a shows the schematic flow of the facile deposition method to prepare  $\alpha$ -Fe<sub>2</sub>O<sub>3</sub> films. Figure 4.2b displays the  $\alpha$ -Fe<sub>2</sub>O<sub>3</sub> films prepared with different concentrations of FeCl<sub>3</sub> precursor solution and various numbers of DA cycles. The films appear to be very uniform. The film transparency, related to the film thickness and/or the size of individual  $\alpha$ -Fe<sub>2</sub>O<sub>3</sub> nanoparticles (i.e., the density of the film), decreases with increasing number of DA cycles and concentration of the FeCl<sub>3</sub> solution.

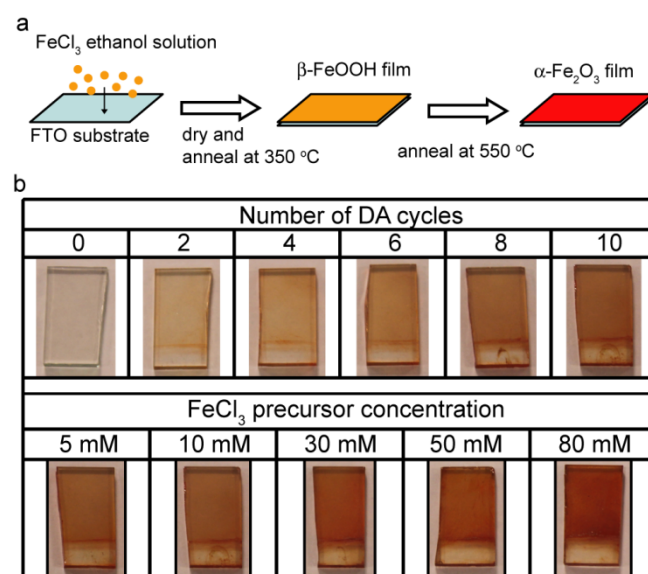


**Figure 4. 2.** (a) A scheme showing the DA procedure for the growth of  $\alpha$ -Fe<sub>2</sub>O<sub>3</sub> films. (b) Digital pictures of  $\alpha$ -Fe<sub>2</sub>O<sub>3</sub> films on FTO substrates, prepared with different numbers of DA cycles and concentrations of FeCl<sub>3</sub> precursor solutions.

Scanning electron microscopy (SEM) images were collected for the  $\alpha$ -Fe<sub>2</sub>O<sub>3</sub> films prepared with increasing precursor concentration and number of DA cycles in order to understand the correlation of these key growth parameters to the material morphology. Figure 4.3 shows the SEM images of the  $\alpha$ -Fe<sub>2</sub>O<sub>3</sub> films prepared with FeCl<sub>3</sub> precursor concentrations in a range from 5 to 80 mM. These images reveal that the size of  $\alpha$ -Fe<sub>2</sub>O<sub>3</sub> nanoparticles in the films decreases with precursor concentration. The films appear densely packed when precursor concentrations of 10 and 5 mM were used, possibly due to the reduced size of the nanoparticles.



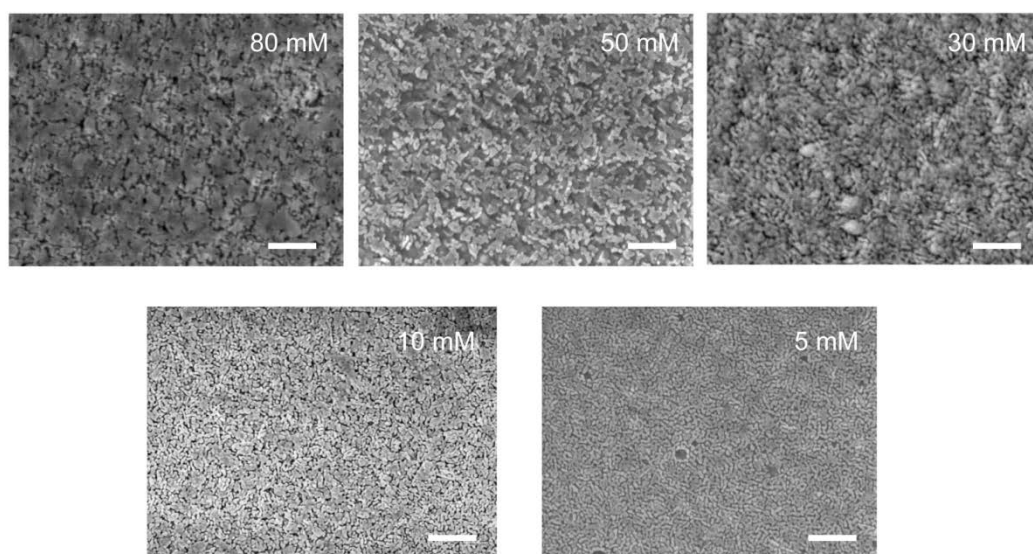


**Figure 4.3.** SEM images collected for  $\alpha$ -Fe<sub>2</sub>O<sub>3</sub> films prepared with 80, 50, 30, 10, and 5 mM FeCl<sub>3</sub> precursor solutions. All scale bars are 500 nm.

Raman spectra were collected for these samples to shed further light on the correlation between concentration and particle size (Figure 4.4). The Raman spectrum of the  $\alpha$ -Fe<sub>2</sub>O<sub>3</sub> film prepared at the highest precursor concentration of 80 mM exhibits all six characteristic Raman peaks of  $\alpha$ -Fe<sub>2</sub>O<sub>3</sub>.<sup>69</sup> These peaks become broader and featureless as the precursor concentration is decreased. This can be understood based on a phonon confinement effect in the  $\alpha$ -Fe<sub>2</sub>O<sub>3</sub> lattice. In a finite crystal, phonons are confined in a space defined by the crystal boundaries or defects. This causes uncertainty in the phonon momentum, allowing phonons not at the center of the Brillouin Zone to contribute to the Raman scattering. This uncertainty increases with decreasing grain size in the material and leads to broadening of the Raman peaks,<sup>70, 71</sup> thus supporting the hypothesis that the film morphology is correlated with a size reduction of the

$\alpha$ -Fe<sub>2</sub>O<sub>3</sub> nanoparticles.

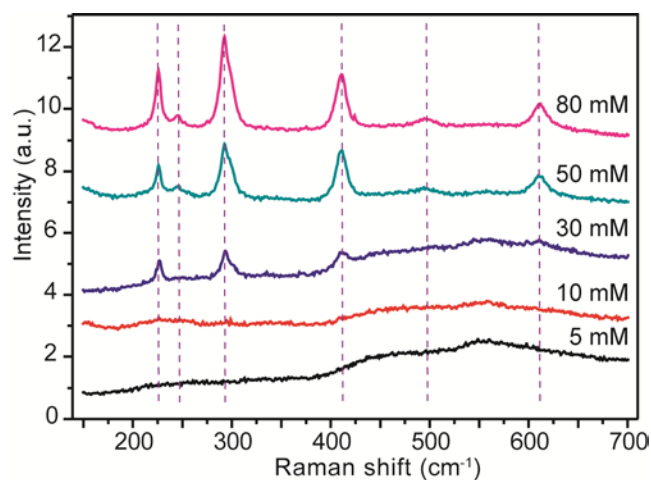


**Figure 4.4.** Raman spectra of  $\alpha$ -Fe<sub>2</sub>O<sub>3</sub> films prepared with different FeCl<sub>3</sub> precursor concentrations. The dashed lines highlight the characteristic Raman peaks of  $\alpha$ -Fe<sub>2</sub>O<sub>3</sub>.

PEC performance of  $\alpha$ -Fe<sub>2</sub>O<sub>3</sub> films was measured in a 1.0 M NaOH electrolyte solution using a three-electrode electrochemical cell coupled with a solar simulator. The measured potentials vs. Ag/AgCl were converted to the reversible hydrogen electrode (RHE) scale according to the Nernst equation,

$$E_{\text{RHE}} = E_{\text{Ag/AgCl}} + 0.059 \text{ pH} + E^{\circ}_{\text{Ag/AgCl}}$$

where  $E_{\text{RHE}}$  is the converted potential vs. RHE,  $E^{\circ}_{\text{Ag/AgCl}} = 0.1976 \text{ V}$  at 25 °C, and  $E_{\text{Ag/AgCl}}$  is the experimentally measured potential against Ag/AgCl reference.

The reference electrode has been calibrated. Figure 4.5 shows plots of the photocurrent densities of  $\alpha$ -Fe<sub>2</sub>O<sub>3</sub> films, prepared with various FeCl<sub>3</sub> precursor concentrations, as a function of the number of DA cycles. For each precursor concentration and with increasing number of DA cycles, the photocurrent densities of  $\alpha$ -Fe<sub>2</sub>O<sub>3</sub> films initially increase to a maximal value and then

decrease again. This suggests that the photocurrent is strongly correlated with the thickness and density of the  $\alpha\text{-Fe}_2\text{O}_3$  film. The initial increase of photocurrent can be ascribed to the increased amount of photoactive material, which enhances the light absorption as well as the total number of photoexcited carriers. Once the  $\alpha\text{-Fe}_2\text{O}_3$  film thickness reaches a certain threshold, charge carrier recombination becomes increasingly important, since the very short carrier diffusion length effectively limits the ability to remove charges from the semiconductor.

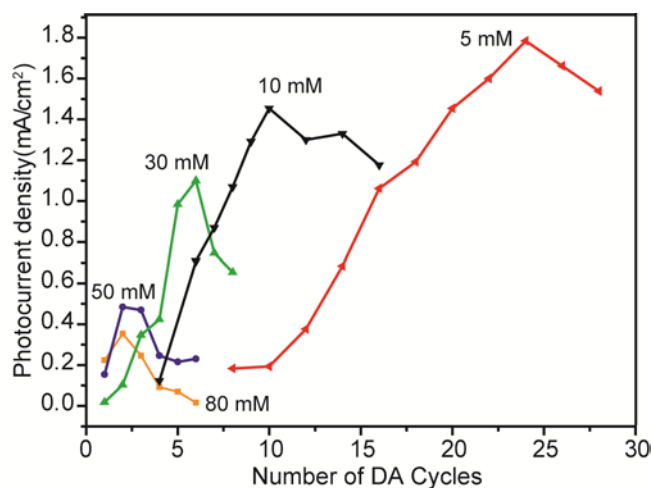


**Figure 4.5.** Plots of the photocurrent density of  $\alpha\text{-Fe}_2\text{O}_3$  films prepared with different precursor concentrations as a function of the number of DA cycles. All photocurrent densities were measured at 1.47 V vs. RHE.

We further studied the correlation between film thickness and the photocurrent density of the prepared  $\text{Fe}_2\text{O}_3$  with different precursor concentrations. We used scanning electron microscopy (SEM) to measure the cross sectional film thickness of the optimized  $\text{Fe}_2\text{O}_3$  with 10, 30, 50 and 80 mM  $\text{FeCl}_3$  as precursors,

shown in figure 4.6. With the concentration increase, the film thickness and particle size increase. Based on the maximal photocurrent densities obtained at each precursor concentration, the optimal hematite thickness is estimated to be in a range of 80-160 nm.

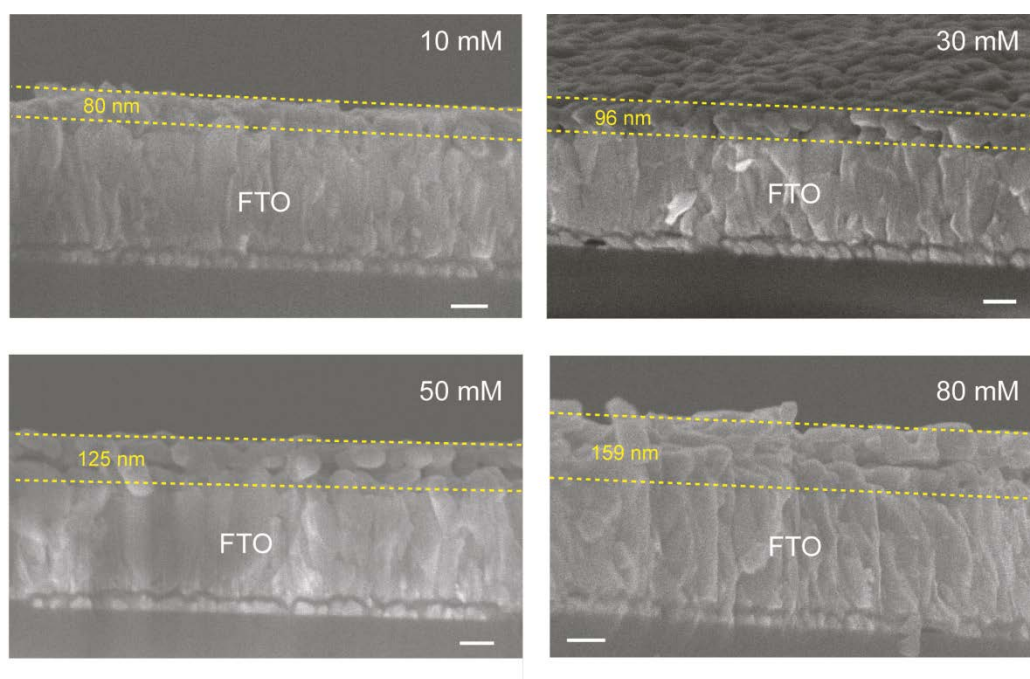


**Figure 4.6.** Cross-sectional SEM images collected for optimized  $\alpha$ -Fe<sub>2</sub>O<sub>3</sub> films prepared with different FeCl<sub>3</sub> precursor concentrations. All  $\alpha$ -Fe<sub>2</sub>O<sub>3</sub> films were annealed at 550 °C for 4 hours. Scale bar is 100 nm.

Moreover, the maximal photocurrent densities of  $\alpha$ -Fe<sub>2</sub>O<sub>3</sub> films increase with decreasing precursor concentration (Figure 4.7). The film prepared with the lowest precursor concentration of 5 mM achieved the highest peak photocurrent density of 1.78 mA/cm<sup>2</sup> at 1.47 V vs. RHE. The improved PEC activity of this  $\alpha$ -Fe<sub>2</sub>O<sub>3</sub> film is due to the reduced size of  $\alpha$ -Fe<sub>2</sub>O<sub>3</sub> nanoparticles, although an

increased number of DA cycles (24) was required to achieve the optimal film thickness when using such a diluted precursor solution.

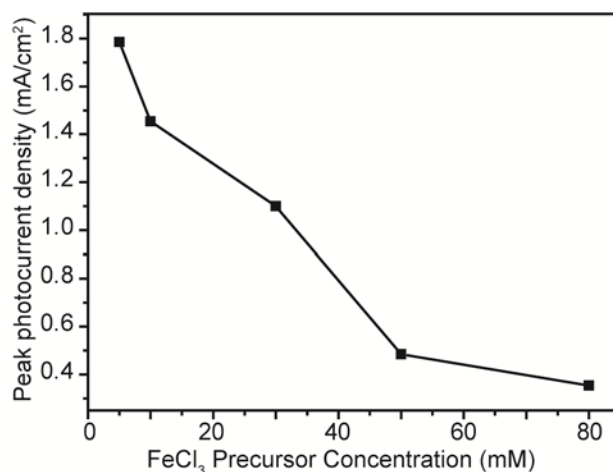


**Figure 4.7.** Plots of the photocurrent density of  $\alpha$ -Fe<sub>2</sub>O<sub>3</sub> films prepared with different precursor concentrations as a function of the FeCl<sub>3</sub> precursor concentration. All photocurrent densities were measured at 1.47 V vs. RHE.

The effect of particle size on the PEC performance of  $\alpha$ -Fe<sub>2</sub>O<sub>3</sub> can be understood in terms of the charge separation and transport at the semiconductor/electrolyte interface. In small particles, the average distance between the photoexcited holes and the semiconductor/electrolyte interface is reduced, which improves the hole collection efficiency. Furthermore, the decrease of particle size can enhance the charge separation by depleting the  $\alpha$ -Fe<sub>2</sub>O<sub>3</sub> nanoparticle. When a semiconductor nanoparticle is brought into contact with the electrolyte, a space-charge layer<sup>72</sup> and an interface dipole will be formed at the semiconductor/electrolyte interface, replacing the surface band bending and surface dipole at the former semiconductor surface. In contrast, the

particle core (of sufficiently large particles) can be regarded as a diffusion region (Figure 4.8). Photoexcited electrons and holes are more effectively separated by the electric field in the space-charge layer than in the diffusion region. For  $\alpha\text{-Fe}_2\text{O}_3$ , most of the electron-hole pairs that are created beyond the depletion layer are very likely lost via recombination, due to the very short electron and hole diffusion lengths. Therefore, the increased contribution of the depletion layer in small  $\alpha\text{-Fe}_2\text{O}_3$  particles can reduce the electron-hole recombination loss.

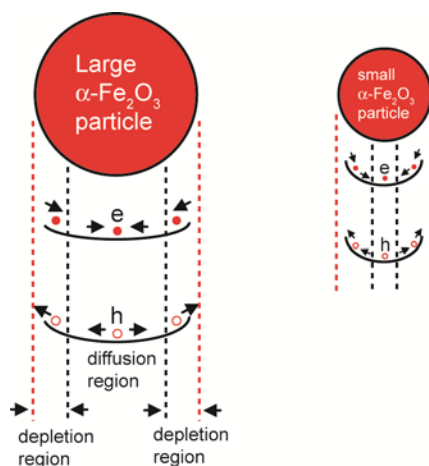


**Figure 4.8.** Schematic diagram of the diffusion region and the depletion region of  $\alpha\text{-Fe}_2\text{O}_3$  nanoparticles with different particle size (surface dipoles are omitted). As the particle size decreases, a significant portion of the  $\alpha\text{-Fe}_2\text{O}_3$  particles will be depleted.

The PEC performance of  $\alpha\text{-Fe}_2\text{O}_3$  films was also analyzed by varying the annealing temperature and time. Here, we used  $\alpha\text{-Fe}_2\text{O}_3$  films prepared with 10 mM  $\text{FeCl}_3$  solution as an example to elucidate the effects of the annealing

process. Figure 4.9 shows the linear sweep curves of  $\alpha$ -Fe<sub>2</sub>O<sub>3</sub> films annealed at different temperatures. The photocurrent densities of these films are enhanced as the annealing temperature is increased from 400 to 600 °C, and then decrease with further increase of annealing temperature.

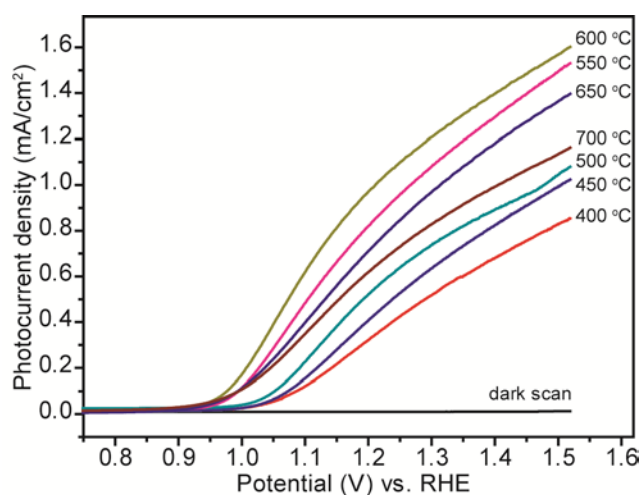


**Figure 4.9.** Linear sweeps collected for  $\alpha$ -Fe<sub>2</sub>O<sub>3</sub> films prepared with 10 mM FeCl<sub>3</sub> precursor solution at different annealing temperatures for 4 hours.

The PEC performance of  $\alpha$ -Fe<sub>2</sub>O<sub>3</sub> films was also analyzed by varying the annealing temperature and time. Here, we use  $\alpha$ -Fe<sub>2</sub>O<sub>3</sub> films prepared with 10 mM FeCl<sub>3</sub> solution as an example to elucidate the effects of the annealing process. Figure 4.10a shows the linear sweep curves of  $\alpha$ -Fe<sub>2</sub>O<sub>3</sub> films annealed at different temperatures. The photocurrent densities of these films are enhanced as the annealing temperature is increased from 400 to 600 °C, and then decrease with further increase of annealing temperature (the photocurrent densities at 0.45 V vs. Ag/AgCl are shown in Figure 4.10b). The enhanced photocurrent at

lower annealing temperatures is attributed to the reduced defect density in annealed  $\alpha$ -Fe<sub>2</sub>O<sub>3</sub> samples, while the decrease of photocurrent after annealing at temperatures higher than 600 °C is ascribed to an increased resistance of the FTO substrate (from 22 to 167  $\Omega$  after 4 hours annealing at 700 °C). In addition, a prolonged annealing at temperature above 550 °C causes glass distortion. Therefore, 550 °C was chosen as optimal annealing temperature. The photocurrent densities of the  $\alpha$ -Fe<sub>2</sub>O<sub>3</sub> films were also measured as a function of annealing time. Figure 4.10c shows that the photocurrent densities achieved a maximal level after 3-4 hours annealing. The resistance of the substrate was slightly increased from 22 to 32  $\Omega$  after 4 hours annealing at 550 °C.



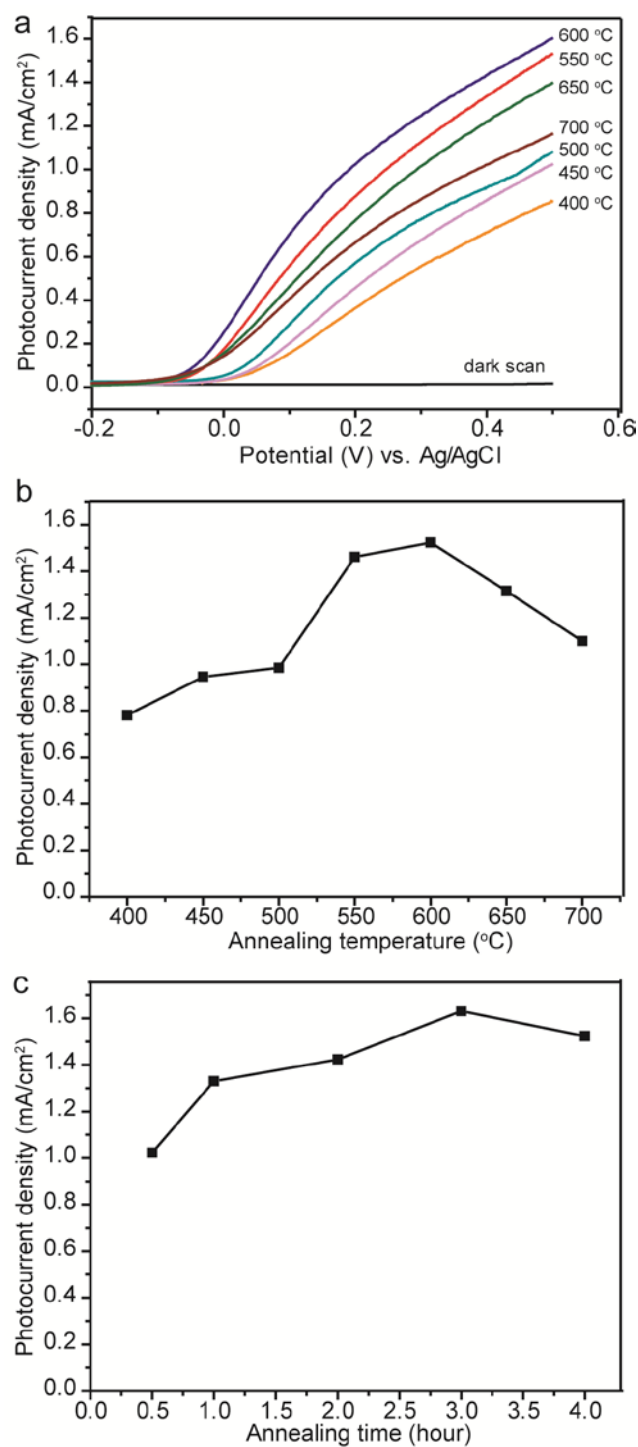


**Figure 4.10.** (a) Linear sweeps collected for  $\alpha$ -Fe<sub>2</sub>O<sub>3</sub> films prepared with 10 mM FeCl<sub>3</sub> precursor solution at different annealing temperatures for 4 hours. (b) Photocurrent densities of these  $\alpha$ -Fe<sub>2</sub>O<sub>3</sub> films measured at 0.45 V vs. Ag/AgCl as a function of annealing temperature. (c) Photocurrent densities of the  $\alpha$ -Fe<sub>2</sub>O<sub>3</sub> films at 0.45 V vs. Ag/AgCl as a function of annealing time at 550 °C.

To study the impact of annealing, Raman spectra were collected for  $\alpha$ -Fe<sub>2</sub>O<sub>3</sub> films prepared at different annealing temperatures (Figure 4.11). Upon annealing, the as-prepared  $\beta$ -FeOOH film is converted into  $\alpha$ -Fe<sub>2</sub>O<sub>3</sub>, which is consistent with the XRD results discussed earlier. All six characteristic Raman peaks<sup>69</sup> of  $\alpha$ -Fe<sub>2</sub>O<sub>3</sub> are observed after annealing up to 600 °C. Importantly, the full-width-half-maximum of the Raman peaks decreases as the annealing temperature is increased, suggesting an enhancement of  $\alpha$ -Fe<sub>2</sub>O<sub>3</sub> crystallinity.<sup>73,</sup>  
<sup>74</sup> Therefore, photocurrent increases with annealing temperature from 400 to 600 °C is believed to be the result of reduced defect density in annealed  $\alpha$ -Fe<sub>2</sub>O<sub>3</sub> samples. Furthermore, the high-temperature annealing could also increase inter-particle connections and/or improve the contact at the interface of  $\alpha$ -Fe<sub>2</sub>O<sub>3</sub> film and substrate. On the other hand, the prolonged annealing at temperature of 550 °C or above causes glass distortion. The decrease of photocurrent after annealing at temperatures higher than 600 °C is ascribed to an increased resistance of the FTO substrate (from 22 to 167  $\Omega$  after 4 hours annealing at 700 °C). Therefore, 550 °C was chosen as the optimal annealing temperature.

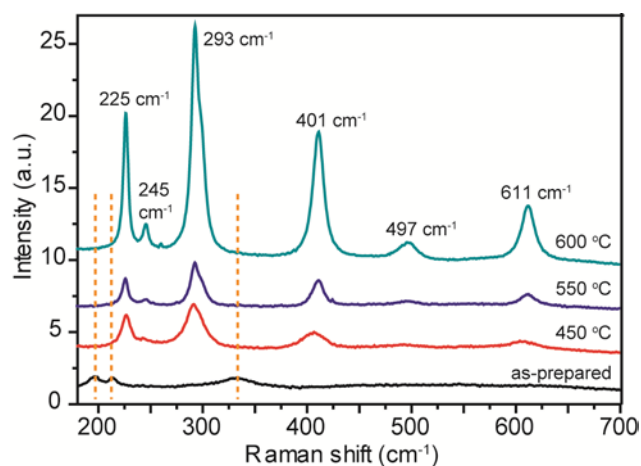


**Figure 4.11.** Raman spectra collected for an as-prepared  $\beta$ -FeOOH film and the  $\alpha$ -Fe<sub>2</sub>O<sub>3</sub> films prepared with 80 mM FeCl<sub>3</sub> precursor solution, annealed at 450, 550, and 600 °C. The dashed lines highlight the peak position for the  $\beta$ -FeOOH film. All six characteristic Raman shifts of  $\alpha$ -Fe<sub>2</sub>O<sub>3</sub> are labeled.

Based on the precursor concentration (10 mM), the number of DA cycles (10) and hence the film thickness (ca. 140 nm), annealing temperature (550 °C), and annealing time (4 hours), an optimized photocurrent density of 0.96 mA/cm<sup>2</sup> at 0.23 V *vs.* Ag/AgCl (1.23 V *vs.* RHE) was achieved. To our knowledge, this photocurrent density is considerably higher than the undoped  $\alpha$ -Fe<sub>2</sub>O<sub>3</sub> films prepared by hydrothermal methods using the same FeCl<sub>3</sub> precursor {Beermann, 2000 #52; Lindgren, 2002 #54}. The enhanced photocurrent density can be attributed to the small size of the  $\alpha$ -Fe<sub>2</sub>O<sub>3</sub> particles, which reduces the impact of unfavorably short diffusion lengths for photoexcited holes and facilitates the charge separation due to a large contribution of the depletion region in these

$\alpha$ -Fe<sub>2</sub>O<sub>3</sub> particles. Moreover, the unique consecutive deposition-annealing process might lead to an improved semiconductor/substrate interface. A good interfacial contact would reduce the loss of charge carriers in transportation.

To further enhance the PEC performance, we have studied the impact of deliberate doping of the  $\alpha$ -Fe<sub>2</sub>O<sub>3</sub> films. Despite the fact that  $\alpha$ -Fe<sub>2</sub>O<sub>3</sub> has a favorable optical bandgap for light absorption, its potential use as a photoanode for water splitting is limited by the relatively poor electronic properties, as discussed above, as well as the large potential difference between flatband position and H<sup>+</sup>/H<sub>2</sub> reduction potential. Elemental doping is known to be a promising approach to alter the electronic properties of semiconductors. In this work, we report the synthesis of Ti-doped  $\alpha$ -Fe<sub>2</sub>O<sub>3</sub> films and investigate the Ti-doping effect on donor density, electronic structure, and excited state lifetime of  $\alpha$ -Fe<sub>2</sub>O<sub>3</sub> films. Ti was introduced into  $\alpha$ -Fe<sub>2</sub>O<sub>3</sub> films by mixing titanium butoxide into the FeCl<sub>3</sub> precursor solution. In comparison to undoped samples,  $\alpha$ -Fe<sub>2</sub>O<sub>3</sub> films prepared in the presence of titanium butoxide have less densely packed structure with relatively large  $\alpha$ -Fe<sub>2</sub>O<sub>3</sub> particles (Figure 4.12).

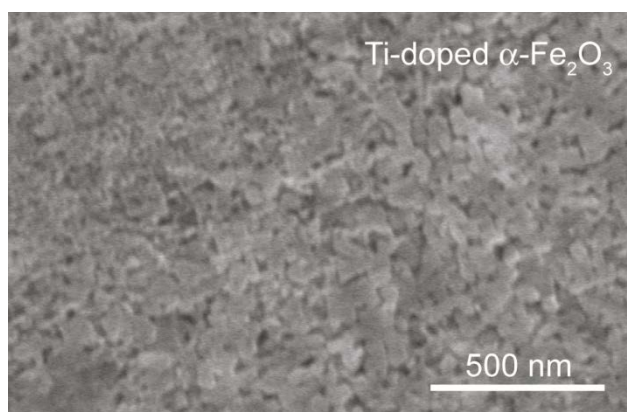


**Figure 4.12.** SEM image of Ti-doped  $\alpha$ -Fe<sub>2</sub>O<sub>3</sub> film prepared with 10 mM FeCl<sub>3</sub> solution and 10 % Ti precursor concentration.

X-ray photoelectron spectroscopy (XPS) survey spectra of a Ti-doped  $\alpha$ -Fe<sub>2</sub>O<sub>3</sub> film with 10 mM FeCl<sub>3</sub> precursor concentration confirm the presence of Ti (Figure 4.13a), while no Ti signal is found for the undoped sample, as expected. We note that the Ti signal at the surface of the Ti-doped  $\alpha$ -Fe<sub>2</sub>O<sub>3</sub> film is substantial, indicating that Ti concentration levels are higher than traditional “doping” levels, as discussed in the experimental section. The Ti-doped sample shows significant Na and C signals at the surface, while the Na signal and, to some degree, the C signal is reduced for the undoped sample. Both samples show small Cl peaks, while only the undoped sample exhibits a Sn signal. Sn and Na most likely originate from the FTO layer and the glass substrate, respectively. The presence of Cl is presumably due to the use of FeCl<sub>3</sub> solutions as the Fe precursor. Carbon is believed to be included during sample preparation (in air) and subsequent handling. Note that the ratio between the Fe signals (e.g., the Fe 2p) and the O 1s signal is much lower for the Ti-doped sample than for

the undoped sample. This indicates that the Ti atoms present at the surface of the Ti-doped sample very likely are bound in an oxide environment, as will be discussed in the following.

The Ti 2p detail spectrum of the Ti-doped sample is shown in Fig. 4.13b, together with a metallic Ti reference spectrum. From the peak position and line shape, it is evident that the Ti atoms in the Ti-doped sample are not in a metallic environment. The Ti 2p<sub>3/2</sub> binding energy of 458.6 eV is fully consistent with typical values reported for TiO<sub>2</sub> (458.7 eV<sup>73</sup> and ca. 458.6 to 459.3 eV<sup>74</sup>). Furthermore, the peaks of the Ti-doped sample exhibit a symmetric line shape, which is generally found when a band gap inhibits low-energy excitations in the photoemission process; the metallic Ti peaks, in contrast, show the well-known asymmetry towards higher binding energy (Figure 4.13b). Note that the Ti 2p<sub>1/2</sub> peak is significantly broader than the Ti 2p<sub>3/2</sub> peak due to presence of a Coster-Kronig decay channel of the Ti 2p<sub>1/2</sub> core hole, leading to lifetime broadening of the photoemission line. The Fe 2p<sub>3/2</sub> line of the Ti-doped  $\alpha$ -Fe<sub>2</sub>O<sub>3</sub> film in Fig. 4.13c is found at a binding energy of ~711.2 eV. Within the common variations of binding energy determination of band-gap materials, this value is consistent with typical values observed for Fe<sub>2</sub>O<sub>3</sub> (Fe<sup>3+</sup>, 710.9 eV<sup>73</sup> or 711.2 eV<sup>75</sup>, FeOOH (Fe<sup>3+</sup>, ~711.2 eV<sup>75</sup> and 711.3 to 711.9 eV<sup>74</sup>), and Fe<sub>3</sub>O<sub>4</sub> (a mix of Fe<sup>2+</sup>/Fe<sup>3+</sup>, 709.5/711.2 eV<sup>75</sup> and 711.6 eV<sup>76</sup>). The binding energy is not compatible with that of FeO (Fe<sup>2+</sup>, 709.6 eV<sup>73</sup> and 709.1 to 709.5 eV<sup>74</sup>). A

satellite peak of the Fe 2p<sub>3/2</sub> main line is observed at approximately 719.3 eV, i.e., approximately 8.1 eV below the main line. This satellite is most likely indicative of the presence of Fe<sup>3+</sup> species.<sup>77</sup> Again, there is no evidence to support the presence of Fe<sup>2+</sup>, which should give rise to a satellite peak located at 6.0 eV from the main peak (as indicated by the vertical dashed line in Fig. 4.13c). In comparison to the undoped  $\alpha$ -Fe<sub>2</sub>O<sub>3</sub> film, the Ti-doped sample shows evidence for an additional Fe species at a binding energy of ~708 eV (figure 4.14a). This shoulder does not match the binding energy of metallic Fe (706.7 to 707.1 eV<sup>73, 74</sup>), FeOOH, or any of the other oxides discussed above. We speculate that it might be due to the presence of Fe–C or Fe–Ti bonds in the Ti-doped sample – Peng et al. reported 706.9 eV as the Fe 2p<sub>3/2</sub> binding energy in Fe–Ti and Fe–Ti–N thin films,<sup>78</sup> and the Fe 2p<sub>3/2</sub> binding energy for Fe<sub>3</sub>C is reported to be 708.1 eV.<sup>73</sup> Figure 4.13d shows the O 1s XPS spectra collected from the doped and undoped  $\alpha$ -Fe<sub>2</sub>O<sub>3</sub> films. The binding energy of the main line (530.1 eV for the undoped and 530.3 eV for the Ti-doped sample) is consistent with the reported value for Fe<sub>2</sub>O<sub>3</sub> (530.0 eV,<sup>74, 77</sup> and 529.9 eV<sup>76</sup>) and Fe<sub>3</sub>O<sub>4</sub> (530.0 eV<sup>73</sup> and 530.3 eV<sup>76</sup>). Both samples show a shoulder at higher binding energy (more pronounced for the undoped sample), which could be attributed to O–H and/or O–C bonds.<sup>79, 80</sup>

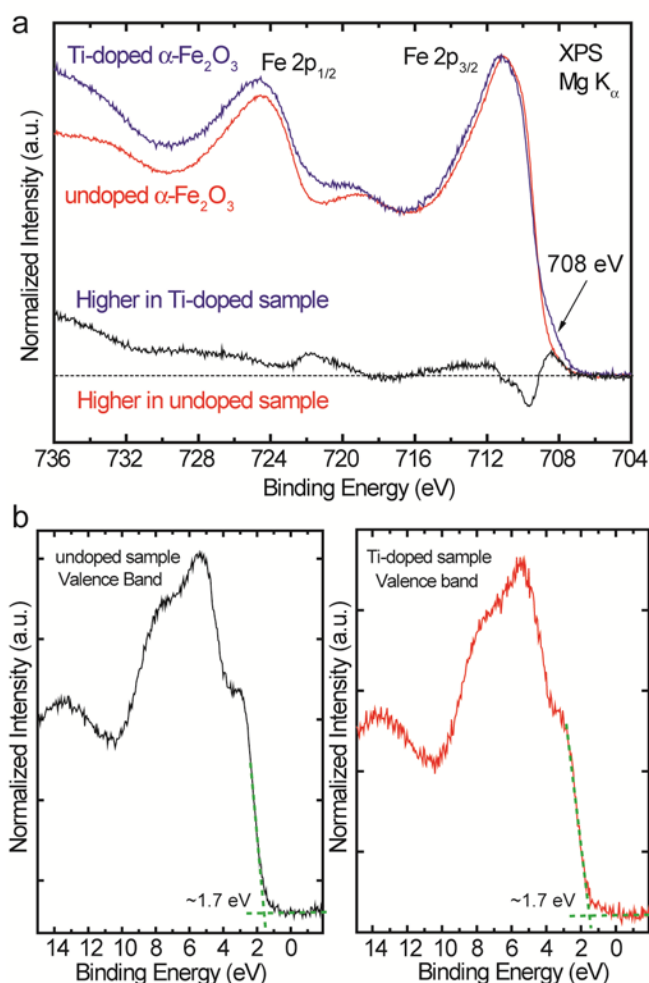


**Figure 4.13.** (a) XPS survey spectrum; and high resolution (b) Ti 2p; (c) Fe 2p; and (d) O 1s XPS spectra collected for the Ti-doped  $\alpha$ -Fe<sub>2</sub>O<sub>3</sub> film (10 mM FeCl<sub>3</sub> precursor). The Ti 2p spectrum of a metallic Ti reference is also included in (b), and the O 1s spectrum of the undoped  $\alpha$ -Fe<sub>2</sub>O<sub>3</sub> film was added in (d) for comparison.

Finally, the valence band region of the two  $\alpha$ -Fe<sub>2</sub>O<sub>3</sub> films was also measured by Mg K<sub>α</sub> XPS (Figure 4.14b). The two valence band spectra are similar, and an estimate of the valence band maximum by linear extrapolation to the baseline derives a band edge position of  $\sim 1.70 (\pm 0.20)$  eV below the Fermi energy in each case. Assuming that the optical band gap of (bulk)  $\alpha$ -Fe<sub>2</sub>O<sub>3</sub> of



$\sim 2.2$  eV<sup>18</sup> is preserved at the surface, this would place the surface conduction band minimum of the  $\alpha$ -Fe<sub>2</sub>O<sub>3</sub> films approximately 0.5 eV above the Fermi energy (note that the assumption of identical *bulk* and *surface* band gaps has been shown to be incorrect for a variety of compound semiconductors.<sup>81, 82</sup> The fact that both films exhibit the same position of the valence band maximum indicates a negligible effect of Ti-doping on the valence band position at the surface (most likely due to Fermi level pinning at the surface).

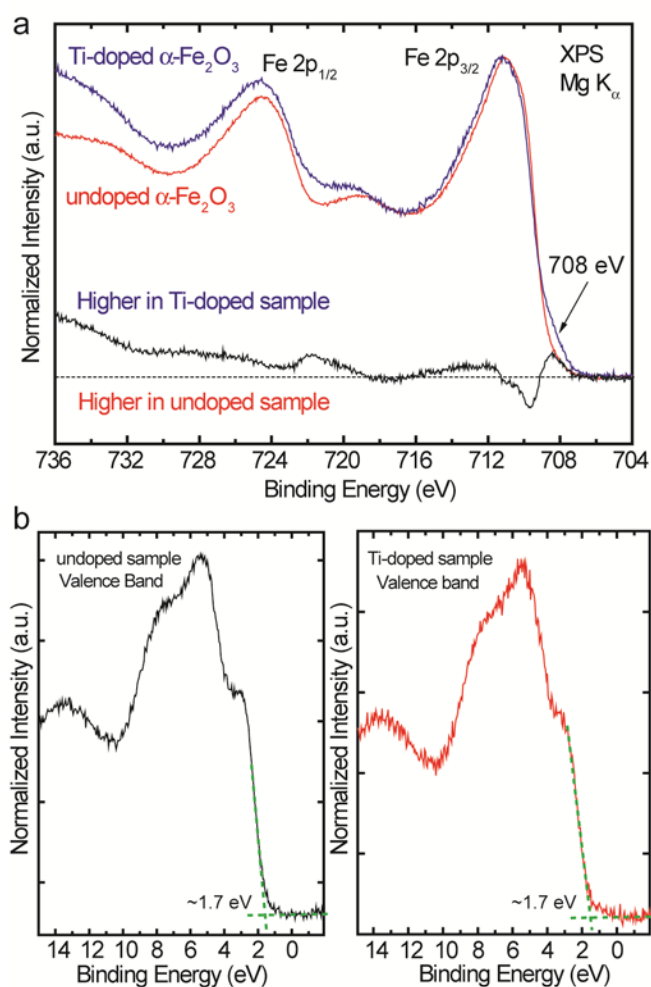


**Figure 4.14.** (a) The overlay of Fe 2p XPS spectra of undoped and Ti-doped  $\alpha$ -Fe<sub>2</sub>O<sub>3</sub> films. (b) Valence band spectra of undoped and Ti-doped  $\alpha$ -Fe<sub>2</sub>O<sub>3</sub> films.

The PEC performance of Ti-doped  $\alpha$ -Fe<sub>2</sub>O<sub>3</sub> films was investigated and optimized as a function of Ti precursor concentration and the number of DA cycles (Figure 4.15). As shown in Figure 4.15a, photocurrent densities of  $\alpha$ -Fe<sub>2</sub>O<sub>3</sub> films (prepared with 10 mM FeCl<sub>3</sub> solution and 10 DA cycles) increase drastically with the addition of a small amount of Ti precursor. The photocurrent reaches a maximal value at 10 % (atomic ratio of Ti:Fe) Ti precursor concentration, and decreases gradually for higher precursor concentration. By fixing the Ti precursor concentration at 10 %, the PEC performance of the  $\alpha$ -Fe<sub>2</sub>O<sub>3</sub> films was further optimized by varying the number of DA cycles. The highest photocurrent density was achieved at 14 DA cycles (Figure 4.15b), which is equivalent to a film thickness of ca. 160 nm.

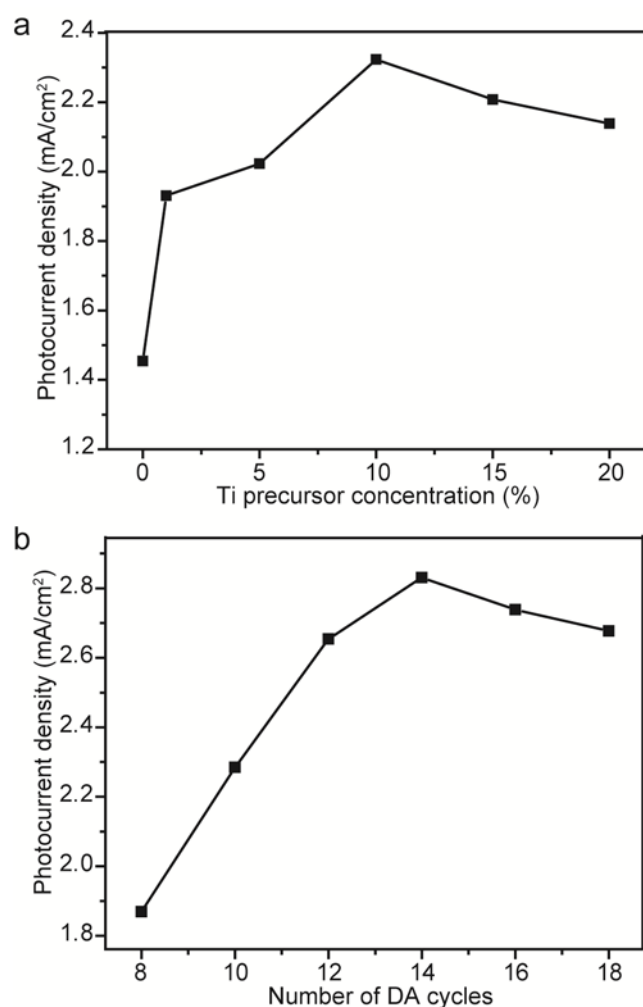


**Figure 4.15.** Photocurrent densities of  $\alpha$ -Fe<sub>2</sub>O<sub>3</sub> films prepared from a 10 mM FeCl<sub>3</sub> solution and using 10 DA cycles, measured at 0.45 V vs. Ag/AgCl as a function of (a) Ti precursor concentration; and (b) the number of DA cycles (10 % Ti precursor concentration).

Figure 4.16a compares the linear sweeps of optimized undoped and Ti-doped  $\alpha$ -Fe<sub>2</sub>O<sub>3</sub> films. Both current-bias curves can be discerned into three regions with the increase of applied bias. At small bias, the photocurrent density increases slowly and non-linearly, being indicative of a limited separation rate for the photogenerated electron-hole pairs in  $\alpha$ -Fe<sub>2</sub>O<sub>3</sub> under a low electric field. As the

applied bias is increased, the electron-hole pairs are separated more efficiently and the charge transport in the  $\alpha\text{-Fe}_2\text{O}_3$  film becomes the rate-limiting step. Therefore, the photocurrent density shows a linear variation with the applied bias. The Ti-doped  $\alpha\text{-Fe}_2\text{O}_3$  film shows an earlier photocurrent onset (i.e., at a lower voltage) than the undoped sample, suggesting that the carrier transport in the Ti-doped sample is more efficient. Finally, the photocurrent density saturates at higher applied bias as a result of insufficient numbers of photoexcited carriers (depending on the light intensity). The Ti-doped  $\alpha\text{-Fe}_2\text{O}_3$  film shows a two-fold enhanced photocurrent density compared to the undoped sample over the entire potential window studied. The Ti-doped  $\alpha\text{-Fe}_2\text{O}_3$  film achieved a remarkable photocurrent density of  $2.85\text{ mA/cm}^2$  at  $0.23\text{ V vs. Ag/AgCl}$  ( $1.23\text{ V vs. RHE}$ ), which is comparable to the benchmark values previously reported for  $\alpha\text{-Fe}_2\text{O}_3$  structures at the same potential.<sup>3, 8, 16</sup> Compared to the undoped sample, the photocurrent onset potential of Ti-doped  $\alpha\text{-Fe}_2\text{O}_3$  is shifted about  $0.1\text{--}0.2\text{ V}$  to lower potential, thus improving the photocurrent at lower bias voltage. A similar shift of onset potential was demonstrated in previous studies for Si-<sup>30</sup> and Ti-doped samples<sup>38, 51</sup>. Significantly, our Ti-doped  $\alpha\text{-Fe}_2\text{O}_3$  film achieved a photocurrent density of  $1.83\text{ mA/cm}^2$  at  $0\text{ V vs. Ag/AgCl}$  ( $1.0\text{ V vs. RHE}$ ), which is substantially higher than that observed in other  $\alpha\text{-Fe}_2\text{O}_3$  structures.<sup>3, 8, 16</sup> To our knowledge, this is the highest photocurrent density for  $\alpha\text{-Fe}_2\text{O}_3$  obtained at this bias.

To quantitatively investigate the photoactivity of the  $\alpha$ -Fe<sub>2</sub>O<sub>3</sub> films as a function of wavelength, incident-photon-to-current-conversion efficiency (IPCE) measurements were performed on the optimized undoped and Ti-doped  $\alpha$ -Fe<sub>2</sub>O<sub>3</sub> films at 0 V vs. Ag/AgCl. IPCE can be expressed as<sup>83</sup>:

$$\text{IPCE} = (1240 \times I) / (\lambda \times J_{\text{light}}),$$

where  $I$  is the measured photocurrent density,  $\lambda$  is the wavelength of the incident light, and  $J_{\text{light}}$  is the measured irradiance at the specific measurement wavelength. In comparison to the undoped sample, the optimized Ti-doped  $\alpha$ -Fe<sub>2</sub>O<sub>3</sub> film shows substantially enhanced IPCE values over the entire wavelength range of 350-610 nm (Figure 4.16b). The Ti-doped sample exhibits the highest IPCE values for  $\alpha$ -Fe<sub>2</sub>O<sub>3</sub> obtained at 0 V vs. Ag/AgCl to date. Above 620 nm, the photoresponse of both  $\alpha$ -Fe<sub>2</sub>O<sub>3</sub> films drops to zero, in accordance with the band gap of  $\alpha$ -Fe<sub>2</sub>O<sub>3</sub>.

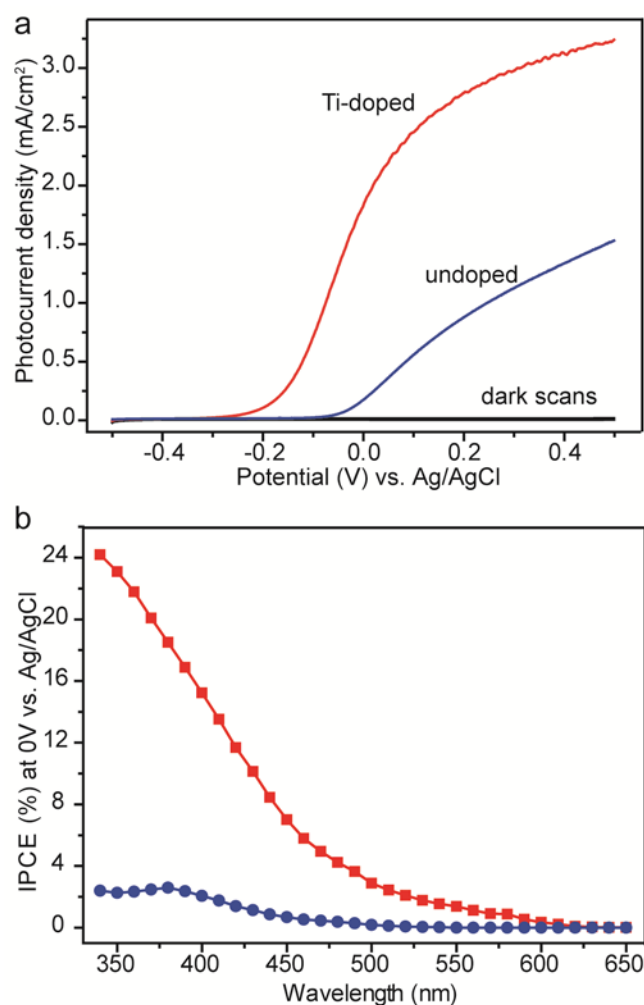


**Figure 4.16.** (a) Comparison of photocurrent densities collected for optimized undoped and Ti-doped  $\alpha$ -Fe<sub>2</sub>O<sub>3</sub> films. (b) IPCE spectra of these two films collected at 0 V vs. Ag/AgCl (1.0 V vs. RHE).

To elucidate the strong correlation between Ti-doping and the enhanced photocurrent and IPCE values, electrochemical impedance measurements and ultrafast spectroscopy were carried out. First, electrochemical impedances of undoped and Ti-doped  $\alpha$ -Fe<sub>2</sub>O<sub>3</sub> films were collected in the dark at 5 kHz. Both samples show a positive slope in the Mott-Schottky plots, indicating that they are *n*-type semiconductors with electrons as majority carriers (Figure 4.17). The

slopes determined from the Mott-Schottky plots were used to estimate the carrier densities using the equation

$$N_d = (2/e_0\epsilon\epsilon_0)[d(1/C^2)/dV]^{-1},$$

where  $e_0$  is the electron charge,  $\epsilon$  the dielectric constant of  $\alpha\text{-Fe}_2\text{O}_3$ ,  $\epsilon_0$  the permittivity of vacuum,  $N_d$  the dopant density, and  $V$  the potential applied at the electrode. With an  $\epsilon$  value of 80 for  $\alpha\text{-Fe}_2\text{O}_3$ ,<sup>30</sup> the electron densities of the undoped and Ti-doped  $\alpha\text{-Fe}_2\text{O}_3$  films were calculated to be  $3.4 \times 10^{18}$  and  $4.8 \times 10^{20} \text{ cm}^{-3}$ , respectively. The Ti-doping thus led to an increase of two orders of magnitude in the carrier density of our  $\alpha\text{-Fe}_2\text{O}_3$  films. The electron density of Ti doped  $\alpha\text{-Fe}_2\text{O}_3$  is consistent with reported values for Si-doped  $\alpha\text{-Fe}_2\text{O}_3$  structures prepared by APCVD,<sup>30</sup> and is believed to be a major contributing factor for the pronounced photocurrent density enhancement.

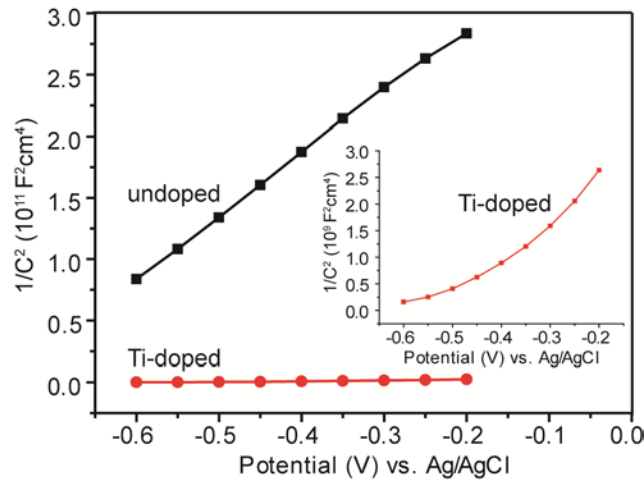


**Figure 4.17.** Mott-Schottky plots of the undoped and Ti-doped  $\alpha\text{-Fe}_2\text{O}_3$  films collected in the dark at frequencies of 5 kHz. Inset: magnified Mott-Schottky plot of the Ti-doped  $\alpha\text{-Fe}_2\text{O}_3$  film.

Moreover, electrochemical impedance spectroscopy was used to investigate the kinetics of the oxidation process at the electrode surface. The Nyquist plot collected for Ti-doped  $\alpha$ -Fe<sub>2</sub>O<sub>3</sub>, in the dark at 0 V *vs.* Ag/AgCl, exhibits one capacitive arc, suggesting that the Faradaic charge transfer is the limiting step for the oxidation process in the electrode surface (Figure 4.18). Under illumination (100 mW/cm<sup>2</sup>), two capacitive arcs were observed in the Nyquist plot. The arcs observed in the high (left) and the low (right) frequencies are correlated to the charge transfer resistance and the mass transfer limitation, respectively. The capacitive arcs obtained under illumination have much smaller radii (i.e., smaller charge transfer resistance) than those in the dark, indicating that the photoexcited carriers increase the conductivity of the  $\alpha$ -Fe<sub>2</sub>O<sub>3</sub> film.



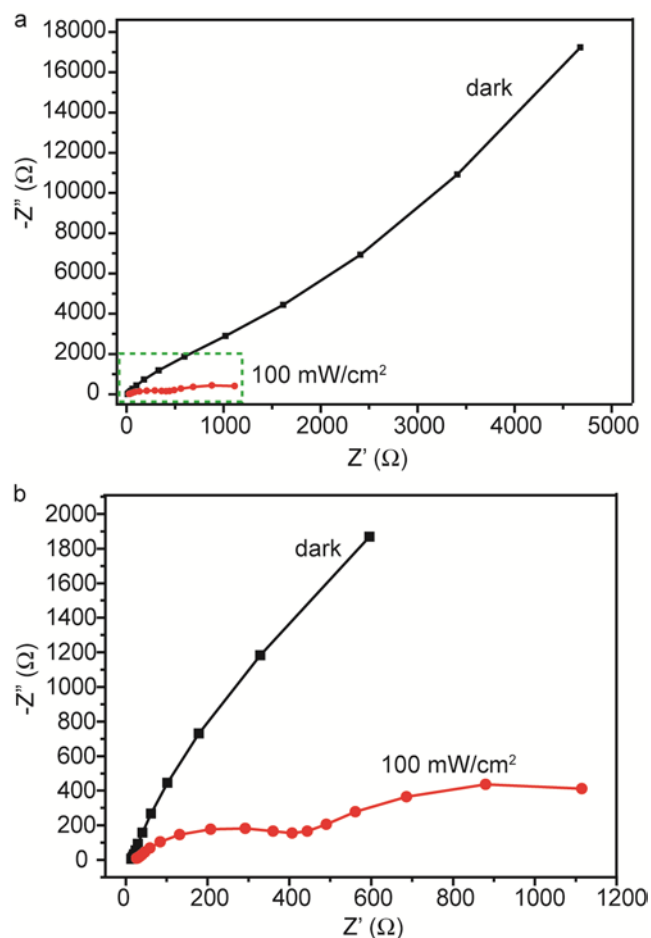


**Figure 4.18.** (a) Nyquist plots collected for a Ti-doped  $\alpha$ -Fe<sub>2</sub>O<sub>3</sub> film prepared with 10 mM FeCl<sub>3</sub> solution in the dark and under illumination (100 mW/cm<sup>2</sup>) at 1.02 V *vs.* RHE. (b) Magnified view of the region highlighted by the green dashed rectangle in (a).

Ultrafast spectroscopy studies<sup>84</sup> were carried out to probe the fundamental charge carrier dynamics following photoexcitation and to understand the possible effect of Ti-doping on the photoexcited electron dynamics in  $\alpha$ -Fe<sub>2</sub>O<sub>3</sub> films. The normalized ultrafast transient absorption profiles of undoped and

Ti-doped  $\alpha$ -Fe<sub>2</sub>O<sub>3</sub> films are shown on two different time scales in Figure 10. A pulse-width limited rise of the signal is followed by a decay that can only be fit to a multiple exponential. To achieve a satisfactory fit result, at least three exponential functions need to be employed. The fit-derived time constants for the undoped and Ti-doped  $\alpha$ -Fe<sub>2</sub>O<sub>3</sub> films are 0.329, 2.225, and 70.84 ps; and 0.336, 2.310, and 70.55 ps, respectively. These time constants were convolved with a Gaussian (fwhm 130 fs), representing the cross-correlation of the 440 nm pump [150 nJ/(pulse-cm<sup>2</sup>), attenuated with neutral density filters] and 620 nm probe pulses. The overall charge carrier decay for both  $\alpha$ -Fe<sub>2</sub>O<sub>3</sub> films is very fast, without measurable transient absorption beyond 300 ps. The very fast decay is likely due to a high density of electronic states in the band gap caused by internal defects and/or surface defects. This indicates that the early time dynamics of the photogenerated charge carriers are dominated by the intrinsic properties of the  $\alpha$ -Fe<sub>2</sub>O<sub>3</sub>, and consistent with the decay profiles reported previously for  $\alpha$ -Fe<sub>2</sub>O<sub>3</sub> nanoparticles.<sup>20, 21</sup> In comparison to the undoped sample, the Ti-doped  $\alpha$ -Fe<sub>2</sub>O<sub>3</sub> film decays slightly faster on the shortest time scale (Figure 4.19). For time scales above 4 ps, the absorption decay profile of the Ti-doped sample is slightly higher than that of the undoped sample, indicating a reduced electron-hole recombination on that time scale. This might contribute to the enhanced photocurrent of the Ti-doped sample observed in the PEC measurements. Furthermore, we believe that the improved donor density and

electrical conductivity described above will also contribute to the enhanced photoactivity.

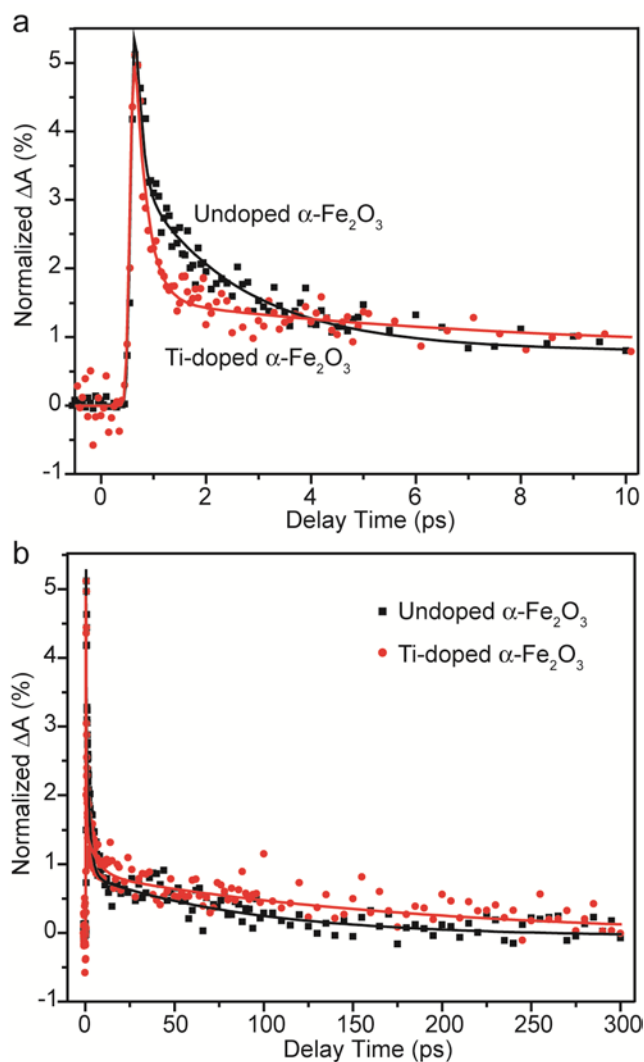


**Figure 4.19.** Normalized ultrafast transient absorption decay profiles of undoped and Ti-doped  $\alpha\text{-Fe}_2\text{O}_3$  films. (a) the 0-10 ps, (b) the 0-300 ps window, which are fit simultaneously using a nonlinear least-squares fitting algorithm to a triple-exponential decay convolved with a Gaussian, representing the cross-correlation of the 440 nm pump and 620 nm probe pulses. The solid lines are fitted curves.

## Conclusion

In summary, we have demonstrated a facile deposition-annealing process to fabricate highly photoactive undoped and Ti-doped  $\alpha$ -Fe<sub>2</sub>O<sub>3</sub> films on FTO substrates. The size of  $\alpha$ -Fe<sub>2</sub>O<sub>3</sub> particles and the film thickness can be controlled by varying the Fe precursor concentration and the number of DA cycles. In comparison to undoped  $\alpha$ -Fe<sub>2</sub>O<sub>3</sub>, the Ti-doped film shows enhanced photocurrent density and IPCE as a result of improved charge carrier density. The optimized Ti-doped  $\alpha$ -Fe<sub>2</sub>O<sub>3</sub> films showed a remarkable photocurrent density of 1.83 mA/cm<sup>2</sup> at 0 V *vs.* Ag/AgCl (1.0 V *vs.* RHE), which is the best value for  $\alpha$ -Fe<sub>2</sub>O<sub>3</sub> photoanodes at such a low bias. Further improvement of PEC performance of these  $\alpha$ -Fe<sub>2</sub>O<sub>3</sub> films could potentially be accomplished by coupling them with efficient oxygen-evolving catalysts, such as Co<sup>2+</sup>-based compounds<sup>85</sup> and iridium oxide<sup>16</sup>, as well as improving the intrinsic electronic structure of  $\alpha$ -Fe<sub>2</sub>O<sub>3</sub> in order to achieve longer photoexcited charge carrier lifetimes.

## Reference

1. Fujishima, A.; Honda, K. *Nature* **1972**, 238, (5358), 37-38.
2. Cesar, I.; Kay, A.; Martinez, J. A. G.; Gratzel, M. *J. Am. Chem. Soc.* **2006**, 128, (14), 4582-4583.
3. Kay, A.; Cesar, I.; Gratzel, M. *J. Am. Chem. Soc.* **2006**, 128, (49),

15714-15721.

4. Wang, G. M.; Yang, X. Y.; Qian, F.; Zhang, J. Z.; Li, Y. *Nano Lett.* **2010**, 10, (3), 1088-1092.
5. Mor, G. K.; Prakasam, H. E.; Varghese, O. K.; Shankar, K.; Grimes, C. A. *Nano Lett.* **2007**, 7, (8), 2356-2364.
6. Park, J. H.; Kim, S.; Bard, A. J. *Nano Lett.* **2006**, 6, (1), 24-28.
7. Lin, Y.; Zhou, S.; Liu, X.; Sheehan, S. W.; Wang, D. *J. Am. Chem. Soc.* **2009**, 131, (8), 2772-2773.
8. Lin, Y.; Zhou, S.; Sheehan, S. W.; Wang, D. *J. Am. Chem. Soc.* **2011**, 133, (8), 2398-2401.
9. Liu, R.; Lin, Y.; Chou, L.; Sheehan, S. W.; He, W.; Zhang, F.; Hou, J. M.; Wang, D. *Angew. Chem. Int. Ed.* **2011**, 50, (2), 499-502.
10. Khan, S. U. M.; Al-Shahry, M.; Ingler, W. B. *Science* **2002**, 297, (5590), 2243-2245.
11. Feng, X. J.; Shankar, K.; Varghese, O. K.; Paulose, M.; Latempa, T. J.; Grimes, C. A. *Nano Lett.* **2008**, 8, (11), 3781-3786.
12. Yang, X. Y.; Wolcott, A.; Wang, G. M.; Sobo, A.; Fitzmorris, R. C.; Qian, F.; Zhang, J. Z.; Li, Y. *Nano Lett.* **2009**, 9, (6), 2331-2336.
13. Hensel, J.; Wang, G. M.; Li, Y.; Zhang, J. Z. *Nano Lett.* **2010**, 10, (2), 478-483.
14. Solarska, R.; Krolikowska, A.; Augustynski, J. *Angew. Chem. Int. Ed.*

- 2010**, 49, (43), 7980-7983.
15. Su, J.; Feng, X. J.; Sloppy, J. D.; Guo, L.; Grimes, C. A. *Nano Lett.* **2011**, 11, (1), 203-208.
  16. Tilley, S. D.; Cornuz, M.; Sivula, K.; Gratzel, M. *Angew. Chem. Int. Ed.* **2010**, 49, (36), 6405-6408.
  17. Qian, F.; Wang, G.; Li, Y. *Nano Lett.* **2010**, 10, 4686-4691.
  18. Klahr, B. M.; Martinson, A. B. F.; Hamann, T. W. *Langmuir* **2011**, 27, 461-468.
  19. Ling, Y.; Wang, G.; Wheeler, D. A.; Zhang, J. Z.; Li, Y. *Nano Lett.* **2011**, 11, (5), 2119-2125.
  20. Duret, A.; Gratzel, M. *J. Phys. Chem. B* **2005**, 109, (36), 17184-17191.
  21. Murphy, A. B.; Barnes, P. R. F.; Randeniya, L. K.; Plumb, I. C.; Grey, I. E.; Horne, M. D.; Glasscock, J. A. *Int. J. Hydrogen Energy* **2006**, 31, (14), 1999-2017.
  22. Joly, A. G.; Williams, J. R.; Chambers, S. A.; Xiong, G.; Hess, W. P.; Laman, D. M. *J. Appl. Phys.* **2006**, 99, (5), 6.
  23. Cherepy, N. J.; Liston, D. B.; Lovejoy, J. A.; Deng, H. M.; Zhang, J. Z. *J. Phys. Chem. B* **1998**, 102, (5), 770-776.
  24. Stojic, D. L.; Marceta, M. P.; Sovilj, S. P.; Miljanic, S. S. *J. Power Sources* **2003**, 118, (1-2), 315-319.

25. Khaselev, O.; Turner, J. A. *Science* **1998**, 280, (5362), 425-427.
26. Kennedy, J. H.; Frese, K. W. *J. Electrochem. Soc.* **1977**, 124, (3), C130-C130.
27. Hahn, N. T.; Mullins, C. B. *Chem. Mater.* **2010**, 22, (23), 6474-6482.
28. Sivula, K.; Zboril, R.; Le Formal, F.; Robert, R.; Weidenkaff, A.; Tucek, J.; Frydrych, J.; Gratzel, M. *J. Am. Chem. Soc.* **2010**, 132, (21), 7436-7444.
29. Kennedy, J. H.; Anderman, M. *J. Electrochem. Soc.* **1983**, 130, (4), 848-852.
30. Frites, M.; Khan, S. U. M. *ECS Transactions* **2009**, 19, (3), 137-145.
31. Guo, L. Q.; Chen, F.; Fan, X. Q.; Cai, W. D.; Zhang, J. L. *Appl. Catal., B* **2010**, 96, (1-2), 162-168.
32. Cesar, I.; Sivula, K.; Kay, A.; Zboril, R.; Graetzel, M. *J. Phys. Chem. C* **2009**, 113, (2), 772-782.
33. Khan, S. U. M.; Zhou, Z. Y. *J. Electroanal. Chem.* **1993**, 357, (1-2), 407-420.
34. Saremi-Yarahmadi, S.; Wijayantha, K. G. U.; Tahir, A. A.; Vaidhyanathan, B. *J. Phys. Chem. C* **2009**, 113, (12), 4768-4778.
35. Brillet, J.; Gratzel, M.; Sivula, K. *Nano Lett.* **2010**, 10, (10), 4155-4160.
36. Le Formal, F.; Gratzel, M.; Sivula, K. *Adv.Funct. Mater.* **2010**, 20,

- (7), 1099-1107.
37. Kennedy, J. H.; Shinar, R.; Ziegler, J. P. *J. Electrochem. Soc.* **1980**, 127, (10), 2307-2309.
  38. Kennedy, J. H.; Anderman, M.; Shinar, R. *J. Electrochem. Soc.* **1981**, 128, (11), 2371-2373.
  39. Khan, S. U. M.; Akikusa, J. *J. Phys. Chem. B* **1999**, 103, (34), 7184-7189.
  40. Zhang, M. L.; Luo, W. J.; Li, Z. S.; Yu, T.; Zou, Z. G. *Appl. Phys. Lett.* **2010**, 97, (4), 3.
  41. Sartoretti, C. J.; Alexander, B. D.; Solarska, R.; Rutkowska, W. A.; Augustynski, J.; Cerny, R. *J. Phys. Chem. B* **2005**, 109, (28), 13685-13692.
  42. Kleiman-Shwarsstein, A.; Hu, Y. S.; Forman, A. J.; Stucky, G. D.; McFarland, E. W. *J. Phys. Chem. C* **2008**, 112, (40), 15900-15907.
  43. 41. Glasscock, J. A.; Barnes, P. R. F.; Plumb, I. C.; Savvides, N. J. *Phys. Chem. C* **2007**, 111, (44), 16477-16488.
  44. Hu, Y. S.; Kleiman-Shwarsstein, A.; Stucky, G. D.; McFarland, E. W. *Chem. Commun.* **2009**, (19), 2652-2654.
  45. Ingler, W. B.; Khan, S. U. M. *Int. J. Hydrogen Energy* **2005**, 30, (8), 821-827.
  46. Zhong, D. K.; Sun, J. W.; Inumaru, H.; Gamelin, D. R. *J. Am. Chem.*



- Soc.* **2009**, 131, (17), 6086-6087.
47. Wang, H. L.; Turner, J. A. *J. Electrochem. Soc.* **2010**, 157, (11), F173-F178.
  48. Ingler, W. B.; Khan, S. U. M. *Electrochem. Solid-State Lett.* **2006**, 9, (4), G144-G146.
  49. Ingler, W. B.; Baltrus, J. P.; Khan, S. U. M. *J. Am. Chem. Soc.* **2004**, 126, (33), 10238-10239.
  50. Ingler, W. B.; Khan, S. U. M. *Thin Solid Films* **2004**, 461, (2), 301-308.
  51. Aroutiounian, V. M.; Arakelyan, V. M.; Shahnazaryan, G. E.; Stepanyan, G. M.; Khachaturyan, E. A.; Wang, H.; Turner, J. A. *Solar Energy* **2006**, 80, (9), 1098-1111.
  52. Aroutiounian, V. M.; Arakelyan, V. M.; Shahnazaryan, G. E.; Stepanyan, G. M.; Turner, J. A.; Khaselev, O. *Int. J. Hydrogen Energy* **2002**, 27, (1), 33-38.
  53. Morin, F. J. *Phys. Rev.* **1951**, 83, (5), 1005-1010.
  54. Beermann, N.; Vayssieres, L.; Lindquist, S. E.; Hagfeldt, A. *J. Electrochem. Soc.* **2000**, 147, (7), 2456-2461.
  55. Lindgren, T.; Wang, H. L.; Beermann, N.; Vayssieres, L.; Hagfeldt, A.; Lindquist, S. E. *Sol. Energ. Mat. Sol. Cells* **2002**, 71, (2), 231-243.

56. Niu, M. T.; Huang, F.; Cui, L. F.; Huang, P.; Yu, Y. L.; Wang, Y. S. *ACS Nano* **2010**, 4, (2), 681-688.
57. Miller, E. L.; Rocheleau, R. E.; Khan, S. *Int. J. Hydrogen Energy* **2004**, 29, (9), 907-914.
58. Sartoretti, C. J.; Ulmann, M.; Alexander, B. D.; Augustynski, J.; Weidenkaff, A. *Chem. Phys. Lett.* **2003**, 376, (1-2), 194-200.
59. Kleiman-Shwarsstein, A.; Huda, M. N.; Walsh, A.; Yan, Y. F.; Stucky, G. D.; Hu, Y. S.; Al-Jassim, M. M.; McFarland, E. W. *Chem. Mater.* **2010**, 22, (2), 510-517.
60. Spray, R. L.; Choi, K. S. *Chem. Mater.* **2009**, 21, (15), 3701-3709.
61. Hu, Y. S.; Kleiman-Shwarsstein, A.; Forman, A. J.; Hazen, D.; Park, J. N.; McFarland, E. W. *Chem. Mater.* **2008**, 20, (12), 3803-3805.
62. Gash, A. E.; Tillotson, T. M.; Satcher, J. H.; Poco, J. F.; Hrubesh, L. W.; Simpson, R. L. *Chem. Mater.* **2001**, 13, (3), 999-1007.
63. Prakasam, H. E.; Varghese, O. K.; Paulose, M.; Mor, G. K.; Grimes, C. A. *Nanotechnology* **2006**, 17, (17), 4285-4291.
64. Mohapatra, S. K.; John, S. E.; Banerjee, S.; Misra, M. *Chem. Mater.* **2009**, 21, (14), 3048-3055.
65. LaTempa, T. J.; Feng, X. J.; Paulose, M.; Grimes, C. A. *J. Phys. Chem. C* **2009**, 113, (36), 16293-16298.
66. Rao, P. M.; Zheng, X. L. *Nano Lett.* **2009**, 9, (8), 3001-3006.

67. Perednis, D.; Gauckler, L. J. *J. Electroceram.* **2005**, 14, (2), 103-111.
68. Kim, S. G.; Choi, K. H.; Eun, J. H.; Kim, H. J.; Hwang, C. S. *Thin Solid Films* **2000**, 377, 694-698.
69. Massey, M. J.; Baier, U.; Merlin, R.; Weber, W. H. *Phys. Rev. B* **1990**, 41, 7822-7827.
70. Richter, H.; Wang, Z. P.; Ley, L. *Solid State Commun.* **1981**, 39, (5), 625-629.
71. Campbell, I. H.; Fauchet, P. M. *Solid State Commun.* **1986**, 58, (10), 739-741.
72. Gratzel, M. *Nature* **2001**, 414, (6861), 338-344.
73. Frey, M. H.; Payne, D. A. *Phys. Rev. B* **1996**, 54, (5), 3158-3168.
74. Wang, W.; Howe, J. Y.; Gu, B. H. *J. Phys. Chem. C* **2008**, 112, (25), 9203-9208.
75. Briggs, D.; Seah, M. P., *Auger and X-Ray Photoelectron Spectroscopy: Practical Surface Analysis*. Wiley: New York, 1990; Vol. 1, p Appendix 1.
76. Moulder, J. F.; Stickle, W. F.; Sobol, P. E.; Bomben, K. D., *Handbook of X-ray Photoelectron Spectroscopy*. In Physical Electronics Division, Perkin-Elmer Corporation: Eden Prairie, Mn, 1992.
77. Wandelt, K. *Surf. Sci. Rep.* **1982**, 2, 1-121.
78. Mills, P.; Sullivan, J. L. *J. Phys. D: Appl. Phys.* **1983**, 16, 723-732.

79. Fujii, T.; de Groot, F. M. F.; Sawatzky, G. A.; Voogt, F. C.; Hibma, T.; Okada, K. *Phys. Rev. B* **1999**, 59, (4), 3195-3202.
80. Peng, D. L.; Sumiyama, K.; Oku, M.; Li, D. X.; Suzuki, K. *Phys. Status Solidi A* **1996**, 157, (1), 139-152.
81. Yamamoto, S.; Kendelewicz, T.; Newberg, J. T.; Ketteler, G.; Starr, D. E.; Mysak, E. R.; Andersson, K. J.; Ogasawara, H.; Bluhm, H.; Salmeron, M.; Brown, G. E.; Nilsson, A. *J. Phys. Chem. C* **2010**, 114, (5), 2256-2266.
82. Bär, M.; Ahn, K. S.; Yan, Y.; Weinhardt, L.; Fuchs, O.; Blum, M.; George, K.; Pookpanratana, S.; Yang, W.; Denlinger, J. D.; Al-Jassim, M.; Heske, C. *Appl. Phys. Lett.* **2009**, 94, 012110.
83. Bär, M.; Weinhardt, L.; Pookpanratana, S.; Heske, C.; Nishiwaki, S.; Shafarman, W.; Fuchs, O.; Blum, M.; Yang, W.; Denlinger, J. D. *Appl. Phys. Lett.* **2008**, 93, 244103.
84. Weinhardt, L.; Blum, M.; Bär, M.; Heske, C.; Cole, B.; Marsen, B.; Miller, E. L. *J. Phys. Chem. C* **2008**, 112, 3078-3082.
85. Chen, Z.; Jaramillo, T. F.; Deutsch, T. G.; Kleiman-Shwarsstein, A.; Forman, A.; Gaillard, N.; Garland, R.; Takanabe, K.; Heske, C.; Sunkara, M.; McFarland, E. W.; Domen, K.; Miller, E. L.; Turner, J. A.; Dinh, H. N. *J. Mater. Res.* **2010**, 25, 3-16.
86. Newhouse, R. J.; Wang, H. N.; Hensel, J. K.; Wheeler, D. A.; Zou, S.

L.; Zhang, J. Z. *J. Phys. Chem. Lett.* **2011**, 2, (3), 228-235.

87. Kanan, M. W.; Nocera, D. G. *Science* **2008**, 321, 1072-1075.

## Chapter 5

### Hydrogen Treated TiO<sub>2</sub> Nanostructures for PEC Water Splitting

#### Abstract

We report the first demonstration of hydrogen-treated TiO<sub>2</sub> (H:TiO<sub>2</sub>) nanowire-arrayed photoanodes for photoelectrochemical water splitting. H:TiO<sub>2</sub> nanowires were prepared by annealing the pristine TiO<sub>2</sub> nanowires in hydrogen atmosphere at various temperatures in a range of 200-550 °C. In comparison to pristine TiO<sub>2</sub> nanowires, H:TiO<sub>2</sub> nanowires exhibit at least two times enhanced photocurrent in the entire potential window we studied. More importantly, H:TiO<sub>2</sub> nanowires exhibit exceptionally low photocurrent saturation potential of -0.6 V vs. Ag/AgCl (0.4 V vs. RHE), indicating very efficient charge separation and transportation. The H:TiO<sub>2</sub> nanowires annealed at 350 °C yield a photocurrent density of ~1.97 mA/cm<sup>2</sup> at -0.6 V vs. Ag/AgCl, in 1 M NaOH solution under the illumination of simulated solar light (100 mW/cm<sup>2</sup> from 150W xenon lamp coupled with a AM 1.5G filter). This photocurrent density corresponds to a STH conversion efficiency of ~1.63 %. After eliminating the discrepancy between the irradiance spectra of xenon lamp and solar light by integrating the IPCE spectrum of the H:TiO<sub>2</sub> nanowires with a standard AM

1.5G solar spectrum, the solar-to-hydrogen (STH) efficiency is calculated to be ~1.1 %, which is the best value for TiO<sub>2</sub> material. The H:TiO<sub>2</sub> nanowires produced hydrogen and oxygen at a constant rate and showed excellent stability in continuous operation. IPCE analyses confirm the photocurrent enhancement is mainly due to the improved photoactivity of TiO<sub>2</sub> in the UV region. Hydrogen treatment increases the donor density of TiO<sub>2</sub> nanowires by three orders of magnitudes, which is attributed to a high density of oxygen vacancies that serve as electron donor. In addition, we have also observed similar photocurrent enhancement in anatase H:TiO<sub>2</sub> nanotubes. This work demonstrates a new and effective strategy to fundamentally improve the performance of TiO<sub>2</sub> materials through hydrogen treatment (both rutile and anatase phase) for water splitting.

## **Introduction**

Titanium dioxide (TiO<sub>2</sub>) has been extensively investigated as photoanode for photoelectrochemical (PEC) water splitting<sup>1-8</sup> because of its favorable band-edge positions, strong optical absorption, superior chemical stability and photocorrosion resistance, and low cost<sup>9</sup>. However, the STH efficiency of TiO<sub>2</sub> is substantially limited by its large band-gap energy and usually fast electron-hole recombination due to a high density of trap states<sup>10-12</sup>. Enormous amount of research efforts have been focused on enhancing the visible light absorption of large band-gap metal oxides. For instance, sensitization with small

band-gap semiconductors and/or band-gap narrowing via elemental doping are two versatile approaches shown to improve the conversion efficiency of metal oxide photoelectrodes by modifying their optical absorption coefficient and wavelength<sup>3, 13-19</sup>. On the other hand, it is equally important to fundamentally improve the morphology and electronic structure of TiO<sub>2</sub> for effective separation and transportation of photoexcited charge carriers. It has been predicted that a maximum photoconversion efficiency of 2.25% can be achieved by rutile TiO<sub>2</sub> with an optical band-gap of 3.0 eV, at 100 mW/cm<sup>2</sup> AM 1.5 global illumination<sup>20</sup>. Yet, the reported photocurrent densities and photoconversion efficiencies of TiO<sub>2</sub> photoanodes are substantially lower than the theoretical limit. Our work demonstrates that hydrogen treatment is a simple and general strategy that can significantly enhance the photoconversion efficiency of TiO<sub>2</sub> materials by improving their donor density and electrical conductivity.

Our strategy of increasing the PEC performance is to develop TiO<sub>2</sub> nanostructures with increased donor density. One-dimensional nanowire-arrayed photoanode with large surface area and short diffusion distance for photogenerated minority carriers is expected to facilitate the charge separation, and thus, reduce the loss due to electron-hole recombination<sup>4, 6, 14</sup>. Additionally, it has been demonstrated that some dopants such as nitrogen and carbon serve as electron donors<sup>3, 21-23</sup>. The dopants introduce impurity states in various positions



in the band-gap of  $\text{TiO}_2$  lead to different degrees of modification in electrical conductivity<sup>24, 25</sup> Oxygen vacancies are known to be shallow donors for rutile  $\text{TiO}_2$ , with relatively low formation energies<sup>26</sup>. It has been reported that oxygen vacancies play a critical role in determining the surface and electronic properties of  $\text{TiO}_2$ <sup>24, 27, 28</sup>. We hypothesized that annealing  $\text{TiO}_2$  nanostructures in a reducing gas atmosphere will substantially increase the density of oxygen vacancies (donor density), and thereby, enhance the electrical conductivity as well as charge transportation. To prove this hypothesis, we have focused on the hydrogen-treated  $\text{TiO}_2$  (denoted as  $\text{H}:\text{TiO}_2$ ) nanowire arrays (rutile) and nanotube arrays (anatase). Hydrogen gas was chosen because it is a reducing gas with very light weight that may facilitate diffusion of the gas into  $\text{TiO}_2$ . In comparison to other reducing agents, ultrahigh purity hydrogen can also avoid the possibility of integrating dopants from the reducing agent or solvent into the  $\text{TiO}_2$  structure. To our knowledge, hydrogen-treated  $\text{TiO}_2$  one-dimensional nanostructures (nanowires and nanotubes) have not been reported for PEC water splitting.

## **Experimental section:**

### **Preparation of $\text{TiO}_2$ nanowire arrays:**

Rutile  $\text{TiO}_2$  nanowire arrays were grown on a fluorine-doped tin oxide (FTO) glass substrate using a previously reported hydrothermal method. 15 ml of

concentrated hydrochloric acid was diluted with 15 ml deionized (DI) water, and mixed with 0.5 ml titanium n-butoxide in a 100 ml beaker. This clear solution mixture and a clean FTO glass substrate were transferred to a Teflon-lined stainless steel autoclave (40 ml volume), where the FTO substrate was submerged in the solution. The sealed autoclave was heated in an electric oven at 150 °C for 5 hours, and then cooled down to room temperature slowly. A white TiO<sub>2</sub> nanowire film was uniformly coated on the FTO glass substrate. The sample was thoroughly washed with DI water and air dried. Finally, the sample was annealed in air at 550 °C for 3 hours to increase the crystallinity of TiO<sub>2</sub> nanowires and improve their contact to the substrate.

#### **Preparation of TiO<sub>2</sub> nanotube arrays:**

Anatase TiO<sub>2</sub> nanotube arrays were prepared by electrochemical anodization of a titanium foil (0.25mm thick, 99.8% purity, Aldrich). 1×2 cm titanium foil was cleaned by sonication in acetone, ethanol and then deionized water successively before anodization. Titanium foil was used as an anode, with a Pt wire as cathode in an ethylene glycol electrolyte solution containing 0.3 wt% NH<sub>4</sub>F and 1 wt% water. Electrochemical anodization was carried out on a DC regulated power supply (B&K Precision Corp Model 1623A) with a constant voltage of 60 V at room temperature for 30 min. The as-prepared TiO<sub>2</sub> nanotube arrays were thoroughly washed with ethanol and then DI water, and then annealed in the air at 500 °C for 2h.

**Hydrogen Treatment:**

TiO<sub>2</sub> nanowire and nanotube arrays were annealed in hydrogen atmosphere at various temperatures, in a range of 200-550 °C, for 30 min. The preparation was performed in a home-built tube furnace filled with ultrahigh purity hydrogen gas (Praxair).

**Material Characterization:**

Scanning electron microscopy (SEM) images were collected with a field-emission SEM (Hitachi S-4800 II). Transmission electron microscopy (TEM) images were collected in a FEI Monochromated F20 UT Technai TEM/STEM operated at 200 kV. X-ray diffraction (XRD) spectra of TiO<sub>2</sub> and H:TiO<sub>2</sub> nanowire/nanotube arrays (on FTO substrate) were collected with a Rigaku Americas Miniflex Plus powder diffractometer. Diffraction spectra were recorded from a 2θ angle of 20 to 70 degree with a step size of 0.04 degree at a rate of 1 degree/min. X-ray Photoelectron Spectroscopy (XPS) was performed on a RBD upgraded PHI-5000C ESCA system (Perkin-Elmer) using Al-monochromatic X-ray at a power of 25 W with an X-ray-beam diameter of 10 mm, and a pass energy of 29.35 eV. The pressure of analyzer chamber was maintained below 5×10<sup>-8</sup> Pa during the measurement. The binding energy was calibrated using the C 1s photoelectron peak at 284.6 eV as the reference.

**Photoelectrochemical Measurements:**

TiO<sub>2</sub> and H:TiO<sub>2</sub> nanowire (nanotube) arrays were fabricated into photoanodes

by soldering a copper wire onto a bare part of the FTO (Ti foil) substrate. The substrate edges and the metal contact region were sealed with insulating epoxy resin. The working electrode area is in the range of 0.2-0.25 cm<sup>2</sup>. 1 M NaOH aqueous solution (pH = 13.6) was used as an electrolyte for PEC measurements. Linear sweeps and I-t scans were measured by a CHI 660D electrochemical station, with Ag/AgCl as reference and Pt wire as counter electrode, under simulated sunlight with a 150 W xenon lamp (Newport 6255) coupled with an AM 1.5 global filter (Newport 81094). Incident-photon-to-current-conversion-efficiencies (IPCE) were collected by a Solartron 1280B electrochemical station with a solar simulator (Newport 69920, 1000 W xenon lamp), coupled with an infrared water filter (Oriel 6127) and aligned monochromator (Oriel Cornerstone 130 1/8 m). Mott-Schottky plots were measured at a frequency of 5000 Hz by the same Solartron 1280B electrochemical station in the dark.

### **Gas Collection:**

Gas generated in water splitting was collected in a home-made device. The device is made of a hollow PDMS matrix, with a chamber size of 5 ml. The chamber was filled with 1 M NaOH electrolyte solution, and Ag/AgCl reference electrode and Pt wire counter electrode were inserted into the electrolyte. All the electrode positions were sealed with insulating epoxy resin to avoid gas leakage. The composition of the produced gas was analyzed by a GC (Agilent 3000).

## Results and Discussion

Rutile TiO<sub>2</sub> nanowire arrays were prepared on a fluorine-doped tin oxide (FTO) glass substrate by a previously reported hydrothermal method <sup>29</sup> (Experimental Section). Scanning electron microscopy (SEM) image reveals that the white, homogenous film obtained on the FTO substrate consists of dense and vertically aligned nanowire arrays (Figure 5.1). These nanowires are uniform with a rectangular cross-section. The nanowire diameters are in the range of 100-200 nm and the typical nanowire lengths are 2-3  $\mu$ m.

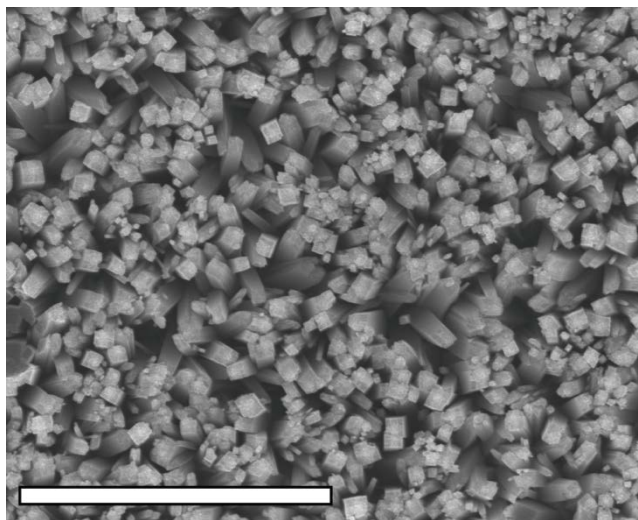


**Figure 5.1** Top view SEM image of TiO<sub>2</sub> nanowire arrays grown on FTO glass by a hydrothermal method. The scale bar is 4  $\mu$ m.

Transmission electron microscopy (TEM) analysis shows that each individual nanowire observed under TEM is indeed consisting of a bundle of smaller nanowires, which have diameters of 10-20 nm (Figure 5.2a). A lattice-resolved TEM image collected from the small nanowire reveals clear lattice fringes with

interplanar spacings of 0.32 nm and 0.29 nm, which are consistent with the  $d$ -spacings of (110) and (001) planes of rutile  $\text{TiO}_2$  (Figure 5.2b). These data further confirm the single-crystalline structure, and demonstrate that the  $\text{TiO}_2$  nanowires grow along the  $\langle 001 \rangle$  direction.

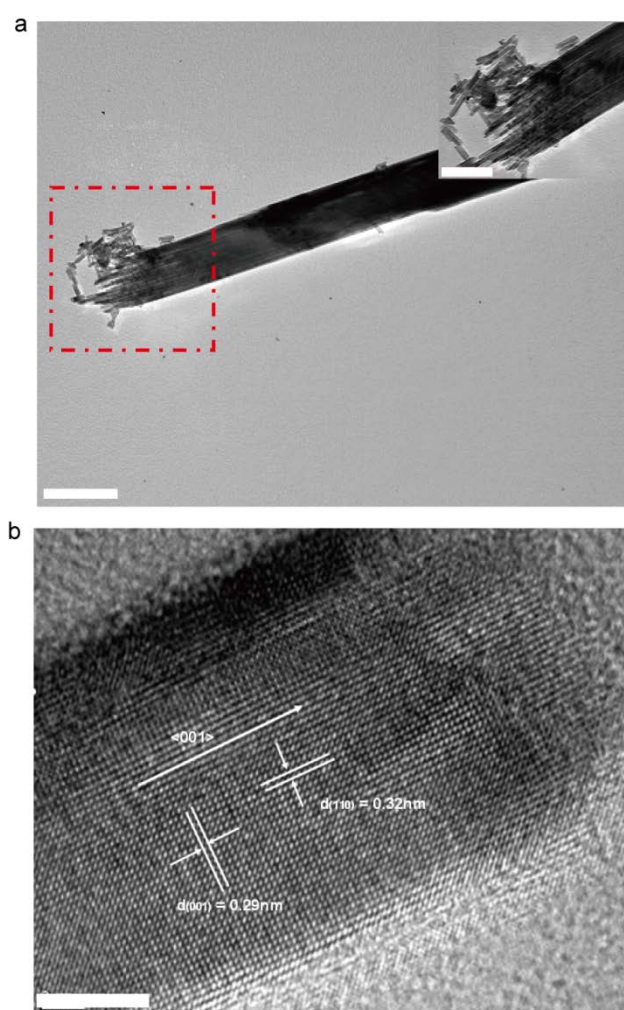


**Figure 5.2** (a) Low resolution TEM image of a single  $\text{TiO}_2$  nanowires. Scale bar is 200nm. (b) High resolution TEM image of a single  $\text{TiO}_2$  nanowires. Scale bar is 5 nm.

The as-prepared  $\text{TiO}_2$  nanowire arrays were first annealed in air at 550 °C

for 3h, followed by annealing in hydrogen atmosphere for an additional 30 min, at various temperatures in a range of 200 to 550 °C (Experimental section,). As shown in Figure 5.3, the color of the H:TiO<sub>2</sub> nanowire films depends on the hydrogen annealing temperature, it changes from white (untreated sample) to yellowish green (350 °C) and finally black (450 °C or above). The dark color suggests that the TiO<sub>2</sub> has visible light absorption as a result of hydrogen treatment. Chen *et al.* has recently reported the preparation of “black” anatase TiO<sub>2</sub> nanoparticles through hydrogenation in a 20 bar hydrogen atmosphere at 200 °C for five days<sup>30</sup>. Those TiO<sub>2</sub> nanoparticles showed visible light and near infrared absorption, with a narrowed band-gap of around 1.0 eV. The black color was ascribed to the surface disorder of TiO<sub>2</sub> nanoparticles. In this work, we studied the photoactivity of H:TiO<sub>2</sub> nanowires annealed at different temperatures for PEC water splitting as a function of wavelength, in order to understand the interplay between the light absorption and PEC performance. The details will be discussed later in the text.

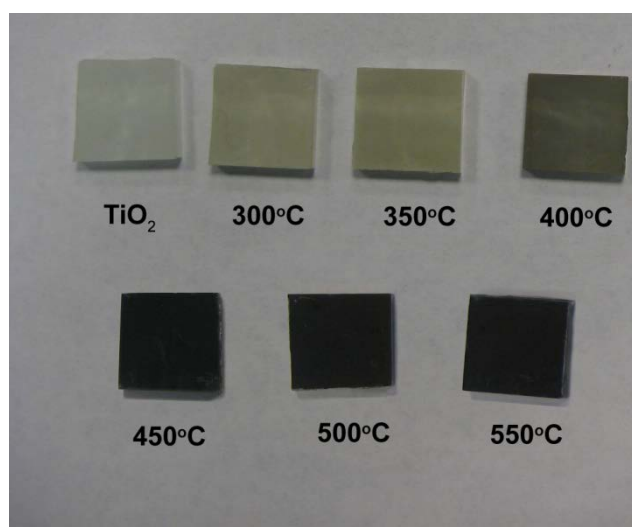


**Figure 5.3** Digital images of  $\text{TiO}_2$  nanowire arrays and hydrogen treated  $\text{TiO}_2$  nanowire arrays at different temperatures.

To determine the crystal structure and possible phase changes during hydrogen annealing, X-ray diffraction (XRD) spectra were collected from the pristine  $\text{TiO}_2$  nanowires and  $\text{H}:\text{TiO}_2$  nanowire arrays prepared at various annealing temperatures (Figure 5.4). After subtracting the diffraction peaks from FTO glass, two diffraction peaks centered at a  $2\theta$  angle of  $36.5^\circ$  and  $63.2^\circ$  were observed in every sample. These two sharp peaks can be indexed to the characteristic peaks of tetragonal rutile  $\text{TiO}_2$  (JCPDS No. 88-1175), and thus, confirmed the as-prepared nanowires are rutile  $\text{TiO}_2$ . The peak centered at  $63.2^\circ$  corresponds to the (002) diffraction which is dominant over the (101) peak providing evidence that the  $\text{TiO}_2$  nanowires are highly oriented in  $\langle 001 \rangle$  direction on the FTO substrate, which is consistent with the observed growth axis of  $\text{TiO}_2$  nanowires. As shown in Figure 5.4, there is no phase change after



hydrogenation, although the  $\text{TiO}_2$  peak intensity decreases with the increase of the annealing temperature. This can be due to the increase of defect density in  $\text{TiO}_2$  structure, which has also been observed in the recent study of hydrogenated  $\text{TiO}_2$  nanoparticles<sup>30</sup>. In addition, the diffraction peaks of FTO glass gradually disappeared and a group of new peaks (highlighted by arrows) corresponding to Sn metal are emerged when annealing temperature was higher than 450 °C. It indicates that the hydrogen treatment at high temperature damaged the FTO conducting layer by reducing  $\text{SnO}_2$  to Sn metal.

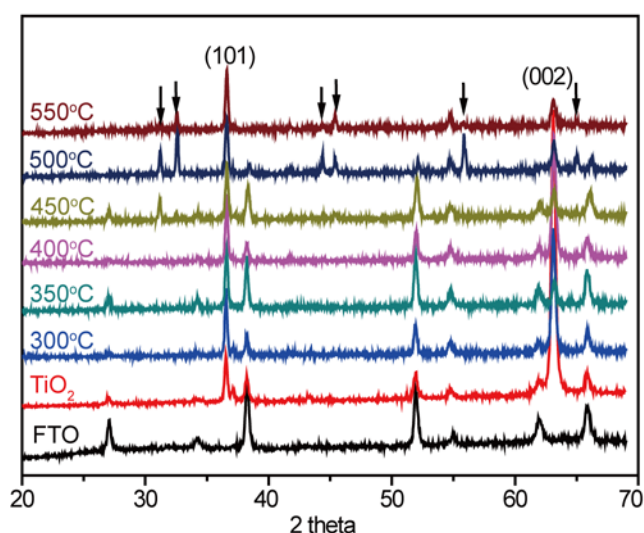


**Figure 5.4** XRD patterns of FTO glass,  $\text{TiO}_2$  nanowires and hydrogen treated  $\text{TiO}_2$  at different temperatures.

We have studied the photocurrents of colored H: $\text{TiO}_2$  nanowire-arrayed photoanode as a function of annealing temperatures, and compared to the pristine  $\text{TiO}_2$  nanowires. The nanowire samples were fabricated into photoanodes with a well defined area of 0.2-0.25 cm<sup>2</sup>. All PEC and impedance

measurements were performed in a three-electrode electrochemical system, using Ag/AgCl as reference electrode and a Pt wire as the counter electrode. Linear sweeps were collected for H:TiO<sub>2</sub> nanowires in 1 M NaOH electrolyte (pH=13.6), under simulated sunlight illumination at 100 mW/cm<sup>2</sup> from a 150 W xenon lamp coupled with an AM 1.5G filter (Figure 5.5). Figure 5.5 shows that the photocurrent densities of H:TiO<sub>2</sub> nanowires, obtained at a potential bias of 0.23 V vs. Ag/AgCl [1.23 V vs. reversible hydrogen electrode (RHE)], increase gradually with the increase of the hydrogen annealing temperature from 200 to 350 °C. The H:TiO<sub>2</sub> nanowires prepared at 350 °C yield a maximum photocurrent density of ~2.5 mA/cm<sup>2</sup> at 0.23 V vs. Ag/AgCl. This is comparable to the best reported value of ~2.8 mA/cm<sup>2</sup> for TiO<sub>2</sub> photoanodes measured by the same type of xenon lamp coupled to an AM 1.5G filter at 100 mW/cm<sup>2</sup> irradiance<sup>2</sup>. The photocurrent density of H:TiO<sub>2</sub> nanowires decreases, as the annealing temperatures was further increased above 350 °C. Beyond the possible effect of hydrogen treatment, one of the reasons is due to the increased resistance of FTO substrate from 25 Ω at 350 °C to 64 Ω at 400 °C and 165 Ω at 450 °C. This is consistent with the XRD analysis that the FTO layer degrades at temperatures of 450 °C or above.

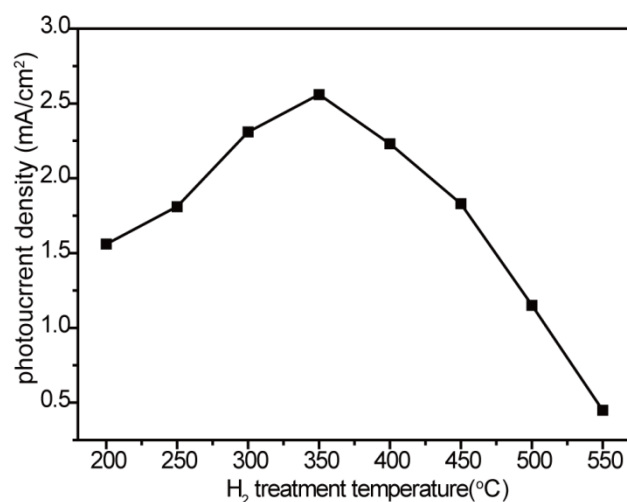


**Figure 5.5** Temperature dependent photocurrent density of hydrogen treated TiO<sub>2</sub> nanowires at 0.23 V vs. Ag/AgCl.

To investigate the effect of hydrogen treatment on the PEC performance of TiO<sub>2</sub>, Figure 5.6 compares the linear sweeps of pristine TiO<sub>2</sub> (white) with H:TiO<sub>2</sub> nanowire samples prepared at 350 °C (yellow), 400 °C (grey) and 450 °C (black), in a potential range of -1.0 to 0.5 V vs. Ag/AgCl. By analyzing these data, we reach two important conclusions. First, the photocurrents of H:TiO<sub>2</sub> nanowire samples are at least two times higher than the pristine TiO<sub>2</sub> nanowires in the entire potential windows we studied. It confirms that hydrogen treatment is a simple and effective method in enhancing the PEC performance of TiO<sub>2</sub>. Second, the photocurrent density of pristine TiO<sub>2</sub> sample increases gradually with the applied potential, and reaches a saturated current of 0.6 mA/cm<sup>2</sup> at 0 V vs. Ag/AgCl (Figure 5.6). In contrast, all H:TiO<sub>2</sub> samples show a drastic increase in photocurrent density at a onset potential of -0.9 V vs.

Ag/AgCl, and the photocurrent saturated at a substantially lower potential of -0.4 V vs. Ag/AgCl (0.6 V vs. RHE). The negative shift of saturation potential indicates that the charge separation and transportation in the H:TiO<sub>2</sub> samples are more efficient, compared to the pristine TiO<sub>2</sub> nanowires.

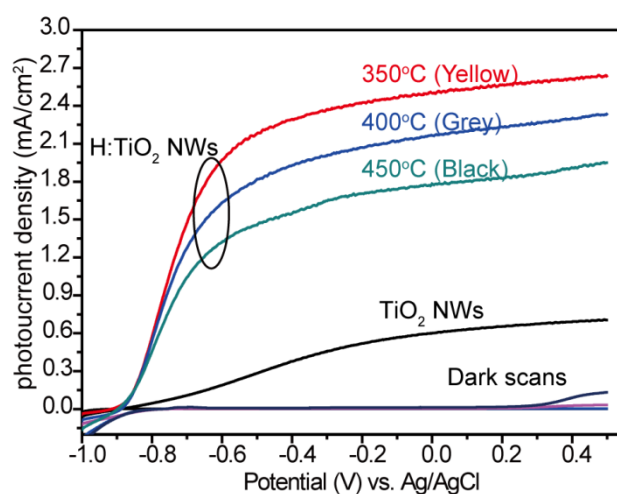


**Figure 5.6** I-V curves of air annealed TiO<sub>2</sub> NWs and hydrogen treated TiO<sub>2</sub> NWs at 350, 400 and 450 °C.

Achieving a low photocurrent onset and saturation potential is extremely important because it reduces the applied bias required to achieve the maximum photocurrent, and thus, increases the overall efficiency of PEC hydrogen generation. The STH efficiencies ( $\eta$ ) of nanowire-arrayed photoanodes were calculated using the equation:

$$\eta = I(1.23 - V)/J_{\text{light}}$$

where  $V$  is the applied bias vs. RHE;  $I$  is the photocurrent density at the measured bias; and  $J_{\text{light}}$  is the irradiance intensity of 100 mW/cm<sup>2</sup> (AM 1.5G).

We plot the calculated STH efficiency as a function of the applied bias in Figure 5/7. The pristine  $\text{TiO}_2$  sample exhibits an optimal conversion efficiency of 0.24 % at -0.33 V vs. Ag/AgCl. Significantly, the yellow  $\text{H}:\text{TiO}_2$  (350 °C) sample achieves the highest efficiency of ~1.63 % at a very low bias of -0.6 V vs. Ag/AgCl (0.4 V vs. RHE). To our knowledge, this is the best STH efficiency achieved by  $\text{TiO}_2$  materials. Likewise, the  $\text{H}:\text{TiO}_2$  samples annealed at 400 and 450 °C exhibit the optimal efficiency of ~1.35 and 1.08 % at a similar applied bias. Hydrogen treatment substantially enhances the photoconversion efficiency of  $\text{TiO}_2$  nanowires by improving the maximum photocurrent and reducing the current saturation potential.

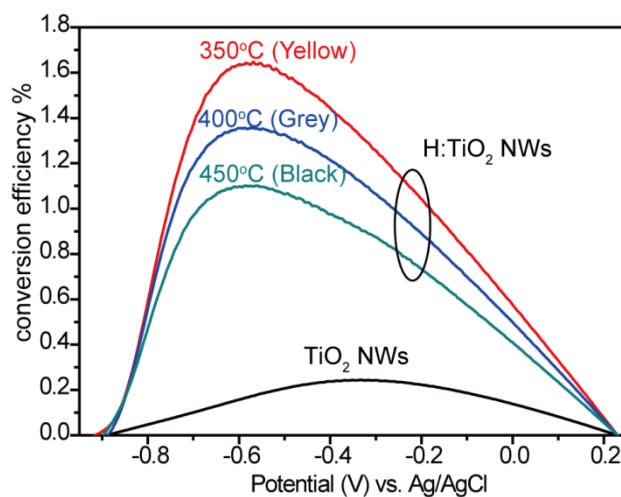


**Figure 5.7** Solar to hydrogen conversion efficiency of  $\text{TiO}_2$  and hydrogen treated  $\text{TiO}_2$  at 350, 400 and 450 °C.

Furthermore, we have investigated the hydrogen generation and the stability of  $\text{TiO}_2$  nanowire-arrayed photoanodes. Under light illumination ( $100 \text{ mW/cm}^2$ ),

we observed gas production at both photoanode and Pt cathode. A home-made device was fabricated for gas collection shown in figure 5.8. The light irradiation is shined on the backside of TiO<sub>2</sub>/FTO glass.

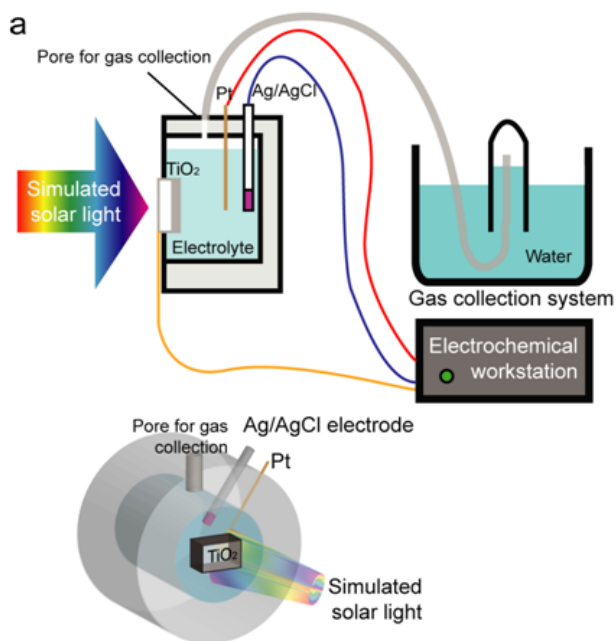


**Figure 5.8** the schematic diagram of the home built gas collection system.

Figure 5.9a shows the collected gas volume as a function of time. We replaced the gas collection device (1 mL syringe) every 2 hours under light illumination, which is counted as one gas collection cycle. After four cycles, we kept the device in the dark for 12 hours, and restarted the gas collection for an additional four cycles. Importantly, the gas production shows a linear relation with illumination time in the entire 16 hours measurement, suggesting gas production is persistent for continuous operation. In addition, Figure 5.9b shows the

measured photocurrents for the H:TiO<sub>2</sub> nanowire photoanode during each gas production cycles are nearly the same, supporting that the H:TiO<sub>2</sub> nanowires are very stable in the process. GC analysis demonstrates the collected gas is composed of H<sub>2</sub> and O<sub>2</sub>, however, we were not able to get a quantitative H<sub>2</sub>/O<sub>2</sub> ratio due to the instrumental limitation. The gas production rate is calculated to be ~0.47 ml/h at an applied bias of -0.6 V vs. Ag/AgCl.

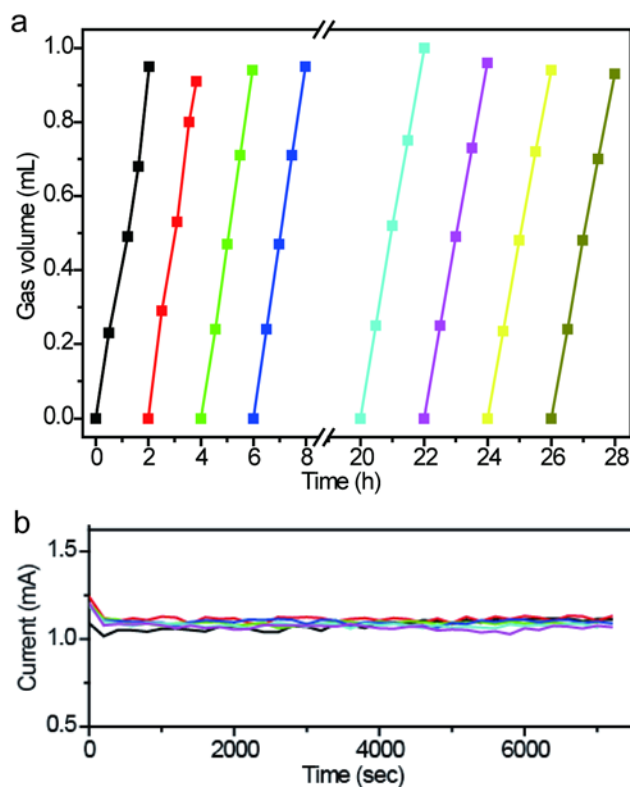


**Figure 5.9** (a) Gas production profile of H-TiO<sub>2</sub> nanowires. (b) The corresponding photocurrents observed during gas production.

Due to design of gas collection device, the nanowire samples were illuminated from the backside (Figure 5.10). As a result, a significant portion of UV light was absorbed by the FTO glass substrate, and we observed the halved

photocurrent density compared to the front side illumination. Based on the photocurrent obtained from the back side illumination, the theoretical gas production rate is calculated to be  $\sim 0.67$  ml/h. It is lower than the experimental data due to the back reaction of oxygen reduction on Pt electrode and possible gas leakage, which can be solved by a better design of gas collection device.

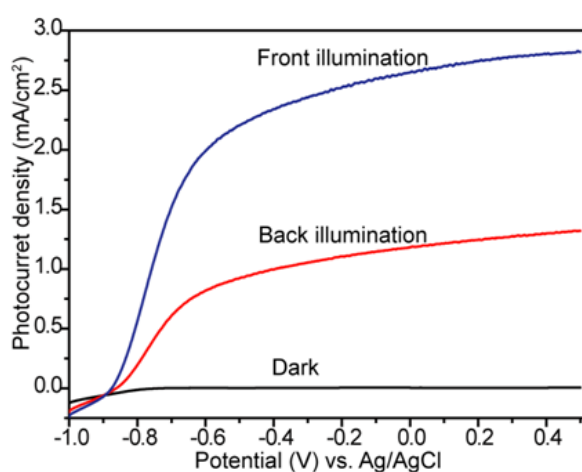


**Figure 5.10** I-V curves of H-TiO<sub>2</sub> NWs with front and back side light illumination.

To understand the interplay between the photoactivity and the light absorption of H-TiO<sub>2</sub> nanowires prepared at various annealing temperatures (different colors), we have quantitatively investigated their photoactivity as a function of light wavelength. In comparison to photocurrent density obtained under white light illumination, incident-photon-to-current-conversion efficiency (IPCE) is a better parameter to characterize the photoconversion efficiency of different photoanodes because it is independent from the light sources and filters



used in the measurement <sup>20</sup>. IPCE measurements were performed on pristine TiO<sub>2</sub> and H:TiO<sub>2</sub> nanowire-arrayed photoanodes at -0.6 V vs. Ag/AgCl (Figure 5.11a). IPCE can be expressed by the equation <sup>9</sup>:

$$\text{IPCE} = (1240 \times I) / (\lambda \times J_{\text{light}}),$$

where  $I$  is the measured photocurrent density obtained under a specific wavelength light illumination,  $\lambda$  is the wavelength of incident light, and  $J_{\text{light}}$  is the measured irradiance at a specific wavelength. In comparison to pristine TiO<sub>2</sub> nanowires, all H:TiO<sub>2</sub> nanowires exhibit significantly enhanced photoactivity over the entire UV region. Particularly, the H:TiO<sub>2</sub> nanowire sample annealed at 350 °C has the IPCE values uniformly higher than 95 % in the wavelength range from 300 to 370 nm. It indicates that the UV light was effectively used for PEC water splitting, in which the separation and transportation of photoexcited charge carriers are very efficient in the H:TiO<sub>2</sub> nanowires. The IPCE values decrease gradually from ~95 % at 370 nm to ~1 % at 420 nm, which is consistent with the band-gap energy (3.0 eV) of rutile TiO<sub>2</sub>. Significantly, we observed small photoactivity in the visible light region for the H:TiO<sub>2</sub> nanowire samples, whereas the IPCE values increase slowly from almost zero at 440 nm to 0.7 % at 650 nm, in contrast to the negligible IPCE values for pristine TiO<sub>2</sub> in the same region (Figure 5.11a, inset). Although the IPCE values are much lower than that in the UV region, it is a direct evidence of showing visible light photoresponse of H:TiO<sub>2</sub> nanowires as a result of hydrogen treatment. These

results confirm that the enhanced photocurrent in H:TiO<sub>2</sub> nanowires is mainly attributed to the improved IPCE in the UV region, while the newly developed visible light absorption also made a small contribution.

Given that the irradiance spectrum may vary from different light sources (e.g, lamp lifetime and power) and filters being used in the measurements, it is challenging to compare the calculated STH efficiency is based on the measured photocurrent densities in literature (or in different labs)<sup>20</sup>. In this regard, IPCE that independent from light source is a better parameter for comparison. We have calculated the STH efficiency of H:TiO<sub>2</sub> nanowires by integrating their IPCE spectra with a standard AM 1.5G solar spectrum (ASTM G-173-03), using the following equation:

$$\eta\% = \int_{300}^{650} \frac{1}{1240} \lambda(1.23 - V_{bias}) IPCE(\lambda) E(\lambda) d(\lambda)$$

where  $E(\lambda)$  is the solar irradiance at a specific wavelength ( $\lambda$ );  $V_{bias}$  is applied bias vs. RHE, IPCE is the obtained photoresponse profile of H:TiO<sub>2</sub> nanowire sample at a specific wavelength ( $\lambda$ ) at -0.6 V vs. Ag/AgCl. Figure 5.11b shows the simulated STH conversion efficiencies as a function of wavelength in the range from 300 to 650 nm. The pristine TiO<sub>2</sub> and H:TiO<sub>2</sub> nanowire samples prepared at 350, 400 and 450 °C achieve the optimal STH efficiencies of ~0.1 %, 1.1 %, 0.89 %, and 0.68 % at -0.6 V vs. Ag/AgCl, respectively. Between 420 to 650 nm, there are very slight increase in efficiencies for the H:TiO<sub>2</sub> nanowire

samples due to the relatively weak photoresponse in the visible region. The calculated STH conversion efficiencies are slightly lower than the values (1.63 % for the H:TiO<sub>2</sub> nanowires annealed at 350 °C) obtained from the measured photocurrent density at the same potential, due to the discrepancy between the irradiance spectrum and the standard solar spectrum. Significantly, the optimal conversion efficiency of 1.1% is still the best value for TiO<sub>2</sub> materials under the standard AM 1.5G solar light illumination.

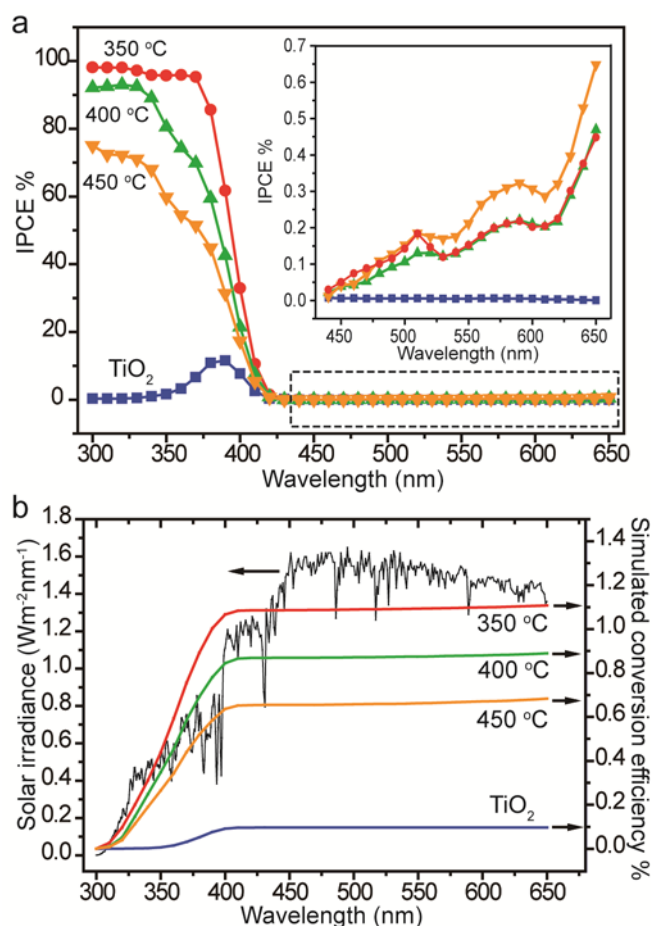


**Figure 5.11** (a) IPCE spectra of TiO<sub>2</sub> and hydrogen treated TiO<sub>2</sub>. (b) Calculated solar to hydrogen conversion efficiency by integrating IPCE with standard solar spectrum.

In order to elucidate the effect of hydrogen treatment in enhancing the photoactivity in both the UV and visible regions, we have further carried out X-ray photoelectron spectroscopy (XPS) and electrochemical impedance measurements. Specifically, XPS was performed to investigate the change of surface bonding of TiO<sub>2</sub> nanowires induced by hydrogen treatment, as well as the electronic valence band position of H:TiO<sub>2</sub> nanowires. As shown in Figure 5.12 Supporting Information, XPS survey spectra collected from pristine TiO<sub>2</sub> (white) and H:TiO<sub>2</sub> (black) nanowire arrays treated at 450 °C are very similar. In addition to the Ti and O peaks that are expected for TiO<sub>2</sub>, carbon signals were observed in both samples, believed to be included during sample preparation and subsequent handling. It proves that hydrogen treatment is a clean process that does not introduces impurities into the TiO<sub>2</sub> structure, and more importantly, the H:TiO<sub>2</sub> nanowires are not doped with other elements.

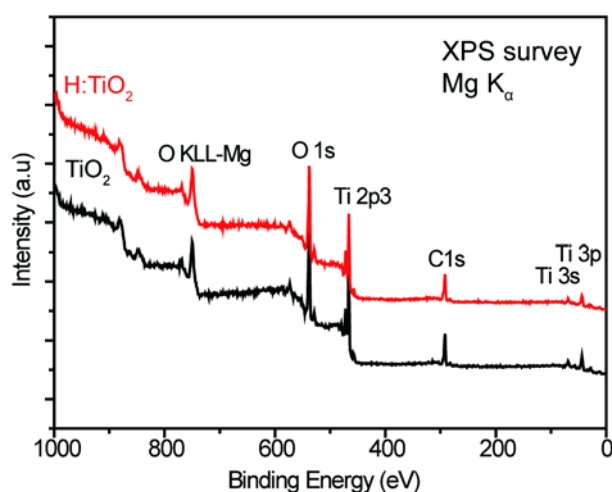


**Figure 5.12** XPS surve of TiO<sub>2</sub> nanowires and hydrogen treated TiO<sub>2</sub> nanowires.

Figure 5.13a and 5.13b show the high-resolution Ti 2p and O 1s spectra of the TiO<sub>2</sub> and H:TiO<sub>2</sub> nanowires. Their Ti 2p XPS spectra are identical, with Ti 2p<sub>3/2</sub> and 2p<sub>1/2</sub> peaks centered at binding energies of 458.8 and 464.6 eV, which are consistent with the typical values for TiO<sub>2</sub><sup>30, 31</sup>. The H:TiO<sub>2</sub> nanowires exhibits a broader O 1s peak (530.4 eV) with additional shoulder at higher binding energy, compared to the pristine TiO<sub>2</sub> nanowires. This broad peak can be deconvoluted into two peaks centered at 530.2 and 532.0 eV. The 532.0 peak is attributed to Ti-OH, which has been reported to be located at ~1.5-1.8 eV higher binding energy corresponding to the O 1s of TiO<sub>2</sub><sup>31, 32</sup>. The data confirm the formation of hydroxyl group on TiO<sub>2</sub> surface after hydrogen treatment.

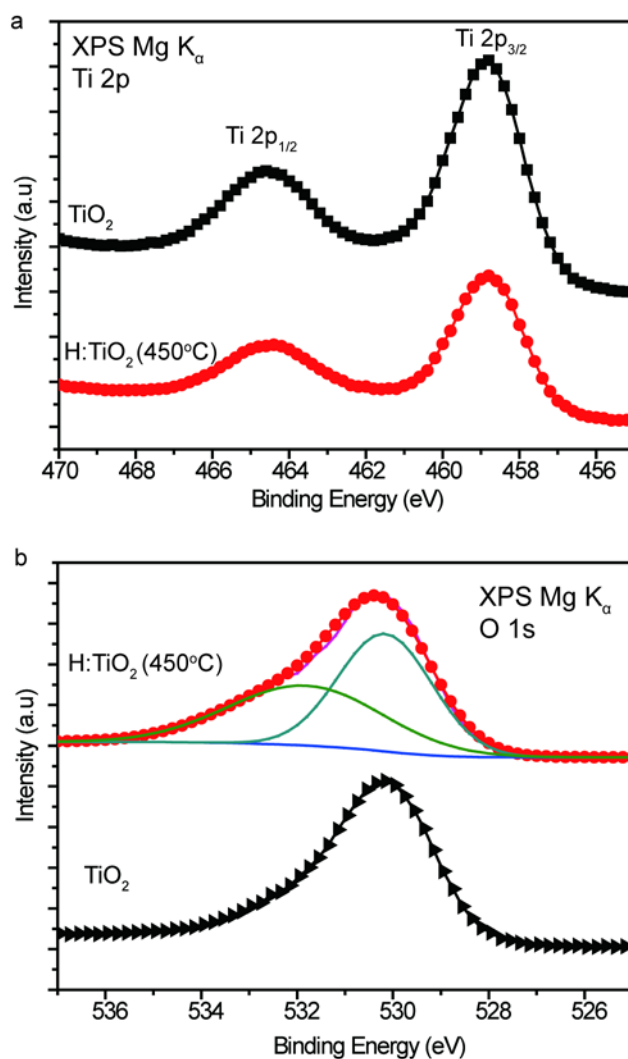


**Figure 5.13** XPS Ti 2p (a) and O 1s (b) spectra of  $\text{TiO}_2$  and hydrogen treated  $\text{TiO}_2$ .

Finally, the valence band spectra of both the  $\text{TiO}_2$  and  $\text{H:TiO}_2$  nanowires were measured to investigate the effect hydrogen treatment on the electronic band structure of  $\text{TiO}_2$  (Figure 5.14a). For the hydrogenated  $\text{TiO}_2$  nanoparticles reported by Chen et al., the black color was attributed to a substantial shift (2.18 eV) of valence band position, as a result of surface disorder<sup>30</sup>. Surprisingly, our work reveal that the valence band spectra of  $\text{TiO}_2$  and  $\text{H:TiO}_2$  nanowires are

very similar. Their valence band maxima are estimated by linear extrapolation of the peaks to the baselines, which derives a band edge position of  $\sim 1.2$  eV below the Fermi energy in both cases. In fact, H:TiO<sub>2</sub> nanowires annealed at different temperatures (Figure 5.14b) exhibit almost the same valence band maximum, which confirms hydrogen treatment has a negligible effect on the valence band position at the TiO<sub>2</sub> nanowire surface.

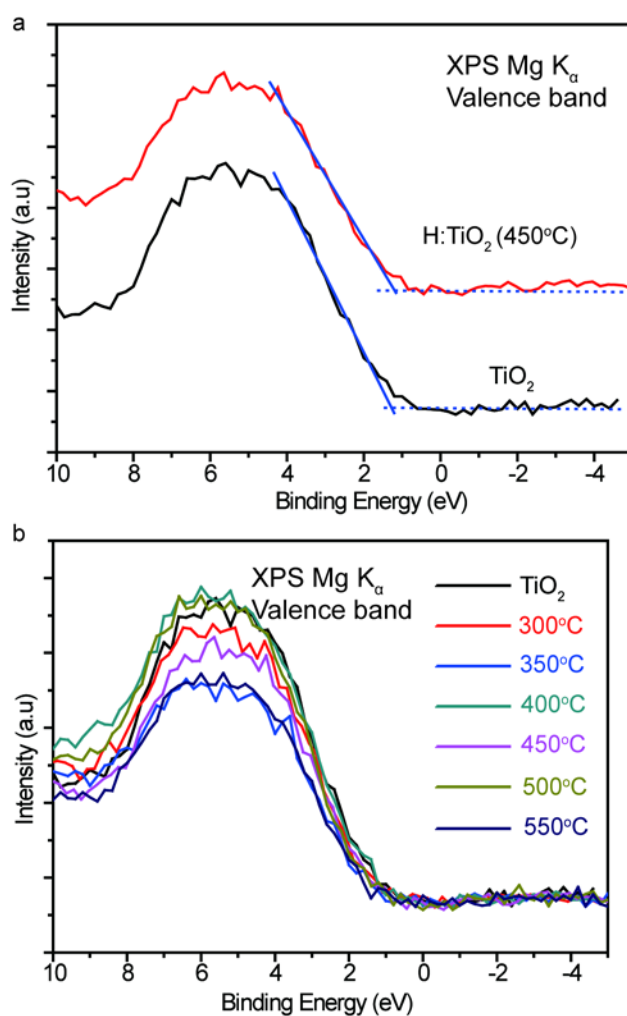


**Figure 5.14** XPS valence band spectra of TiO<sub>2</sub> and hydrogen treated TiO<sub>2</sub> samples.

Given that there is no shift of the valence band edge, the dark color of H:TiO<sub>2</sub> nanowires is attributed to the formation of impurity/defect states in the band-gap of TiO<sub>2</sub> during hydrogen treatment. XPS data confirmed that the H:TiO<sub>2</sub> samples are not doped with other element, so the possible defect states are attributed to the formation of oxygen vacancies and surface hydroxyl groups on TiO<sub>2</sub>. The O 2p energy levels for Ti-OH-Ti and Ti-OH were reported to be located at 2.6 and 0.7 eV below the valence band of rutile TiO<sub>2</sub>, respectively. It has been reported that these states are energetically stable and cannot be oxidized by the valence band holes via electron-transfer<sup>33, 34</sup>. This is supported by the high stability of H:TiO<sub>2</sub> nanowire photoanodes. The presence of these Ti-OH energy states that below the valence band of TiO<sub>2</sub> should not lead to visible light absorption. We believe oxygen vacancies in the TiO<sub>2</sub> structure created during hydrogenation, play a critical role in the visible light absorption and thereby the dark color of TiO<sub>2</sub>. Energy levels of oxygen vacancies have been reported to be about 0.75 eV and 1.18 eV below the conduction band of hydrogen reduced rutile TiO<sub>2</sub> single crystal plates<sup>24, 27</sup>. A simplified energy diagram of H:TiO<sub>2</sub> nanowires [referenced to normal hydrogen electrode (NHE)] is constructed based on the XPS valence band spectrum as well as the reported rutile TiO<sub>2</sub> band-gap and the energy levels of oxygen vacancies and surface hydroxyl group (Figure 5.15). The strong UV absorption of TiO<sub>2</sub> is due to the electronic transition from the valence band to the conduction band. High-temperature hydrogen treatment



creates oxygen vacancies in the band-gap of TiO<sub>2</sub> nanowires. The visible and near IR light absorption can be attributed to the transitions from the TiO<sub>2</sub> valence band to the oxygen vacancy levels or from the oxygen vacancies to the TiO<sub>2</sub> conduction band<sup>24, 27, 28</sup>. However, the photoexcited electrons located at oxygen vacancies are not involved in water splitting because their energy levels are well below the H<sub>2</sub>O/H<sub>2</sub> reduction potential. Additionally, the electronic transition between the localized oxygen vacancy states and the delocalized conduction band is not expected to be significant because the coupling between the localized and the delocalized energy states should be weak. It explains the observation of weak photoactivity in the visible region for H:TiO<sub>2</sub> nanowires, and the negligible contribution to the photocurrent.

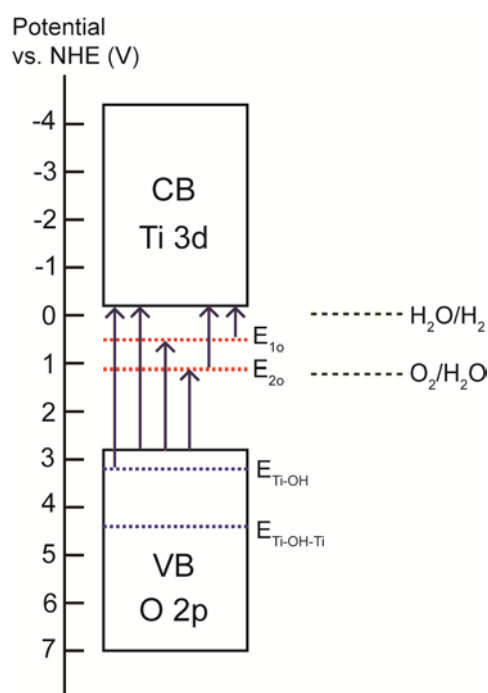


**Figure 5.15** Band structure of hydrogen treated TiO<sub>2</sub> and possible transitions.

Additionally, we have conducted electrochemical impedance measurements on the pristine TiO<sub>2</sub> and H:TiO<sub>2</sub> nanowire sample annealed at 350 °C at a frequency of 5 kHz in the dark, to investigate the influence of hydrogen treatment on the TiO<sub>2</sub> electronic properties. All TiO<sub>2</sub> nanowire samples show a positive slope in the Mott-Schottky plots, as expected for n-type semiconductor (Figure 5.16). Importantly, the H:TiO<sub>2</sub> nanowire samples show substantially smaller slopes of Mott-Schottky plot compared to the TiO<sub>2</sub> sample, suggesting an increase of donor densities. The donor density increases with the hydrogen treatment temperature (Figure 5.16, inset). Carrier densities of these nanowires were calculated from the slopes of Mott-Schottky plots using the equation:

$$N_d = (2/e_0\epsilon\epsilon_0)[d(1/C^2)/dV]^{-1},$$

where  $e_0$  is the electron charge,  $\epsilon$  the dielectric constant of TiO<sub>2</sub> ( $\epsilon=170$ )<sup>35</sup>,  $\epsilon_0$  the permittivity of vacuum,  $N_d$  the donor density, and  $V$  the applied bias at the electrode. The calculated electron densities of the pristine TiO<sub>2</sub> and H:TiO<sub>2</sub> (350 °C) nanowires were  $5.3 \times 10^{18}$  and  $2.1 \times 10^{22} \text{ cm}^{-3}$ , respectively. Although the fact that Mott-Schottky is derived from a flat electrode model and may have errors in determining the absolute value of donor density, hydrogen treatment leads to a significant enhancement of carrier density in TiO<sub>2</sub> is evident through a qualitatively comparison of the slopes of Mott-Schottky plots. The enhanced

donor density is due to the increased oxygen vacancies, which are known to be an electron donor for  $\text{TiO}_2$ <sup>26</sup>. The increased donor density improves the charge transport in  $\text{TiO}_2$ , as well as the electron transfer at the interface between the semiconductor and the FTO substrate. Moreover, the increased electron density is expected to shift the Fermi level of  $\text{TiO}_2$  towards the conduction band<sup>24</sup>. The upward shift of the Fermi level facilitates the charge separation at the semiconductor/electrolyte interface, by increasing the degree of band-bending at the  $\text{TiO}_2$  surface. The enhanced charge separation and transportation are believed to be the major reasons for the observed IPCE enhancement in the UV region.

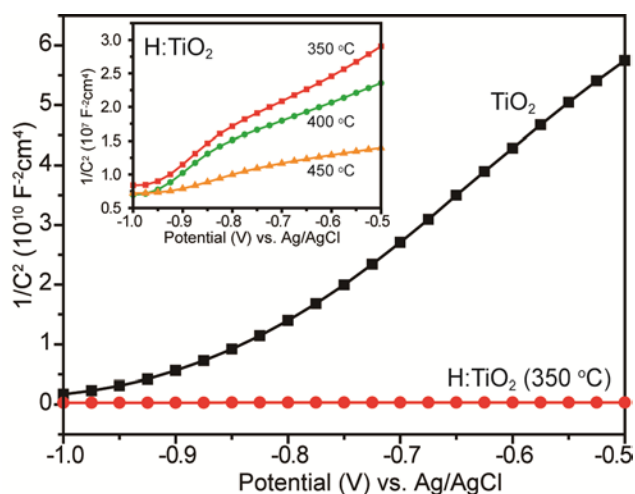


**Figure 5.16** Mott-schottky curves of  $\text{TiO}_2$  and hydrogen treated  $\text{TiO}_2$  samples.

Finally, to confirm the hydrogen treatment is a general strategy for enhancing the performance of  $\text{TiO}_2$  for water splitting, we have also conducted PEC studies

on the pristine and hydrogen-treated anatase  $\text{TiO}_2$  nanotubes. The uniform  $\text{TiO}_2$  nanotube arrays with tube diameter of 150 nm were fabricated by a reported electrochemical anodization method <sup>5</sup> (Figure 5.17a). XRD data confirm the nanotube arrays are anatase phase  $\text{TiO}_2$  (Figure 5.17b), and there is no phase change after hydrogenation at 350 and 450 °C.

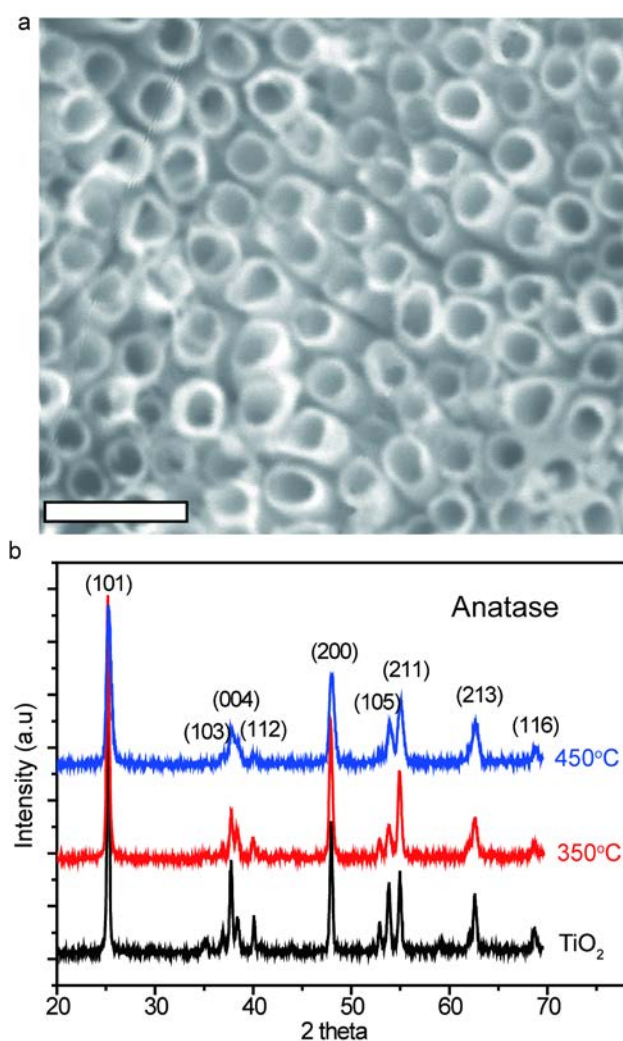


**Figure 5.17** (a) SEM image of  $\text{TiO}_2$  nanotube arrays fabricated by electrochemical anodization. Scale bar is 600nm. (b) XRD patterns of  $\text{TiO}_2$  and hydrogen treated  $\text{TiO}_2$  nanotubes.

Significantly, we observed a two fold enhanced photocurrent density for  $\text{TiO}_2$  nanotubes after hydrogen treatment, as it has demonstrated for the rutile  $\text{H}:\text{TiO}_2$  nanowires in figure 5.18. IPCE measurements also confirm that the enhanced photocurrent of  $\text{H}:\text{TiO}_2$  nanotubes is due to the improved photoactivity in the UV region. The weak photoactivity of pristine anatase  $\text{TiO}_2$  nanotube in the 400-420 nm is believed due to the fluorine doping that unintentionally incorporated during anodization synthesis in  $\text{NH}_4\text{F}$ , which has been reported previously<sup>36</sup>.

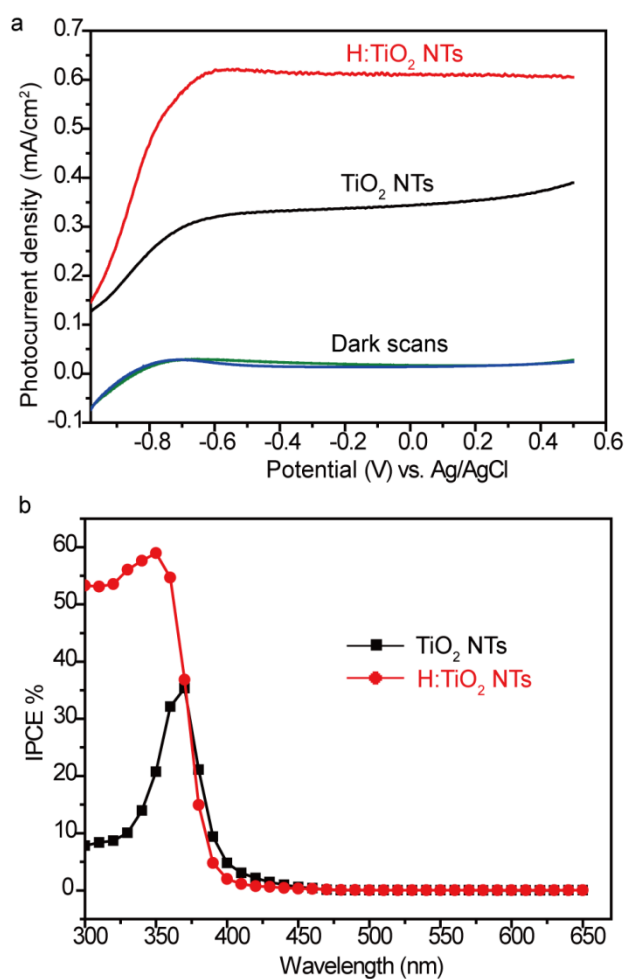


**Figure 5.18** (a) I-V and (b) IPCE curves of TiO<sub>2</sub> and hydrogen treated TiO<sub>2</sub> nanotubes.

## Conclusion

In summary, our work has demonstrated that hydrogen treatment can be used as a general strategy to fundamentally improve the performance of TiO<sub>2</sub> materials as photoanodes for PEC water splitting. H:TiO<sub>2</sub> nanomaterials (rutile nanowire and anatase nanotubes) yield substantially enhanced photocurrent densities, and the photocurrents saturated at a very low applied bias of -0.4 V vs. Ag/AgCl (0.6 vs. RHE). IPCE analyses confirm that the photocurrent enhancement is mainly due to the greatly improved photoactivity in UV region, as a result of increased donor density due to the formation of oxygen vacancies in H:TiO<sub>2</sub> samples. By integrating the IPCE spectra with a standard AM 1.5G solar spectrum, the H:TiO<sub>2</sub> nanowires hydrogen annealed at 350 °C exhibits a STH efficiency of 1.1 %, which is the best value for TiO<sub>2</sub> materials. More importantly, the capability of making highly photoactive H:TiO<sub>2</sub> nanowires opens up new opportunities in various areas, including PEC water splitting, dye-sensitized solar cells and photocatalysis. By replacing TiO<sub>2</sub> with new H:TiO<sub>2</sub> materials, the efficiencies of these processes and/or devices are expected to be enhanced.

## References

1. Fujishima, A.; Honda, K. *Nature* **1972**, 238, (5358), 37-+.
2. Liu, M. Z.; Snapp, N. D.; Park, H. *Chemical Science* **2011**, 2, (1), 80-87.
3. Park, J. H.; Kim, S.; Bard, A. J. *Nano Letters* **2006**, 6, (1), 24-28.
4. Hwang, Y. J.; Boukai, A.; Yang, P. D. *Nano Letters* **2009**, 9, (1), 410-415.
5. Mor, G. K.; Shankar, K.; Paulose, M.; Varghese, O. K.; Grimes, C. A. *Nano Letters* **2005**, 5, (1), 191-195.
6. Feng, X. J.; Shankar, K.; Varghese, O. K.; Paulose, M.; Latempa, T. J.; Grimes, C. A. *Nano Letters* **2008**, 8, (11), 3781-3786.
7. Lin, Y. J.; Zhou, S.; Liu, X. H.; Sheehan, S. W.; Wang, D. W. *J. Am. Chem. Soc.* **2009**, 131, (8), 2772-2773.
8. Khan, S. U. M.; Al-Shahry, M.; Ingler, W. B. *Science* **2002**, 297, (5590), 2243-2245.
9. Bak, T.; Nowotny, J.; Rekas, M.; Sorrell, C. C. *International Journal of Hydrogen Energy* **2002**, 27, 991-1022.
10. Ni, M.; Leung, M. K. H.; Leung, D. Y. C.; Sumathy, K. *Renewable and sustainable energy reviews* **2007**, 11, 401-405.
11. Li, Y.; Zhang, J. Z. *Laser & Photonics Reviews* **2010**, 4, (4), 517-528.
12. Walter, M. G.; Warren, E. L.; McKone, J. R.; Boettcher, S. W.; Mi, Q. X.; Santori, E. A.; Lewis, N. S. *Chemical Reviews* **2010**, 110, (11), 6446-6473.
13. Kongkanand, A.; Tvrđy, K.; Takechi, K.; Kuno, M.; Kamat, P. V. *Journal of*

*the American Chemical Society* **2008**, 130, (12), 4007-4015.

14. Yang, X. Y.; Wolcott, A.; Wang, G. M.; Sobo, A.; Fitzmorris, R. C.; Qian, F.; Zhang, J. Z.; Li, Y. *Nano Letters* **2009**, 9, (6), 2331-2336.

15. Mor, G. K.; Varghese, O. K.; Wilke, R. H. T.; Sharma, S.; Shankar, K.; Latempa, T. J.; Choi, K. S.; Grimes, C. A. *Nano Letters* **2008**, 8, (7), 1906-1911.

16. Mor, G. K.; Prakasam, H. E.; Varghese, O. K.; Shankar, K.; Grimes, C. A. *Nano Letters* **2007**, 7, (8), 2356-2364.

17. Leschkies, K. S.; Divakar, R.; Basu, J.; Enache-Pommer, E.; Boercker, J. E.; Carter, C. B.; Kortshagen, U. R.; Norris, D. J.; Aydil, E. S. *Nano Letters* **2007**, 7, (6), 1793-1798.

18. Wang, G. M.; Yang, X. Y.; Qian, F.; Zhang, J. Z.; Li, Y. *Nano Letters* **2010**, 10, (3), 1088-1092.

19. Hensel, J.; Wang, G. M.; Li, Y.; Zhang, J. Z. *Nano Letters* **2010**, 10, (2), 478-483.

20. Murphy, A. B.; Barnes, P. R. F.; Randeniya, L. K.; Plumb, I. C.; Grey, I. E.; Horne, M. D.; Glasscock, J. A. *International Journal of Hydrogen Energy* **2006**, 31, (14), 1999-2017.

21. Burda, C.; Lou, Y.; Chen, X.; Samia, A. C. S.; Stout, J.; Gole, J. L. *Nano Lett.* **2003**, 3, (8), 1049-1051.

22. Asahi, R.; Morikawa, T.; Ohwaki, T.; Aoki, K.; Taga, Y. *Science* **2001**, 293, (5528), 269-271.



23. Di Valentin, C.; Pacchioni, G.; Selloni, A. *Chemistry of Materials* **2005**, 17, (26), 6656-6665.
24. Cronmeyer, D. C. *Physical Review* **1959**, 113, (5), 1222-1226.
25. Fabregat-Santiago, F.; Barea, E. M.; Bisquert, J.; Mor, G. K.; Shankar, K.; Grimes, C. A. *J. Am. Chem. Soc.* **2008**, 130, 11312-11316.
26. Janotti, A.; Varley, J. B.; Rinke, P.; Umezawa, N.; Kresse, G.; Van de Walle, C. G. *Phys. Rev. B* **2010**, 81, 085212.
27. Cronmeyer, D. C.; Gilleo, M. A. *Physical Review* **1951**, 82, (6), 975-976.
28. Kim, W. T.; Kim, C. D.; Choi, Q. W. *Phys. Rev. B* **1984**, 30, 3625-3628.
29. Liu, B.; Aydil, E. S. *Journal of the American Chemical Society* **2009**, 131, (11), 3985-3990.
30. Chen, X.; Liu, L.; Yu, P. Y.; Mao, S. S. *Science* **2011**, 331, (6018), 746-750.
31. Lazarus, M. S.; Sham, T. K. *Chemical Physics Letters* **1982**, 92, (6), 670-673.
32. McCafferty, E.; Wightman, J. P. *Surface and Interface Analysis* **1998**, 26, (8), 549-564.
33. Nakamura, R.; Nakato, Y. *Journal of the American Chemical Society* **2004**, 126, (4), 1290-1298.
34. Imanishi, A.; Okamura, T.; Ohashi, N.; Nakamura, R.; Nakato, Y. *Journal of the American Chemical Society* **2007**, 129, (37), 11569-11578.
35. Parker, R. A. *Phys. Rev.* **1961**, 124, 1719-1722.

36. Park, H.; Choi, W. *J. Phys. Chem. B* **2004**, 108, (13), 4086-4093.

## Chapter 6

### Hydrogen Treated WO<sub>3</sub> Nanoflakes for Enhanced Photoactivity and Photostability for PEC Water Splitting

#### Abstract

Here we report that photostability and photoactivity of WO<sub>3</sub> for water oxidation can be simultaneously enhanced by controlled introduction of oxygen vacancies into WO<sub>3</sub> in hydrogen atmosphere at elevated temperatures. In comparison to pristine WO<sub>3</sub>, the hydrogen-treated WO<sub>3</sub> nanoflakes show an order of magnitude enhanced photocurrent, and more importantly, exhibit extraordinary stability for water oxidation without photoactivity loss for at least seven hours. This work constitutes the first example where WO<sub>3</sub> can be stabilized for water oxidation in neutral medium without the need of oxygen evolution catalysts. The demonstration of electrochemically stable WO<sub>3</sub> could open up new opportunities for WO<sub>3</sub> based photoelectrochemical and photocatalytic applications.

#### Introduction

Photoelectrochemical (PEC) water splitting using semiconductor photoelectrodes is a promising and environmentally friendly method to produce

solar hydrogen<sup>1-11</sup>. Among semiconductors, WO<sub>3</sub> has attracted extensive attention due to its relatively small bandgap ( $E_g = 2.6$  eV), which could theoretically utilize ~12 % solar light<sup>12-18</sup>. For example, Su *et al.* recently reported a solvothermal method of fabricating WO<sub>3</sub> nanowire and nanoflake arrays, and their implementation as photoanodes for PEC water oxidation. They found that material morphology plays an important role in determining PEC performance of WO<sub>3</sub><sup>13</sup>. Moreover, Liu *et al.* demonstrated a novel WO<sub>3</sub>/TiSi<sub>2</sub> nanonet structure for PEC water splitting. This core-shell nanostructure reduces the diffusion length for minority carriers and achieved a maximum photo-conversion efficiency of 1.1 % at 0.8 V vs. RHE<sup>16</sup>. Despite the significant progress in improving the photoactivity of WO<sub>3</sub>, it is known to be thermodynamically unstable in electrolyte solution with pH > 4 due to OH<sup>-</sup> induced chemical dissolution (  $WO_3(s) + OH^{-1} \rightarrow WO_4^{2-}(aq) + H^+$  )<sup>19, 20</sup>. Additionally, photocorrosion of WO<sub>3</sub> were observed in neutral pH solution and even in acidic solution<sup>16, 17, 21-23</sup>, induced by the peroxo-species, intermediates created during water oxidation<sup>24</sup>. Although the formation of peroxo-species ( $E^0 = 1.78$  V) is energetically less favorable than photo-oxidation of water to O<sub>2</sub> ( $E^0 = 1.23$  V), it is kinetically competitive with O<sub>2</sub> production that needs to overcome large overpotential<sup>23</sup>. Therefore, the instability has been one of the major hurdles for the application of WO<sub>3</sub> for PEC water oxidation.

In spite of the importance of the stability issues, most research efforts have

been focused on increasing the photoactivity of  $\text{WO}_3$ , for example, through material structural design<sup>17, 18</sup>, doping<sup>21, 25</sup>, and plasmonic effect<sup>15</sup>. The stabilization of  $\text{WO}_3$  photoanode for water oxidation is rarely studied. Recently, Liu *et al.* and Seabold *et al.* reported an effective approach to stabilize  $\text{WO}_3$  by coating a layer of oxygen evolution catalyst (OEC) such as manganese and cobalt based catalysts on  $\text{WO}_3$ <sup>16, 23, 26, 27</sup>. The OEC was used to reduce the oxygen evolution overpotential and therefore suppress the formation of peroxo species. A thin layer OEC coating can stabilize the photoactivity of  $\text{WO}_3$  for several hours<sup>16</sup> and a heavy coating can extend its stability to 12 hours<sup>23</sup>. Nevertheless, a thick OEC layer also blocks light penetration, and decreases the photoactivity of  $\text{WO}_3$ <sup>23</sup>. Therefore, it is highly desirable to improve the stability of  $\text{WO}_3$  without losing photoactivity.

Recently, we demonstrated the enhanced photoactivity of hydrogen-treated  $\text{TiO}_2$  nanowires as a result of increased donor density by introducing moderate amount of oxygen vacancies<sup>28</sup>. Similar effect is expected to be observed in hydrogen-treated  $\text{WO}_3$ . More importantly, it has been reported that substoichiometric  $\text{WO}_{3-x}$ , formed by creating oxygen vacancies ( $\text{W}^{5+}$ ) in  $\text{WO}_3$ , is thermodynamic stable at room temperature, which can only be re-oxidized at high temperature higher than 400 °C in air<sup>29</sup>. For instance, substoichiometric  $\text{WO}_{3-x}$  has been used as a passive layer to protect tungsten metal from further

dissolution in chemical mechanical polishing, indicating  $\text{WO}_{3-x}$  is resistive to the peroxo-species induced dissolution<sup>30</sup>. Therefore, we hypothesized that hydrogen treatment can create substoichiometric  $\text{WO}_{3-x}$ , which could simultaneously improve the photoactivity and stability of  $\text{WO}_3$  for oxidation. In this work, we demonstrate that substoichiometric  $\text{WO}_{3-x}$  can be prepared by controlled introduction of oxygen vacancies (reducing  $\text{W}^{6+}$  to  $\text{W}^{5+}$ ) in hydrogen atmosphere at elevated temperatures. In comparison to pristine  $\text{WO}_3$ , hydrogen-treated  $\text{WO}_{3-x}$  showed an order of magnitude enhanced photocurrent density and extraordinary stability, without significant loss of photoactivity at least for seven hours.

## **Experimental Section**

### **Materials:**

Fluorine doped tin oxide (FTO, TEC 8) glass substrates were purchased from Hartford Glass Company Inc.  $\text{WCl}_6$  (99.9%),  $\text{HCl}$  (36.5% - 38%),  $\text{Na}_2\text{WO}_4 \cdot 2\text{H}_2\text{O}$  and  $\text{H}_2\text{O}_2$  (30%) were purchased from Fisher Scientific Company.

### **Preparation of $\text{WO}_3$ nanoflakes:**

$\text{WO}_3$  nanoflakes were grown on a FTO glass substrate using a seed mediated solvothermal method. The  $\text{WO}_3$  seed solution was prepared as follows: 0.5 mmol  $\text{WCl}_6$  was dissolved in 20 ml ethanol solution; the dissolved  $\text{WCl}_6$  was quickly hydrolyzed by water moisture and produced blue precipitates. 30%

H<sub>2</sub>O<sub>2</sub> solution was added into the blue precipitate-containing solution with stirring until the solution became clear. This WO<sub>3</sub> seed solution was dropped onto a piece of clean FTO glass. The excess solution was blow away by compressed air after 30 s. The FTO substrate was then annealed at 350 °C on a hotplate in air for 10 min. Repeat this deposition-annealing process for two or three times to get a uniform WO<sub>3</sub> seed layer on FTO substrate. Meanwhile, 1.03 g Na<sub>2</sub>WO<sub>4</sub> was dissolved in 25 ml deionized water and mixed with 1 ml concentrated hydrochloric acid. The yellow precipitates produced in the reaction were re-dissolved by adding 0.3 ml 30% H<sub>2</sub>O<sub>2</sub>. This W precursor solution was boiled for five minutes to remove excess H<sub>2</sub>O<sub>2</sub>. The WO<sub>3</sub> seeded FTO substrate was placed into a Teflon-lined stainless steel autoclave (30 ml volume) with the seeded side facing down. 3 ml W precursor solution and 20 ml ethanol was transferred into the autoclave. The sealed autoclaves was heated in an electric oven at 180 °C for 5 hours, and then cooled down to room temperature naturally. The seeded FTO substrate was coated with a uniform blue film. After washed with ethanol and water, the film was calcined in the air at 500 °C for 2 hours.

**Hydrogen treatment:**

Hydrogen treatment was carried out in a home built tube furnace system. The calcined WO<sub>3</sub> nanoflake films were further annealed in hydrogen (1 bar, 50 sccm H<sub>2</sub> flow) at different temperatures in a range of 250-500°C for 20 minutes.

**Material characterization:**

Scanning electron microscopy (SEM) images were collected with a field-emission SEM (Hitachi S-4800II). Transmission electron microscopy (TEM) images were collected in a FEI Monochomated F20 UT Technai TEM/STEM operated at 200 kV. X-ray diffraction (XRD) spectra were collected with a Rigaku Americas Miniflex Plus powder diffractometer. Diffraction spectra were recorded from a two-theta angle of 20 to 70 degree with a step size of 0.04 degree at a rate of 1 degree/min. Raman spectroscopy measurements were carried out on a Nicolet Almega XR Dispersive Raman spectrometer (laser wavelength 780 nm). X-ray photoelectron Spectroscopy (XPS) was performed on a RBD upgraded PHI-5000C ESCA system (Perkin-Elmer) using Mg-monochromatic X-ray at a power of 25 W with an X-ray-beam diameter of 10 mm, and a pass energy of 29.35 eV. The pressure of analyzer chamber was maintained below  $5 \times 10^{-8}$  Pa during the measurement. The binding energy was calibrated using the C 1s photoelectron peak at 284.6 eV as reference.

**Photoelectrochemical measurement:**

WO<sub>3</sub> and hydrogen-treated WO<sub>3</sub> samples were fashioned into photoanodes by soldering a copper wire onto a bare part of FTO substrate. The substrate edges and the metal contact region were sealed with insulating epoxy resin. The working electrode area is in a range of 0.2-0.25 cm<sup>2</sup>. 0.5 M Na<sub>2</sub>SO<sub>4</sub> aqueous solution (pH = 6.8) was used as an electrolyte. Linear sweep voltammograms and I-t scans were collected on a CHI 660D electrochemical station, with



Ag/AgCl as reference and Pt wire as counter electrode, under a simulated sunlight generated with a 150 W xenon lamp (Newport 6255) coupled with an AM 1.5 global filter (Newport 81094). All linear sweep voltammograms were collected at a scan rate of 10 mV/s. Incident-photon-to-current conversion efficiency (IPCE) were collected by a CHI 660D with a solar simulator (Newport 69920, 1000W xenon lamp), coupled with an infrared water filter (Oriel 6127) and aligned monochromator (Oriel Cornerstone 130 1/8m). Electrochemical impedance spectroscopy (EIS) was collected using a CHI 660D electrochemical station with 5 mV perturbation and a frequency range from 100000 to 1Hz at different potentials. Mott-Schottky plots were generated from capacitance obtained from the EIS spectra at each potential with a frequency of 10000 Hz.

### **Electrochromism studies**

Electrochromism studies were carried out in a 1.0 M H<sub>2</sub>SO<sub>4</sub> solution on a three-electrode system with Ag/AgCl as reference, Pt wire as counter electrode and WO<sub>3</sub> film as working electrode. H<sub>x</sub>WO<sub>3</sub> electrode was prepared by applied a negative bias of 1.0 V vs. Ag/AgCl on WO<sub>3</sub> in 1.0 M H<sub>2</sub>SO<sub>4</sub> solution for 3 s. The PEC performance of H<sub>x</sub>WO<sub>3</sub> electrode was investigated in 0.5 M Na<sub>2</sub>SO<sub>4</sub> aqueous solution.

## Results and Discussion

WO<sub>3</sub> nanoflake films were fabricated on fluorine-doped tin oxide (FTO) substrates, using a seed mediated solvothermal method (Experimental Section). The uniform WO<sub>3</sub> films are covered by submicron-sized nanoflake bundles with a typical length of 4-5  $\mu\text{m}$  (Figure 6.1a). Each bundle is composed of a stack of thin nanoflakes. TEM images recorded from representative WO<sub>3</sub> nanoflake bundles showed that these nanoflakes are single crystals (Inset, Figure 6.1b) and have smooth surface (Figure 6.1b).

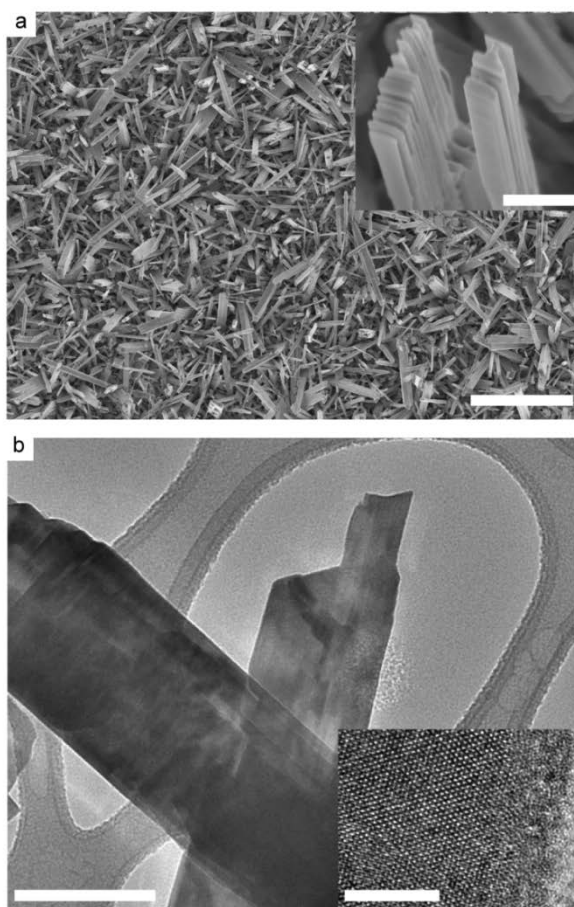


**Figure 6. 1** SEM and TEM images of WO<sub>3</sub> nanoflakes.

The as-prepared nanoflakes were first calcined in air at 500 °C for 2h, followed by high temperature annealing (250-500 °C) in hydrogen atmosphere for another 20 minutes to create oxygen vacancies in WO<sub>3</sub>. As shown in Figure 6.2, the pristine WO<sub>3</sub> film is yellow in color. As the hydrogen annealing temperature increases, the film color changes from yellowish green (300 °C) to green (350 °C), then light blue (400 °C) and eventually to deep blue when the temperature is 450 °C or above. The color change suggests possible modification in crystal structure and/or phase change during hydrogen treatment.

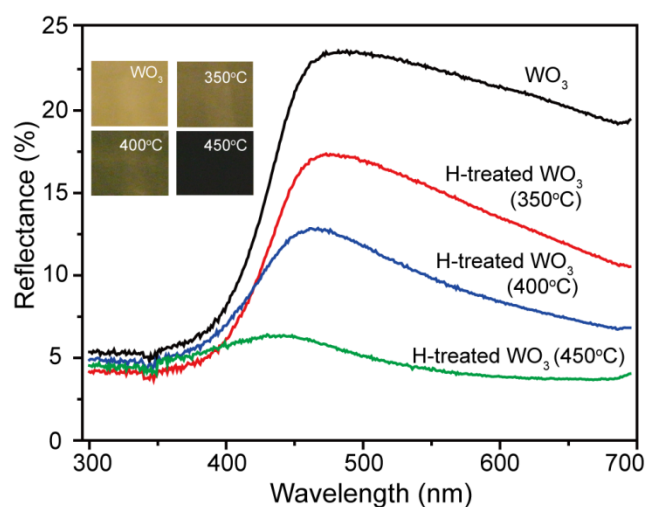


**Figure 6.2** UV-vis spectra and corresponding colors of WO<sub>3</sub> and hydrogen treated WO<sub>3</sub> at 350, 400 and 450 °C.

XRD spectra collected from pristine WO<sub>3</sub> and hydrogen-treated WO<sub>3</sub> samples prepared at 350 and 500 °C (Figure 6.3a) confirmed this hypothesis. After

subtracting the diffraction peaks from FTO substrate, the peaks collected from pristine  $\text{WO}_3$  can be indexed as monoclinic  $\text{WO}_3$  (PCPDF #: 72-1465). There is no obvious shift in the diffraction peaks between pristine  $\text{WO}_3$  and the hydrogen-treated  $\text{WO}_3$  samples at 350 °C. However, these monoclinic  $\text{WO}_3$  diffraction peaks gradually disappear accompanied with the emergence of new peaks in the samples hydrogen treated at temperature of 500 °C. These new peaks can be indexed as monoclinic  $\text{WO}_{2.9}$  (PCPDF #: 05-0386) and small amount of monoclinic  $\text{WO}_{2.92}$  (PCPDF #: 30-1387) highlighted by \* and + in Figure 6.3a, indicating the successful reduction of  $\text{WO}_3$ . Diffraction peaks corresponding to Sn metal are also identified as a result of the reduction of FTO substrate. Furthermore, Raman analysis also confirms the conversion of monoclinic  $\text{WO}_3$  to  $\text{WO}_{2.9}$  during hydrogen treatment (Figure 6.3b). The characteristic Raman peaks for  $\text{WO}_3$  become broader as the annealing temperature increases, suggesting gradual degradation of  $\text{WO}_3$  crystallinity, which is expected for the increased amount of oxygen vacancies. For the  $\text{WO}_3$  sample hydrogen-treated at 500 °C, all the Raman peaks of  $\text{WO}_3$  disappeared, and left a broad peak in the region of 700-1000  $\text{cm}^{-1}$ , which is consistent to the reported Raman spectrum of  $\text{WO}_{2.9}$ <sup>31</sup>. Additionally, the formation of  $\text{W}^{5+}$  allows the intervalence charge transfer between  $\text{W}^{5+}$  to  $\text{W}^{6+}$  in the substoichiometric  $\text{WO}_{3-x}$ <sup>32</sup>, which explains the observed color change gradually from yellow ( $\text{WO}_3$ ) to deep blue ( $\text{WO}_{2.9}$  and  $\text{WO}_{2.92}$ ). Taken together, these results support

the successful introduction of oxygen vacancies into monoclinic  $\text{WO}_3$  by hydrogen treatment, and the amount of oxygen vacancies can be controlled by annealing temperature.

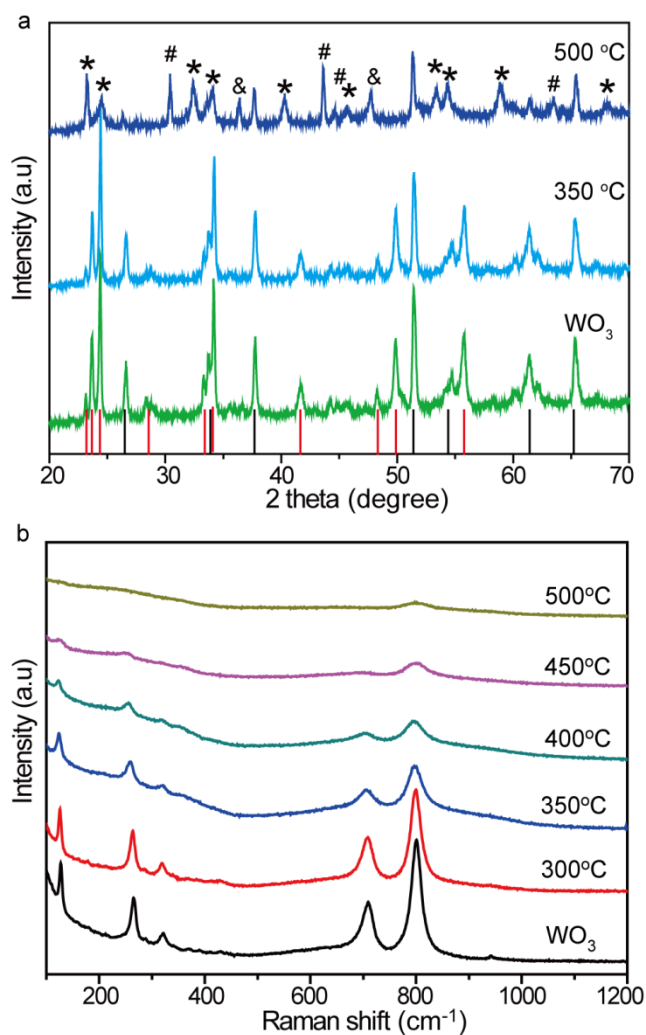


**Figure 6.3** (a) XRD patterns and Raman spectra of  $\text{WO}_3$  and hydrogen treated  $\text{WO}_3$  at different temperatures.

The PEC properties of pristine  $\text{WO}_3$  and hydrogen-treated  $\text{WO}_3$  samples were measured in a three-electrode electrochemical cell (using  $\text{Ag}/\text{AgCl}$  in sat.  $\text{KCl}$  as reference electrode and Pt wire as counter electrode) with 0.5 M  $\text{Na}_2\text{SO}_4$

solution as electrolyte (Experimental Section). Figure 6.4a compares the linear sweep voltammograms collected for pristine  $\text{WO}_3$  and hydrogen-treated  $\text{WO}_3$  samples at temperatures of 350, 400 and 450 °C. The photocurrent density of pristine  $\text{WO}_3$  sample is  $0.1 \text{ mA/cm}^2$  at 1.0 V vs. Ag/AgCl, which is comparable to the value obtained for  $\text{WO}_3$  nanowires<sup>18</sup>. The photocurrent densities of  $\text{WO}_3$  increase gradually with the increase of hydrogen treatment temperature from 250 to 350 °C (Figure 6.4b). The  $\text{WO}_3$  sample hydrogen treated at 350 °C achieved a maximum value of  $0.88 \text{ mA/cm}^2$  at the 1.0 V vs. Ag/AgCl, which is about an order of magnitude enhancement compared to pristine  $\text{WO}_3$  at the same potential. The enhancement is believed due to the increased amount of oxygen vacancies that serve as shallow electron donor for  $\text{WO}_3$ <sup>33</sup>. It confirms our hypothesis that hydrogen treatment could improve the photoactivity of  $\text{WO}_3$ . Photocurrent densities decrease gradually with increasing temperature when the annealing temperature is 400 °C or above. There are two possible explanations. First,  $\text{WO}_3$  transforms into  $\text{WO}_{2.9}$  during hydrogen treatment (as confirmed by XRD and Raman results), and  $\text{WO}_{2.9}$  is known to be photoelectrochemically inactive for water oxidation<sup>34</sup>. Second, the resistance of FTO substrate increased from 13 to 760  $\Omega$  as a result of degradation of FTO layer (Sn metal formation as confirmed by XRD results), which increases the voltage drop at the interface of  $\text{WO}_3$  and substrate.

To investigate the stability of pristine WO<sub>3</sub> and hydrogen-treated WO<sub>3</sub> for water oxidation, we define a parameter of photocurrent density retention in the first six minute irradiation as  $I_{\text{initial}} / I_{\text{final}}$ . Where  $I_{\text{initial}}$  and  $I_{\text{final}}$  are the photocurrent densities at time = 0 and 6 min, respectively. All the samples for the stability investigation are freshly prepared. As shown in Figure 6.4b, photocurrent density retention for pristine WO<sub>3</sub> is only about 30 %, which is comparable to the reported values for WO<sub>3</sub> nanostructures<sup>16, 22, 23</sup>. Significantly, the retention values of hydrogen-treated WO<sub>3</sub> samples increase substantially with annealing temperature, achieving excellent photocurrent density retention more than 80 % for those samples annealed at 350 °C or above.

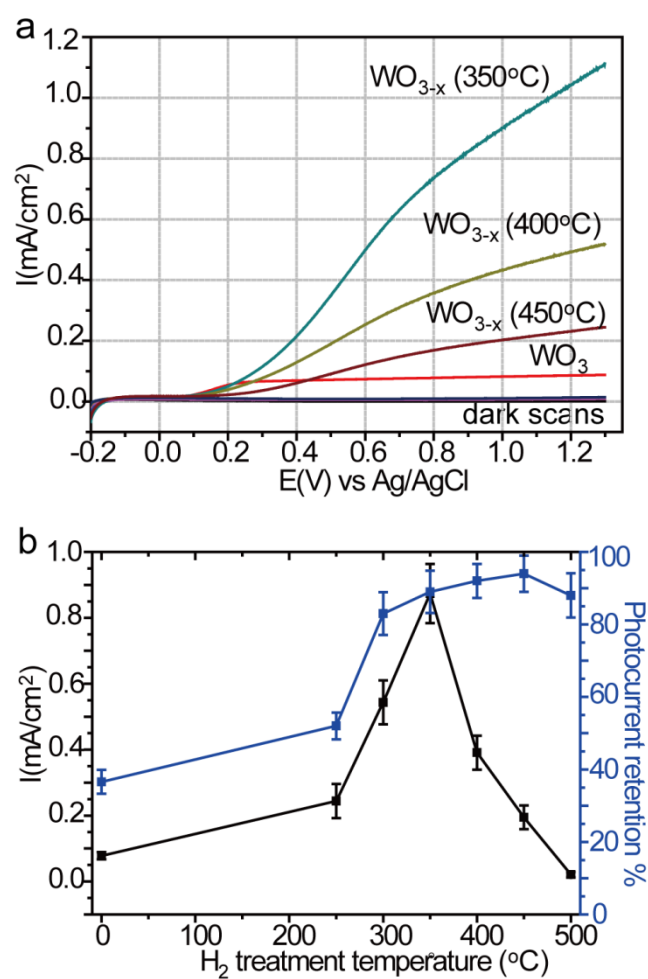


**Figure 6.4** (a) I-V curves of  $WO_3$  and hydrogen treated  $WO_3$  samples under dark and light illumination. (b) Temperature dependent photocurrents and corresponding photocurrent retention.

Furthermore, we investigated the long time stability of these samples (Figure 6.5). The photocurrent density of  $WO_3$  drops about 65 % within the first two minutes, and then decrease slowly (Figure 6.5 inset). After two-hour illumination, 80 % of the photoactivity of  $WO_3$  was lost. In contrast, the photocurrent density for the hydrogen-treated  $WO_3$  sample prepared at 350 °C drops 17 % within the first 2 minutes, and then achieves a stable photocurrent



without decay under the irradiation for at least seven hours (Figure 6.5). The photocurrent increases slightly with time could be due to self-activation and increasing trap filling of the  $\text{WO}_{3-x}$  sample<sup>3, 35</sup>. These  $I-t$  data are direct evidence of supporting our hypothesis that hydrogen treatment can stabilize the photoactivity of  $\text{WO}_3$  for water oxidation. The superior stability of hydrogen-treated  $\text{WO}_3$  for water oxidation is believed due to the formation of partially reduced substoichiometric  $\text{WO}_{3-x}$ , which has been reported to be thermodynamic stable at room temperature towards re-oxidation and highly resistive to peroxide species induced dissolution<sup>30</sup>.

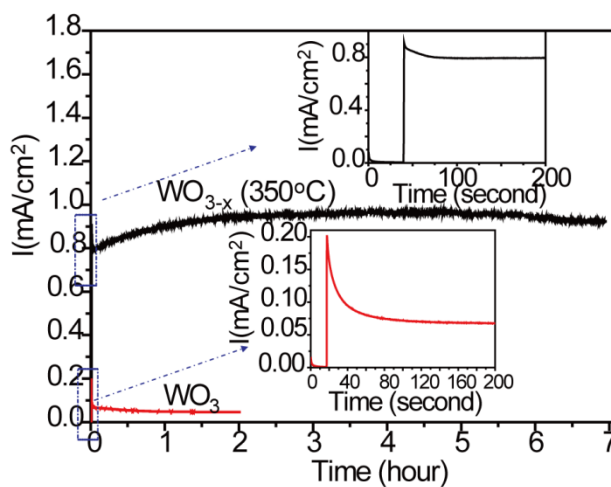


**Figure 6.5** Photostability of  $\text{WO}_3$  and hydrogen treated  $\text{WO}_3$  at 350 °C.

The color changes of  $\text{WO}_3$  during hydrogen treatment suggest a modification in light absorption profile. In order to quantitatively investigate the relation between the photoactivity and the light absorption, we measured their

photoactivity as a function of wavelength of incident light. Figure 4 shows the IPCE data collected from WO<sub>3</sub> and hydrogen-treated WO<sub>3</sub> samples with green (350 °C), blue (400 °C) and deep blue (450 °C) colors. IPCE can be expressed by the equation:

$$\text{IPCE} = (1240 \times I)/(\lambda \times J_{\text{light}}),$$

where  $I$  is the measured photocurrent density at a specific wavelength,  $\lambda$  is the wavelength of incident light, and  $J_{\text{light}}$  is the measured irradiance at a specific wavelength. In comparison to pristine WO<sub>3</sub>, all hydrogen-treated WO<sub>3</sub> samples exhibit enhanced IPCE in the entire absorption region (300-480 nm) in figure 6.6. They show similar absorption edges at around ~480 nm, which is consistent to the WO<sub>3</sub> bandgap of 2.6 eV<sup>18</sup>. We did not observe any photoactivity in visible light region beyond 480 nm, indicating the observed color change is not due to the bandgap engineering of WO<sub>3</sub> or the transition between the impurity states and conduction/valence band edges. Therefore, the color changes could be due to intervalence charge transition from W<sup>6+</sup> to W<sup>5+</sup>, which have been previously reported<sup>29, 36</sup>.

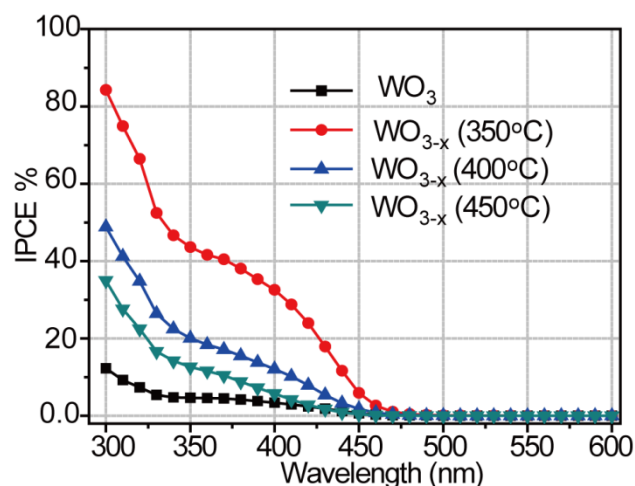


**Figure 6.6** IPCE spectra of WO<sub>3</sub> and hydrogen treated WO<sub>3</sub> samples.

To further elucidate the effect of hydrogen treatment on the chemical states of WO<sub>3</sub> and how it interplays with their photoactivity, we measured the X-ray photoelectron spectroscopy (XPS) of pristine WO<sub>3</sub> and hydrogen-treated WO<sub>3</sub> samples prepared at temperatures of 350 °C and 450 °C. As shown in the normalized high resolution W 4f spectra (Figure 6.7), they all have a broad peak, corresponding to the characteristic W 4f<sub>5/2</sub> and W 4f<sub>7/2</sub> peaks for WO<sub>3</sub><sup>37,38</sup>. The XPS W4f of pristine WO<sub>3</sub> can be deconvoluted into one pairs of peaks, corresponding to the typical binding energies of W<sup>6+</sup> oxidation states (centered at 37.7 and 35.5 eV) (Figure 6.7a). Note that the W 4f peaks of hydrogen-treated samples are slightly broader than that of pristine WO<sub>3</sub>, with a shoulder at the lower binding energy region. The peak can be deconvoluted into two pairs of peaks, corresponding to the typical binding energies of two W oxidation states,

$W^{6+}$  (centered at 37.7 and 35.5 eV) and  $W^{5+}$  (centered at 37.0 and 34.3 eV) respectively (Figure 6.7b) <sup>37, 38</sup>. The data suggest the presence of  $W^{5+}$  (oxygen vacancies) in the hydrogen-treated  $WO_3$  samples, in agreement with the Raman and XRD results. It is known that the substoichiometric  $WO_{3-x}$  favorable to form shear defects.

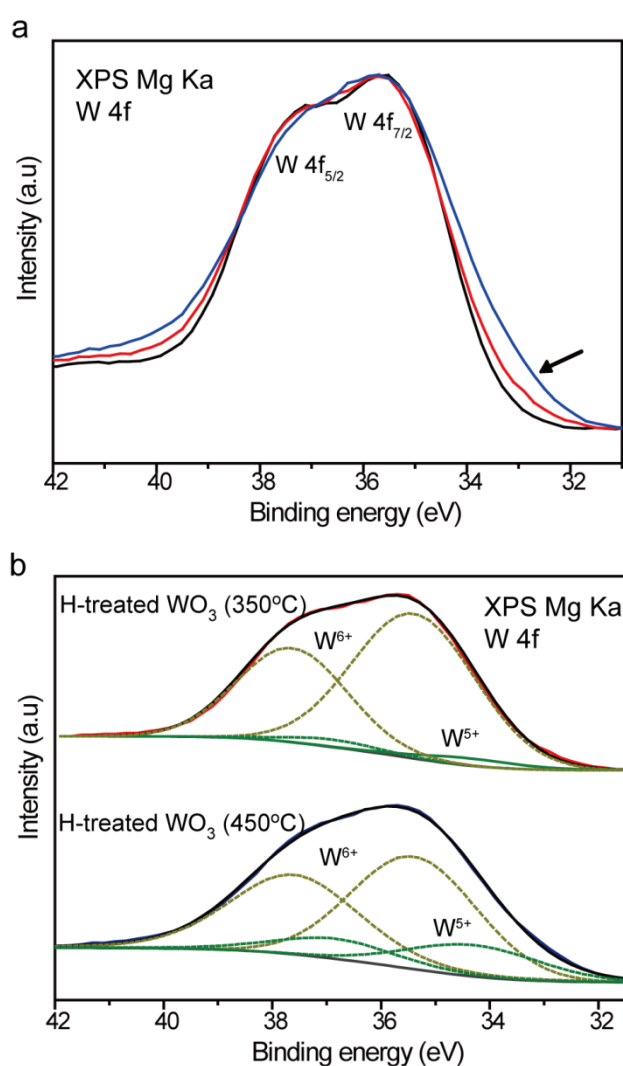


**Figure 6.7** (a) the comparison of XPS W 4f spectra of  $WO_3$  and hydrogen treated  $WO_3$ . (b) The XPS fitting curves of hydrogen treated  $WO_3$  at 350 and 450 °C.

The normalized XPS O1s spectra collected from  $\text{WO}_3$  and hydrogen-treated  $\text{WO}_{3-x}$  samples are similar (Figure 6.8), indicating that these plane defects do not significantly affect the coordination polyhedron of oxygen about each W<sup>39, 40</sup>. In addition, the absence of hydroxyl (O-H) peak or broader shoulder that expected to be observed at around 532 eV indicates that the hydrogen treatment did not lead to the formation of tungsten bronze  $\text{H}_x\text{WO}_3$ , which is also blue in color<sup>41</sup>.

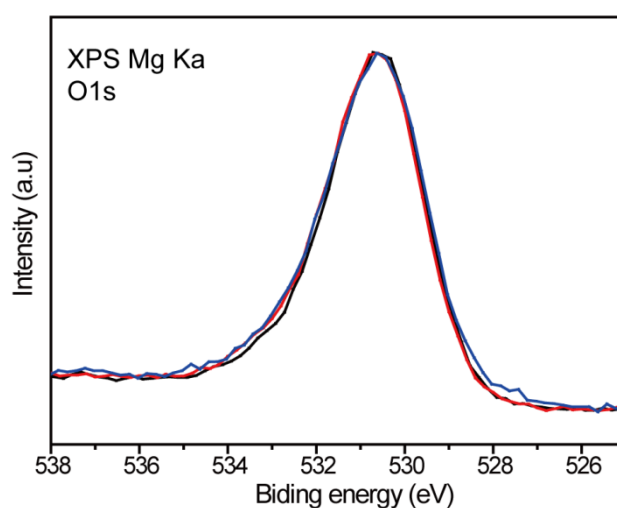


**Figure 6.8** XPS O1s of  $\text{WO}_3$  and hydrogen treated  $\text{WO}_3$ .

$\text{H}_x\text{WO}_3$  is well known for its electrochromism, as it can be easily bleached by applying a positive bias. To differentiate  $\text{WO}_{3-x}$  from  $\text{H}_x\text{WO}_3$ , we studied the PEC water oxidation stability of the hydrogen-treated  $\text{WO}_3$  and  $\text{H}_x\text{WO}_3$  control samples.  $\text{H}_x\text{WO}_3$  was electrochemically prepared on pristine  $\text{WO}_3$  (Experimental Section)<sup>42</sup>. We compared the performance of  $\text{H}_x\text{WO}_3$  and

hydrogen-treated  $\text{WO}_3$  for water oxidation at a bias of 1.0 V vs. Ag/AgCl in 0.5 M  $\text{Na}_2\text{SO}_4$  solution. As shown in Figure 6.9,  $\text{H}_x\text{WO}_3$  was quickly bleached due to its electrochromatic property within 3 minutes either in dark or under illumination, as expected. In contrast, there is no obvious change in color and photoactivity for the hydrogen-treated  $\text{WO}_3$  sample measured at the same potential under light illumination for 3 hours. It proves that the hydrogen-treated samples are not  $\text{H}_x\text{WO}_3$  and they are stable and resistive to electrochemical oxidation.

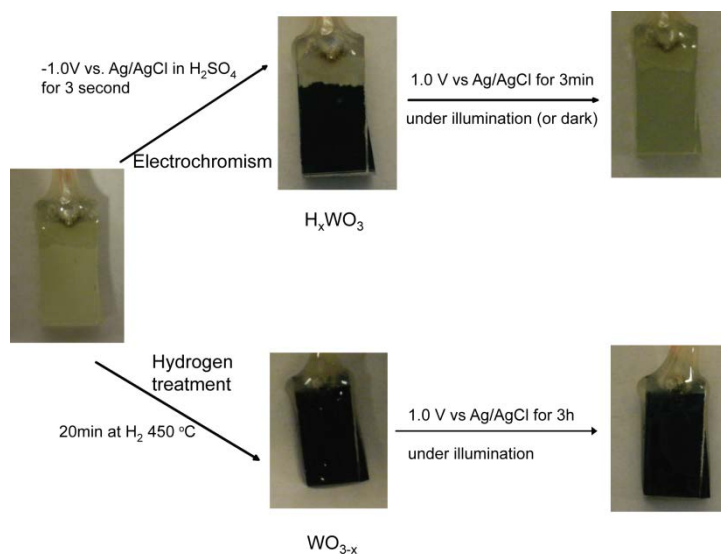


**Figure 6.9** The study of the photostability of hydrogen treated  $\text{WO}_3$  and electrochemical reduced  $\text{WO}_3$ .

Finally, the XPS valence band spectra collected from  $\text{WO}_3$  and  $\text{WO}_{3-x}$  samples are similar and an estimate of the valence band maximum by linear extrapolation to the baseline derives a band edge position of  $\sim 2.0$  eV below the

Fermi energy in both cases (Figure 6.10). The fact that all the films exhibit almost the same position of the valence band maximum indicates a negligible effect of hydrogen treatment on the valence band position at the surface of  $\text{WO}_3$ .

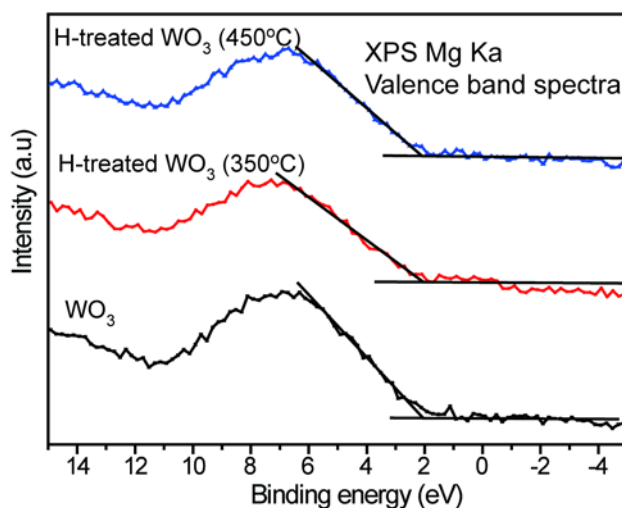


**Figure 6.10** XPS valence band spectra of  $\text{WO}_3$  and hydrogen treated  $\text{WO}_3$ .

To investigate the effect of hydrogen treatment on the electronic properties of  $\text{WO}_3$ , we measured electrochemical impedance for pristine  $\text{WO}_3$  and hydrogen-treated  $\text{WO}_3$  samples. Capacitances were derived from the electrochemical impedance spectroscopy (EIS) obtained at each potential with 10 kHz frequency in the dark. Figure 6.11 shows the Mott-Schottky plots generated from the capacitance values. All samples show positive slopes in the Mott-Schottky plots, as expected for *n*-type semiconductor. The hydrogen-treated  $\text{WO}_3$  samples show substantially smaller slopes compared to  $\text{WO}_3$  sample, suggesting significantly increased donor densities based on the

Mott-Schottky equation,

$$N_d = (2/e_0\epsilon\epsilon_0)[d(1/C^2)/dV]^{-1},$$

where  $e_0$  is the electron charge,  $\epsilon$  the dielectric constant of  $\text{WO}_3$  ( $\epsilon=20$ ),  $\epsilon_0$  the permittivity of vacuum,  $N_d$  the donor density, and  $V$  the applied bias at the electrode. The donor densities of  $\text{WO}_3$  and hydrogen-treated  $\text{WO}_3$  prepared at 350 °C are calculated to be  $1.0\times 10^{19}$  and  $5.0\times 10^{22} \text{ cm}^{-3}$ , respectively. Although Mott-Schottky equation is derived based on planar structure and it may not able to determine precisely the donor density of nanostructured materials, it is reasonable to qualitatively compare the changes of donor density between  $\text{WO}_3$  and hydrogen-treated  $\text{WO}_3$  samples as they have similar morphology. The enhanced donor density is attributed to the introduction of oxygen vacancies, which serve as shallow electron donor<sup>33</sup>, and therefore improves the charge transport in  $\text{WO}_{3-x}$  and at the interface between FTO and  $\text{WO}_{3-x}$ <sup>28, 43, 44</sup>. Furthermore, the capacitance of pristine  $\text{WO}_3$  reaches a plateau at around 0.2 V vs. Ag/AgCl, which suggests the depletion layer does not increase with further increase of applied potential<sup>45</sup>. It explains the photocurrent density saturation of  $\text{WO}_3$  at around 0.2 V vs. Ag/AgCl. Meanwhile, we did not observe photocurrent density saturation for hydrogen-treated  $\text{WO}_3$  in the potential range we studied which is consistent to its linear Mott-Schottky plot. Furthermore, there is a negative shift of flat band potential in hydrogen-treated samples. It could be due to the substantially increased donor density that shifts the Fermi level of  $\text{WO}_3$



upward. Additionally, the contribution of Helmholtz layer capacitance become significant when there is a three orders of magnitude increase in the donor density of  $\text{WO}_3$ , which will cause a negative shift of the flat band potential (x-intercept) in the Mott-Schottky plot as well <sup>46</sup>. We also measured the Mott-Schottky plots for  $\text{WO}_3$  and hydrogen-treated  $\text{WO}_3$  samples with applied frequencies of 1 kHz, 4 kHz, and 7 kHz (data not shown). As expected, the slopes of Mott-Schottky plots of these samples increase with the increase of applied frequency, because dielectric constant is frequency dependent. Similar flat-band potentials were obtained from Mott-Schottky plots generated at different frequencies.

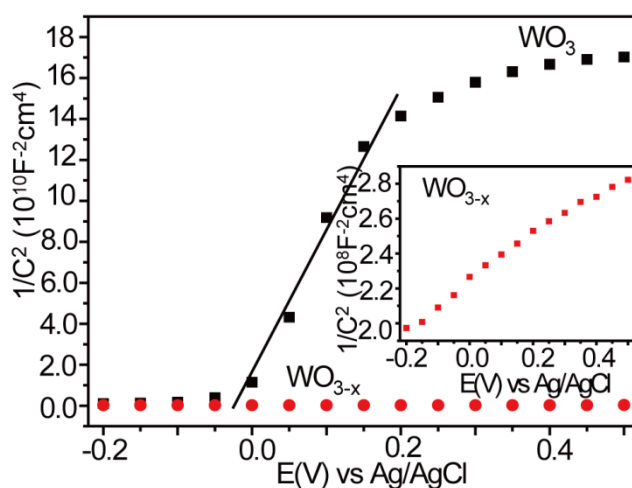


**Figure 6.11** Mot-schottky curve of  $\text{WO}_3$  and hydrogen treated  $\text{WO}_3$ .

## Conclusion

In summary, hydrogen treatment represents a novel method to

simultaneously activate and stabilized the photoactivity of WO<sub>3</sub> nanoflakes for PEC water oxidation. By annealing pristine WO<sub>3</sub> in hydrogen atmosphere at different temperatures, they can be partially reduced to substoichiometric WO<sub>3-x</sub>. These hydrogen-treated WO<sub>3</sub> samples showed an order of magnitude enhancement in photocurrent density compared to pristine WO<sub>3</sub>, as a result of three orders of magnitude increased donor density of WO<sub>3</sub> by introduction of oxygen vacancies. More importantly, we demonstrated, for the first time, that the hydrogen-treated WO<sub>3</sub> photoanodes (without coating of OEC) have outstanding stability for water oxidation, without significant loss of photoactivity for seven hours. The capability of producing photoactive and electrochemically stable WO<sub>3</sub> could open up new opportunities for WO<sub>3</sub>-based photoelectrochemical and photocatalytic applications.

## Reference

1. A. Fujishima and K. Honda, *Nature*, 1972, **238**, 37-38.
2. X. J. Feng, K. Shankar, O. K. Varghese, M. Paulose, T. J. Latempa and C. A. Grimes, *Nano Lett.*, 2008, **8**, 3781-3786.
3. X. Y. Yang, A. Wolcott, G. M. Wang, A. Sobo, R. C. Fitzmorris, F. Qian, J. Z. Zhang and Y. Li, *Nano Lett.*, 2009, **9**, 2331-2336.
4. G. M. Wang, X. Y. Yang, F. Qian, J. Z. Zhang and Y. Li, *Nano Lett.*, 2010, **10**,

1088-1092.

5. J. Hensel, G. M. Wang, Y. Li and J. Z. Zhang, *Nano Lett.*, 2010, **10**, 478-483.
6. Y. C. Ling, G. M. Wang, D. A. Wheeler, J. Z. Zhang and Y. Li, *Nano Lett.*, 2011, **11**, 2119-2125.
7. J. E. Yourey and B. M. Bartlett, *J. Mater. Chem.*, 2011, **21**, 7651-7660.
8. J. K. Kim, K. Shin, S. M. Cho, T. W. Lee and J. H. Park, *Energy Environ. Sci.*, 2011, **4**, 1465-1470.
9. J. W. Sun, D. K. Zhong and D. R. Gamelin, *Energy Environ. Sci.*, 2010, **3**, 1252-1261.
10. J. R. McKone, E. L. Warren, M. J. Bierman, S. W. Boettcher, B. S. Brunschwig, N. S. Lewis and H. B. Gray, *Energy Environ. Sci.*, 2011, **4**, 3573-3583.
11. X. B. Chen, L. Liu, P. Y. Yu and S. S. Mao, *Science*, 2011, **331**, 746-750.
12. G. Hodes, D. Cahen and J. Manassen, *Nature*, 1976, **260**, 312-313.
13. H. L. Wang, T. Lindgren, J. J. He, A. Hagfeldt and S. E. Lindquist, *J. Phys. Chem. B*, 2000, **104**, 5686-5696.
14. C. Santato, M. Odziemkowski, M. Ulmann and J. Augustynski, *J. Am. Chem. Soc.*, 2001, **123**, 10639-10649.
15. R. Solarzka, A. Krolikowska and J. Augustynski, *Angew. Chem. Int. Edit.*, 2011, **49**, 7980-7983.
16. R. Liu, Y. J. Lin, L. Y. Chou, S. W. Sheehan, W. S. He, F. Zhang, H. J. M.

- Hou and D. W. Wang, *Angew. Chem. Int. Edit.*, 2011, **50**, 499-502.
17. J. Z. Su, L. J. Guo, N. Z. Bao and C. A. Grimes, *Nano Lett.*, 2011, **11**, 1928-1933.
  18. J. Z. Su, X. J. Feng, J. D. Sloppy, L. J. Guo and C. A. Grimes, *Nano Lett.*, 2011, **11**, 203-208.
  19. R. S. Lillard, G. S. Kanner and D. P. Butt, *J. Electrochem. Soc.*, 1998, **145**, 2718-2725.
  20. M. Anik and T. Cansizoglu, *J. Appl. Electrochem.*, 2006, **36**, 603-608.
  21. V. Chakrapani, J. Thangala and M. K. Sunkara, *Int. J. Hydrogen Energy*, 2009, **34**, 9050-9059.
  22. W. Z. Li, J. Li, X. Wang, J. Ma and Q. Y. Chen, *Int. J. Hydrogen Energy*, 2010, **35**, 13137-13145.
  23. J. A. Seabold and K. S. Choi, *Chem. Mater.*, 2011, **23**, 1105-1112.
  24. R. Nakamura and Y. Nakato, *J. Am. Chem. Soc.*, 2004, **126**, 1290-1298.
  25. M. Bar, L. Weinhardt, B. Marsen, B. Cole, N. Gaillard, E. Miller and C. Heske, *Appl. Phys. Lett.*, 2010, **96**, 3.
  26. M. W. Kanan and D. G. Nocera, *Science*, 2008, **321**, 1072-1075.
  27. J. Limburg, J. S. Vrettos, L. M. Liable-Sands, A. L. Rheingold, R. H. Crabtree and G. W. Brudvig, *Science*, 1999, **283**, 1524-1527.
  28. G. M. Wang, H. Y. Wang, Y. C. Ling, Y. C. Tang, X. Y. Yang, R. C. Fitzmorris, C. C. Wang, Z. J. Zhang and Y. Li, *Nano Lett.*, 2011, **11**,

3026-3033.

29. Y. Zhao, Z. C. Feng, Y. Liang and H. W. Sheng, *Appl. Phys. Lett.*, 1997, **71**, 2227-2229.
30. D. Tamboli, S. Seal, V. Desai and A. Maury, *J. Vac. Sci. Technol. A: Vac. Surf. Films*, 1999, **17**, 1168-1173.
31. J. G. Liu, Y. Zhao and Z. J. Zhang, *J. Phys.: Condes. Matter*, 2003, **15**, L453-L461.
32. S. N. Alamri, *Smart Mater. Struct.*, 2009, **18**, 025010-025015.
33. S. K. Deb, *Phys. Rev. B*, 1977, **16**, 1020-1024.
34. S. O'Neill, I. P. Parkin, R. J. H. Clark, A. Mills and N. Elliott, *Chem. Vapor Deposition*, 2004, **10**, 136-142.
35. F. G. Wakim, *Phys. Status Solidi A*, 1970, **1**, 479-485.
36. R. J. Colton, A. M. Guzman and J. W. Rabalais, *Acc. Chem. Res.*, 1978, **11**, 170-176.
37. B. A. Deangelis and M. Schiavello, *J. Solid State Chem.*, 1977, **21**, 67-72.
38. S. C. Moulzolf, S. A. Ding and R. J. Lad, *Sens. Actuator B: Chem.*, 2001, **77**, 375-382.
39. H. T. Sun, C. Cantalini, L. Lozzi, M. Passacantando, S. Santucci and M. Pelino, *Thin Solid Films*, 1996, **287**, 258-265.
40. F. S. Manciu, J. L. Enriquez, W. G. Durrer, Y. Yun, C. V. Ramana and S. K. Gullapalli, *J. Mater. Res.*, 2010, **25**, 2401-2406.

41. S. R. Bathe and P. S. Patil, *Solid State Ionics*, 2008, **179**, 314-323.
42. J. M. Wang, E. Khoo, P. S. Lee and J. Ma, *J. Phys. Chem. C*, 2009, **113**, 9655-9658.
43. G. M. Wang, Y. C. Ling, D. A. Wheeler, K. E. N. George, K. Horsley, C. Heske, J. Z. Zhang and Y. Li, *Nano Lett.*, 2011, **11**, 3503-3509.
44. A. Kay, I. Cesar and M. Gratzel, *J. Am. Chem. Soc.*, 2006, **128**, 15714-15721.
45. R. P. Lynch, A. Ghicov and P. Schmuki, *J. Electrochem. Soc.*, 2010, **157**, G76-G84.
46. F. Cardon and W. P. Gomes, *J. Phys. D: Appl. Phys.*, 1978, **11**, L63-L67.

## Chapter 7

### Hydrogen Treated BiVO<sub>4</sub> for Enhanced Photoactivity for PEC Water

#### Splitting

##### Abstract

We demonstrate hydrogenation as a facile method to significantly enhance the performance of BiVO<sub>4</sub> films for photoelectrochemical water oxidation. Hydrogenation was performed for BiVO<sub>4</sub> films by annealing them in hydrogen atmosphere at elevated temperatures between 200 and 400 °C. Hydrogen gas can reduce BiVO<sub>4</sub> to form oxygen vacancies as well as hydrogen impurities. DFT calculation predicted that both oxygen vacancies and hydrogen impurities are shallow donors for BiVO<sub>4</sub>, with low formation energies. These defects could increase the donor densities of BiVO<sub>4</sub> without introducing deep trap states. Electrochemical impedance measurements showed that the donor densities of BiVO<sub>4</sub> films were significantly enhanced upon hydrogenation. Hydrogen-treated BiVO<sub>4</sub> (H-BiVO<sub>4</sub>) photoanodes achieved a maximum photocurrent density of 3.5 mA/cm<sup>2</sup> at 1.0 V vs. Ag/AgCl, which is one order of magnitude higher than that of air-annealed BiVO<sub>4</sub> obtained at the same potential. The enhanced photoactivities were attributed to increased donor densities of H-BiVO<sub>4</sub>, which facilitates the charge transport and collection.

## Introduction

Photoelectrochemical (PEC) water splitting for solar hydrogen production has attracted extensive interest in the last few decades.<sup>1-10</sup> Previous studies have primarily focused on binary metal oxides consisting of earth-abundant elements such as  $\text{TiO}_2$ ,<sup>11-15</sup>,  $\text{ZnO}$ ,<sup>16-18</sup>  $\text{WO}_3$ ,<sup>19-23</sup> and  $\alpha\text{-Fe}_2\text{O}_3$ ,<sup>24-29</sup> due to their low cost and high chemical stability. However, one of the fundamental constraints of these binary metal oxides is their valence bands are typically composed of O 2p character, which lies below water's oxidation potential. As a result, there is an intrinsic limitation on visible light absorption and with the conduction band lying above water's reduction potential. Recently, ternary metal oxides such as  $\text{BiVO}_4$  are emerging as new photoelectrodes for PEC water oxidation.<sup>3, 19, 21, 30-36</sup> Ternary metal oxides could provide new opportunities in developing photoelectrode, as their electronic bands are formed by atomic orbitals from more than one element and the modulation of the stoichiometric ratio of the elements could finely tune the potentials of valence and conduction bands as well as the band-gap energy.

$\text{BiVO}_4$  is a direct band-gap ternary metal oxide semiconductor with a favorable band-gap of 2.3-2.5 eV for solar light absorption. Furthermore, its conduction band is close to 0 V vs. RHE at pH = 0, as a result of the overlap of empty Bi 6p orbitals with anti-bonding V 3d-O 2p states,<sup>3, 37</sup> which can reduce the need for



external bias for PEC water splitting. However, charge transport and the interfacial charge transfer have been found to be key limiting factors for its PEC performance.<sup>32, 38</sup> A number of methods have been explored to address this limitation.<sup>39-45</sup> For example, a BiVO<sub>4</sub> and graphene composite structure has been reported showing improved interfacial charge transfer between BiVO<sub>4</sub> and the back contact.<sup>32</sup> However, the addition of graphene could affect the light absorption of BiVO<sub>4</sub>, and graphene does not improve the intrinsic electronic properties of BiVO<sub>4</sub>. Alternatively, elements such as Mo and W have been used as *n*-type dopants to increase electrical conductivity and PEC performance of BiVO<sub>4</sub>.<sup>30, 31, 46-48</sup> Recently, we have reported that hydrogen treatment can significantly enhance the PEC performance of TiO<sub>2</sub> and WO<sub>3</sub> photoanodes by increasing their carrier densities via the formation of oxygen vacancies, which act as shallow donors.<sup>7, 12, 22</sup> Previously reported simulation results have predicted that oxygen vacancies also act as shallow donors in BiVO<sub>4</sub>.<sup>49</sup> These results inspired us to explore the influence of hydrogen treatment on the electronic and PEC properties of BiVO<sub>4</sub>. Indeed, we found that hydrogen treatment can considerably enhance the PEC performance of BiVO<sub>4</sub>. The enhancement is believed to be due to the substantially increased donor density as result of formation of oxygen vacancies and hydrogen impurities.

## Experimental Section

### Simulation method

We used the generalized gradient approximation in the PBE<sup>1</sup> version to approximate the exchange-correlation term. Core electrons were modeled with pseudo-potentials constructed with the projector augmented-wave method<sup>2</sup> and we used plane wave basis set with a cutoff of 500 eV to expand the charge density, as implemented in the VASP code.<sup>3</sup> For integrals over the Brillouin zone, we used the tetrahedron method including Bloëchl corrections<sup>4</sup> with the Monkhorst-Pack sampling scheme.<sup>5</sup> For the primitive cell, we used a mesh of 10×10×10 k-points to converge the charge density, but found no appreciable difference from results obtained with a 4×4×4 mesh in terms of the resulting band structure and projected density of states. Accordingly, for the supercells used for defect calculations, we used a 2×2×2 k-point mesh. For all systems, the atomic configurations were optimized using the conjugate gradient algorithm until all Hellmann-Feynman forces were below 0.01 eV/Å.

### Synthesis of BiVO<sub>4</sub> films:

1 mmol NH<sub>4</sub>VO<sub>4</sub>, 1 mmol BiVO<sub>4</sub> and 2.5 mL concentrated HNO<sub>3</sub> were mixed together with 50 ml deionized water. NH<sub>4</sub>OH was used to neutralize the mixed solution, until no precipitate was further produced. Then, the precipitates were centrifuged out. The as-prepared bright yellow BiVO<sub>4</sub> precipitates were dispersed in 30 ml ethanol solution (precursor solution) 0.2 g

polyvinylpyrrolidone was added to increase the precursor solution viscosity for spin coating. A piece of FTO glass substrate was cleaned with ethanol, acetone and then water. The precursor solution was spin coated on the FTO substrate at a rate of 2500 rpm. The  $\text{BiVO}_4$  coated FTO glass was annealed in air at 500 °C for 1h to remove organic binder. Repeat the spin coating and annealing processes for 2 times. The prepared  $\text{BiVO}_4$  on FTO glass works as seeded substrate for further hydrothermal growth.

$\text{BiVO}_4$  film was synthesized on a FTO glass substrate by a modified  $\text{BiVO}_4$  seed-mediated hydrothermal method.<sup>6</sup> The seeded-substrate was put into a 30 ml Teflon lined autoclave, filled with precursor solution containing 1 ml  $\text{HNO}_3$ , 25 ml water, 0.5 mmol  $\text{Bi}(\text{NO}_3)_3$  and 0.5 mmol  $\text{NH}_4\text{VO}_4$ . The autoclave was heated in electric oven at 150 °C for 12h. The as-prepared bright yellow  $\text{BiVO}_4$  film was washed with ethanol, deionized water and then annealed in air at 550 °C for 2h.

### **Hydrogen treatment**

Hydrogen treatment was carried out in a home-built tube furnace. The calcined  $\text{BiVO}_4$  films were further annealed in hydrogen (1 bar, 50 sccm  $\text{H}_2$  flow) for 10 minutes in a range of temperatures between 200 and 400°C.

### **Photoelectrochemical measurement**

$\text{BiVO}_4$  and hydrogen-treated  $\text{BiVO}_4$  (denoted as H- $\text{BiVO}_4$ ) samples were fabricated as photoanodes by soldering a copper wire onto a bare part of FTO

substrate. The substrate edges and the metal contact region were sealed with insulating epoxy resin. The area of the working electrode is in a range of 0.2-0.25 cm<sup>2</sup>. Linear sweep voltammograms were collected by a CHI 660D electrochemical station, using Ag/AgCl (1M KCl) as reference, Pt wire as counter electrode, and 0.5 M Na<sub>2</sub>SO<sub>4</sub> aqueous solution (pH = 6.8) as an electrolyte, under a simulated sunlight (100 mW/cm<sup>2</sup>) generated with a 150 W xenon lamp (Newport 6255) coupled with an AM 1.5 global filter (Newport 81094). All linear sweep voltammograms were collected at a scan rate of 20 mV/s. Incident-photon-to-current conversion efficiency (IPCE) were collected by the same electrochemical workstation with a solar simulator (Newport 69920, 1000W xenon lamp), coupled with an infrared water filter (Oriel 6127) and aligned monochromator (Oriel Cornerstone 130 1/8m). Electrochemical impedance spectroscopy (EIS) was collected with 5 mV perturbation and a frequency range from 100000 to 1Hz at different potentials. Mott-Schottky plots were generated from capacitance obtained from the EIS spectra at each potential with a frequency of 10k Hz. Carrier densities were calculated from the slopes of Mott-Schottky plots using the equation:

$$N_d = (2/e_0\epsilon\epsilon_0)[d(1/C^2)/dV]^{-1},$$

where  $e_0$  is the electron charge,  $\epsilon$  the dielectric constant of BiOV<sub>4</sub>,  $\epsilon_0$  the permittivity of vacuum,  $N_d$  the donor density, and  $V$  the applied bias at the electrode.

## Material characterization

Scanning electron microscopy (SEM) images were collected with a field-emission SEM (Hitachi S-4800II). X-ray diffraction (XRD) spectra were collected with a Rigaku Americas Miniflex Plus powder diffractometer. Diffraction spectra were recorded from a two-theta angle of 20 to 70 degree with a step size of 0.04 degree at a rate of 1 degree/min. Raman spectroscopy measurements were carried out on a Nicolet Almega XR Dispersive Raman spectrometer (laser wavelength 780 nm). X-ray Photoelectron Spectroscopy (XPS, ESCALab250, Thermo VG) with 200 W Al K $\alpha$  radiations in twin anodes. The binding energy was calibrated using the C 1s photoelectron peak at 284.6 eV as reference.

## Results and Discussion

To provide guidance to experimental studies, we carried out parameter-free quantum simulations based on density functional theory (DFT),<sup>50, 51</sup> investigating the effects of hydrogen treatment on the electronic properties of BiVO<sub>4</sub>. We used a monoclinic primitive cell of symmetry C62h composed of two units of BiVO<sub>4</sub> (16 atoms), as indicated in blue in Figure 7.1a. The optimized lattice parameters were 7.323, 11.786, 5.173 Å with an angle of 134.85° between the non orthogonal lattice vectors, in good agreement with previous experimental and theoretical reports.<sup>52, 53</sup> As reported previously,<sup>52</sup> the

band structure of  $\text{BiVO}_4$  has several direct and indirect transitions from local valence band maxima to local conduction band minima that are close in energy. Experimental measurements indicated a direct gap of energy between 2.4 and 2.5 eV.<sup>46, 47</sup> We found a band-gap of 2.14 eV, similar to previous DFT results,<sup>52, 53</sup> with the highest filled states formed by binding combinations of O 2p and Bi s orbitals, whereas the lowest empty states are formed predominantly by d orbitals from vanadium. The supercells used for defect calculations, indicated in Figure 1, are  $2 \times 2 \times 2$  repetitions of the primitive cell, with a total of 96 atoms.

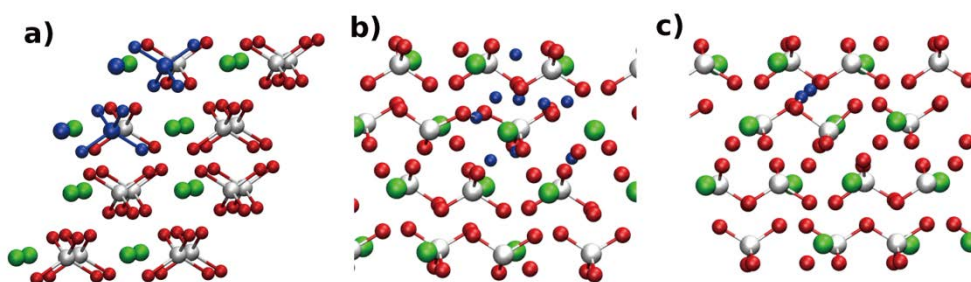


**Figure 1.** (a) Supercell of  $\text{BiVO}_4$  formed by  $2 \times 2 \times 2$  repetitions of the primitive cell, which is highlighted by the blue circles. The white, red and green circles represent vanadium, oxygen and bismuth atoms, respectively. (b) Different sites for interstitial H atoms in impurity calculations are indicated in blue. (c) The position of an interstitial hydrogen molecule is indicated in blue.

In Figure 7.1b we show several sites that were tested for the incorporation of interstitial H atoms in the structure of  $\text{BiVO}_4$ . We observed little variation in the formation energy of these defects on different sites and no appreciable difference in the electronic properties. We have also tested interstitial molecular

hydrogen, which can also be incorporated because of the fairly open crystal structure of BiVO<sub>4</sub> (Figure 7.1c). Furthermore, we tested H atoms in association with oxygen vacancies, *i.e.*, substituting one of the red circles in Figure 7.1. In order to assess the relative frequency of the hydrogen related defects to the intrinsic ones, we conducted an extensive analysis of the latter, including vacancies and self-interstitials of Bi, V and O, as well as Bi<sub>V</sub> and V<sub>Bi</sub> antisites. The formation energies are given by the expression<sup>54</sup>:

$$E_f = E_d - (E_p - \mu_r + \mu_a) + q(E_{VBM} + \mu_e), \quad (1)$$

where  $E_{d,p}$  are the total energies of the supercells containing the defect and the pristine one, respectively,  $\mu_{r,a}$  is the atomic chemical potential of the elements removed or added to the defect,  $q$  is the charge state considered for the defect and  $\mu_e$  is the potential of the reservoir with which the system exchanges electrons or holes (Fermi level). The value of the atomic chemical potentials  $\mu_{r,a}$  depends on the stoichiometric regime under which the crystal is formed. In order to sustain conditions for the formation of the desired compound, certain conditions must be kept<sup>55, 56</sup>: i) The chemical potential of each element must not be larger than the chemical potential of the bulk element; ii) the sum of the variation of the chemical potentials of each element relative to their bulk phases ( $\Delta\mu$ ) must equal the heat of formation of the compound, which is defined as  $\Delta H_{abc} \equiv \mu_{abc} - \mu_a^B - \mu_b^B - \mu_c^B$ , where the superscript “B” indicates the value of the bulk phase; iii) the atomic chemical potentials of the elements forming the

compound and impurities must be such that the formation of competing phases, such as  $\text{Bi}_2\text{O}_3$  or  $\text{V}_2\text{O}_5$ , is prevented in the present case. In equations, these conditions can be summarized as follows<sup>55, 56</sup>:

$$i) \Delta\mu_{\text{Bi,V,O}} = \mu_{\text{Bi,V,O}} - \mu_{\text{Bi,V,O}}^B \leq 0$$

$$ii) \Delta H_{\text{BiVO}_4} = \Delta\mu_{\text{Bi}} + \Delta\mu_{\text{V}} + 4\Delta\mu_{\text{O}};$$

$$iii) 2\Delta\mu_{\text{Bi}} + 3\Delta\mu_{\text{O}} \leq \Delta H_{\text{Bi}_2\text{O}_3}; \quad 2\Delta\mu_{\text{Bi}} + 5\Delta\mu_{\text{O}} \leq \Delta H_{\text{V}_2\text{O}_5}$$

These conditions determine the phase space of atomic chemical potentials for Bi, V and O under which it is possible to synthesize  $\text{BiVO}_4$  crystals, as indicated by the shaded area in Figure 7.2. While additional competing phases can be considered,  $\text{V}_2\text{O}_5$  and  $\text{Bi}_2\text{O}_3$  are enough to give a reliable estimate of the phase space of allowed chemical potentials.<sup>53</sup> The upper boundary in Figure 7.2

is given by the equations:  $\Delta\mu_{\text{V}} = \frac{\Delta H_{\text{V}_2\text{O}_5} - 5\Delta\mu_{\text{O}}}{2}$  and

$\Delta\mu_{\text{Bi}} = \Delta H_{\text{BiVO}_4} - \frac{\Delta H_{\text{V}_2\text{O}_5}}{2} - \frac{3\Delta\mu_{\text{O}}}{2}$ ; so that point A in Figure 7.2 corresponds to

the condition in equilibrium with Bi bulk ( $\Delta\mu_{\text{Bi}} = 0$ , bismuth rich) the poorest in oxygen possible ( $\Delta\mu_{\text{O}} = -2.307$ ,  $\Delta\mu_{\text{V}} = -1.384$  eV). Point C is oxygen rich,  $\Delta\mu_{\text{O}} = 0$ , but is the poorest possible condition in bismuth, with  $\Delta\mu_{\text{Bi}} = -3.46$  and  $\Delta\mu_{\text{V}} = -7.15$  eV.

The lower boundary of the shaded area in Figure 7.2 is defined by the

conditions:  $\Delta\mu_{\text{Bi}} = \frac{\Delta H_{\text{Bi}_2\text{O}_3} - 3\Delta\mu_{\text{O}}}{2}$ ;  $\Delta\mu_{\text{V}} = \Delta H_{\text{BiVO}_4} - \frac{\Delta H_{\text{Bi}_2\text{O}_3}}{2} - \frac{5\Delta\mu_{\text{O}}}{2}$ . Point B

corresponds to equilibrium with Bi bulk, but is less oxygen poor than point A:



$\Delta\mu_{\text{Bi}} = 0$ ,  $\Delta\mu_{\text{O}} = -1.752$ ,  $\Delta\mu_{\text{V}} = -3.6$  eV. Finally, point D corresponds to the condition poorest in vanadium, with  $\Delta\mu_{\text{O}} = 0$ ,  $\Delta\mu_{\text{Bi}} = -2.63$ ,  $\Delta\mu_{\text{V}} = -7.98$  eV. Since we consider many defects involving hydrogen, we also calculated its atomic chemical potential from  $\text{H}_2$  gas, which is  $\mu_{\text{H}} = -3.35$  eV, taken as constant in all conditions (always hydrogen rich).

The formation energies of the intrinsic and hydrogen-related defects in  $\text{BiVO}_4$  were calculated using Eq. (1) for the conditions indicated by points A, B, C and D in Figure 7.2. To minimize the effect of spurious electrostatic interactions in charged defect calculations due to the periodic cell approximation, we have included the Makov-Payne correction<sup>57</sup> by evaluating the Ewald energy of a point charge in our supercell screened by the dielectric constant of  $\text{BiVO}_4$ , which we calculated as 7.48, 6.28, and 7.48  $\epsilon_0$  along the three lattice vectors, in good agreement with previous results.<sup>52</sup> The upper limit for these corrections for our supercell varies from 0.3 eV for singly charged defects to 10.8 eV for defects of charge 6.

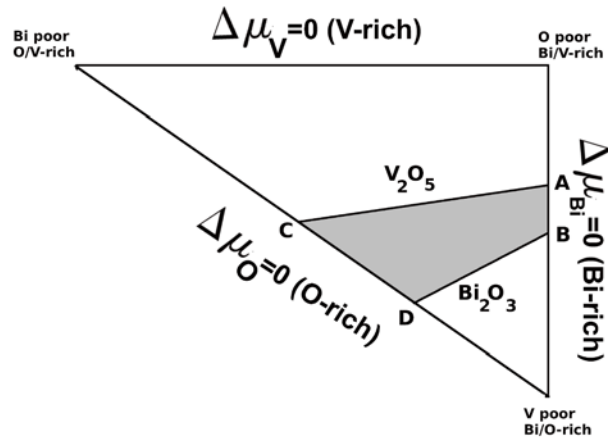


**Figure 7.2.** Range of possible stoichiometric regimes (shaded area) for the atomic chemical potentials of bismuth, vanadium and oxygen to sustain stable growth of  $\text{BiVO}_4$ .

Figure 7.3 demonstrates several important features. First, all three H-related defects studied are positively charged throughout most of the band-gap of  $\text{BiVO}_4$ , and therefore they are shallow donors of electrons to the crystal. Second, the formation energy of interstitial atomic H atoms in  $\text{BiVO}_4$  is lower than that of any intrinsic defect in  $\text{BiVO}_4$  through most of the gap of the system in any stoichiometric condition. The other H-related defects are also fairly low in formation energy relative to the intrinsic defects. Third, for O-rich crystals (conditions “C” and “D”) shown in figure 7.3c and 7.3d, the presence of Bi vacancies, which are acceptors, becomes significant, reducing the net concentration of free electrons in the conduction band, despite the presence of the shallow hydrogen donors. These defects also introduce a transition state near the middle of the band-gap ( $E_{\text{VBM}}+1$  eV) which indicates the presence of a trap state, detrimental to the transport properties that we want to enhance for the purpose of the photoelectrochemical cell. Therefore, oxygen-deficient crystal (conditions “A” and “B”) in figure 7.3a and 7.3b upon hydrogen treatment should result in a material with optimal properties for PEC water oxidation.

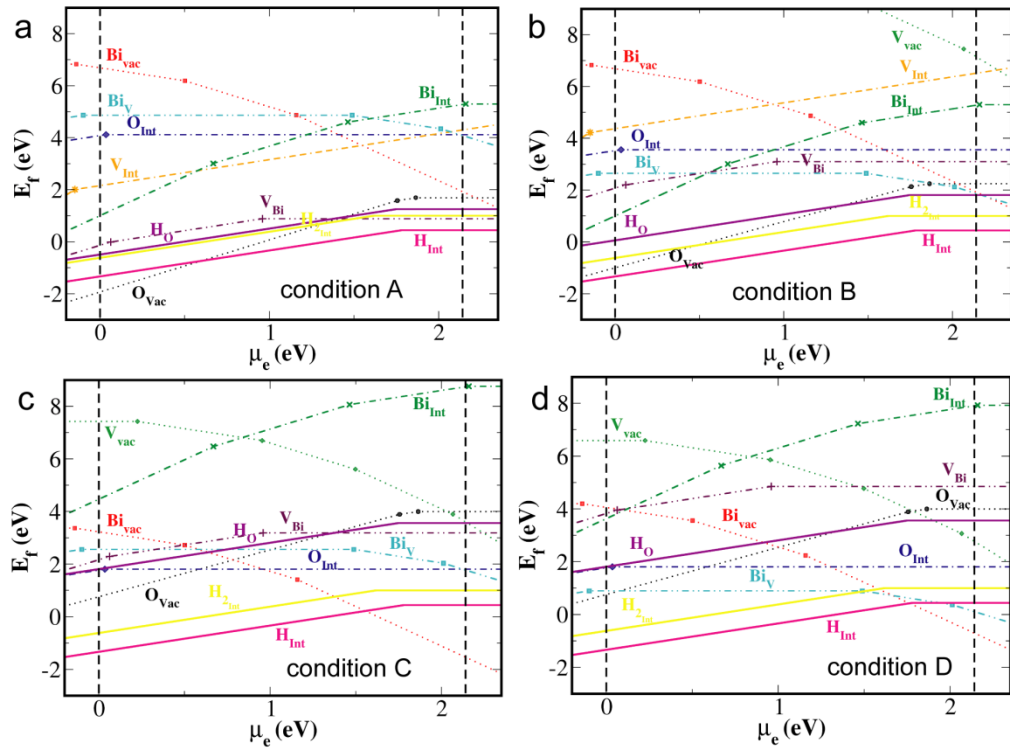


**Figure 7.3.** (a-d) Plots of formation energies of defects in  $\text{BiVO}_4$  versus the electron chemical potential (fermi level) for conditions “A” to “D” indicated in Figure 7.2. Vacancies are indicated by dotted lines, self-interstitials are indicated by dashed lines and antisites by dot-dashed lines. H-related defects are indicated by solid lines. The specific element related to these defects is indicated next to the corresponding curve. Condition “A” corresponds to oxygen-poorest, Bi-rich, condition “B” is intermediate V/O-poor and Bi rich, condition “C” is bismuth-poorest, O-rich and condition “D” is V poorest, O-rich. The vertical dashed lines indicate the calculated band-edges of the crystal ( $E_{\text{VBM}}$  set to 0). The slope of the curves indicate the charge state and the kinks in the curves indicate transition of charge states.

To prove our hypothesis and provide experimental confirmation of the DFT simulation results, we studied the effect of hydrogenation on the PEC performance of  $\text{BiVO}_4$  photoelectrodes.  $\text{BiVO}_4$  films were fabricated on fluorine-doped tin oxide (FTO) glass substrate using a seed-mediated hydrothermal method (Experimental Section).<sup>58</sup> As shown in Figure 7.4a, the FTO substrate was uniformly coated with  $\text{BiVO}_4$  particles. The cross sectional

image revealed the thickness of the seed layer and  $\text{BiVO}_4$  particle film are around 2-3  $\mu\text{m}$ .

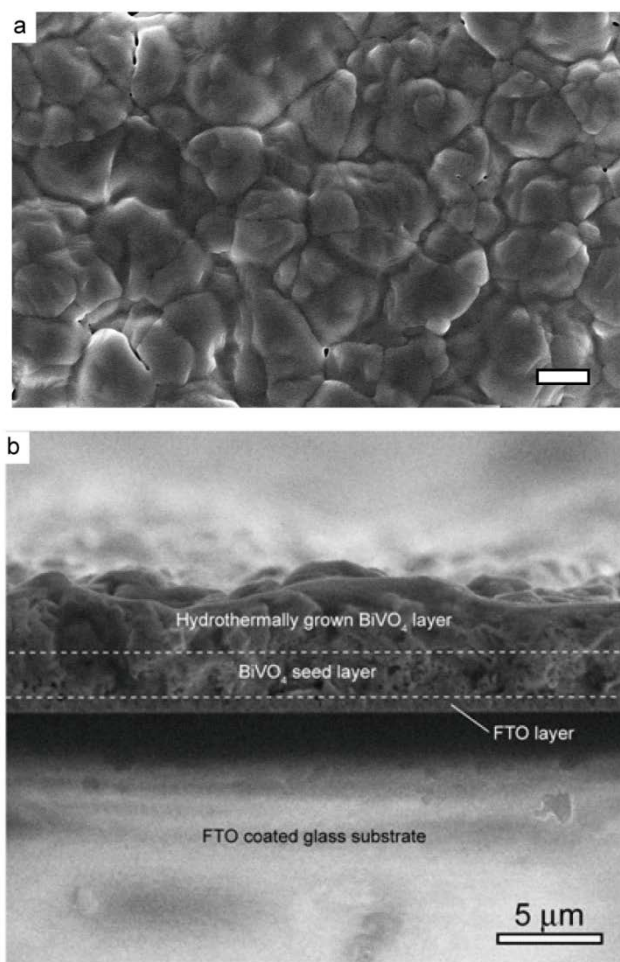


**Figure 7.4** Cross-sectional SEM image of  $\text{BiVO}_4$  film on FTO glass.

The calcined  $\text{BiVO}_4$  films were further annealed in hydrogen atmosphere in a home-built tube furnace. As shown in Figure 7.5 inset, air-annealed  $\text{BiVO}_4$  is bright yellow in color. Upon hydrogenation, it turned to yellowish green and eventually dark green as annealing temperature increased. To quantitatively

analyze the color changes, we collected diffuse reflectance UV-visible spectra for air-annealed  $\text{BiVO}_4$  and hydrogen-treated  $\text{BiVO}_4$  (denoted as  $\text{H-BiVO}_4$ ) samples. All the samples exhibited strong UV and visible light absorption. The  $\text{BiVO}_4$  sample showed an abrupt absorption onset at around 530 nm, which is consistent with its optical band-gap of 2.3-2.4 eV.<sup>30, 38</sup> In contrast,  $\text{H-BiVO}_4$  samples showed enhanced visible light absorption at wavelengths beyond 530 nm, which could be attributed to electronic transitions between defect states and band-edge states.<sup>59</sup> The UV-Vis spectral results are consistent with the observed color change for  $\text{H-BiVO}_4$  samples.

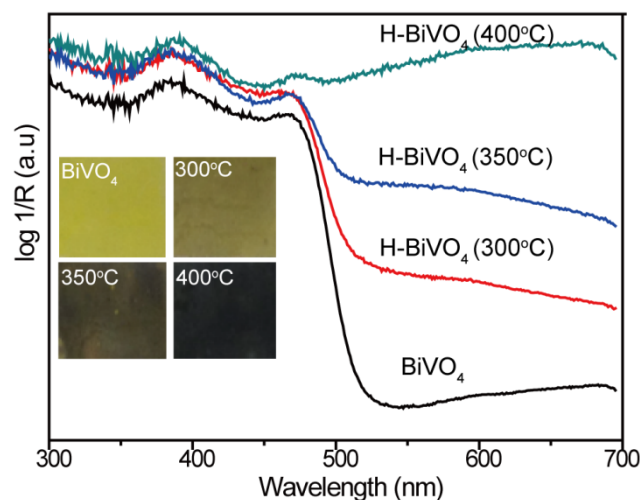


**Figure 7.5** UV-vis spectra of  $\text{BiVO}_4$  and hydrogen treated  $\text{BiVO}_4$  at 350, 400 and 450 °C.

To determine the effect of hydrogenation on the structure of  $\text{BiVO}_4$ , we compared the X-ray diffraction (XRD) spectra and Raman spectra collected for  $\text{BiVO}_4$  and  $\text{H-BiVO}_4$  samples.  $\text{BiVO}_4$  and  $\text{H-BiVO}_4$  samples exhibited similar

XRD diffraction peaks, which can be indexed to monoclinic  $\text{BiVO}_4$  (Figure 7.6a). There is no apparent change of crystal phase during hydrogenation. Furthermore, these samples exhibited characteristic Raman peaks for monoclinic  $\text{BiVO}_4$  (Figure 7.6b). Note that the  $\text{H-BiVO}_4$  samples showed considerably broader Raman peaks compared to  $\text{BiVO}_4$ , and the peak broadening becomes more substantial with the increase of hydrogen annealing temperature. The peak broadening is indicative of the degradation of material crystallinity, which could be attributed to the formation of defects such oxygen vacancies and hydrogen impurities, as predicted by the computational studies.

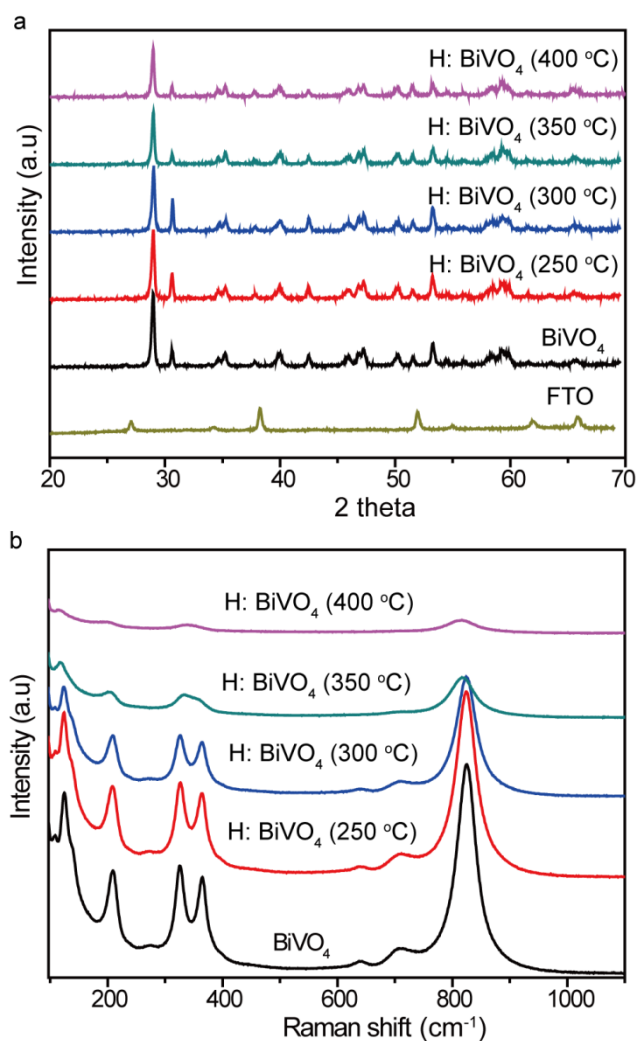


**Figure 7.6** XRD and Raman spectra of BiVO<sub>4</sub> and hydrogen treated BiVO<sub>4</sub>.

We further carried out X-ray photoelectron spectroscopy (XPS) to characterize the modification on the chemical states of BiVO<sub>4</sub> surface upon hydrogenation. As shown in Figure 7.7a, the XPS spectra of BiVO<sub>4</sub> and H-BiVO<sub>4</sub> are essentially the same. Sn and Na peaks are most likely originated from the FTO layer and the glass substrate, respectively.<sup>26</sup> Carbon is believed to be incorporated during sample preparation and subsequent handling. Figure 7.7b

shows the core level O 1s XPS spectra of BiVO<sub>4</sub> and H-BiVO<sub>4</sub> annealed at 300 °C and 400 °C. They exhibited two distinct peaks centered at 529.4 eV and 531.8 eV. The O 1s binding energy of 529.4 eV peak is consistent with the typical value reported for BiVO<sub>4</sub>.<sup>60</sup> The peak at 531.8 eV can be ascribed to the O-H bonds.<sup>60, 61</sup> The H-BiVO<sub>4</sub> sample prepared at 400 °C showed a significantly stronger signal at 531.8 eV, indicating the increased density of hydroxyl groups on the BiVO<sub>4</sub> surface as a result of hydrogenation. To balance the overall charge of the crystal, BiVO<sub>4</sub> is likely to form extra hydroxyl groups on the surface, which would lead to the creation of oxygen vacancies.



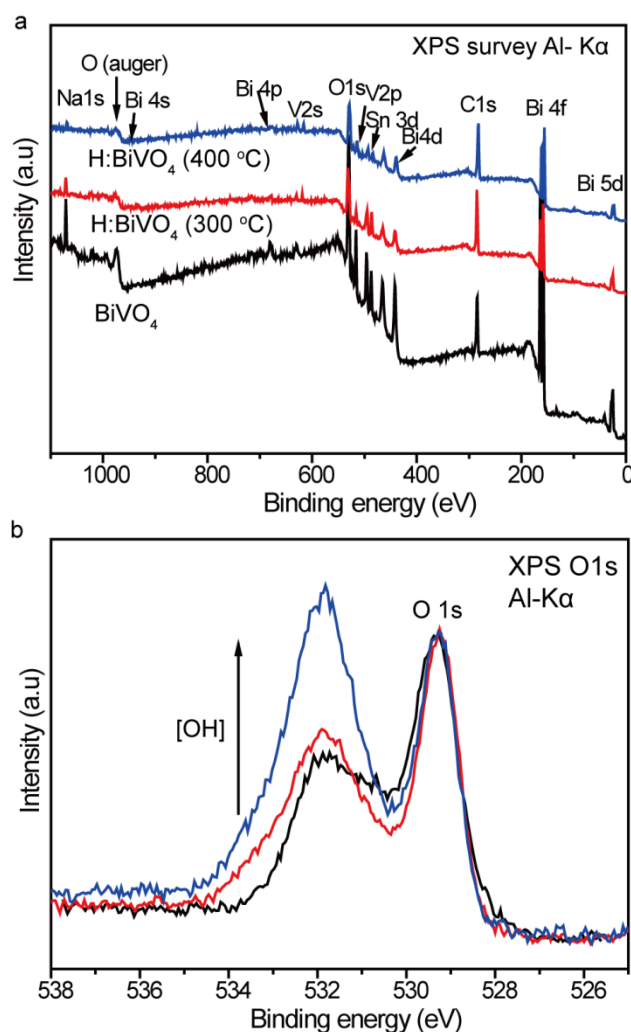


**Figure 7.7** (a) XPS survey of BiVO<sub>4</sub> and hydrogen treated BiVO<sub>4</sub>. (b) XPS O1s spectra of BiVO<sub>4</sub> and hydrogen treated BiVO<sub>4</sub>.

Figure 7.8a shows the core level V 2p XPS spectra of these samples. The binding energies of the V 2p<sub>3/2</sub> and V 2p<sub>1/2</sub> lines of BiVO<sub>4</sub> and H–BiVO<sub>4</sub> are found at 524 eV and 516.3 eV, which are consistent with the reported values for BiVO<sub>4</sub>.<sup>62</sup> The V 2p lines of H–BiVO<sub>4</sub> samples are slightly shifted to lower binding energy, which is indicative of the presence of V<sup>4+</sup> species that usually appears at the binding energy 1.1 eV lower than the V<sup>5+</sup> 2p<sub>3/2</sub> line.<sup>63, 64</sup> To

identify the tiny amount of  $V^{4+}$  (which correlates with oxygen vacancies), we analyzed the difference spectra between H-BiVO<sub>4</sub> samples (300 and 400 °C) and BiVO<sub>4</sub> (Figure 7.8b). The peaks at the binding energies of 515.0 and 516.1 eV can be attributed to  $V^{4+}$  2p<sub>3/2</sub> line and  $V^{5+}$  2p<sub>3/2</sub> line, respectively. The  $V^{4+}$  2p<sub>3/2</sub> line located at a binding energy of 1.1 eV lower than the  $V^{5+}$  2p<sub>3/2</sub> line is consistent with the values reported in previous studies.<sup>63, 64</sup> Figure 5c shows the core level Bi 4f XPS spectra of BiVO<sub>4</sub> and H-BiVO<sub>4</sub>. The Bi 4f<sub>5/2</sub> and Bi 4f<sub>7/2</sub> lines are found at the binding energies of 163.9 and 158.5 eV, respectively.<sup>62</sup> In comparison to BiVO<sub>4</sub>, the Bi 4f<sub>5/2</sub> and Bi 4f<sub>7/2</sub> lines of H-BiVO<sub>4</sub> also showed a shift of 0.2 eV toward lower binding energy, suggesting the reduction of Bi<sup>3+</sup> to lower oxidation states.<sup>65</sup> These XPS results clearly support the hypothesis that oxygen vacancies were created in H-BiVO<sub>4</sub> samples upon hydrogenation.

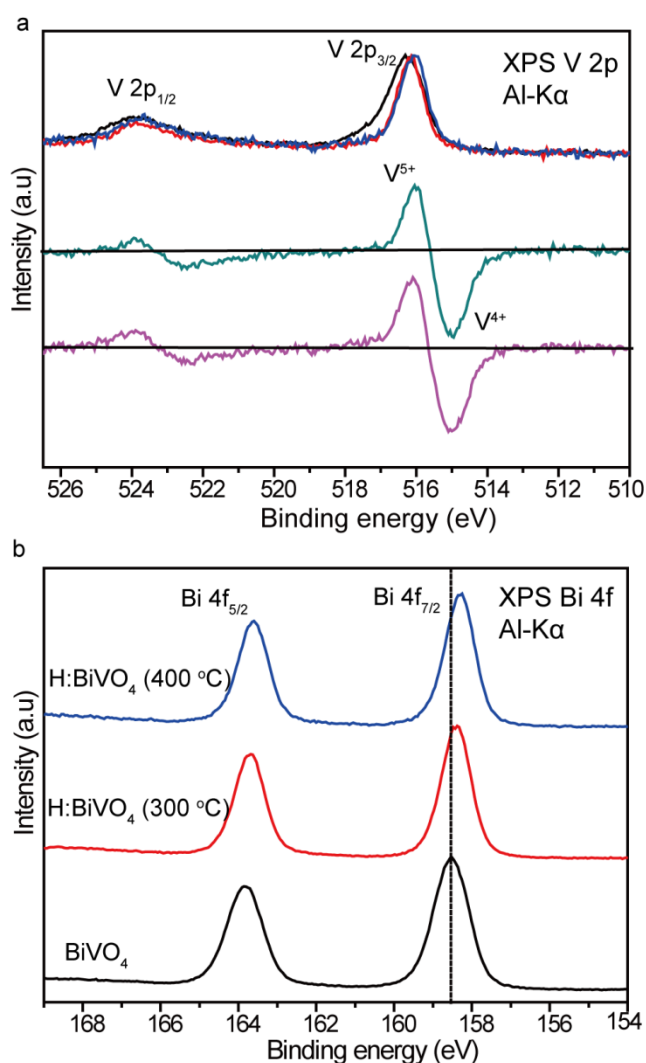


**Figure 7.8** XPS spectra of V 2p and Bi 4f spectra of BiVO<sub>4</sub> and hydrogen treated BiVO<sub>4</sub>.

According to the simulation results, both oxygen vacancies and hydrogen impurities are shallow donors for BiVO<sub>4</sub>. We determined the donor densities of BiVO<sub>4</sub> samples using electrochemical impedance spectroscopy (EIS). Electrochemical impedance was measured for BiVO<sub>4</sub> and H-BiVO<sub>4</sub> samples using a CHI 660D electrochemical station with 5 mV perturbation and a frequency range from 1 Hz to 100 kHz at different potentials. Mott-Schottky

plots were generated for BiVO<sub>4</sub> and H-BiVO<sub>4</sub> annealed at 300 °C from capacitances obtained from the EIS spectra at each potential with a frequency of 10 kHz (Figure 7.9a). Both samples showed positive slopes, as expected for *n*-type semiconductor. Since the Mott-Schottky plot was developed based on a planar electrode model, the deviation from a linear profile is commonly observed when it is used for nanostructured electrode. We chose the linear region of the Mott-Schottky profile in the range of between 0.2 V and 0.6 V vs. Ag/AgCl to calculate the slope and donor density. In comparison to BiVO<sub>4</sub>, the H-BiVO<sub>4</sub> showed a considerably smaller slope, indicating a significantly enhanced donor density. The carrier density of BiVO<sub>4</sub> and H-BiVO<sub>4</sub> (300 °C) were calculated to be  $6 \times 10^{14} \text{ cm}^{-3}$  and  $6.08 \times 10^{15} \text{ cm}^{-3}$ , respectively. While the calculation may have errors in determining the absolute value of donor density, however, the comparison of the donor densities between the pristine BiVO<sub>4</sub> and H-BiVO<sub>4</sub> is reasonable.<sup>12</sup> The increased donor density is consistent with the simulation results, which predicted that oxygen vacancies and hydrogen impurities are shallow donors for BiVO<sub>4</sub>. More importantly, the increased donor density could improve the PEC performance of BiVO<sub>4</sub> by enhancing charge transfer at the interface of BiVO<sub>4</sub> and FTO substrate. We also carried out electrochemical impedance spectroscopic measurements to study the charge transfer at the semiconductor/electrolyte interface (Figure 7.9b). The H-BiVO<sub>4</sub> electrode showed a much smaller semicircular arc in Nyquist plot, indicating

more efficient charge transfer at the interface.<sup>19</sup> By fitting the Nyquist curves, the charge transfer resistances were estimated to be around 19394 and 2256  $\Omega$  for pristine  $\text{BiVO}_4$  and H- $\text{BiVO}_4$ , respectively.

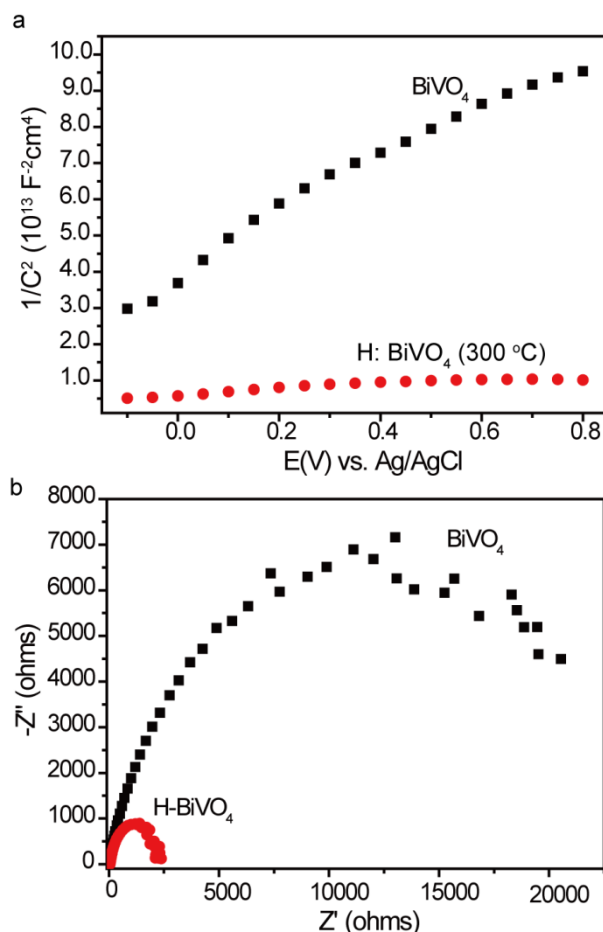


**Figure 7.9** Mott-schottky plots (a) and Nyquist plots (b) of  $\text{BiVO}_4$  and hydrogen treated  $\text{BiVO}_4$ .

We measured the PEC properties of  $\text{BiVO}_4$  and H- $\text{BiVO}_4$  with a goal of correlating their optical and electronic properties with the PEC performance. Figure 7.10a shows linear sweep voltammograms collected for  $\text{BiVO}_4$  and H- $\text{BiVO}_4$  annealed at 300  $^\circ\text{C}$ . Photocurrent density of the H- $\text{BiVO}_4$  sample is

substantially higher than the  $\text{BiVO}_4$  sample in the whole range of potentials studied. The H- $\text{BiVO}_4$  sample achieved a maximum photocurrent density of  $3.5 \text{ mA/cm}^2$  at  $1.0 \text{ V vs. Ag/AgCl}$ , which is an order of magnitude higher than that of  $\text{BiVO}_4$  ( $0.3 \text{ mA/cm}^2$ ) measured at the same potential. Figure 7.10a inset shows the photocurrent densities measured for H- $\text{BiVO}_4$  samples at  $1.0 \text{ V vs. Ag/AgCl}$  as a function of annealing temperatures. The photocurrent density gradually increases when the annealing temperature was increased from  $250$  to  $300^\circ\text{C}$ , and reached an optimal value of  $3.5 \text{ mA/cm}^2$ . Then, the photocurrent density decreases with further increase of temperature beyond  $300^\circ\text{C}$ , which could be due to the degradation of FTO substrates,<sup>11</sup> as well as the occurrence of defects such as Bi vacancies that possibly introduce trap states into the band-gap of  $\text{BiVO}_4$  as predicted by the computational studies.

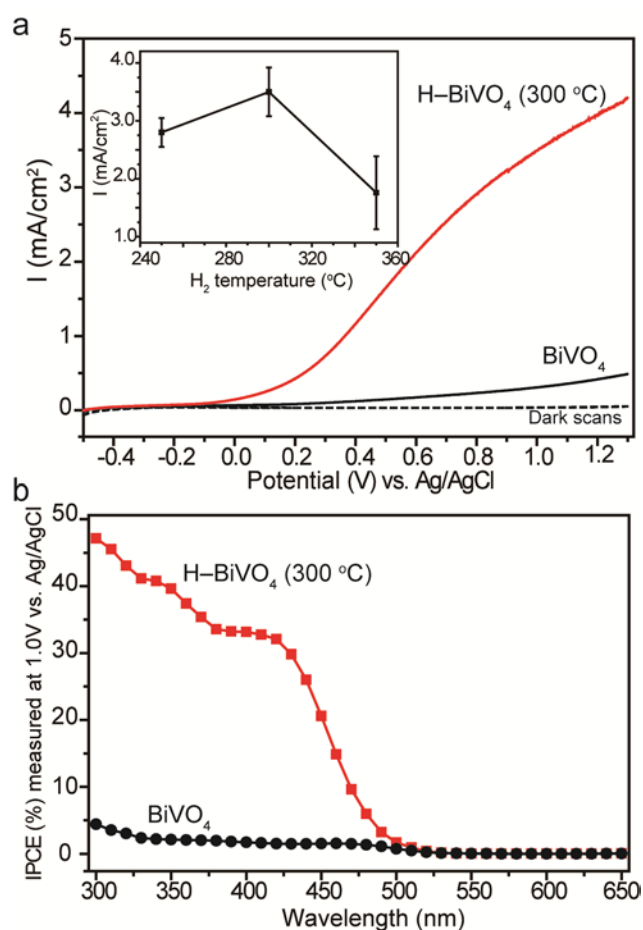


**Figure 7.10** I-V curves and IPCE spectra of BiVO<sub>4</sub> and hydrogen treated BiVO<sub>4</sub>.

To study the interplay between photoactivity and light absorption of H-BiVO<sub>4</sub> photoanodes, we also measured their incident-photon-to-current-conversion efficiency (IPCE) spectra. IPCE spectra collected for BiVO<sub>4</sub> and H-BiVO<sub>4</sub> at 1.0 V vs. Ag/AgCl showed a gradual decrease of photoactivity from 300 to 530 nm with a cutoff wavelength around 530 nm (Figure 7.10b), which is consistent with the band-gap of BiVO<sub>4</sub> (2.3-2.4 eV).<sup>30, 38</sup> Importantly, the results also indicate that there is no photoactivity beyond 530 nm, even though the H-

$\text{BiVO}_4$  samples have absorption in the entire visible light region (confirmed by UV-vis results). The light absorption at wavelength beyond 530 nm could be due to electronic transitions involving defect levels, which do not seem to directly contribute to photocurrent generation.<sup>59</sup> In comparison to  $\text{BiVO}_4$ ,  $\text{H-BiVO}_4$  showed significantly enhanced photoactivity in the wavelength region between 300 and 500 nm, which is believed to be due to the improved electrical conductivity of  $\text{H-BiVO}_4$ , and thus, the increased efficiency in charge transfer and collection. Finally, we tested the long term stability of  $\text{H-BiVO}_4$  electrodes. Figure 8 shows the photocurrent retention collected for  $\text{H-BiVO}_4$  sample at 1.0 V vs. Ag/AgCl. The electrode retains 99 % of the initial photocurrent after 13 hours. It proved that the introduction of oxygen vacancies and hydrogen impurities does not affect the electrochemical stability of  $\text{BiVO}_4$  electrode. We observed continuous evolution of gas bubbles on  $\text{H-BiVO}_4$  electrode (Figure 7.11, inset), suggesting the observed photocurrent is not due to self-oxidation of the photoelectrode. The initial decrease of photocurrent and the small photocurrent fluctuation could be due to the formation of gas bubbles on electrode surface. On the whole, these results unambiguously show that  $\text{H-BiVO}_4$  electrode has excellent photostability for water oxidation.



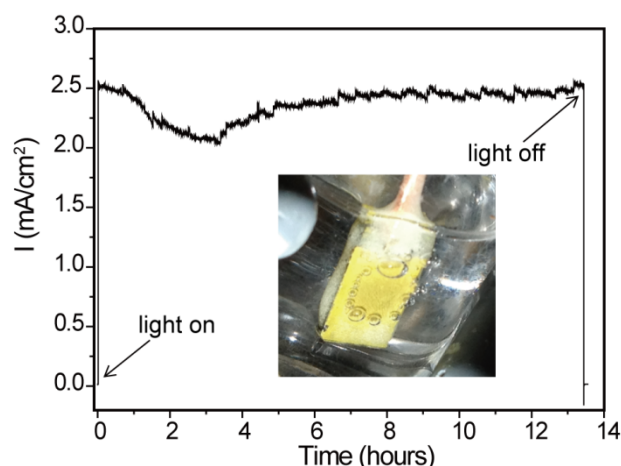


**Figure 7.11.** Photostability of H-BiVO<sub>4</sub> collected at 1.0 V vs. Ag/AgCl in 0.5 M Na<sub>2</sub>SO<sub>4</sub> solution for 13 hours. The inset shows the gas evolution on the H-BiVO<sub>4</sub> photoelectrode under light illumination.

## Conclusion

In summary, our work has demonstrated a facile method to substantially enhance the performance of BiVO<sub>4</sub> electrodes for PEC water oxidation through hydrogen treatment. H-BiVO<sub>4</sub> electrodes achieved a maximum photocurrent density of 3.5 mA/cm<sup>2</sup> at 1.0 V vs. Ag/AgCl, which is one order of magnitude higher than the value of 0.3 mA/cm<sup>2</sup> obtained for the air-annealed BiVO<sub>4</sub> at the same potential. IPCE measurements showed that H-BiVO<sub>4</sub> exhibited significantly enhanced photoactivity compared to air-annealed BiVO<sub>4</sub>, in the same wavelength region. The enhanced photoactivities were attributed to the improved efficiency in charge collection as a result of enhanced donor densities of hydrogenated BiVO<sub>4</sub> films. Indeed, our DFT calculations have predicted that oxygen vacancies as well as hydrogen impurities, whose occurrence is greatly favored by our hydrogen treatment, are shallow donors with low formation

energies for BiVO<sub>4</sub>. Further investigation of trap states in BiVO<sub>4</sub> could lead to even better performance by avoiding detrimental impurities that reduce the lifetime of carriers in the material, thus allowing even better charge collection. These H-BiVO<sub>4</sub> with higher donor density could potentially be used for other photoelectrochemical or photocatalytic applications such as dye degradation and solar driven oxygen evolution reaction.

## Reference

1. Kudo, A.; Miseki, Y., *Chem. Soc. Rev.* **2009**, 38, 253-278.
2. Walter, M. G.; Warren, E. L.; McKone, J. R.; Boettcher, S. W.; Mi, Q. X.; Santori, E. A.; Lewis, N. S., *Chem. Rev.* **2010**, 110, 6446-6473.
3. Berglund, S. P.; Flaherty, D. W.; Hahn, N. T.; Bard, J. *Phys. Chem. C* **2011**, 115, 3794-3802.
4. Cho, I. S.; Chen, Z.; Forman, A.; Kim, D. R.; Rao, P. M.; Jaramillo, T. F.; Zheng, X. *Nano Lett.* **2011**, 11, 4978-4984.
5. Li, Y.; Zhang, J. Z. *Laser Photon. Rev.* **2010**, 4, 517-528.
6. Fujishima, A.; Honda, K. *Nature* **1972**, 238, 37-38.
7. Wang, G. M.; Ling, Y. C.; Li, Y. *Nanoscale* **2012**, 4, 6682-6691.
8. Wheeler, D. A.; Wang, G. M.; Ling, Y. C.; Li, Y.; Zhang, J. Z. *Energy Environ. Sci.* **2012**, 5, 6682-6702.
9. Yang, Y.; Ling, Y. C.; Wang, G. M.; Lu, X. H.; Tong, Y. X.; Li, Y. *Nanoscale*

**2013**, 5, 1820-1824.

10. Qian, F.; Wang, G. M.; Li, Y. *Nano Lett.* **2010**, 10, 4686-4691.

11. Lin, Y. J.; Zhou, S.; Liu, X. H.; Sheehan, S.; Wang, D. W. *J. Am. Chem. Soc.* **2009**, 131, 2772-2773.

12. Wang, G. M.; Wang, H. Y.; Ling, Y. C.; Tang, Y. C.; Yang, X. Y.; Fitzmorris, R. C.; Wang, C. C.; Zhang, J. Z.; Li, Y. *Nano Lett.* **2011**, 11, 3026-3033.

13. Hwang, Y. J.; Boukai, A.; Yang, P. D. *Nano Lett.* **2009**, 9, 410-415.

14. Liu, L. P.; Wang, G. M.; Li, Y.; Li, Y. D.; Zhang, J. Z. *Nano Res.* **2011**, 4, 249-258.

15. Wang, H. Y.; Wang, G. M.; Ling, Y. C.; Lepert, M.; Wang, C. C.; Zhang, J. Z.; Li, Y., *Nanoscale* **2012**, 4, 1463-1466.

16. Wang, G. M.; Yang, X. Y.; Qian, F.; Zhang, J. Z.; Li, Y. *Nano Lett.* **2010**, 10, 1088-1092.

17. Yang, X. Y.; Wolcott, A.; Wang, G. M.; Sobo, A.; Fitzmorris, R. C.; Qian, F.; Zhang, J. Z.; Li, Y., *Nano Lett.* **2009**, 9, 2331-2336.

18. Lu, X. H.; Wang, G. M.; Xie, S. L.; Shi, J. Y.; Li, W.; Tong, Y. X.; Li, Y. *Chem. Commun.* **2012**, 48, 7717-7719.

19. Hong, S. J.; Lee, S.; Jang, J. S.; Lee, J. S. *Energy Environ. Sci.* **2011**, 4, 1781-1787.

20. Rui, L.; Yongjing, L.; Lien-Yang, C.; Sheehan, S. W.; Wangshu, H.; Fan, Z.; Hou, H. J. M.; Dunwei, W. *Angew. Chem. Int. Ed.* **2011**, 50, 499-502502.

21. Su, J. Z.; Guo, L. J.; Bao, N. Z.; Grimes, C. A. *Nano Lett.* **2011**, 11, 1928-1933.
22. Wang, G. M.; Ling, Y. C.; Wang, H. Y.; Yang, X. Y.; Wang, C. C.; Zhang, J. Z.; Li, Y., *Energy Environ. Sci.* **2012**, 5, 6180-6187.
23. Allam, N. K.; Yen, C. W.; Near, R. D.; El-Sayed, M. A. *Energy Environ. Sci.* **2011**, 4, 2909-2914.
24. Di Valentin, C.; Pacchioni, G.; Selloni, A. *Chem. Mater.* **2005**, 17, 6656-6665.
25. Ling, Y. C.; Wang, G. M.; Wheeler, D. A.; Zhang, J. Z.; Li, Y., *Nano Lett.* **2011**, 11, 2119-2125.
26. Wang, G. M.; Ling, Y. C.; Wheeler, D. A.; George, K. E. N.; Horsley, K.; Heske, C.; Zhang, J. Z.; Li, Y. *Nano Lett.* **2011**, 11, 3503-3509.
27. Wang, G. M.; Ling, Y. C.; Lu, X. H.; Wang, H. Y.; Qian, F.; Tong, Y. X.; Li, Y., *Energy Environ. Sci.* **2012**, 5, 8215-8219.
28. Li, L. S.; Yu, Y. H.; Meng, F.; Tan, Y. Z.; Hamers, R. J.; Jin, S., *Nano Lett.* **2012**, 12, 724-731.
29. Ling, Y. C.; Wang, G. M.; Reddy, J.; Wang, C. C.; Zhang, J. Z.; Li, Y. *Angew. Chem. Int. Ed.* **2012**, 51, 4074-4079.
30. Zhong, D. K.; Choi, S.; Gamelin, D. R. *J. Am. Chem. Soc.* **2011**, 133, 18370-18377.
31. Luo, W. J.; Yang, Z. S.; Li, Z. S.; Zhang, J. Y.; Liu, J. G.; Zhao, Z. Y.; Wang,

- Z. Q.; Yan, S. C.; Yu, T.; Zou, Z. G., *Energy Environ. Sci.* **2011**, 4, 4046-4051.
32. Ng, Y. H.; Iwase, A.; Kudo, A.; Amal, R., *J. Phys. Chem. Lett.* **2011**, 1, 2607-2612.
33. Sayama, K.; Nomura, A.; Arai, T.; Sugita, T.; Abe, R.; Yanagida, M.; Oi, T.; Iwasaki, Y.; Abe, Y.; Sugihara, H., *J. Phys. Chem. B* **2006**, 110, 11352-11360.
34. Li, M. T.; Zhao, L. A.; Guo, L. J., *Int. J. Hydrogen Energy* **2010**, 35, 7127-7133.
35. McDonald, K. J.; Choi, K. S., *Energy Environ. Sci.* **2012**, 5, 8553-8557.
36. Parmar, K. P. S.; Kang, H. J.; Bist, A.; Dua, P.; Jang, J. S.; Lee, J. S., *Chemsuschem* **2012**, 5, 1926-1934.
37. Walsh, A.; Yan, Y.; Huda, M. N.; Al-Jassim, M. M.; Wei, S. H., *Chem. Mater.* **2009**, 21, 547-551.
38. Liang, Y. Q.; Tsubota, T.; Mooij, L. P. A.; van de Krol, R., *J. Phys. Chem. C* **2011**, 115, 17594-17598.
39. Abdi, F. F.; van de Krol, R., *J. Phys. Chem. C* **2012**, 116, 9398-9404.
40. Seabold, J. A.; Choi, K. S., *J. Am. Chem. Soc.* **2012**, 134, 2186-2192.
41. Pilli, S. K.; Furtak, T. E.; Brown, L. D.; Deutsch, T. G.; Turner, J. A.; Herring, A. M., *Energy Environ. Sci.* **2011**, 4, 5028-5034.
42. Jo, W. J.; Jang, J. W.; Kong, K. J.; Kang, H. J.; Kim, J. Y.; Jun, H.; Parmar, K. P. S.; Lee, J. S., *Angew. Chem. Int. Ed.* **2012**, 51, 3147-3151.
43. Zhang, K.; Shi, X. J.; Kim, J. K.; Park, J. H., *Phys. Chem. Chem. Phys.*

**2012**, 14, 11119-11124.

44. Pilli, S. K.; Deutsch, T. G.; Furtak, T. E.; Turner, J. A.; Brown, L. D.;

Herring, A. M., *Phys. Chem. Chem. Phys.* **2012**, 14, 7032-7039.

45. Pilli, S. K.; Deutsch, T. G.; Furtak, T. E.; Brown, L. D.; Turner, J. A.;

Herring, A. M., *Phys. Chem. Chem. Phys.* **2013**, 15, 3273-3278.

46. Ye, H.; Lee, J.; Jang, J. S.; Bard, A. J., *J. Phys. Chem. C* **2010**, 114, 13322-13328.

47. Ye, H.; Park, H. S.; Bard, A. J., *J. Phys. Chem. C* **2010**, 115, 12464-12470.

48. Luo, W. J.; Li, Z. S.; Yu, T.; Zou, Z. G. *J. Phys. Chem. C* **2012**, 116, 5076-5081.

49. Yin, W.-J.; Wei, S.-H.; Al-Jassim, M. M.; Turner, J.; Yan, Y.-f., *Phys. Rev. B (Condensed Matter and Materials Physics)* **2011**, 83, 155102.

50. Hohenberg, P.; Kohn, W., *Phys. Rev. B* **1964**, 136, B864.

51. Kohn, W.; Sham, L. J., *Phys. Rev.* **1965**, 140, 1133.

52. Zhao, Z. Y.; Li, Z. S.; Zou, Z. G., *Phys. Chem. Chem. Phys.* **2011**, 13, 4746-4753.

53. Yin, W. J.; Wei, S. H.; Al-Jassim, M. M.; Turner, J.; Yan, Y. F. *Phys. Rev. B* **2011**, 83, 11.

54. Zhang, S. B.; Northrup, J. E., *Phys. Rev. Lett.* **1991**, 67, 2339-2342.

55. Persson, C.; Zhao, Y. J.; Lany, S.; Zunger, A., *Phys. Rev. B* **2005**, 72, 14.

56. Leao, C. R.; Lordi, V., *Phys. Rev. B* **2011**, 84, 16.

57. Makov, G.; Payne, M. C., *Phys. Rev. B* **1995**, 51, 4014-4022.
58. Su, J. Z.; Guo, L. J.; Yoriya, S.; Grimes, C. A., *Cryst. Growth Des.* **2011**, 10, 856-861.
59. Yao, S. S.; Ding, K. N.; Zhang, Y. F., *Theor. Chem. Acc.* **2010**, 127, 751-757.
60. Liu, Y. X.; Dai, H. X.; Deng, J. G.; Zhang, L.; Au, C. T., *Nanoscale* **2012**, 4, 2317-2325.
61. McCafferty, E.; Wightman, J. P., *Surf. Interface Anal.* **1998**, 26, 549-564.
62. Su, J.; Zou, X. X.; Li, G. D.; Wei, X.; Yan, C.; Wang, Y. N.; Zhao, J.; Zhou, L. J.; Chen, J. S., *J. Phys. Chem. C* **2011**, 115, 8064-8071.
63. Wang, G. M.; Lu X. H.; Ling, Y. C.; Zhai, T.; Wang H. Y.; Tong, Y. X.; Li, Y., *ACS Nano*, **2012**, 6, 10296-10302.
64. Lu, S. W.; Hou, L.; Gan, F. X., *J. Mater. Sci.* **1993**, 28, 2169-2177.
65. Dharmadhikari, V. S.; Sainkar, S. R.; Badrinarayan, S.; Goswami, A., *J. Electron Spectrosc. Relat. Phenom.* **1982**, 25, 181-189.

## Chapter 8

### **A Mechanistic Study into the Catalytic Effect of Ni(OH)<sub>2</sub> on Hematite for Photoelectrochemical Water Oxidation**

#### **Abstract**

Here we report the mechanistic studies on the catalytic effect of Ni(OH)<sub>2</sub> on hematite nanowires for photoelectrochemical water oxidation. Previous studies have shown that the incorporation of Ni(II) catalyst can significantly enhanced the photoelectrochemical performance of hematite photoanode. However, we found that the photocurrents of Ni catalyst decorated hematite photoelectrodes decay rapidly in the current-time measurements, indicating the photocurrents were not stable. We demonstrate that the enhanced photocurrent was mainly due to the photo-induced charging effect. The photoexcited holes generated in hematite efficiently oxidize Ni<sup>2+</sup> to Ni<sup>3+</sup> (0.35 V vs. Ag/AgCl), rather than oxidize water. The instability photocurrent is due to the depletion of Ni<sup>2+</sup>. We proposed that the catalytic mechanism of Ni(II) catalyst for water oxidation is a two-step process that involves the fast initial oxidation of Ni<sup>2+</sup> to Ni<sup>3+</sup>, and followed by the slow oxidation of Ni<sup>3+</sup> to Ni<sup>4+</sup>, which is the active catalytic species for water oxidation. The catalytic effect of Ni(II) catalyst was limited by the slow formation of Ni<sup>4+</sup>. Finally, we elucidate the real catalytic performance



of  $\text{Ni(OH)}_2$  on hematite for photoelectrochemical water oxidation by suppressing the photo-induced charging effect. This work could provide important insights for future studies on Ni catalyst modified photoelectrodes for water oxidation.

## Introduction

Hematite ( $\alpha\text{-Fe}_2\text{O}_3$ ) has been studied extensively as a photoanode material for photoelectrochemical water oxidation. In comparison to other semiconductor metal oxides such as  $\text{ZnO}$ <sup>1, 2</sup>,  $\text{TiO}_2$ <sup>3-5</sup> and  $\text{WO}_3$ <sup>6, 7</sup>, it has more favorable band-gap ( $\sim 2.1$  eV) with a theoretical solar-to-hydrogen efficiency of  $\sim 16\%$ <sup>8-12</sup>. However, the reported solar conversion efficiency of hematite electrodes are considerably lower than its theoretical value<sup>13-18</sup>. Poor electrode kinetics of the oxygen evolution reaction is believed to be one of the major limitations.<sup>19-21</sup> To address this issue, oxygen evolution reaction (OER) catalysts such as Co-Pi<sup>19-21</sup> and nickel based catalysts<sup>22-24</sup> have been developed to reduce the over-potential of hematite photoanode for water oxidation. Here we report a mechanistic study of the catalytic effect of  $\text{Ni(OH)}_2$  on hematite nanowire electrode for photoelectrochemical water oxidation. Significantly, we found that the enhanced anodic photocurrent and the shift of photocurrent onset potential observed for  $\text{Ni(OH)}_2$  decorated hematite electrode are mainly due to the photo-charging of Ni catalyst ( $\text{Ni}^{2+}$  oxidized to  $\text{Ni}^{3+}$ ), instead of water oxidation that was

commonly documented in previous reports. This work elucidates the real performance of  $\text{Ni}(\text{OH})_2$  catalyst on hematite photoelectrode for photoelectrochemical water oxidation, and more importantly, it provides insights into an alternative working mechanism of Ni based OER catalysts.

## Experimental Section

### *Synthesis of Hematite ( $\alpha\text{-Fe}_2\text{O}_3$ ) nanowire arrays:*

Akaganéite ( $\beta\text{-FeOOH}$ ) nanowire arrays were grown on a fluorine-doped tin oxide (FTO, TEC 8) glass substrate using a hydrothermal method reported elsewhere. A Teflon-lined stainless steel autoclave was filled with 20 mL 0.15 M  $\text{FeCl}_3$  and 1 M  $\text{NaNO}_3$  aqueous solution at pH 1.5 (adjusted by HCl). A cleaned FTO substrate was placed into the autoclave with the conductive side facing down. The sealed autoclave was heated at 95 °C for 5h in an electric oven and allowed it to cool down in air. A uniform yellow layer of  $\beta\text{-FeOOH}$  nanowire arrays was coated on the FTO glass. The nanowire-coated FTO glass was washed with ethanol and water, and then air dry.  $\alpha\text{-Fe}_2\text{O}_3$  nanowire arrays were obtained by thermal decomposition  $\beta\text{-FeOOH}$  nanowire. The  $\beta\text{-FeOOH}$  nanowires were annealed in a home-built CVD system. The tube furnace was first vacuumed to a pressure of 15 Torr, and then filled with ultrahigh purity  $\text{N}_2$ . The sample was annealed at 550 °C for 2h at 740 Torr pressure with a  $\text{N}_2$  gas flow of 50 sccm.

#### **Deposition of Ni(OH)<sub>2</sub> catalyst:**

Ni(OH)<sub>2</sub> was deposited onto hematite nanowire arrays by successive dip coating method. The hematite nanowire electrode was first dipped into 0.1 M Ni(NO<sub>3</sub>)<sub>2</sub> solution for 10 seconds, and blow-dried with compressed air. Then the electrode was dipped into 1.0 M KOH solution for 10 seconds, and blow-dried with compressed air. This two-step dip-coating process was repeated for 3 times. For the sample with small loading of Ni catalyst, we reduced the Ni(NO<sub>3</sub>)<sub>2</sub> solution concentration to 5 mM and repeated the deposition cycles for 2 times only.

#### **Material characterization:**

Scanning electron microscopy (SEM) images and energy dispersive X-ray spectroscopy (EDS) spectra were collected on a field emission SEM (Hitachi S-4800II). X-ray diffraction (XRD) spectra of hematite and blank FTO glass were collected on a Rigaku Americas Miniflex Plus powder diffractometer with the angle from 20 to 70 degree. X-ray photoelectron spectroscopy (XPS, ESCALab 250, Thermo VG) with 200W Al KR radiation in twin anode. The binding energy was calibrated using the C 1s at 284.6 eV as a reference. Electrochemical and photoelectrochemical measurements were carried out using an electrochemical workstation CHI 660D coupled with a 150W xenon lamp (Newport 6255) and an AM 1.5 global filter (Newport 81094). The electrolyte was 1.0 M KOH aqueous solution. Ag/AgCl (1 M KCl) and Pt wire were used as

reference and counter electrode in the three-electrode system.

## **Results and Discussion**

Akaganéite ( $\beta$ -FeOOH) nanowire arrays were first synthesized on fluorine-doped tin oxides (FTO) glass substrate by a hydrothermal method reported elsewhere <sup>17</sup>. These nanowires were converted into hematite via thermal annealing in an oxygen deficient condition (Experiment Section) <sup>25</sup>. Scanning electron microscopy (SEM) image revealed that the FTO substrate was uniformly covered with dense and vertically aligned nanowires (Figure 8.1a). X-ray diffraction spectra confirmed that the thermally annealed nanowires were hematite (Figure 8.1b).

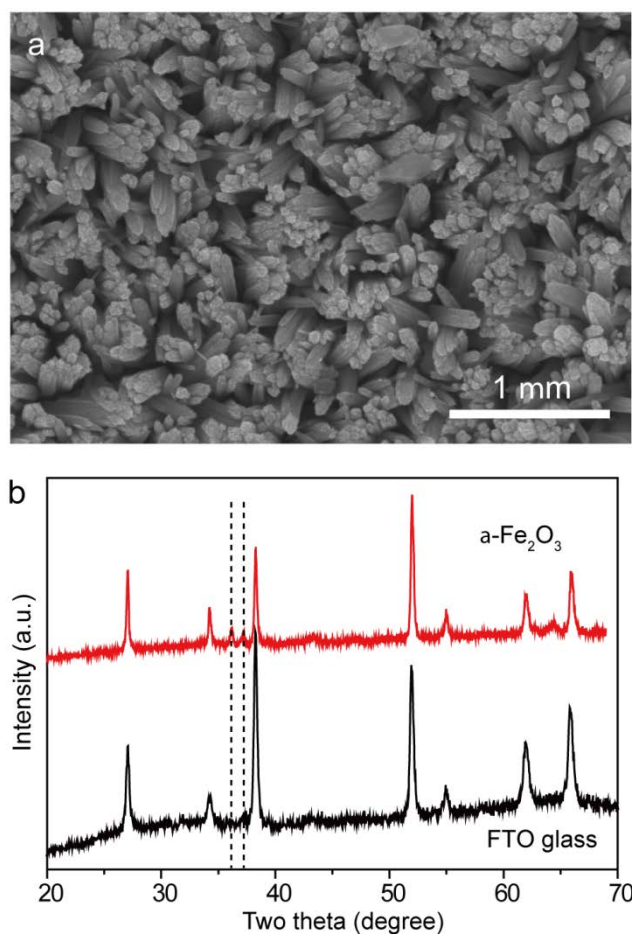


**Figure 8.1** SEM image and XRD spectra of  $\text{Fe}_2\text{O}_3$  nanowires.

$\text{Ni}(\text{OH})_2$  was deposited on hematite nanowire film by successively dipping into  $\text{Ni}(\text{NO}_3)_2$  and  $\text{NaOH}$  solutions<sup>26</sup>. SEM image collected for  $\text{Ni}(\text{OH})_2$  modified hematite nanowire film (denoted as  $\text{Ni-Fe}_2\text{O}_3$ ) showed that the catalyst layer is coated on top of the nanowire film (Figure 8.2a). Energy-dispersive X-ray spectroscopy (Figure 8.2b) analysis confirmed the presence of Ni in the  $\text{Ni-Fe}_2\text{O}_3$  sample and the atomic percentage of nickel  $[\text{Ni}/(\text{Fe}+\text{Ni})]$  was estimated to be 7 %.

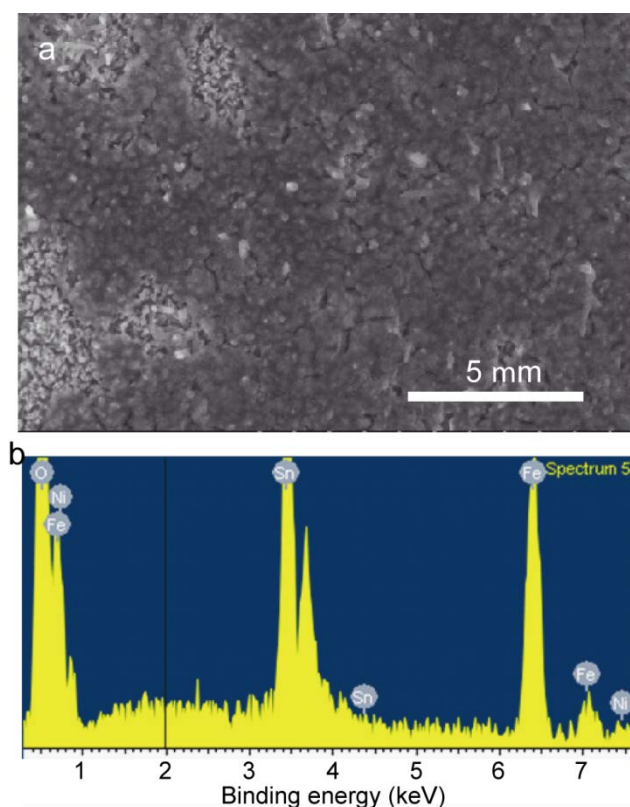


**Figure 8.2** SEM image and EDS spectrum of Ni-Fe<sub>2</sub>O<sub>3</sub>.

Photoelectrochemical measurements were performed in 1 M KOH solution, using Ni-Fe<sub>2</sub>O<sub>3</sub> as working electrode, Ag/AgCl as reference electrode and Pt wire as counter electrode. Figure 8.3 shows the linear sweep voltammograms of  $\alpha$ -Fe<sub>2</sub>O<sub>3</sub> and Ni-Fe<sub>2</sub>O<sub>3</sub> collected at a scan rate of 50 mV/s. The dark scan collected for  $\alpha$ -Fe<sub>2</sub>O<sub>3</sub> shows that water oxidation occurs at 0.6 V vs. Ag/AgCl. The current onset potential of Ni-Fe<sub>2</sub>O<sub>3</sub> electrode shifts to a more negative potential of 0.4 V vs. Ag/AgCl. Likewise, the photocurrent onset potential of Ni-Fe<sub>2</sub>O<sub>3</sub> electrode also negatively shifted by more than 200 mV under light illumination, and therefore, the overall photocurrent density of Ni-Fe<sub>2</sub>O<sub>3</sub> was

enhanced compared to  $\alpha\text{-Fe}_2\text{O}_3$  sample at the same potential. Similar photocurrent enhancement and potential shift have been reported for other Ni- and Co-based OER catalyst modified  $\alpha\text{-Fe}_2\text{O}_3$  photoelectrodes<sup>20, 24</sup>. The improved performance was attributed to the catalytic effect of Ni catalyst that suppressed the over-potential for water oxidation.

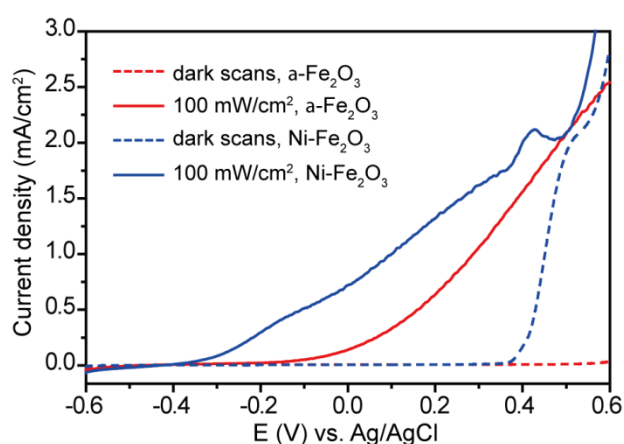


**Figure 8.3** I-V curves of  $\text{Fe}_2\text{O}_3$  and  $\text{Ni-Fe}_2\text{O}_3$  at 50 mV/s scan rate.

However, we found that the photocurrent of  $\text{Ni-Fe}_2\text{O}_3$  sample drops continuously under a constant applied potential (Figure 8.4). Figure 8.4a shows that the photocurrent-time curves collected for  $\alpha\text{-Fe}_2\text{O}_3$  and  $\text{Ni-Fe}_2\text{O}_3$  at 0.3 V vs. Ag/AgCl. The  $\text{Ni-Fe}_2\text{O}_3$  sample shows a sharp spike of photocurrent upon illumination, suggesting efficient charge separation during the initial period of illumination. However, the photocurrent density gradually decreases from 2.7  $\text{mA}/\text{cm}^2$  to  $\sim 0.3 \text{ mA}/\text{cm}^2$  within 200 seconds. The rapid reduction of current was also observed at other potentials. In contrast, the photocurrent density of

$\alpha$ -Fe<sub>2</sub>O<sub>3</sub> remains unchanged during the same period of time. These results show that the Ni-Fe<sub>2</sub>O<sub>3</sub> sample indeed exhibits a smaller “stable” photocurrent than the  $\alpha$ -Fe<sub>2</sub>O<sub>3</sub> sample at the same potential, which is contradict to the results obtained from their I-V curves (Figure 8.3). The relatively small stable photocurrent of Ni-Fe<sub>2</sub>O<sub>3</sub> could be due to the light blocking effect of the Ni(OH)<sub>2</sub> catalyst coating. To evaluate the discrepancy of photocurrent densities obtained from I-V and I-t measurements, we measure the photocurrent density retention [defined as stable  $I_{(I-t \text{ curve})}/I_{(I-V \text{ curve})}$ ] for both  $\alpha$ -Fe<sub>2</sub>O<sub>3</sub> and Ni-Fe<sub>2</sub>O<sub>3</sub> samples, as a function of applied potential. As shown in Figure 8.4b, the photocurrent retentions are less than 5 % in the potential range between -0.3V and 0.1 V vs. Ag/AgCl. The retention percentage increases slowly from 5 to 30 % when the applied potential is increased from 0.1 V to 0.4 V vs. Ag/AgCl. It suggests that the photocurrent obtained in I-V curves could be misleading, especially at lower potentials.



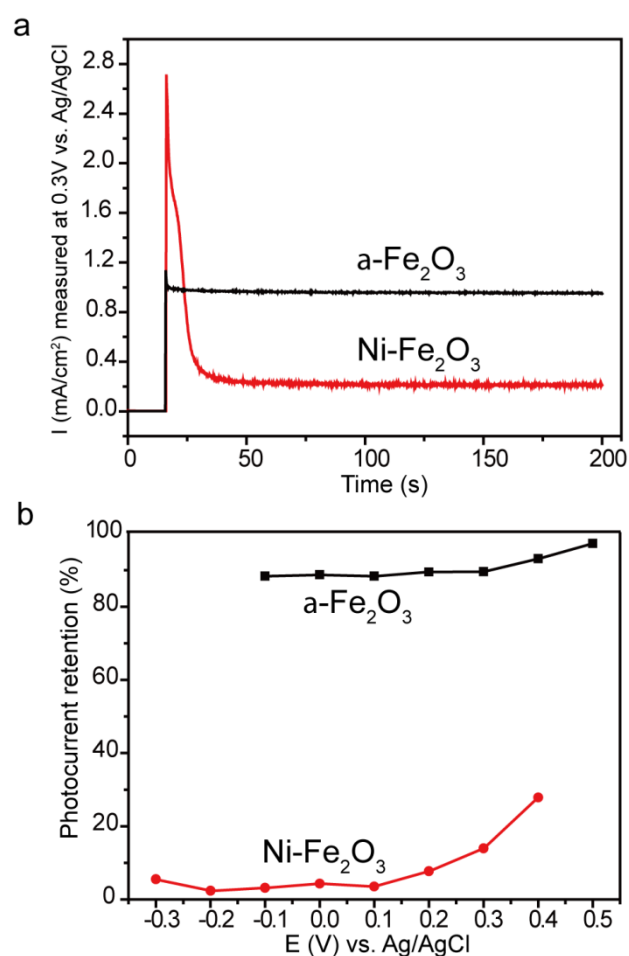


**Figure 8.4** I-t curves and photocurrent retention of Fe<sub>2</sub>O<sub>3</sub> and Ni-Fe<sub>2</sub>O<sub>3</sub>.

Similar photocurrent decay has been reported for Co-catalyst-modified hematite structure<sup>19</sup>. The decay was attributed to the blocking effect of the catalyst layer on ion diffusion into photoelectrode. However, we found that the photocurrent decay observed for Ni-Fe<sub>2</sub>O<sub>3</sub> is not related to the ion diffusion rate (will be discussed later). The continuous decay of photocurrent suggests that the enhanced photocurrent observed for Ni-Fe<sub>2</sub>O<sub>3</sub> could be attributed to chemical oxidation reactions associated with Ni catalyst, rather than water oxidation. It

has been reported that  $\text{Ni}^{4+}$  is the active catalytic species for electrochemical water oxidation<sup>22</sup>. We hypothesize that the catalytic mechanism of  $\text{Ni}(\text{OH})_2$  could be a two-step reaction (Figure 8.5), involving the initial oxidation of  $\text{Ni}^{2+}$  to  $\text{Ni}^{3+}$ , and followed by the oxidation of  $\text{Ni}^{3+}$  to  $\text{Ni}^{4+}$ . While the  $\text{Ni}^{4+}$  generated at the catalyst surface catalyzes water oxidation, it will be reduced back to  $\text{Ni}^{3+}$  immediately. The sharp photocurrent spike observed in the I-V curve of  $\text{Ni-Fe}_2\text{O}_3$  supports that the first step of  $\text{Ni}^{2+}/\text{Ni}^{3+}$  oxidation reaction is a fast process. Under light illumination, photo-excited holes quickly oxidize  $\text{Ni}^{2+}$  to  $\text{Ni}^{3+}$  that results in the efficient separation photoexcited electron-hole pairs. The enhanced photocurrent could be a result of photo-induced charging process, where the  $\text{Ni-Fe}_2\text{O}_3$  electrode functions as a pseudocapacitor electrode. The sequential decay of current suggests the depletion of  $\text{Ni}^{2+}$  species, and the second step of  $\text{Ni}^{3+}/\text{Ni}^{4+}$  oxidation reaction could be a slow process. If this hypothesis is true, the  $\text{Ni}^{3+}$  species should be accumulated at the surface of  $\text{Ni-Fe}_2\text{O}_3$  electrode and the photocurrent should be scan rate dependent as expected for an electrochemical capacitor<sup>27, 28</sup>.

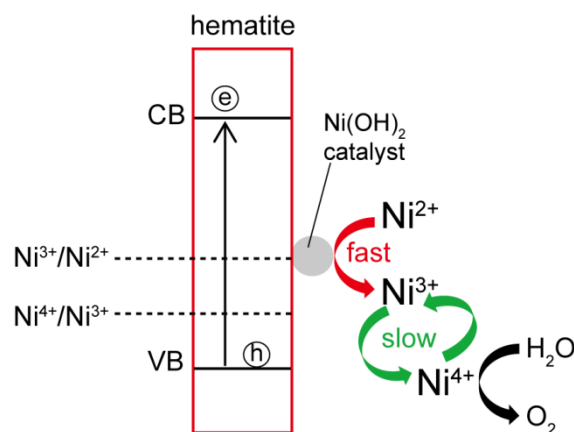


**Figure 8.5** Proposed mechanism for Ni-Fe<sub>2</sub>O<sub>3</sub> during water oxidation.

To prove the hypothesis, we collected the linear sweep voltammograms for Ni-Fe<sub>2</sub>O<sub>3</sub> and  $\alpha$ -Fe<sub>2</sub>O<sub>3</sub> electrodes at various scan rates (Figure 8.6a). The I-V curves of  $\alpha$ -Fe<sub>2</sub>O<sub>3</sub> electrodes collected at different scan rate are well overlapped (Figure 8.6b), as expected. On the contrary, the current densities of Ni-Fe<sub>2</sub>O<sub>3</sub> electrode increase substantially with the increase of scan rates, which is consistent to the electrochemical behavior of a capacitor.

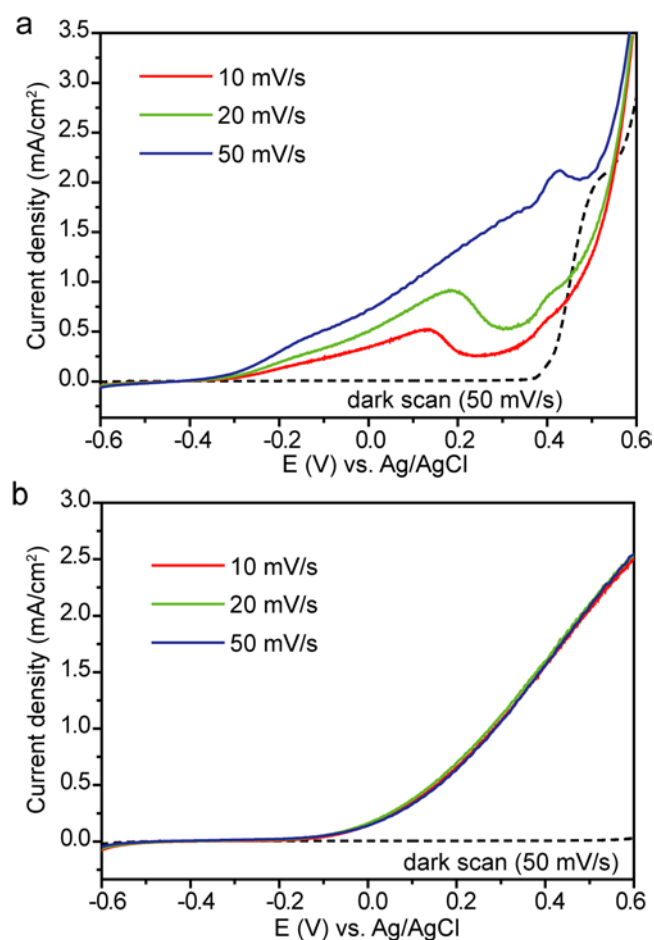


**Figure 8.6** Scan rate dependent photocurrents of Ni-Fe<sub>2</sub>O<sub>3</sub> (a) and Fe<sub>2</sub>O<sub>3</sub> (b).

Furthermore, we observed that the surface color of Ni-Fe<sub>2</sub>O<sub>3</sub> electrode turned from bright red to dark red after illumination at 0.3V vs. Ag/AgCl for 200 seconds (Figure 8.7), suggesting the formation of black Ni<sup>3+</sup> species (*e.g.*, NiOOH) on the surface. Core level X-ray photoelectron spectroscopy (XPS) Ni 2p spectra were collected before and after Ni-Fe<sub>2</sub>O<sub>3</sub> electrode was illuminated at 0.3 V vs. Ag/AgCl for 200 seconds. As shown in Figure 8.7a, the Ni 2p spectra show a complex structure with an intense satellite signals located at higher

binding energies (862.1 and 880.5 eV) adjacent to the main peaks ( $2p_{3/2}$  855.9 and  $2p_{1/2}$  873.6 eV), which can be attributed to multi-electron excitation (shake-up peaks)<sup>29</sup>. Significantly, the Ni 2p peaks became substantially broader after illumination. This Ni  $2p_{3/2}$  broad peak can be deconvoluted into a pair of peaks located at around 855.8 eV and 857.7 eV (Figure 8.7b), which are consistent to the values reported for  $Ni^{2+}$  (855.6 eV) and  $Ni^{3+}$  (857.3 eV), respectively<sup>29</sup>. The XPS analysis confirmed the presence of  $Ni^{3+}$  on  $Ni-Fe_2O_3$  electrode surface after illumination.

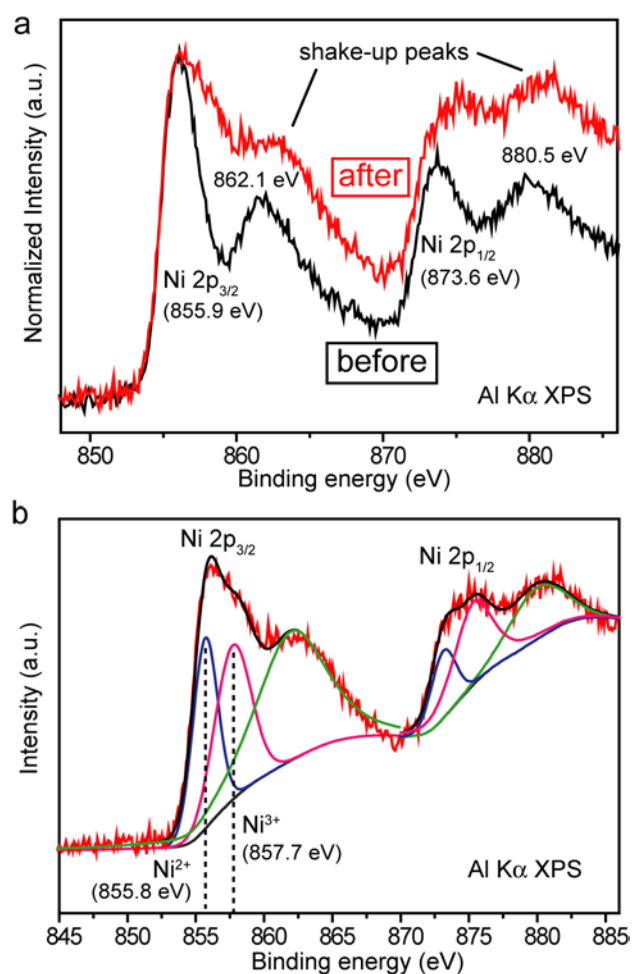


**Figure 8.7** XPS Ni 2p spectra of Ni-Fe<sub>2</sub>O<sub>3</sub> before and after light illumination.

The scan rate dependent electrochemical behavior together with the accumulation of Ni<sup>3+</sup> on hematite electrode surface strongly support that the enhanced photocurrent observed for Ni-Fe<sub>2</sub>O<sub>3</sub> sample is due to the photo-induced charging process as a result of Ni<sup>2+</sup>/Ni<sup>3+</sup> oxidation, rather than water oxidation. The continuous decay of current in the current density-time (I-t) measurement can be attributed to the gradual depletion of surface Ni<sup>2+</sup> (accumulation of Ni<sup>3+</sup>) as a result of Ni<sup>2+</sup>/Ni<sup>3+</sup> oxidation. Therefore, we hypothesized that the photocurrent could be stabilized if Ni<sup>2+</sup> can be continuously and rapidly regenerated by converting Ni<sup>3+</sup> back to Ni<sup>2+</sup>. We have recently reported that Ni<sup>3+</sup> can efficiently catalyze glucose oxidation, and simultaneously Ni<sup>3+</sup> can be reduced back to Ni<sup>2+</sup> <sup>30</sup>. Hence, we carried out electrochemical measurements for Ni-Fe<sub>2</sub>O<sub>3</sub> samples in the presence of glucose (0.1M glucose concentration), with a goal of regenerating Ni<sup>2+</sup> rapidly and therefore avoid the accumulation of Ni<sup>3+</sup> and the formation of Ni<sup>4+</sup> (Figure 8.8a). As shown in Figure 8.8b, the photocurrent density of Ni-Fe<sub>2</sub>O<sub>3</sub> sample is almost doubled in the presence of glucose, which facilitates the collection of photo-excited holes.

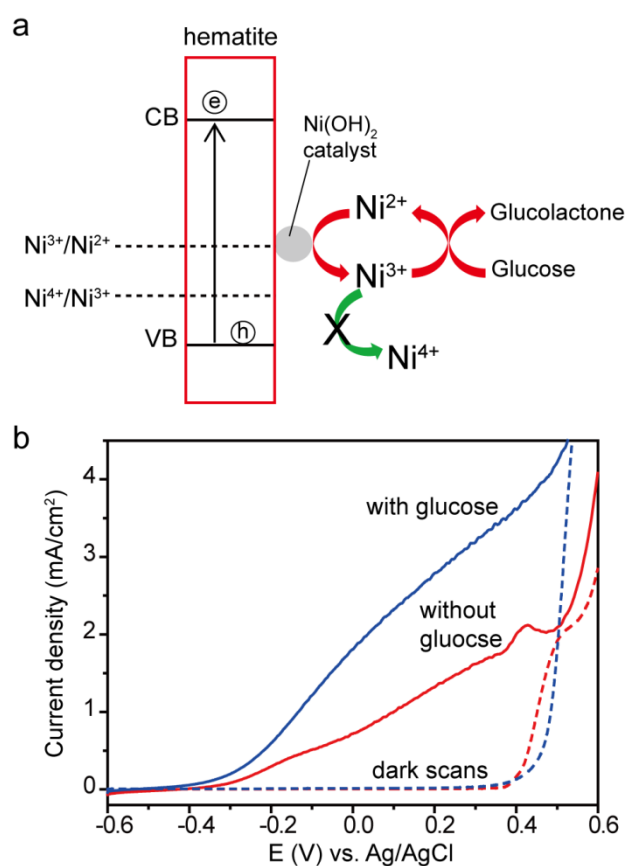


**Figure 8.8** (a) glucose used for Ni<sup>2+</sup> regeneration. (b) I-V curves of Ni-Fe<sub>2</sub>O<sub>3</sub> with/without glucose.

The I-t curves were collected for Ni-Fe<sub>2</sub>O<sub>3</sub> electrode at different potentials in the presence and absence of glucose in figure 8.9a. Significantly, the Ni-Fe<sub>2</sub>O<sub>3</sub> electrode exhibited stable photocurrent in the presence of glucose at all the potentials we studied. The current retentions of the Ni-Fe<sub>2</sub>O<sub>3</sub> sample are almost 100 % in the potential range from -0.4 to 0.4 V vs. Ag/AgCl (Figure 8.9b). Ni 2p XPS spectrum collected for the Ni-Fe<sub>2</sub>O<sub>3</sub> electrode after illumination exhibits only Ni<sup>2+</sup> peaks, indicating Ni<sup>3+</sup> species were not accumulated at the electrode surface in the presence of glucose in figure 8.10. These results support our

hypothesis that the current can be stabilized upon the fast regeneration of  $\text{Ni}^{2+}$  through  $\text{Ni}^{3+}$  catalyzed glucose oxidation. More importantly, these results also proved that the enhanced photocurrent is mainly due to the photo-induced charging process and the current decay is because of the depletion of  $\text{Ni}^{2+}$ . Since the photocurrent can be stabilized by adding glucose without modifying surface catalyst coating, it also suggests that the current decay is not due to the possible blocking effect of catalyst coating on ion diffusions, which was previously observed for Co-based catalysts<sup>19</sup>.

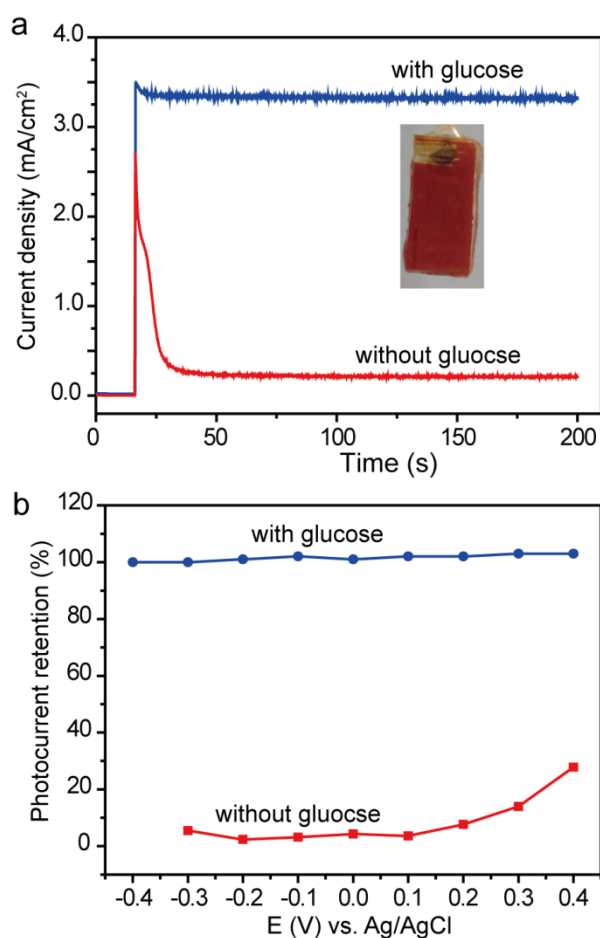


**Figure 8.9** I-t curves and photocurrent retention curve of Ni-Fe<sub>2</sub>O<sub>3</sub> with/without



glucose.

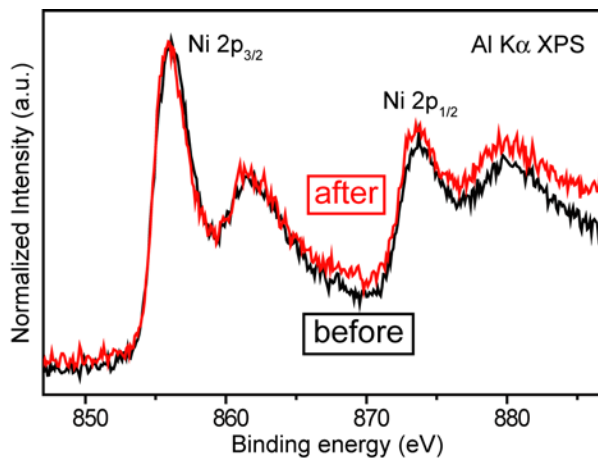


**Figure 8.10** XPS Ni2p of Ni-Fe<sub>2</sub>O<sub>3</sub> before and after light illumination with glucose.

Furthermore, we seek to understand the real catalytic performance of Ni(II) catalyst by suppressing the photo-induced charging effect *via* decreasing the loading amount of Ni(OH)<sub>2</sub> and measured the I-V curves for Ni-Fe<sub>2</sub>O<sub>3</sub> sample at a slow scan rate. We minimized the loading amount of Ni(OH)<sub>2</sub> by decreasing the precursor concentration (Experiment Section). While the catalyst coating was not obvious in the SEM image of Ni-Fe<sub>2</sub>O<sub>3</sub> nanowire arrays, EDX analysis revealed the existence of Ni (Figure 8.11). The atomic percentage of Ni was estimated to be 1 %.

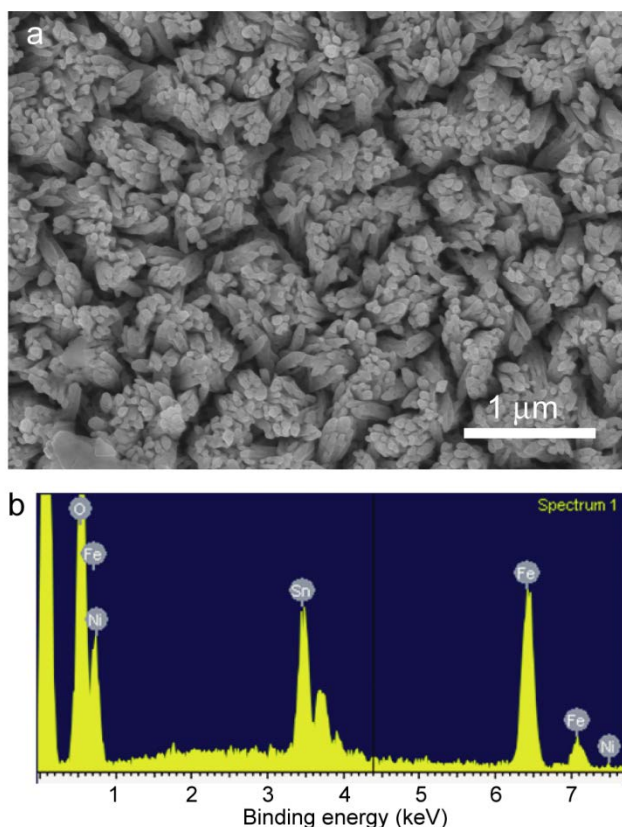


**Figure 8.11** SEM image and EDX of Ni-Fe<sub>2</sub>O<sub>3</sub> with small loading amount of Ni catalyst.

Figure 8.12a shows the I-V curves of Ni-Fe<sub>2</sub>O<sub>3</sub> with small catalyst loading (denoted as s-Ni-Fe<sub>2</sub>O<sub>3</sub>) electrodes collected at different scan rates. In the dark scans, s-Ni-Fe<sub>2</sub>O<sub>3</sub> samples show the same current onset potentials at 0.35 V vs. Ag/AgCl that corresponds to characteristic Ni<sup>2+</sup>/Ni<sup>3+</sup> oxidation potential, again confirming the successful loading of Ni(OH)<sub>2</sub> catalyst<sup>30</sup>. Upon light illumination, the onset potentials were negatively shifted. Significantly, these I-V curves collected at different scan rates are well overlapped at higher potential region (0.3-0.6 V vs. Ag/AgCl), suggesting the effect of photo-induced charging has been substantially reduced in s-Ni-Fe<sub>2</sub>O<sub>3</sub> samples. The

corresponding I-t curves collected for the Ni-Fe<sub>2</sub>O<sub>3</sub> electrode also show stable photocurrent at different potentials (Figure 8.12b). The s-Ni-Fe<sub>2</sub>O<sub>3</sub> electrode exhibits a current retention [stable  $I_{(I-t \text{ curve})}/I_{(I-V \text{ curve})}$ ] percentage of above 85% in the potential range of 0.1-0.4 V vs. Ag/AgCl at the scan rate of 20 mV/s, which is much higher than the values obtained for the Ni-Fe<sub>2</sub>O<sub>3</sub> sample with high catalyst loading, at the same potentials. Apparently, the s-Ni-Fe<sub>2</sub>O<sub>3</sub> collected at 20 mV/s exhibit a slightly negatively shifted onset potential and increased photocurrent density compared to the  $\alpha$ -Fe<sub>2</sub>O<sub>3</sub> sample. Although the enhancement is relatively small, it presents the real catalytic performance of Ni catalyst on hematite electrode for photoelectrochemical water oxidation.

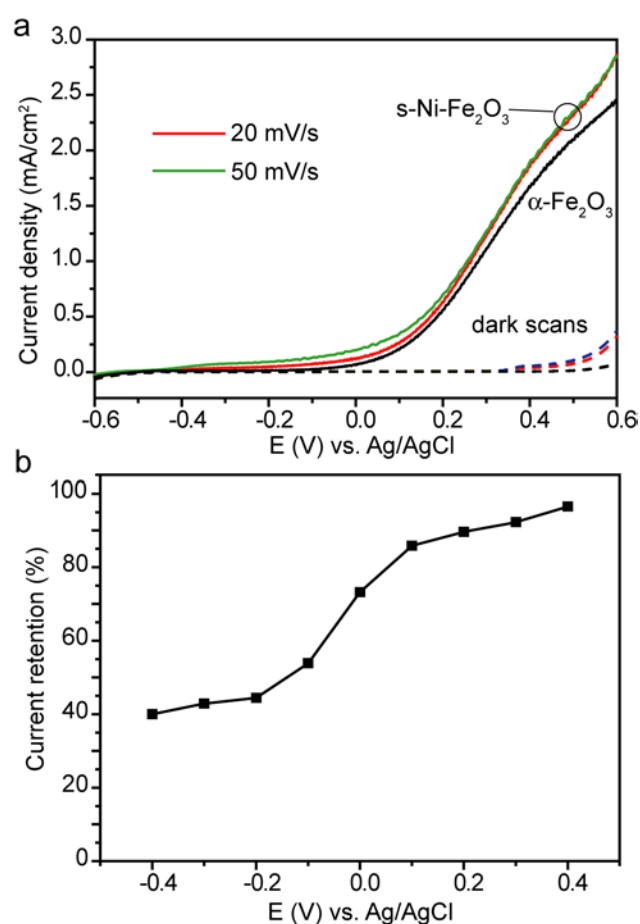


**Figure 8.12** I-V curves and photocurrent retention of Ni-Fe<sub>2</sub>O<sub>3</sub> with small loading amount of Ni catalyst.

## Conclusion

In summary, our studies showed that the enhanced photocurrent observed for Ni-catalyst modified hematite photoanode could be due to the photo-charging effect that converts Ni<sup>2+</sup> to Ni<sup>3+</sup>, rather than water oxidation. Therefore, the rapid decay of current is due to the depletion of Ni<sup>2+</sup>, as well as the slow formation of Ni<sup>4+</sup> (for water oxidation). To evaluate the real catalytic performance of Ni catalyst for photoelectrochemical water oxidation, the loading amount of Ni

catalyst on photoelectrode should be minimized to suppress the photo-induced charging effect. The I-V curves should be collected at a slow scan rate and compare the current obtained from I-V and I-t curves at the same potentials. This work provide important insights for future studies on Ni catalyst modified photoelectrodes for water oxidation.

## Reference

1. Qiu, Y. C.; Yan, K. Y.; Deng, H.; Yang, S. H., *Nano Letters* **2012**, 12, 407.
2. Wang, G. M.; Yang, X. Y.; Qian, F.; Zhang, J. Z.; Li, Y., *Nano Letters* **2010**, 10, 1088.
3. Wang, G. M.; Wang, H. Y.; Ling, Y. C.; Tang, Y. C.; Yang, X. Y.; Fitzmorris, R. C.; Wang, C. C.; Zhang, J. Z.; Li, Y., *Nano Letters* **2011**, 11, 3026.
4. Cho, I. S.; Chen, Z. B.; Forman, A. J.; Kim, D. R.; Rao, P. M.; Jaramillo, T. F.; Zheng, X. L., *Nano Letters* **2011**, 11, 4978.
5. Xu, M.; Da, P. M.; Wu, H. Y.; Zhao, D. Y.; Zheng, G. F., *Nano Letters* **2012**, 12, 1503.
6. Wang, G. M.; Ling, Y. C.; Wang, H. Y.; Yang, X. Y.; Wang, C. C.; Zhang, J. Z.; Li, Y., *Energy & Environmental Science* **2012**, 5, 6180.
7. Qin, D. D.; Tao, C. L.; Friesen, S. A.; Wang, T. H.; Varghese, O. K.; Bao, N. Z.; Yang, Z. Y.; Mallouk, T. E.; Grimes, C. A., *Chemical Communications* **2012**, 48, 729

8. Wheeler, D. A.; Wang, G. M.; Ling, Y. C.; Li, Y.; Zhang, J. Z., *Energy & Environmental Science* **2012**, 5, 6682.
9. Lin, Y. J.; Yuan, G. B.; Sheehan, S.; Zhou, S.; Wang, D. W., *Energy & Environmental Science* **2011**, 4, 4862.
10. Sivula, K.; Le Formal, F.; Gratzel, M., *ChemSusChem* **2011**, 4, 432.
11. Lin, Y. J.; Yuan, G. B.; Liu, R.; Zhou, S.; Sheehan, S. W.; Wang, D. W., *Chemical Physics Letters* **2011**, 507, 209.
12. Wang, G. M.; Ling, Y. C.; Li, Y., *Nanoscale* **2012**, 4, 6682.
13. Li, L.; Yu, Y.; Meng, F.; Tan, Y.; Hamers, R. J.; Jin, S., *Nano Letters* **2012**, 12, 724.
14. Kay, A.; Cesar, I.; Gratzel, M., *Journal of the American Chemical Society* **2006**, 128, 15714.
15. Lin, Y. J.; Zhou, S.; Sheehan, S. W.; Wang, D. W., *Journal of the American Chemical Society* **2011**, 133, 2398.
16. Gao, H. W.; Liu, C.; Jeong, H. E.; Yang, P. D., *Acs Nano* **2012**, 6, 234.
17. Ling, Y. C.; Wang, G. M.; Wheeler, D. A.; Zhang, J. Z.; Li, Y., *Nano Letters* **2011**, 11, 2119.
18. Wang, G. M.; Ling, Y. C.; Wheeler, D. A.; George, K. E. N.; Horsley, K.; Heske, C.; Zhang, J. Z.; Li, Y., *Nano Letters* **2011**, 11, 3503.
19. Zhong, D. K.; Gamelin, D. R., *Journal of the American Chemical Society* **2010**, 132, 4202.

20. Zhong, D. K.; Sun, J. W.; Inumaru, H.; Gamelin, D. R., *Journal of the American Chemical Society* **2009**, 131, 6086.
21. Zhong, D. K.; Cornuz, M.; Sivula, K.; Graetzel, M.; Gamelin, D. R., *Energy & Environmental Science* **2011**, 4, 1759.
22. Yeo, B. S.; Bell, A. T., *Journal of Physical Chemistry C* **2012**, 116, 8394.
23. Liao, P. L.; Keith, J. A.; Carter, E. A., *Journal of the American Chemical Society* **2012**, 134, 13296.
24. Sun, K.; Park, N.; Sun, Z. L.; Zhou, J. G.; Wang, J.; Pang, X. L.; Shen, S. H.; Noh, S. Y.; Jing, Y.; Jin, S. H.; Yu, P. K. L.; Wang, D. L., *Energy & Environmental Science* **2012**, 5, 7872.
25. Ling, Y. C.; Wang, G. M.; Reddy, J.; Wang, C. C.; Zhang, J. Z.; Li, Y., *Angewandte Chemie International Edition* **2012**, 51, 4074.
26. Wang, G. M.; Ling, Y. C.; Lu, X. H.; Wang, H. Y.; Qian, F.; Tong, Y. X.; Li, Y., *Energy & Environmental Science* **2012**, 5, 8215.
27. Yu, G. H.; Hu, L. B.; Liu, N. A.; Wang, H. L.; Vosgueritchian, M.; Yang, Y.; Cui, Y.; Bao, Z. A., *Nano Letters* **2011**, 11, 4438.
28. Wang, G. M.; Ling, Y. C.; Qian, F.; Yang, X. Y.; Liu, X. X.; Li, Y., *Journal of Power Sources* **2011**, 196, 5209.
29. Park, K. W.; Choi, J. H.; Kwon, B. K.; Lee, S. A.; Sung, Y. E.; Ha, H. Y.; Hong, S. A.; Kim, H.; Wieckowski, A., *Journal of Physical Chemistry B* **2002**, 106, 1869.

30. Wang, G. M.; Lu, X. H.; Zhai, T.; Ling, Y. C.; Wang, H. Y.; Tong, Y. X.; Li, Y., *Nanoscale* **2012**, 4, 3123.



## Chapter 9

### Solar Driven Hydrogen gas releasing from Urea and Human Urine

#### Abstract

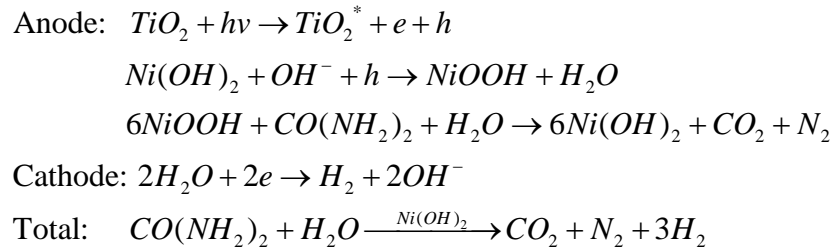
Urea has been considered as a potential hydrogen carrier, while the conventional methods to extract hydrogen from urea are typically energy intensive processes. Here we report the first demonstration of solar driven hydrogen releasing from urea and human urine in a photoelectrochemical cell, with the assistance of  $\text{Ni(OH)}_2$  modified metal oxide photoelectrodes (*e.g.*,  $\text{TiO}_2$  and  $\alpha\text{-Fe}_2\text{O}_3$ ). Under light illumination, photoexcited holes generated in the metal oxide electrode oxidize urea while photoexcited electrons reduce water to produce hydrogen at the Pt counter electrode.  $\text{Ni(OH)}_2$  serves as a urea oxidation catalyst. Urea oxidation was achieved at the metal oxide electrode under a small external bias or even at zero bias. Significantly, we observed continuous and stable hydrogen evolution at Pt electrode in both urea and human urine solution under AM 1.5G ( $100 \text{ mW/cm}^2$ ) light illumination. This work presents a safe, low energy cost, environmental friendly and sustainable method to produce hydrogen, and simultaneously treat urine.

## Introduction

Central to the success of realizing hydrogen economy and the widespread use of hydrogen powered fuel cells is the sustainable supply of hydrogen.<sup>1-8</sup> Numerous chemicals such as hydrazine and metal hydrides have been considered as promising hydrogen carriers.<sup>6</sup> However, most of them are costly, highly toxic, flammable,<sup>3, 4, 9</sup> and more importantly, their supply is not sustainable in origin. These factors limit their potential use as hydrogen storage materials. Recently, urea [ $\text{CO}(\text{NH}_2)_2$ ] has been proposed as an alternative hydrogen carrier. It has a gravimetric hydrogen content of 6.71 %, which fulfills U.S. Department of Energy targets for hydrogen storage in transportation applications.<sup>10</sup> Additionally, it is widely available, low cost, non-flammable, non-toxic, and chemically stable for storage and transportation.<sup>6, 10</sup> More importantly, urea is a major component (with an average of 0.33 M urea) of human/animal urine.<sup>11</sup> Million tons of human urine is produced per day. Urea available in these urines is 500 times more than the market demand of 0.5 Mt/day.<sup>6</sup> However, human urine has been considered as wastewater that could raise environmental issues such as nitrate contamination of ground water.<sup>12, 13</sup> It is scientifically and economically important to recover hydrogen directly from urea in urine. Current methods for hydrogen releasing from urea are typically high energy consuming and not cost effective. For example, hydrogen can be obtained by high temperature cracking of ammonia, which is a product of urea

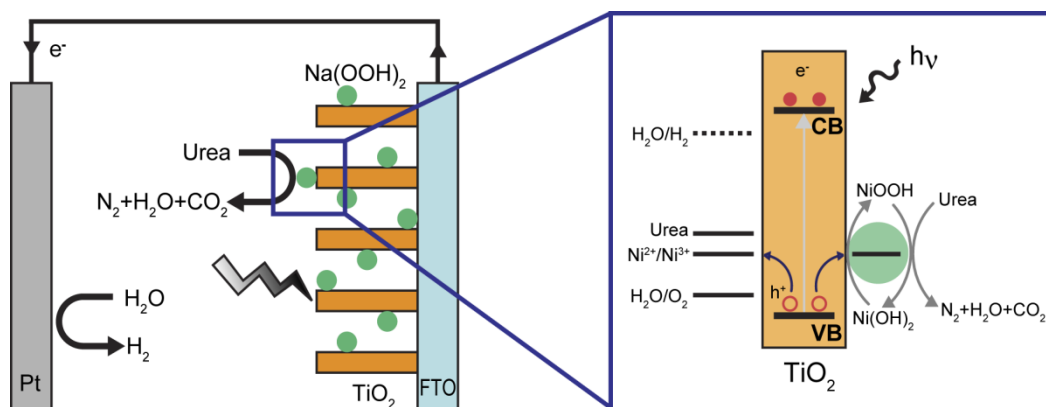
decomposition.<sup>14</sup> This is an energy-intensive process, which also involves potential safety issues and substantially increases the production cost of hydrogen. Alternatively, urea aqueous solution can be electrolyzed to produce hydrogen with the assistance of urea oxidation catalyst under certain external bias.<sup>11, 12</sup> However, urea electrolysis also consumes substantial amount of electrical energy, which makes it less practical. Ideally, the decomposition of urea for hydrogen releasing should be driven by a renewable energy source, and hydrogen can be generated directly from human urine. Here we demonstrated, for the first time, solar-driven hydrogen releasing from urea as well as directly from human urine at zero bias in a photoelectrochemical cell with metal oxide nanowire arrays as photoelectrode and  $\text{Ni(OH)}_2$  as urea oxidation catalyst. In comparison to urea electrolysis and ammonia cracking processes, this method is cheaper, safer, and more importantly, it is a carbon-free, sustainable method to produce hydrogen.

Figure 9.1 illustrates the mechanism of solar-driven hydrogen production from urea in a photoelectrochemical cell that composed of a metal oxide, such as  $\text{TiO}_2$ , photoelectrode modified with electrochemical catalyst  $\text{Ni(OH)}_2$  and a Pt counter electrode. The chemical reactions at electrodes are described by the following equations:



Under light illumination, photoexcited holes ( $h$ ) produced in  $\text{TiO}_2$  will oxidize  $\text{Ni(OH)}_2$  to  $\text{NiOOH}$ , which is known to be a electrochemical catalyst for urea oxidization to produce  $\text{N}_2$  and  $\text{CO}_2$ .<sup>11, 12</sup> On the other counter electrode, the photoexcited electrons ( $e$ ) will reduce water to produce hydrogen. To achieve efficient production of hydrogen from urea under a reduced external bias or even at zero-bias, metal oxide electrode materials should have band-edge positions straddled the water reduction potential and the urea oxidation potential, as well as relatively small band-gap for visible light absorption. In this work, we exemplified this concept with two metal oxide semiconductors  $\text{TiO}_2$  and  $\alpha\text{-Fe}_2\text{O}_3$ , which have been commonly used as electrode materials for photoelectrochemical water oxidation<sup>15-25</sup>.  $\alpha\text{-Fe}_2\text{O}_3$  has a favorable band-gap energy of 2.1 eV, which allows absorption of a significant portion of visible light, and thus, could lead to a good solar conversion efficiency.<sup>16, 24, 26, 27</sup> However, an external bias may need to be applied for hydrogen production due to the low lying conduction band of  $\alpha\text{-Fe}_2\text{O}_3$ . In contrast,  $\text{TiO}_2$  have band-edge positions well aligned with the potentials of urea oxidation and water reduction, and thereby, hydrogen releasing could be achieved at zero bias. The major drawback

of TiO<sub>2</sub> electrode would be the limited absorption of visible light due to its large band-gap (rutile TiO<sub>2</sub>, 3.0 eV).<sup>19, 22, 28-30</sup>



**Figure 9.1.** Energy diagram of a photoelectrochemical device consisting of TiO<sub>2</sub> nanowire-arrayed photoanode decorated with Ni(OH)<sub>2</sub> catalyst, and a Pt counter electrode. It illustrates the basic operation mechanism for hydrogen releasing from urea.

## Experimental Section

### Synthesis of TiO<sub>2</sub> nanowire arrays

TiO<sub>2</sub> nanowire arrays were synthesized on a FTO glass substrate by a hydrothermal method reported elsewhere.<sup>1</sup> A Ti precursor solution was prepared by mixing 15 ml concentrated HCl (36.5%) with 15 ml deionized water, and follow by the addition of 0.5 ml titanium n-butoxide. A piece of FTO substrate was cleaned with acetone, ethanol and then water. The substrate was transferred into a Teflon lined autoclaves, with the substrate against the inner wall of the autoclave, and then filled with Ti precursor solution. The sealed autoclave was heated at 150 °C in an electric oven for 5h. After the autoclave cooled down,

FTO substrate was coated with a uniform white film of TiO<sub>2</sub> nanowire arrays.

The as-prepared TiO<sub>2</sub> nanowires were annealed in air at 550 °C for 3h. The air-annealed TiO<sub>2</sub> nanowires were further annealed in hydrogen atmosphere at 350 °C for additional 30 min in a home-built tube furnace system filled with ultrahigh purity hydrogen gas (99.999%, Praxair). The white TiO<sub>2</sub> nanowire film turns into pale yellow in color after hydrogen treatment.

#### **Synthesis of $\alpha$ -Fe<sub>2</sub>O<sub>3</sub> nanowire arrays**

Hematite ( $\alpha$ -Fe<sub>2</sub>O<sub>3</sub>) nanowire arrays were synthesized by a hydrothermal method described elsewhere.<sup>2</sup> A piece of pre-cleaned FTO substrate was put into an autoclave filled with a 20 ml precursor solution mixed with 0.15 M ferric chloride and 1 M sodium nitrate solution. The pH of the precursor solution was adjusted to be 1.5 by HCl solution. The sealed autoclave was heated at 95 °C for 4h. After the autoclave cooled down, FTO substrate was coated with a uniform yellow film of  $\beta$ -FeOOH nanowire arrays.

The  $\beta$ -FeOOH nanowire film was further annealed in N<sub>2</sub>-air mixture at 550 °C for 2 hr at 740 Torr pressure with a N<sub>2</sub> flow rate of 50 sccm. The tube furnace was first vacuumed to a pressure of 15 Torr, and then filled with ultrahigh purity N<sub>2</sub> (99.998%, Praxair). The initial oxygen content was estimated to be 0.43 % (O<sub>2</sub>/(O<sub>2</sub>+N<sub>2</sub>), volume %).

#### **Deposition of Ni(OH)<sub>2</sub> (urea oxidation catalyst)**

Ni(OH)<sub>2</sub> was deposited onto  $\alpha$ -Fe<sub>2</sub>O<sub>3</sub> and TiO<sub>2</sub> nanowire arrays by successive dip-coating method. 0.1 M Ni(NO<sub>3</sub>)<sub>2</sub> aqueous solution and 1 M NaOH solution were prepared. Nanowire-arrayed electrodes were dipped into Ni(NO<sub>3</sub>)<sub>2</sub> solution for 10 s, then blown dry with compressed air. Then the electrodes were dipped into NaOH solution for another 10 s, and blown dry with compressed air. This process is considered as one dip-coating cycle. The deposition of Ni(OH)<sub>2</sub> was repeated for 3 dip-coating cycles.

### **Material Characterization**

X-ray diffraction (XRD) spectra of TiO<sub>2</sub> and  $\alpha$ -Fe<sub>2</sub>O<sub>3</sub> were collected on a Rigaku Americas Miniflex Plus powder diffractometer. Scanning electron microscopy (SEM) images and energy dispersive X-ray spectroscopy (EDS) spectra were collected with a field emission SEM (Hitachi S-4800II). Electrochemical and photoelectrochemical measurements were collected using an electrochemical workstation CHI 660D coupled with a 150 W xenon lamp (Newport 6255) with an AM 1.5 global filter (Newport 81094). The urea electrolyte was 0.33 M urea in 1.0 M NaOH aqueous solution. Real urine was obtained from a healthy male adult (age: 26). The urine electrolyte was human urine solution mixed with a 1.0 M NaOH solution. Ag/AgCl and a Pt wire were used as reference and counter electrode, respectively. The gas produced on the Pt counter electrode was collected by a 1-mL syringe. The composition of the produced gas was analyzed by a gas chromatography (Agilent 3000).

## Results and Discussion

TiO<sub>2</sub> nanowire arrays were synthesized on fluorine-doped tin oxide (FTO) glass substrate using a hydrothermal method reported elsewhere.<sup>19</sup> The as-prepared TiO<sub>2</sub> nanowires were annealed in air at 550 °C for 3h, followed by annealing in hydrogen atmosphere at 350 °C for additional 30 min. Hydrogen-treatment has been reported to be a effective method in enhancing the photoelectrochemical performance for TiO<sub>2</sub>.<sup>19</sup> SEM image shows that the FTO substrate is covered with dense and aligned TiO<sub>2</sub> nanowires, which have diameters in a range between 100 and 200 nm (Figure 9.2a). X-ray diffraction studies (Figure 9.2b) confirm that TiO<sub>2</sub> nanowires are tetragonal rutile structure (PDF No. 88-1175). To promote urea oxidation at the photoanode, we deposited Ni(OH)<sub>2</sub> as an electrochemical catalyst on TiO<sub>2</sub> nanowires by successively dipping into Ni(NO<sub>3</sub>)<sub>2</sub> and NaOH aqueous solution (Experimental Section,),  $Ni^{2+} + 2OH^{-} \rightarrow Ni(OH)_2$ . While the deposition of Ni(OH)<sub>2</sub> did not change the morphology of TiO<sub>2</sub> nanowires, energy-dispersive X-ray spectroscopy (EDS) analysis confirm the presence of Ni on TiO<sub>2</sub> nanowire arrays. The atom ratio of Ni to Ti [Ni/(Ni+Ti)] was determined to be 1.5 %. These data support the successful preparation of Ni(OH)<sub>2</sub> modified TiO<sub>2</sub> nanowire arrays.



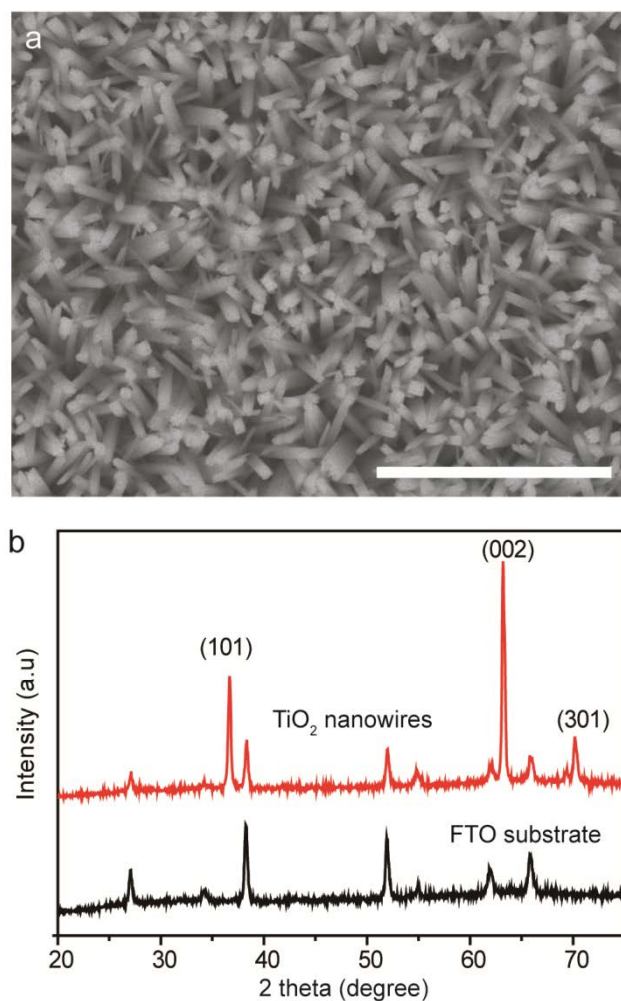


**Figure 9.2.** (a) SEM image of  $\text{TiO}_2$  nanowire arrays grown on a FTO substrate. Scale bar:  $2\ \mu\text{m}$  (b) XRD diffraction spectra collected for a blank FTO substrate and  $\text{TiO}_2$  nanowire arrays grown on a FTO substrate.

We studied the performance of  $\text{TiO}_2$  and  $\text{Ni(OH)}_2$  modified  $\text{TiO}_2$  ( $\text{Ni-TiO}_2$ ) nanowire arrays for electrochemical and photoelectrochemical urea oxidation. Figure 9.3a shows the cyclic voltammograms collected for  $\text{TiO}_2$  and  $\text{Ni-TiO}_2$  in the potential window between  $-0.5$  and  $+1.0$  V vs.  $\text{Ag/AgCl}$ . In the absence or presence of urea, the cyclic voltammograms collected for  $\text{TiO}_2$  (without

$\text{Ni(OH)}_2$  catalyst) show only small background current without obvious redox peaks, indicating that neither water oxidation nor urea oxidation occurs in this potential window. In a NaOH electrolyte solution (absence of urea), Ni-TiO<sub>2</sub> shows a well-defined redox peaks in the potential range between 0.3 and 0.4 V vs. Ag/AgCl (Figure 9.3a inset), corresponding to the  $\text{Ni}^{2+}/\text{Ni}^{3+}$  transition. The drastically increased anodic current at the potential of 0.7 V vs. Ag/AgCl can be attributed to water oxidation. Significantly, the cyclic voltammogram of Ni-TiO<sub>2</sub> shows a substantially enhanced current at the potential of 0.3 V vs. Ag/AgCl or above, in a urea electrolyte solution (0.33 M urea in 1.0 M NaOH aqueous solution). The result suggests that urea was oxidized at the Ni-TiO<sub>2</sub> electrode. Urea oxidation commences at the  $\text{Ni}^{2+}/\text{Ni}^{3+}$  transition potential indicative of  $\text{Ni}^{3+}$  as an electrochemical catalyst for urea oxidation.  $\text{Ni}^{3+}$  species have been reported to be good catalysts for catalytic oxidation of small organic molecules such as glucose.<sup>31</sup> The anodic peak in forward sweep is ascribed to the consumption of active  $\text{Ni}^{3+}$  sites, and the peak in reverse sweep could be due to the desorption of urea molecules from the electrode surface.<sup>12</sup> Note that urea oxidation and water oxidation occur at the potentials of 0.35 and 0.7 V vs. Ag/AgCl, respectively. It indicates that urea oxidation is more favorable than water oxidation, in the presence of  $\text{Ni(OH)}_2$  catalyst. This is consistent to the recent report on the excellent electrochemical catalytic specificity of  $\text{Ni(OH)}_2$  for urea oxidation, compared to water oxidation.<sup>11</sup>

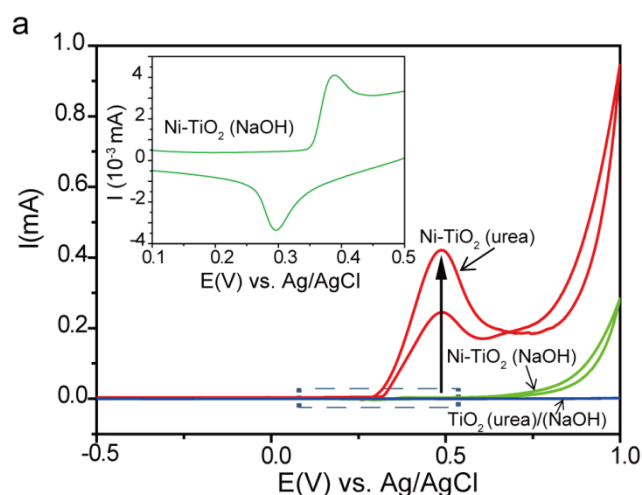


**Figure 9.3** Cyclic voltammograms of  $\text{TiO}_2$ ,  $\text{Ni-TiO}_2$  with/without urea.

We further studied the performance of  $\text{TiO}_2$  and  $\text{Ni-TiO}_2$  for urea oxidation under light illumination. It is expected that photovoltage generated in  $\text{TiO}_2$  and  $\text{Ni-TiO}_2$  can facilitate urea oxidation by reducing the need of external bias. As shown in Figure 9.4, the onset potential of urea oxidation shifts to  $-0.92\text{ V}$  vs.  $\text{Ag/AgCl}$  under light illumination, which is indeed substantially lower than the potential required for urea electrolysis ( $0.35\text{ V}$  vs.  $\text{Ag/AgCl}$ ). In comparison to  $\text{TiO}_2$ ,  $\text{Ni-TiO}_2$  exhibits an even more negative onset potential for urea oxidation (Figure 9.4a). This is because the photoexcited holes in  $\text{Ni-TiO}_2$  oxidized  $\text{Ni(OH)}_2$  to  $\text{NiOOH}$ , which further catalyze the oxidation of urea by reducing the electrode overpotential. Meanwhile, photoexcited electrons transfer to Pt counter electrode to reduce water to hydrogen gas. Figure 9.4b shows the photocurrent density-time response curve measured for  $\text{Ni-TiO}_2$  at zero-bias using a two-electrode electrochemical cell, under chopped AM 1.5G

illumination ( $100 \text{ mW/cm}^2$ ). Significantly, a stable photocurrent density of  $0.25 \text{ mA/cm}^2$  was achieved at zero-bias. To our knowledge, this is the first demonstration of solar driven urea oxidation and hydrogen production without the need of external bias. The photocurrent transient could be due to inefficient charge separation at the interface of electrolyte and  $\text{TiO}_2$  under zero-bias.

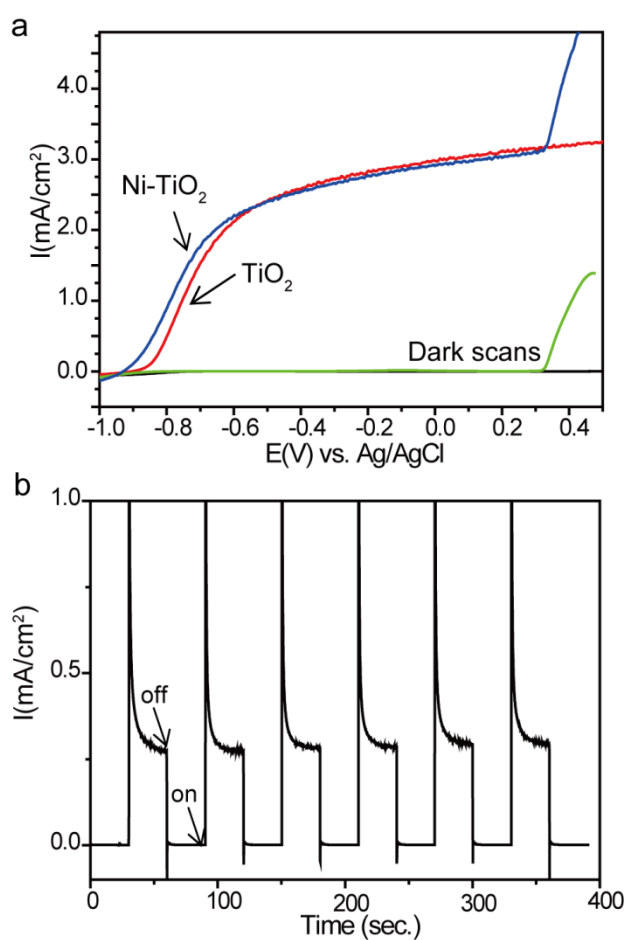


**Figure 9.4** I-V curves of  $\text{TiO}_2$  and  $\text{Ni-TiO}_2$  (a), and I-t curves at zero bias of  $\text{Ni-TiO}_2$  (b).

We also tested the long time stability for solar driven urea oxidation at -0.2 V vs. Ag/AgCl in figure 9.5a. There is no decay in photocurrent density at least for 4000 s, suggesting the solar driven urea oxidation is sustainable for long time operation. Continuous gas evolution was also observed on Pt wires under light illumination on photoanode, as shown in Figure 9.5 inset. Gas chromatography analysis demonstrates that the collected gas on Pt cathode is hydrogen in figure 9.5b.

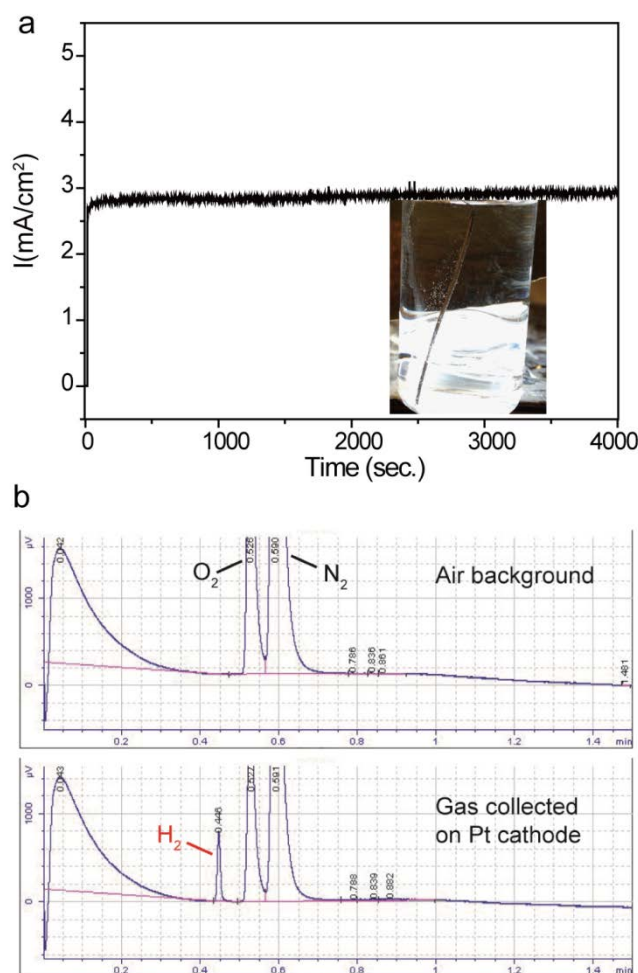


**Figure 9.5** (a) I-t curves of Ni-TiO<sub>2</sub> in urea solution; the inset shows the gas production on Pt cathode. (b) GC analysis indicates the hydrogen gas

production.

Based on the successful demonstration of solar-driven urea oxidation, we extended the efforts to study solar-driven oxidation of urea present in real human urine. The cyclic voltammogram measured for Ni-TiO<sub>2</sub> in a urine electrolyte solution shows an anodic peak at the potential of around 0.35 V vs. Ag/AgCl (Figure 9.6), which is the same as that obtained in the urea electrolyte solution, indicative of catalytic oxidation of urea present in human urine.

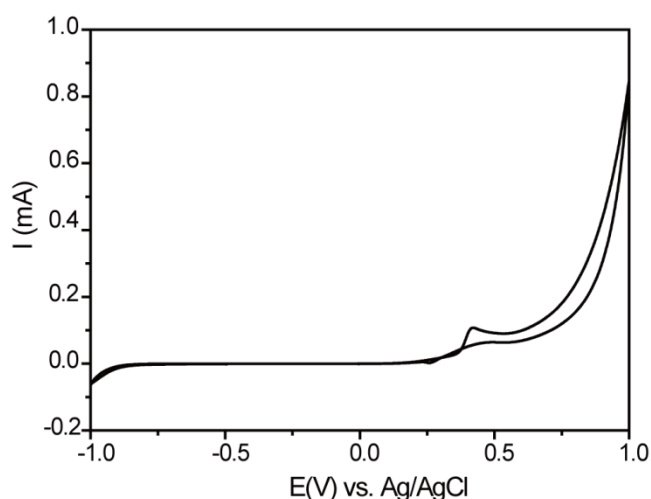


**Figure 9.6** Cyclic voltammograms of Ni-TiO<sub>2</sub> in human solution.

Likewise, this onset potential for urea oxidation also shifts to a lower potential of -0.9 V vs. Ag/AgCl under light illumination, as expected (Figure 9.7a). Significantly, the Ni-TiO<sub>2</sub> electrode also shows a stable photocurrent density in urine solution at least for 4000 s (Figure 9.7b) and we observed continuous hydrogen gas evolution on the Pt wire counter electrode at -0.2 V vs. Ag/Ag.

The successful demonstration of solar driven hydrogen releasing from human urine provides a sustainable solution for hydrogen generation and new insights for wastewater treatment.

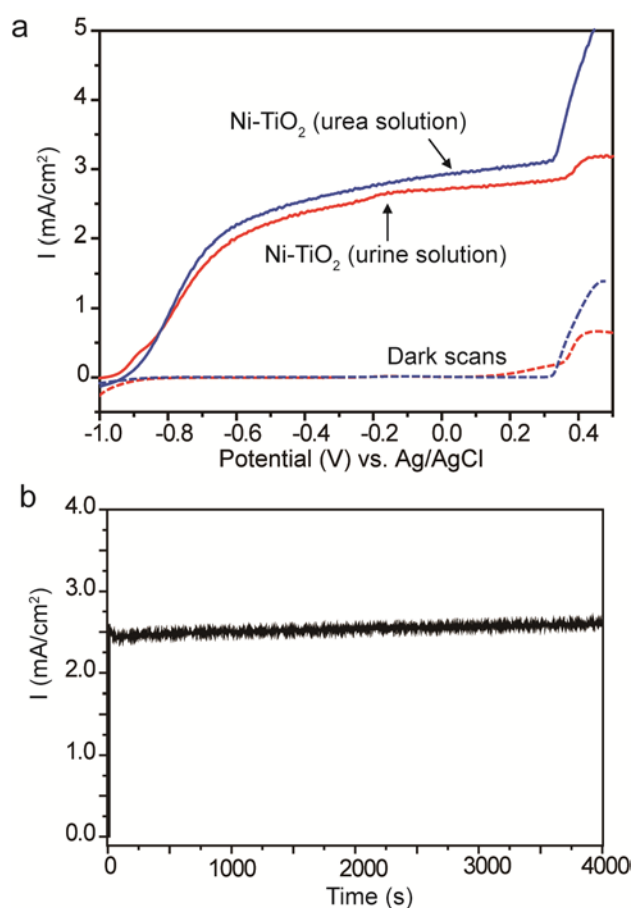


**Figure 9.7** (a) I-V curves of Ni-TiO<sub>2</sub> in urea and human solution. (b) I-t curve of Ni-TiO<sub>2</sub> in human urine solution.

Photocurrent density-time response curve, collected for Ni-TiO<sub>2</sub> electrode in urine solution at zero bias under chopped light illumination, shows a photocurrent density of 0.25 mA/cm<sup>2</sup> (Figure 9.8). This result proves that solar driven urea oxidation in real human urine can also be achieved at zero bias,

which is critical for practical application.

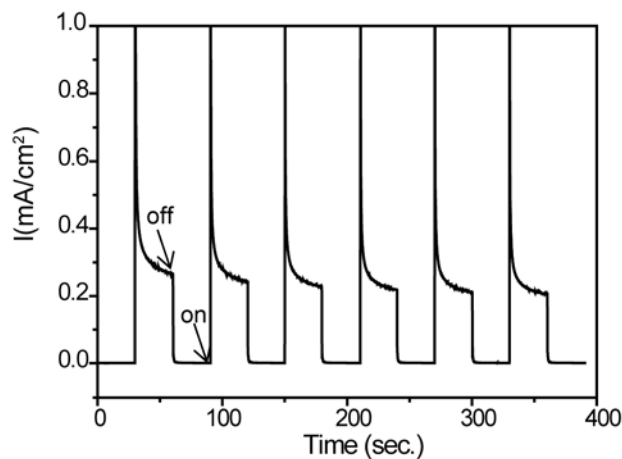


**Figure 9.8** I-t curves of Ni-TiO<sub>2</sub> at zero bias in human urine solution.

Although Ni-TiO<sub>2</sub> shows great promises as a photoanode for urea oxidation, the solar conversion efficiency of TiO<sub>2</sub> electrode is still limited by its large band-gap. In this regard, we also explore the potentials of  $\alpha$ -Fe<sub>2</sub>O<sub>3</sub> nanowire arrays for urea oxidation.  $\alpha$ -Fe<sub>2</sub>O<sub>3</sub> have a favorable band-gap of 2.1 eV for visible light absorption, has recently attracted a lot of attention for its potential use as electrode materials for water oxidation.<sup>16, 24, 26, 27, 32</sup> Recently, we have demonstrated a facile method to improve the electrical conductivity of  $\alpha$ -Fe<sub>2</sub>O<sub>3</sub>, which is one of the major limitations for  $\alpha$ -Fe<sub>2</sub>O<sub>3</sub>.<sup>15</sup>  $\alpha$ -Fe<sub>2</sub>O<sub>3</sub> nanowire arrays were synthesized according to a hydrothermal method reported elsewhere,<sup>15</sup> and coated with Ni(OH)<sub>2</sub> by the same dip-coating method used for TiO<sub>2</sub> samples.  $\alpha$ -Fe<sub>2</sub>O<sub>3</sub> nanowires are densely packed on the FTO substrate with average



diameter in a range between 100 and 150 nm (Figure 9.9a). XRD spectra collected from the nanowire film show characteristic diffraction peaks for  $\alpha$ -Fe<sub>2</sub>O<sub>3</sub> (Figure 9.9b).

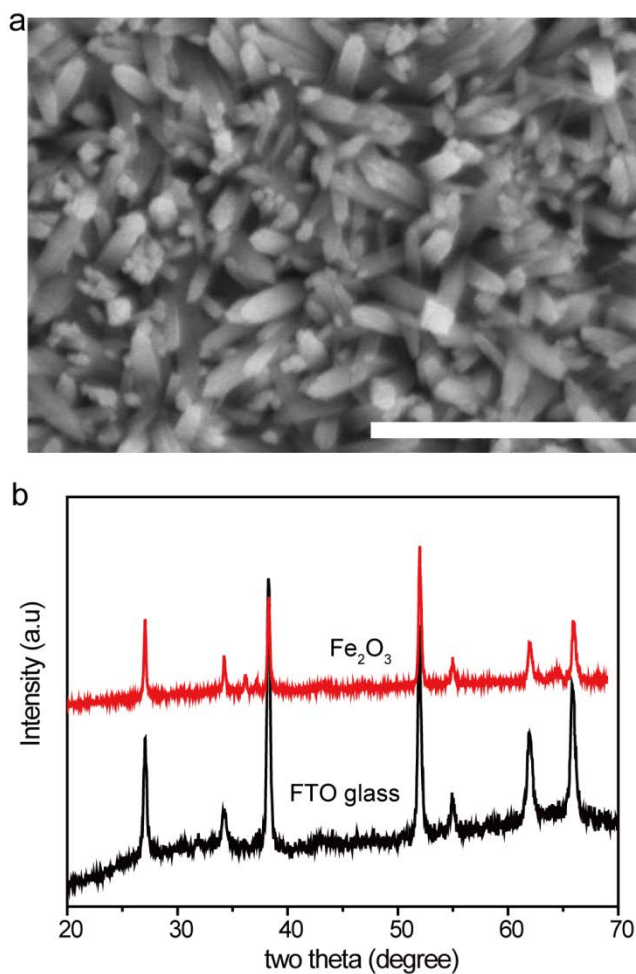


**Figure 9.9** SEM and XRD of Fe<sub>2</sub>O<sub>3</sub> on FTO glass.

Figure 9.10 shows the cyclic voltammograms collected for  $\alpha$ -Fe<sub>2</sub>O<sub>3</sub> and Ni-Fe<sub>2</sub>O<sub>3</sub> in NaOH solution and urea electrolyte solution. The significantly enhanced anodic current with an onset potential of 0.3 V vs. Ag/AgCl in the

presence of urea indicates the oxidation of urea on electrode, and urea oxidation is more favorable than water oxidation.

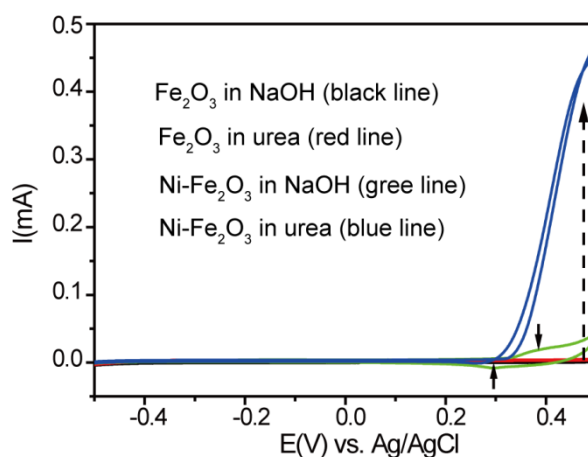


**Figure 9.10** Cyclic voltammograms of  $\text{Fe}_2\text{O}_3$  and  $\text{Ni-Fe}_2\text{O}_3$  with/without urea.

Figure 9.11a shows the linear sweep voltammograms of  $\alpha\text{-Fe}_2\text{O}_3$  and  $\text{Ni-Fe}_2\text{O}_3$  in urea solution under light illumination. As expected, the onset potential for urea oxidation substantially shift to more negative potential of  $-0.1\text{ V}$  vs.  $\text{Ag/AgCl}$ , due to the photovoltage generated in  $\alpha\text{-Fe}_2\text{O}_3$ . In comparison to  $\text{TiO}_2$  electrode,  $\alpha\text{-Fe}_2\text{O}_3$  electrode needs a larger external bias for urea oxidation due to the relative low lying conduction band of  $\alpha\text{-Fe}_2\text{O}_3$ . Significantly, the onset potential for  $\text{Ni-Fe}_2\text{O}_3$  negatively shifted for more than  $400\text{ mV}$ , compared to  $\alpha\text{-Fe}_2\text{O}_3$ . This result supports that  $\text{Ni(OH)}_2$  serve as a efficient electrochemical catalyst for urea oxidation. Furthermore, similar linear sweep voltammogram was obtained for  $\text{Ni-Fe}_2\text{O}_3$  electrode in a urine electrolyte solution (Figure

9.11b). These results confirm that solar driven urea oxidation can also be achieved on  $\alpha$ - $\text{Fe}_2\text{O}_3$  electrodes.

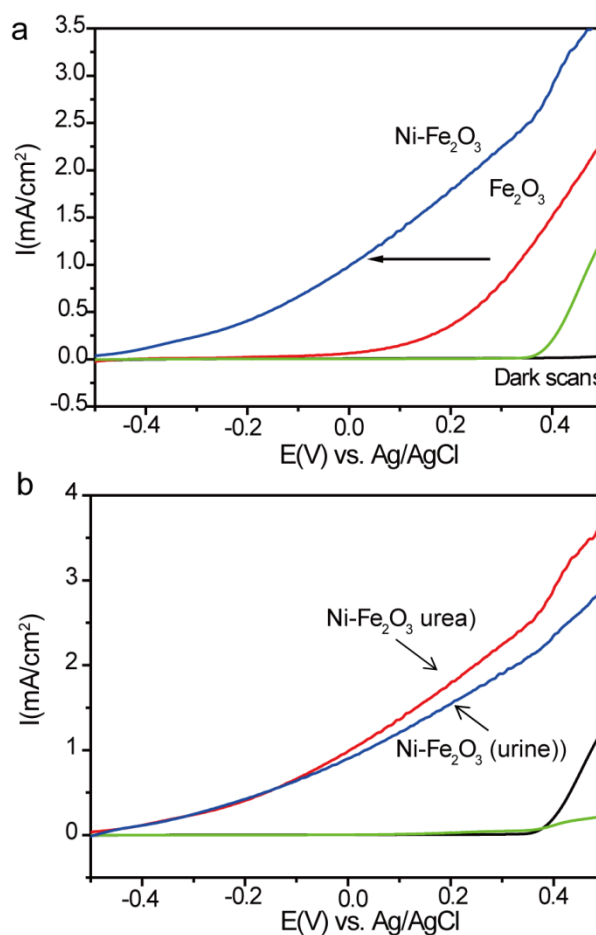


**Figure 9.11** (a) I-V curves of  $\text{Fe}_2\text{O}_3$  and  $\text{Ni-Fe}_2\text{O}_3$  in urea solution. (b) I-V curves of  $\text{Ni-Fe}_2\text{O}_3$  in urea and human urine solution.

## Conclusion

We have developed a simple, low-cost and safe method for hydrogen production from urea and directly from human urine, with the assistance of solar light and metal oxide photoelectrodes such as  $\text{TiO}_2$  or  $\alpha$ - $\text{Fe}_2\text{O}_3$ . By using  $\text{Ni(OH)}_2$  modified  $\text{TiO}_2$  nanowire arrays as photoelectrode, we demonstrated solar driven

urea oxidation at zero bias, in both urea electrolyte solution and urine electrolyte solution. Urea oxidation also achieved on Ni(OH)<sub>2</sub> modified  $\alpha$ -Fe<sub>2</sub>O<sub>3</sub> nanowire arrays under a small external bias. Ni(OH)<sub>2</sub> served as a good electrochemical catalyst by shifting the onset potential for urea oxidation by more than 400 mV. Importantly, hydrogen gas evolved at the Pt counter electrode under light illumination, and both Ni-TiO<sub>2</sub> and Ni-Fe<sub>2</sub>O<sub>3</sub> electrodes showed excellent stability for urea oxidation. The successful demonstration of solar driven hydrogen releasing from human urine could provide a sustainable solution for hydrogen production and new insights for wastewater treatment.

## Reference

1. J. Graetz, *Chem. Soc. Rev.*, 2009, **38**, 73-82.
2. Y. H. P. Zhang, *Energy Environ. Sci.*, 2009, **2**, 272-282.
3. R. Bardhan, A. M. Ruminski, A. Brand and J. J. Urban, *Energy Environ. Sci.*, 2011, **4**, 4882-4895.
4. Y. Z. Lu, R. T. Jin and W. Chen, *Nanoscale*, 2011, **3**, 2476-2480.
5. L. F. Wang and R. T. Yang, *Energy Environ. Sci.*, 2008, **1**, 268-279.
6. A. N. Rollinson, J. Jones, V. Dupont and M. V. Twigg, *Energy Environ. Sci.*, 2011, **4**, 1216-1224.
7. M. G. Walter, E. L. Warren, J. R. McKone, S. W. Boettcher, Q. X. Mi, E. A.

- Santori and N. S. Lewis, *Chem. Rev.*, 2010, **110**, 6446-6473.
- 8.F. Qian, G. M. Wang and Y. Li, *Nano Lett.*, 2010, **10**, 4686-4691.
- 9.D. W. Himmelberger, C. W. Yoon, M. E. Bluhm, P. J. Carroll and L. G. Sneddon, *J. Am. Chem. Soc.*, 2009, **131**, 14101-14110.
10. S. Satyapal, J. Petrovic, C. Read, G. Thomas and G. Ordaz, *Catal. Today*, 2007, **120**, 246-256.
11. B. K. Boggs, R. L. King and G. G. Botte, *Chem. Commun.*, 2009, **32**, 4859-4861.
12. R. L. King and G. G. Botte, *J. Power Sources*, 2011, **196**, 2773-2778.
13. J. Kim, D. Monllor-Satoca and W. Choi, *Energy Environ. Sci.*, 2012, **DOI: 10.1039/C2EE21310A**.
14. G. Thomas and G. Parks, *Potential Roles of Ammonia in a Hydrogen Economy: a Study of Issues Related to the Use of Ammonia for onboard Vehicular Hydrogen Storage*, 2006, US Department of Energy, Washington, DC
15. Y. C. Ling, G. M. Wang, J. Reddy, C. C. Wang, J. Z. Zhang and Y. Li, *Angewandte Chemie International Edition*, 2012, **51**, 4074-4079.
16. Y. C. Ling, G. M. Wang, D. A. Wheeler, J. Z. Zhang and Y. Li, *Nano Lett.*, 2011, **11**, 2119-2125.
17. K. Sun, Y. Jing, C. Li, X. Zhang, R. Aguinaldo, A. Kargar, K. Madsen, K. Banu, Y. Zhou, Y. Bando, Z. Liu and D. Wang, *Nanoscale*, 2012, **4**,

1515-1521.

18. G. M. Wang, Y. C. Ling, H. Y. Wang, X. Y. Yang, C. C. Wang, J. Z. Zhang and Y. Li, *Energy Environ. Sci.*, 2012, **5**, 6180-6187.
19. G. M. Wang, H. Y. Wang, Y. C. Ling, Y. C. Tang, X. Y. Yang, R. C. Fitzmorris, C. C. Wang, J. Z. Zhang and Y. Li, *Nano Lett.*, 2011, **11**, 3026-3033.
20. G. M. Wang, X. Y. Yang, F. Qian, J. Z. Zhang and Y. Li, *Nano Lett.*, 2010, **10**, 1088-1092.
21. X. Y. Yang, A. Wolcott, G. M. Wang, A. Sobo, R. C. Fitzmorris, F. Qian, J. Z. Zhang and Y. Li, *Nano Lett.*, 2009, **9**, 2331-2336.
22. J. Hensel, G. M. Wang, Y. Li and J. Z. Zhang, *Nano Lett.*, 2010, **10**, 478-483.
23. Y. J. Lin, S. Zhou, X. H. Liu, S. Sheehan and D. W. Wang, *J. Am. Chem. Soc.*, 2009, **131**, 2772-2773.
24. G. M. Wang, Y. C. Ling, D. A. Wheeler, K. E. N. George, K. Horsley, C. Heske, J. Z. Zhang and Y. Li, *Nano Lett.*, 2011, **11**, 3503-3509.
25. I. S. Cho, Z. Chen, A. Forman, D. R. Kim, P. M. Rao, T. F. Jaramillo and X. L. Zheng, *Nano Lett.*, 2011, **11**, 4978-4984.
26. L. Li, Y. Yu, F. Meng, Y. Tan, R. J. Hamers and S. Jin, *Nano Lett.*, 2012, **12**, 724-731.
27. Y. J. Lin, G. B. Yuan, S. Sheehan, S. Zhou and D. W. Wang, *Energy*

- Environ. Sci.*, 2011, **4**, 4862-4869.
28. H. L. Zhou, Y. Q. Qu, T. Zeid and X. F. Duan, *Energy Environ. Sci.*, 2012, **DOI: 10.1039/C2EE03447F**
29. Y. Li and J. Z. Zhang, *Laser Photon. Rev.*, 2010, **4**, 517-528.
30. H. Y. Wang, G. M. Wang, Y. C. Ling, M. Lepert, C. C. Wang, J. Z. Zhang and Y. Li, *Nanoscale*, 2012, **4**, 1463-1466.
31. G. M. Wang, X. H. Lu, T. Zhai, Y. C. Ling, H. Y. Wang, Y. X. Tong and Y. Li, *Nanoscale*, 2012, **DOI: 10.1039/C2NR30302G**
32. D. A. Wheeler, G. M. Wang, Y. C. Ling, Y. Li and J. Z. Zhang, *Energy Environ. Sci.*, 2012, **DOI: 10.1039/C2EE00001F**